The Modelling and Design of Radio Tomography Antennas

Declan Richard Vogt

A thesis presented for the degree of Doctor of Philosophy

Department of Electronics
University of York

September 2000

Abstract

In this thesis, Radio Tomography is the name of a geophysical technique for imaging the attenuation of high frequency continuous wave radio waves in the plane between two boreholes in the earth. One of the central problems of radio tomography imaging is the conversion from measured field strength to attenuation. To create tomographic images from cross-hole radio-wave amplitude data, the gain of the antennas is required.

A Finite-Difference Time-Domain modelling code has been written to model radio tomography antennas. Experimental measurements of rock properties are incorporated into the code through the use of materials with multiple Debye relaxation times. The first novel contribution reported here is the adaption of the modelling code to radio tomography antennas by using a novel subcell extension to efficiently model thin insulating layers around thin wire antennas.

The gain of arbitrary electric dipole antennas can now be calculated as a function of frequency and rock type and used improve the quality of RT images. The rock dependent conversion of measured signal strength to attenuation is the second novel contribution reported here.

Modelling also shapes the way that new antennas are designed: all the antennas modelled performed poorly when they were less than half a wavelength long. Insulated antennas have more predictable performance, as the wavelength is determined predominantly by the insulation rather than by the surrounding rock. They are physically longer than bare antennas so a hybrid antenna is proposed as a compromise. The final novel contribution reported in this thesis is the design of a hybrid insulated/bare RT antenna and receiver system.

The numerical model shows that it is not possible to simply isolate the antenna from the geometry of the rock around it, as assumed by straight ray path inversion models. The modelling technique developed here can be used as the forward model of a full wave inversion, to further improve of RT images.

Contents

List of Figures

List of Tables

Acknowledgements

I would like to acknowledge the help and assistance of my supervisors, Julian Tealby and Andy Marvin at the University of York. I have benefited greatly from their guidance and experience. The workshop staff at the University were very helpful especially Pete Dirkin and Mark Hough. I would also like to thank Bal Randhawa for his encouragement during the early part of this work and for passing on his enthusiasm for the Finite-Difference Time-Domain Method; Ian Flintoft for many helpful discussions on aspects of computational electromagnetics; and Yee Hui Lee for guiding me in the ways of genetic algorithms.

I must thank the CSIR for sponsoring the bulk of my work. Within the CSIR I am indebted to many people for their support before and during my studies. I would like to thank Eric Wedepohl, Jochen Schweitzer and Jeanne Tricket for their roles in enabling me to undertake this work. For many interesting technical discussions on Radio Tomography, I'd like to thank Eric again, Michael Van Schoor and Andrew Kramers. Thanks also to Margaret Swan for administering my affairs in my absence. A lot of other people at the CSIR have assisted me, while working on RT. I'd like to thank Martin Higginson, Karlo Walker, Reinhard Bilgeri, Roy Maritz and Andrew Kelly in particular. I'd also like to thank Fred Stevenson for his financial support of an untried technique while he was at Gold Fields and Mark Grodner for answering my geology questions.

Finally, I would like to thank my wife Fatima for her support at every level, without which it would not have been possible for me to complete this work.

Declaration

I declare that the work in this thesis is my own work, except where indicated. It has not been submitted previously in its entirety or in part for any other degree at this or any other university. Work contained in this thesis has been previously reported in:

Vogt, D. R., Tealby, J. M. and Marvin, A. C. (1999). Modelling of radio tomography antennas using the Finite-Difference Time-Domain technique. In *IEE Conference Publication 461*, pages 225–229.

Vogt, D. R., Tealby, J. M. and Marvin, A. C. (2000). Optimizing the design of a Geophysical Radio Tomography Antenna. In *AP-2000, Millenium conference on Antennas and Propagation*, ESA Publication SP-444, page 351.

For Vincent and Luke.

1

Introduction

The field of study of Geophysics consists of the techniques that allow us to determine details of the interior of the earth from measurements of physical properties made outside the volume of interest. It varies in scale from the planetary seismic measurements that determined the existence and position of the Moho discontinuity and the core-mantle boundary (Mohorovičić, 1910), to Ground Penetrating Radar (GPR) surveys of stress fracturing a few centimetres from the rock face in deep level mine workings(Grodner, 1998).

Geophysical techniques can be divided into those that are passive and those that are active. Passive techniques measure a parameter such as gravity or magnetic field, while those that are active, measure the response of the earth to an applied signal. Active techniques can make use of potential sources such as DC current, or wave sources including sonar and radio waves. Each type of source can be used to distinguish certain properties of the earth.

Radio Tomography (RT) is an active geophysical technique: a single frequency radio wave is transmitted from one borehole to another to determine the attenuation between the boreholes. If many transmitter and receiver positions are used, a tomographic image of the attenuation of the rock between the two boreholes can be created.

RT is analogous to a scaled up medical Computed Tomography or CT scan. A CT scan is created by transmitting X-rays at many angles through the body of a patient to create an image of X-ray attenuation.

In the same way that X-ray attenuation in the body corresponds to tissue density, radio wave attenuation in rock corresponds to electrical conductivity. Tissue density images can be used to infer information about the internal organs of a patient; electrical conductivity images can be used to infer the geology of the rock in the image plane.

RT is a high-resolution technique, useful for second phase exploration (Wedepohl, 1996). After an orebody has been discovered using regional scale geophysical techniques or more conventional geological techniques, it must be delineated. The delineation is ongoing, starting with an estimate of the size of the orebody for economic decision making. In practice, for many orebodies this can be done using a technique with a range of between 50 and 200 m with a resolution of a few metres. Once mining is underway more accurate mapping is required to guide operations. RT is intended to assist with strategic mine planning, providing information three to six months ahead of mining.

Geophysical tools have some trade-off between range and resolution. For most active wave based techniques, increasing the frequency of the waves used increases the resolution while decreasing the range. The trade-off point for a particular technique can be improved by using equipment with higher power, but there are diminishing returns. Alternatively, a different technique could be applied. In environments where radio propagation is feasible at ranges of 100 m – 200 m, the frequency required for penetration usually allows RT to achieve the desired resolution of a few metres.

The earlier comparison between RT and CT ignored some important differences between the two techniques:

- CT achieves complete angular coverage in the plane of the image, by scanning the patient from every angle through an arc of 180°. RT is limited to those angles that can be achieved by moving the transmitter and receiver to the limits of their boreholes.
- The CT source produces X-rays with accurately controlled energy confined to narrow beams. The X-ray receiver is similarly well understood and the patient doesn't affect the characteristics of the source or the receiver. In RT, the source and receiver are electric dipole antennas in rock. Antenna gain and pattern are both required for imaging,

but change as a function of rock type. An incorrect estimate of either parameter can lead to artefacts in the image that is produced.

Inversion is the process of turning measured data into an image. The limitation in angular coverage leads to inherent ambiguity in RT images, reducing their horizontal resolution. In practice, many images can fit the measured data, so a single image has to be chosen by optimizing some characteristic of the image. Inversion is a large and active field of study in its own right and is not considered in this thesis.

The Division of Mining Technology of the CSIR in Johannesburg (Miningtek), has built an RT system for sale (Vogt, 1995). There is room for improvement in its performance by better understanding the physics behind its radio antennas. The work reported in this thesis was initiated to improve its performance by overcoming the second problem listed above: the conversion of measured signal strength data to attenuation. To do so, a good model for antenna gain is required. Such a model will also lead to better imaging procedures and to design criteria for future antennas.

Chapter 2 describes the RT technique in detail and compares it to other geophysical techniques that use similar principles. The basic RT equation is derived and examined in detail to determine how the system design and the rock properties of the target application influence RT data quality. The electrical properties of rock in the frequency band of interest are investigated through the processing of Miningtek's electrical properties database. The chapter will be of interest to people using RT and other electromagnetic geophysical techniques including GPR and borehole radar.

Chapter 3 introduces Computational Electromagnetics (CEM) as a technique suitable for modelling RT antennas and systems. The Finite–Difference Time–Domain (FDTD) method is motivated as the technique to be applied for RT modelling in this thesis. The chapter will be of interest to readers not familiar with CEM who wish to gain an introduction to the techniques available.

Chapter 4 describes the FDTD code written to model RT antennas. The chapter provides a thorough introduction to the FDTD technique and a detailed derivation of the novel extension written to model

insulated dipole antennas buried in rock. The model has body-of-revolution (BOR) symmetry and can model Debye dispersive media with more than one relaxation time. The model is verified in detail, both numerically and by comparison with experiment. The chapter should satisfy a reader who wishes to understand the detailed design decisions made in the implementation of the FDTD model that is used to model various RT antennas in later chapters.

In Chapter 5, the model is applied to simple RT antennas. The aim of the chapter is to discover how the basic parameters of a dipole antenna are influenced by rock. Bare and insulated antennas are modelled and the advantages and disadvantages of insulation are discussed. A hybrid antenna is proposed as a compromise for RT imaging. Readers involved with borehole antennas should find the results interesting.

Chapter 6 contains a series of case studies of RT antennas in RT problem environments. The case studies have been selected to highlight how rock influences RT antennas and also how antennas interact with their support structure and other antennas. The chapter will be of greatest interest to people working directly with RT as a geophysical imaging method.

In Chapter 7, the lessons learnt in Chapters 4–6 are drawn together and proposals are made for extending the work reported in this thesis. In particular: the numerical model developed here should be incorporated as the forward model in a full wave inversion scheme.

2

Radio Tomography

2.1 INTRODUCTION

The idea of using radio waves to image targets in the ground isn't new: the first patent was issued to Hülsmeyer in 1904 (Noon, 1996). Since the 1950s, GPR systems based on the reflection of radio waves by targets in the ground have been described. The technique has moved from being a scientific curiosity to being a regular subsurface imaging technique (Turner, 1993). The time-domain representation of reflected waves in early GPR systems was very convenient, because it was in the same form as the data captured by seismic systems. Techniques for interpreting time domain reflection data were well developed and understood at the time.

RT is similar to GPR in that it uses radio waves to image targets within the ground, but it differs from GPR in two ways: it is normally conducted at one frequency in the frequency domain rather than in the time domain; and it measures the transmission of radio waves, rather than their reflection.

RT can be thought of as a scaled-up version of the medical CT scan. In a CT scan, X-rays are used to illuminate a human body. Dense tissues such as bone absorb X-rays more than less dense tissues such as skin. In RT, radio waves are used to illuminate the rock in the plane between two boreholes. Conductive rock absorbs the radio waves more than resistive rock. In a CT scanner, the X-ray equipment

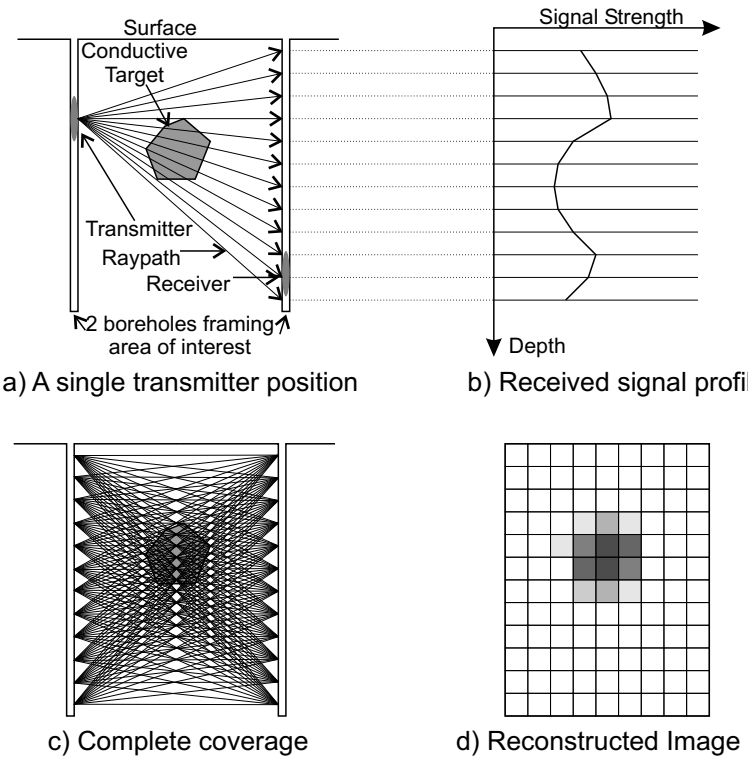

Figure 2.1: The RT imaging process.

is rotated around the body to illuminate a slice through the body from every direction. The attenuation data collected can then be inverted by computer to produce an image of tissue density in the plane of the slice. In RT the transmitter and receiver are moved to propagate radio waves from one borehole to the other at various angles. The resulting data is inverted to produce an image of rock conductivity.

The RT process is illustrated in Figure 2.1. The area of interest is framed by two boreholes. A radio transmit antenna is lowered in one borehole, while a receive antenna is lowered in the other borehole. If the transmit antenna is fixed at one position, the receive antenna can be moved along the length of its borehole, recording a profile of signal strength (Figure 2.1a and b). If the transmitter is then moved to different positions along the length of its borehole, a succession of profiles can be collected (Figure 2.1c). The received signal strength is converted to attenuation and inverted to produce an image of the rock conductivity between the two boreholes. Often the conductivity corresponds to geology and can give insight into the structure of the

rock in the plane between the boreholes (Figure 2.1d).

Inverting the data to produce an output image is an interesting problem, because there are infinitely many images that can fit a given RT data set. In mathematical terms, the problem is ill-posed and cannot be solved without some constraint. Conventional inversion algorithms such as the simultaneous iterative reconstruction technique, or SIRT , become seriously degraded in the presence of noise (Wedepohl, 1993; Lager and Lytle, 1977). Miningtek uses the Maximum Entropy constraint in the inversion process. The inversion attempts to create the image with the maximum entropy or least structure in a mathematical sense. The maximum entropy algorithm has shown itself to be stable in the presence of noise and to create good reproductions of synthetically modelled data, but improvements are possible (Van Schoor et al., 1997).

Inverting geophysical data is a large and active area of research in itself. It is not considered further in this thesis.

The value of RT is its ability to deliver more information from existing exploration boreholes, or to deliver a similar amount of information to that currently obtained using fewer boreholes. With boreholes costing in the region of £25/metre in 1999 (Stevenson, *pers. comm.*) RT is economically attractive.

2.1.1 Radio imaging systems

Transmission techniques for geophysical radio imaging cover a wide frequency spectrum. Reflection techniques are usually only used at higher frequencies. GPR is a reflection technique that relies on the reflection of waves from discontinuities: abrupt changes in electrical properties. Fracturing is a common target for GPR, as are the interfaces between layers of different materials. By contrast, RT is a transmission technique. It can produce images of targets where there is no clearly defined boundary between the target and the host rock. Disseminated sulphide mineralization is a good RT target, because the rock becomes gradually more conductive towards the center of the mineralized area.

Because reflection techniques detect discontinuities, they are sens-

itive to very thin structures. The response of a transmission technique is an average of the volume between transmitter and receiver. For both techniques, range and resolution are a function of frequency.

GPR systems equipped with borehole antennas can be used to acquire cross-hole tomographic data, but it is normally processed to produce images of velocity rather than attenuation (Saito et al., 1990; Vasco et al., 1997). Borehole radar is normally used at higher frequencies than RT, typically 100 MHz – 1000 MHz. Tomographic imaging only became possible with the advent of fast, cheap computers in the mid 1980s (Wedepohl, 1993). At that time, borehole radar equipment existed and could easily be applied to the imaging problem. Tomography was not routine, possibly because at GPR frequencies resolution is more important than range. Continuous wave GPR systems can normally achieve better performance, because of their higher average power (Hamran et al., 1995; Noon, 1996).

At the opposite end of the frequency spectrum are radio techniques operating at very low frequencies. These are often referred to as the Radio Imaging Method, or RIM, after the name of a commercial system (Stolarczyk, 1992). The low frequency systems have the advantage of considerable range, but at the cost of relatively poor resolution. They have been applied in coal field mapping, (Greenfield and Wu, 1991), oil-shale retort monitoring (Daly, 1984; Somerstein et al., 1984) and oil field characterization (Wilt et al., 1995). Frequencies as low as 8 Hz have been used, although the technique then becomes very similar to conventional borehole electromagnetic geophysics (Takasugi et al., 1996).

The Miningtek RT system hardware was originally inspired by Nickel and Cerny (1989) who used continuous wave radio waves at HF frequencies in an empirical method they called the “radio wave shadow” method. Rao and Rao (1983) use much the same type of technique. There is not much literature in English on Russian radio wave shadowing work, but Buselli (1980) claims that about 300 systems were in use in the Soviet Union in 1980. At HF–UHF, RT has been used for tunnel and cavity detection (Degauque et al., 1992; Côte et al., 1995) and mineral exploration (Yu et al., 1998; Fullagar et al., 1996; Zhou et al., 1998). Miningtek has also undertaken a con-

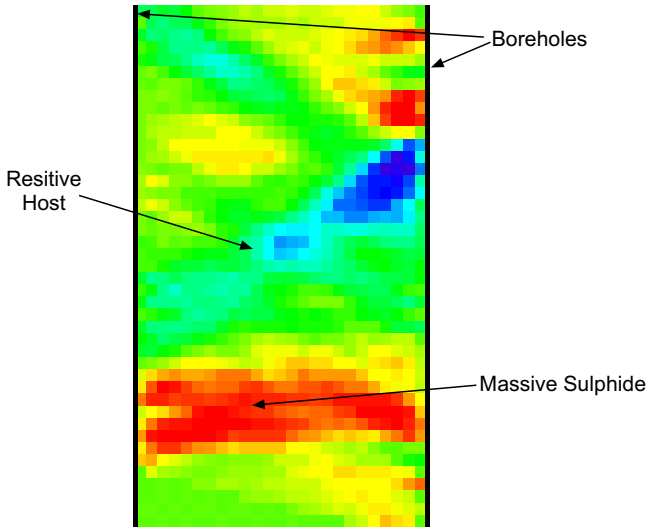

Figure 2.2: An RT image of a massive sulphide prospect. The hotter colours are the more conductive target rock and the cooler colours are the more resistive host rock.

siderable number of RT surveys, mostly for base metal exploration (Pitts and Kramers, 1995; Van Schoor et al., 1997).

RT occupies a niche between RIM and borehole radar because of its frequency and imaging method. In favourable environments it can operate over 50 m – 200 m while delivering resolution of a few metres. The other radio imaging systems use different frequencies to image with greater resolution or longer range.

2.1.2 Real constraints

In reality, RT works very well in environments where the host rock is resistive, with a loss tangent of less than about 0.1, and the target is more conductive (Van Schoor et al., 1997). Possibly the best such environments are massive sulphide orebodies in resistive hosts. An example of an RT image is shown in Figure 2.2.

Base metal targets are usually sampled using diamond drilling: boreholes are drilled into the orebody using a drill bit that consists of a hollow rod, with diamond teeth around the circumference of the open end. Drilling normally proceeds for the length of one drill rod. The whole drill string is then removed from the borehole and the

core is extracted from the drill rod. The process is then repeated, with an additional rod added to the drill string after each piece of core is extracted (Heinz, 1985). Diamond drilled holes provide core that is invaluable to geologists, but in hard rock environments they are usually relatively narrow and are expensive to drill.

The narrow diameter of the drill hole provides the practical limitation to RT equipment: it has to fit into existing boreholes. Exploration in hard rock environments is typically undertaken using equipment that drills holes with a diameter of 48, 72 or 96 mm. Drilling is often carried out on a grid of 100 m or 200 m. Ideally, RT should offer sufficient range to fit in with the existing drilling grid, but additional holes may be drilled specifically for RT if the results have enough value.

At ranges of 100 m – 200 m, in low to medium conductivity host rocks, the minimum wavelength required for penetration is typically of the order of several metres. Two choices of antenna present themselves: electric and magnetic. Magnetic antennas require area to be efficient and area is not available in typical narrow boreholes, so electric antennas are used. The borehole shape simplifies the choice of antenna further to electric dipoles and these are the only antennas considered in this thesis.

2.1.3 A practical RT *system*

Before I started work on this thesis, I was involved in the design of a commercial RT system (Vogt, 1995). That system is described as background to the work undertaken here.

An RT system consists of a transmit antenna, a receive antenna, a positioning system and a data recording system. The transmit antenna needs to be driven by a transmitter and the signal at the receive antenna needs to be measured. At its most fundamental, an RT system can consist of an HF transmitter, two lengths of coaxial cable, two antennas and a measurement receiver. Data can be measured manually and recorded in a notebook and position can be controlled by lowering the antennas on their coaxial cables.

For routine surveying, several elements need to be added:

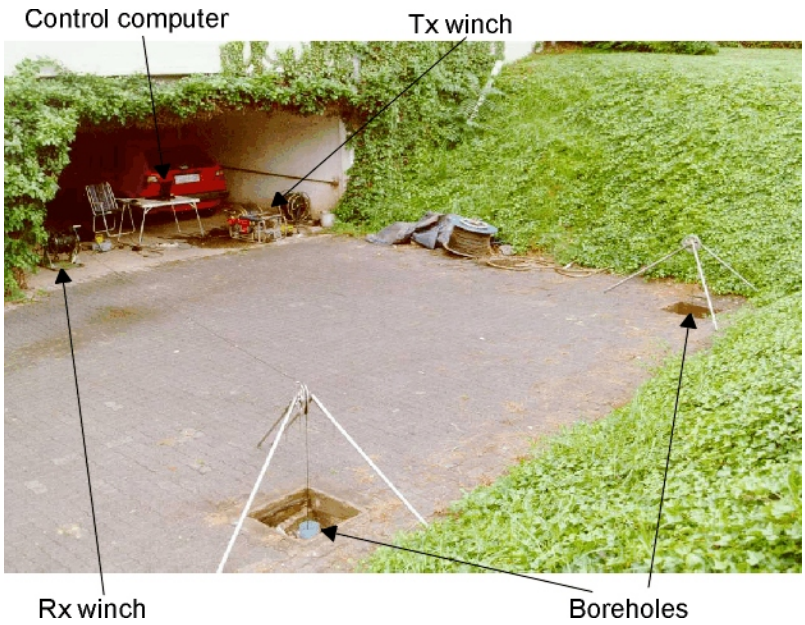

Figure 2.3: The test site.

- If the antennas are suspended on optical fibre, the cable is guaranteed not to interfere with the antenna electrically.
- Data capture should occur on a computer, to automate all routine tasks.
- Automatic winching removes the last requirement for manual intervention during a routine survey.

The Pluto–6 system

The Miningtek Pluto–6 system meets all the requirements listed above. It consists of a ruggedized PC for data acquisition and control, a pair of computer controlled winches, a transmitter probe and a receiver probe. The winches are each loaded with 1000 m of optical fibre cable. The transmitter and receiver probes are both insulated electric dipole antennas. In the central portion of the probe, the two arms of the dipole contain the battery and the probe electronics. The length of the dipole can be adjusted by adding extensions to the top and the bottom of the probe. In Figure 2.3 the system is shown in use on a test site at Miningtek.

The transmitter is based around a direct digital synthesis integrated circuit that can synthesize a sine wave having any frequency

from less than 1 Hz up to 30 MHz. The synthesizer feeds a power amplifier with gain control followed by a power meter. The power meter measures the real power delivered to the antenna and the on-board microprocessor adjusts the gain to maintain the real power at 1 W as far as possible. The transmitter is capable of delivering 1 W into loads of between 20 Ω and 200 Ω.

The receiver is a microprocessor controlled superhet design and uses a simple digital divider to provide its local oscillator (LO). Two crystals, of 24 and 36 MHz are divided down to provide a choice of 19 discrete frequencies between 1 MHz and 30 MHz. The input amplifier has an impedance of 50 Ω. There is a narrow band filter to lower the noise floor, followed by a detector and analogue to digital converter (ADC).

The winch controllers provide low level control of probe depth, and also function as communications switches. They route communications from the control computer to their attached probes, or to the other winch controller. Distributing intelligence to the winch controllers and probes leads to simpler, more reliable communications links and reduces the load on the control PC (Vogt, 1995).

The control PC runs software that acquires RT data while allowing the operator to monitor data quality as each data point is acquired. The operator can also use the software to edit data, to remove bad points and to invert the data to produce output images. Once an image is available, it is exported to an image processing package for a colour table and annotation to be added, then released to the customer.

The probes are completely insulated dipoles. The probe housing is a tube of high-strength glass fibre, containing the antenna arms made of conductive copper tube. The upper antenna extension is a piece of insulated wire, with a core diameter of 4 mm and an insulation thickness of 1 mm. The probe itself has 3 mm of glass-fibre insulation, with a relative permittivity of 2.1. The lower antenna extension is contained within hydraulic hose to ensure that it descends below the probe, rather than becoming entangled around it. Although the conductor is also about 4 mm in diameter, the total thickness of insulation, consisting of air and a variety of plastics, is about 10 mm. The total dipole length can be varied between 4 m and 16 m using the

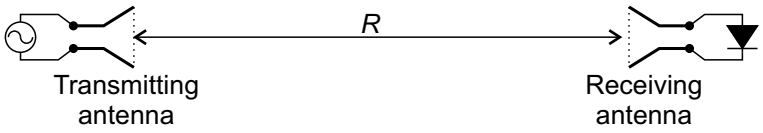

Figure 2.4: Configuration for calculation of the Friis equation, from Balanis (1982).

extensions.

2.2 THE RT EQUATION

RT data is collected as a series of measurements of transmitted power and received signal strength. To invert the data to produce an attenuation image, the relationship between attenuation and the measured quantities has to be defined. The resulting equation is the RT equation.

The power density, W_t, at a distance R from a transmitting antenna buried in an lossy homogenous medium is given by (Balanis, 1982)

$$W_t = \frac{P_t G_t(\theta_t, \phi_t)}{4\pi R^2} \mathrm{e}^{-2\alpha R} \tag{2.1}$$

where P_t is the power applied to the terminals of the transmitting antenna, G_t is the gain of the antenna in the direction (θ_t, ϕ_t) and α is the attenuation constant of the medium.

A receive antenna will convert the power density flowing past it into received power, as shown in Figure 2.4. The antenna has an effective capture area or aperture of A_e, given by

$$A_e = G_r(\theta_r, \phi_r) \frac{\lambda^2}{4\pi} \tag{2.2}$$

where G_r is the receive antenna gain and λ is the wavelength in the medium (Balanis, 1982). The power received is then simply $P_r = A_e W_t$. Expressed as a proportion of power transmitted, the power received is

$$\frac{P_r}{P_t} = \left(\frac{\lambda}{4\pi R}\right)^2 G_t G_r \mathrm{e}^{-2\alpha R} \tag{2.3}$$

Equation 2.3 is the Friis Transmission Equation (Balanis, 1982), modified for transmission through a lossy medium. In the form given

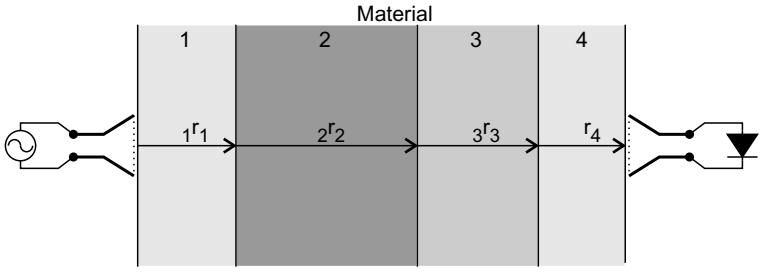

Figure 2.5: The need for a path integral expression for the attenuation.

in Equation 2.3, the antennas are assumed to have the same polarization and the medium is assumed to be isotropic, so the polarization of the transmission is not changed between the two antennas. The term $(\lambda/4\pi R)^2$ is called the free-space loss factor (Balanis, 1982) and the factor $\mathrm{e}^{-2\alpha R}$ is the attenuation.

In an RT system, the ground is not homogenous. The situation is illustrated in Figure 2.5. In RT the reflections across the boundaries are ignored because in practice the boundaries are usually diffuse. If the boundaries are expected to be as sharp as those shown in the figure, GPR or borehole radar may be more appropriate techniques.

In Figure 2.5, the total attenuation is the sum of the attenuation in each material. In general, the total attenuation is the integral of attenuation along the path:

$$a_{\mathrm{tot}} = \mathrm{e}^{2\int_0^R -\alpha.dr} \tag{2.4}$$

Notice that attenuation is in addition to the free-space spreading, which must also be taken into account. If the path integral is inserted into the Friis transmission equation, 2.3, the resulting equation is the basic form of the RT equation:

$$\boxed{\frac{P_r}{P_t} = \left(\frac{\lambda}{4\pi R}\right)^2 G_t G_r \mathrm{e}^{2\int_0^R -\alpha.dr}.} \tag{2.5}$$

It is useful to convert equation 2.5 into decibels by taking $10\log_{10}$ of both sides. I also introduce a different unit of attenuation, $\alpha^* = 8.686\alpha$, where α^* is attenuation in dB/m and α is attenuation in

Nepers/m. The RT equation can then be written as:

$$\begin{aligned}\int_0^R \alpha^*.\,\mathrm{d}r &= P_{t_{\mathrm{dB}}} + 10\log_{10}\left(\frac{\lambda^2 G_t G_r}{(4\pi R)^2}\right) \\ &- P_{r_{\mathrm{dB}}}. \end{aligned} \tag{2.6}$$

The RT problem is the inversion of Equation 2.5 and is normally written in the form of Equation 2.6: the transmitted and received powers are known, or can be calculated and the distribution of attenuation must be discovered. A very simple example is illustrated in Figure 2.6.

Equation 2.6 expresses the unknown distribution of attenuation as a function of the transmitted power, the received power, the distance between transmitter and receiver and the performance of the antennas. If the antenna effects are separated out from the spreading, the equation becomes

$$\begin{aligned}\int_0^R \alpha^*.\,\mathrm{d}r &= P_{t_{\mathrm{dB}}} + 10\log_{10}\left(\frac{1}{4\pi R^2}\right) \\ &+ 10\log_{10}\left(\frac{G_t G_r \lambda^2}{4\pi}\right) \\ &- P_{r_{\mathrm{dB}}}. \end{aligned} \tag{2.7}$$

Equation 2.7 is expressed in terms of both transmitted power and received power. In practice, received power is measured by measuring voltage. The received power is is a consequence of the effective aperture of the receive antenna, $A_e = G\lambda^2/4\pi$, so it is defined with the receive antenna terminated into a conjugate matched load. The open circuit voltage of the receive antenna is then given by

$$V_{r_{oc}} = 2\sqrt{P_r R_r} \tag{2.8}$$

where $R_r = \Re(Z_r)$ is the real part of the antenna impedance. If the antenna feeds a receiver that does not have an infinite input impedance, then the measured voltage becomes

$$V_r = V_{r_{oc}} \frac{Z_{\mathrm{in}}}{Z_{\mathrm{in}} + Z_r}, \tag{2.9}$$

where Z_{in} is the input impedance of the receiver. The voltage divider formed by the receiver input impedance and the antenna impedance

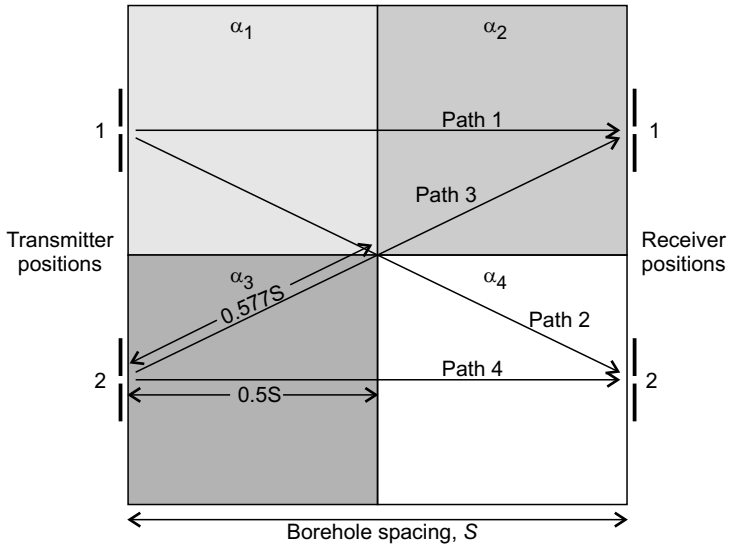

A model has four zones with different attenuation rates. By making four measurements along different raypaths, the attenuation rates can be calculated. Assume that the antenna gains are unity. Each pixel is $S/2$ square. Four equations can be written down and solved simultaneously for α_1–α_4:

$$\begin{aligned}
0.5S\alpha_1^* + 0.5S\alpha_2^* &= P_{t1} - P_{r1} + 20\log_{10}\frac{\lambda}{4\pi S} \\
0.57S\alpha_1^* + 0.57S\alpha_3^* &= P_{t1} - P_{r2} + 20\log_{10}\frac{\lambda}{4\pi 1.15S} \\
0.57S\alpha_2^* + 0.57S\alpha_3^* &= P_{t2} - P_{r1} + 20\log_{10}\frac{\lambda}{4\pi 1.15S} \\
0.5S\alpha_3^* + 0.5S\alpha_4^* &= P_{t2} - P_{r2} + 20\log_{10}\frac{\lambda}{4\pi S}
\end{aligned}$$

Figure 2.6: A simple RT example.

can be incorporated in Equation 2.8 if the resistance R_r is replaced by an effective resistance R_{re},

$$R_{re} = \left| \frac{Z_{\text{in}}}{Z_{\text{in}} + Z_r} \right|^2 R_r. \tag{2.10}$$

If the receiver has infinite input impedance then from Equation 2.10 $R_{re} = R_r$, as expected.

Taking $20 \log_{10}$ of Equation 2.8, rearranging, and noting that 0 dBV=120 dBμV,

$$P_{r_{\text{dBW}}} = V_{r_{\text{dB}\mu\text{V}}} - 126 - 10 \log_{10} R_{re}. \tag{2.11}$$

The RT equation for a system can now be written as

$$\begin{aligned} \int_0^R \alpha^*.\,\mathrm{d}r &= 126 \\ &+ P_{t_{dBW}} \\ &+ 10 \log_{10} \left(\frac{1}{4\pi R^2} \right) \\ &+ 10 \log_{10} \left(\frac{R_{re} G_t G_r \lambda^2}{4\pi} \right) \\ &- V_{r_{\text{dB}\mu\text{V}}}. \end{aligned} \tag{2.12}$$

Equation 2.12 can be rewritten in decibel units, yielding the most useful form of the RT equation:

$$\boxed{\int_0^R \alpha^*.\,\mathrm{d}r = C_u + P_{t_{dBW}} + S + A_p - V_{r_{\text{dB}\mu\text{V}}}.} \tag{2.13}$$

The five terms on the right hand side of Equations 2.12 and 2.13 are

$C_u = 126$	Conversion of units,
$P_{t_{\text{dBW}}}$	Transmitted power,
$S = 10 \log_{10}(1/4\pi R^2)$	Spherical spreading,
$A_p = 10 \log_{10}(R_{re} G_t G_r \lambda^2 / 4\pi)$	Antenna parameters,
$V_{r_{\text{dB}\mu\text{V}}}$	Received signal strength.

The transmitted power and received voltage can be measured and the spreading is simple to calculate. It is the fourth factor, the antenna term, that is not straightforward to calculate. It contains terms for the gains of the both antennas, the wavelength and the impedances of the

receive antenna and attached receiver. The gains are a function of directivity and efficiency:

$$G(\theta,\phi) = \eta D(\theta,\phi) \tag{2.14}$$

where D is the directivity of the antenna as a function of angle, compared to an isotropic radiator and η is the efficiency of the antenna. The efficiency is defined as

$$\eta = \left[\frac{R_r}{R_L + R_r}\right] \tag{2.15}$$

where R_L is the loss resistance and R_r is the radiation resistance (Balanis, 1982). For antennas in air, the loss resistance is defined by the energy lost to resistance in the conductor of the antenna itself. For antennas in rock, there can be considerable loss in the near field which has to be taken into account in calculating the efficiency. The directivity is also a function of the rock surrounding the antenna: the conductivity of the surrounding rock affects the current distribution on the antenna and hence its pattern.

2.3 THE ELECTRICAL PROPERTIES OF ROCK

The antennas of an RT system are always embedded in rock. In order to understand how the antennas work, it is useful to look at how radio waves propagate in rock.

Maxwell's equations describe how electric and magnetic fields interact with one another and with material media. The four equations for a source free region are

$$\nabla \times \boldsymbol{E} = -\frac{\partial \boldsymbol{B}}{\partial t}, \tag{2.16}$$

$$\nabla \times \boldsymbol{H} = \boldsymbol{J}_c + \frac{\partial \boldsymbol{D}}{\partial t}, \tag{2.17}$$

$$\nabla \cdot \boldsymbol{D} = 0, \tag{2.18}$$

$$\nabla \cdot \boldsymbol{B} = 0. \tag{2.19}$$

$\boldsymbol{E}$ is the electric field, $\boldsymbol{H}$ is the magnetic field, $\boldsymbol{B}$ is the magnetic field density, $\boldsymbol{D}$ is the electric displacement and $\boldsymbol{J}_c$ is the conduction current.

The equations cannot be coupled and solved until the constitutive relations are introduced:

$$\boldsymbol{D} = \hat{\varepsilon}(\omega)\boldsymbol{E}, \tag{2.20}$$

$$\boldsymbol{B} = \hat{\mu}(\omega)\boldsymbol{H}, \tag{2.21}$$

$$\boldsymbol{J}_c = \hat{\sigma}(\omega)\boldsymbol{E} \tag{2.22}$$

where $\hat{\varepsilon}$ is the permittivity, $\hat{\mu}$ is the permeability and $\hat{\sigma}$ is the conductivity of the medium.

In general, the constitutive parameters given in equations 2.20 to 2.22 are complex tensor functions of frequency. The tensors simplify to complex functions of frequency if the medium is isotropic. Most rocks are not magnetic, so have $\hat{\mu}(\omega) = \mu_0$, the permeability of free space. Magnetic media and anisotropic media are not considered further in this thesis. The complex permittivity and conductivity are

$$\hat{\varepsilon}(\omega) = \varepsilon'(\omega) + \mathrm{j}\varepsilon''(\omega), \tag{2.23}$$

$$\hat{\sigma}(\omega) = \sigma'(\omega) + \mathrm{j}\sigma''(\omega). \tag{2.24}$$

If the material has complex constitutive parameters, it is often useful to introduce two further constitutive relations (Tai, 1999):

$$\boldsymbol{D} = \varepsilon(\boldsymbol{E} + \boldsymbol{P}), \tag{2.25}$$

$$\boldsymbol{B} = \mu(\boldsymbol{H} + \boldsymbol{M}) \tag{2.26}$$

where $\boldsymbol{P}$ is the electric polarization density and $\boldsymbol{M}$ is the magnetic polarization density. Since materials with complex magnetic permeability are not discussed further here, no use is made of the magnetic polarization density either.

In general, the conductivity describes the movement of free charge and the permittivity describes the effect of bound charge in polar situations. The polar moment may be caused by the permanent dipole moment of individual molecules, or it may result from induced dipole moments or migration of ionic charges (Kong, 1986).

2.3.1 Frequency invariant material parameters

King and Smith (1981) show that it is not possible to distinguish between the effects of complex conductivity and complex permittivity at a single frequency. In general other information is needed

to determine the contribution of each to the overall behaviour of the material. It is useful to derive invariant measures of the material properties.

In an infinite, conductive, source free region, the constitutive relations and Maxwell's equations can be solved to produce a wave equation:

$$\nabla^2 \boldsymbol{E} - \mu\varepsilon\frac{\partial^2 \boldsymbol{E}}{\partial^2 t} - \mu\sigma\frac{\partial \boldsymbol{E}}{\partial t} = 0. \tag{2.27}$$

For time harmonic waves

$$\frac{\partial}{\partial t} = \mathrm{j}\omega \; ; \; \frac{\partial^2}{\partial^2 t} = -\omega^2 \; ; \tag{2.28}$$

and the wave equation reduces to the Helmholtz equation,

$$\nabla^2 \boldsymbol{E} - \mathrm{j}\omega\mu(\sigma + \mathrm{j}\omega\varepsilon)\boldsymbol{E} = 0. \tag{2.29}$$

The Helmholtz equation shows how the permittivity and conductivity are always found in combination and provides the invariant measure of electrical properties required above:

$$\sigma + \mathrm{j}\omega\varepsilon. \tag{2.30}$$

If σ and ε are both complex, the invariant property has real and complex components, which can in turn be related to effective properties. Then

$$\sigma_e(\omega) = \sigma'(\omega) + \omega\varepsilon''(\omega), \tag{2.31}$$

$$\varepsilon_e(\omega) = \varepsilon'(\omega) + \frac{\sigma''(\omega)}{\omega}. \tag{2.32}$$

Because the effective properties in equations 2.31 and 2.32 can be measured directly, they are the most widely quoted properties and the most useful for calculation. If not otherwise specified, all permittivities and conductivities in this thesis are assumed to be the real effective values of the constitutive parameters.

2.3.2 Wave propagation properties

One solution of the Helmholtz equation is given by a plane wave propagating in the z direction,

$$\boldsymbol{E} = \boldsymbol{E}(z) = \boldsymbol{n}_x E_0 \mathrm{e}^{\mathrm{j}(\omega t - kz)} \tag{2.33}$$

where k is the wavenumber, given by

$$k = \sqrt{-\mathrm{j}\omega\mu(\sigma + \mathrm{j}\omega\varepsilon)}. \tag{2.34}$$

If the medium is conductive, k is complex and can be written as

$$\hat{k} = \beta - \mathrm{j}\alpha, \tag{2.35}$$

where α, the plain wave attenuation and β, the phase constant, are given by

$$\alpha = \omega \left[\frac{\mu\varepsilon}{2} \left(\sqrt{1 + \frac{\sigma^2}{\omega^2\varepsilon^2}} - 1 \right) \right]^{1/2} \tag{2.36}$$

$$\beta = \omega \left[\frac{\mu\varepsilon}{2} \left(\sqrt{1 + \frac{\sigma^2}{\omega^2\varepsilon^2}} + 1 \right) \right]^{1/2} \tag{2.37}$$

The phase velocity is then given by

$$v = \left[\frac{\mu\varepsilon}{2} \left(\sqrt{1 + \frac{\sigma^2}{\omega^2\varepsilon^2}} + 1 \right) \right]^{-1/2}. \tag{2.38}$$

The loss tangent can be defined as

$$\tan\delta = \frac{\sigma}{\omega\varepsilon}. \tag{2.39}$$

The loss tangent categorizes materials: poor conductors, also called insulators or dielectrics, with $\sigma \ll \omega\varepsilon$, good conductors, where $\sigma \gg \omega\varepsilon$ and lossy dielectrics, or quasi conductors at intermediate values of conductivity, where $\sigma \approx \omega\varepsilon$. For RT, the host rock must usually be a dielectric or a semiconductor otherwise penetration range will be negligible.

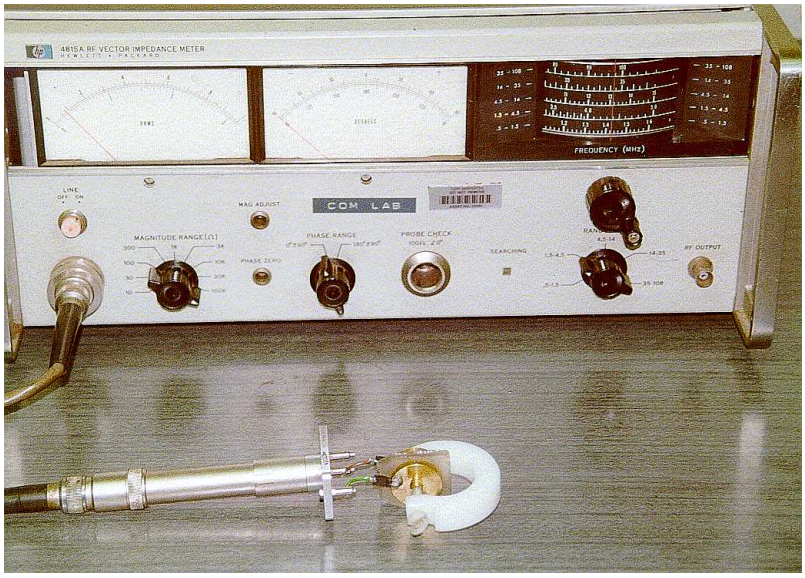

Figure 2.7: The Vector Impedance Meter, with its probe in the foreground, connected to the sample holder containing a rectangular slice of rock.

2.4 MEASURING ROCK ELECTRICAL PROPERTIES

2.4.1 Measurement technique

There are many methods for measuring the electrical properties of material samples, each with its own advantages and disadvantages. A good summary is included in Turner (1993). Miningtek uses the capacitive sensor method to measure electrical properties over a wide bandwidth from 1 MHz to 64 MHz. The rock sample is placed as the dielectric in a capacitor and the complex impedance of the capacitor is then measured. The facility is illustrated in Figure 2.7. The sample holder and measurement system were designed by Martin Higginson and the initial calculation procedure was designed by Eric Wedepohl. I devised the correction for inductance and the calculation of measurement uncertainty presented here.

A rock sample is usually available as a cylindrical piece of core, between 30 and 80 mm in diameter. The simplest way to prepare a sample is to cut a 4 mm slice from the core. After polishing, the slice

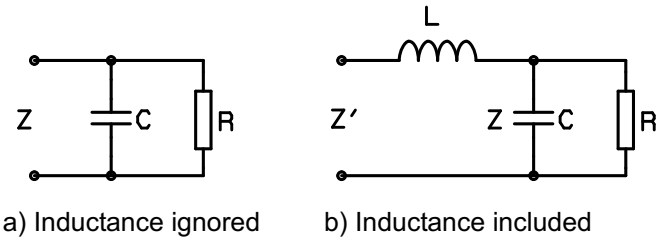

Figure 2.8: Equivalent circuits for rock property measurements.

is placed between two plates each with a diameter of 25 mm and becomes the dielectric in a capacitor. A sheet of silver foil is inserted between each plate and the rock sample to ensure good contact and a mechanism is used to hold the plates and the sample securely, as shown in Figure 2.7. The impedance of the capacitor is then measured using an HP4815A vector impedance meter. Results from the vector impedance meter are entered into a computer program to calculate the effective material properties.

The HP4815A cannot be easily automated, so the process of measurement is manual. Normally, measurements are made at seven frequencies: 1, 2, 4.4, 8, 16, 32 and 64 MHz. High accuracy is not required or expected: the main purpose of the measurements is to make performance predictions for GPR and RT .

Rock electrical properties are highly variable. Even very accurate measurements of rocks in the laboratory do not reflect their electrical properties in situ, so the measurements are made purely to get an indication of the electrical regime of the sampled rocks (Grant and West, 1965).

The vector impedance meter measures the magnitude and phase of the impedance of the test piece. If the inductance of the test leads is ignored, the test piece appears as a lossy capacitor, with the equivalent circuit shown in Figure 2.8a. Considering the cylindrical sample geometry, the capacitance and parallel loss resistance are given by

$$C = \frac{\varepsilon_0 \varepsilon_r \pi r^2}{d} \tag{2.40}$$

$$R = \frac{d}{\sigma \pi r^2}. \tag{2.41}$$

where d is the distance between the plates of the capacitor and r is the radius of the plates. There is some capacitance between the two

Table 2.1: Measurement accuracy of the HP4815A (Hewlett-Packard, 1966).

Frequency	$\pm$ 2% of reading
Impedance	$\pm$[4+(f/30) + (Z/25)]%
Phase	$\pm$ [3+(f/30)+(Z/25)]$^\circ$
where f is the frequency in MHz and Z is the impedance in kΩ.	

sides of the system other than through the sample. The simplest way to take this capacitance into account is to measure it and assume that it is in parallel to the required sample capacitance, C.

The measured parameters are given by

$$|Z| = \frac{d}{\sigma\pi r^2\sqrt{1+\frac{\omega^2\varepsilon^2}{\sigma^2}}}, \tag{2.42}$$

$$\arg Z = \arctan\frac{\varepsilon_0\varepsilon_r\omega}{\sigma}. \tag{2.43}$$

The complex impedance is then

$$Z = \frac{R}{1+\mathrm{j}\omega RC}. \tag{2.44}$$

Combining equations 2.40–2.44 gives the sample electrical properties in terms of the measured impedance:

$$\varepsilon_r = \frac{d}{\pi r^2}\frac{\sin(\arg Z)}{|Z|\omega\varepsilon_0}, \tag{2.45}$$

$$\sigma = \frac{d}{\pi r^2}\frac{\cos(\arg Z)}{|Z|}. \tag{2.46}$$

If the inductance of the test leads is included, then the impedance of the test piece, Z is related to the measured impedance, Z' by

$$|Z| = \sqrt{|Z'|^2+\omega^2L^2+2|Z'|\omega L\sin(\arg Z)} \tag{2.47}$$

$$\arg Z = \arg Z' + \arcsin\frac{\omega L\cos(\arg Z')}{|Z|} \tag{2.48}$$

The instrument accuracy of the HP4815A is presented in Table 2.1. Note that Equations 2.45 and 2.46 are trigonometric functions of $\arg Z$, while the errors quoted in Table 2.1 are linear functions of $\arg Z$. As a result, the accuracy of the calculated permittivity is poor

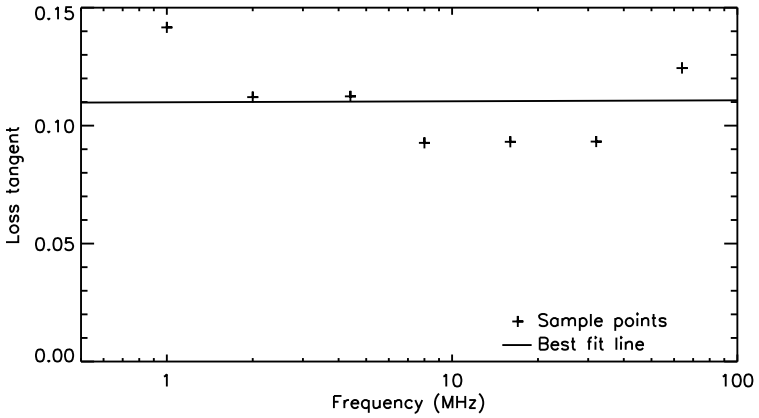

Figure 2.9: Measured and fitted values of loss tangent as a function of frequency in an anorthosite sample.

for low values of $\arg Z$, while the accuracy of the calculated conductivity is poor for high values of $\arg Z$. The correction for stray inductance, Equations 2.47 and 2.48, only has an influence at low impedances or high rock conductivities, but it can then have a marked effect on measured permittivity.

2.4.2 A summary of results

Between 1987 and 1999, 4835 samples were entered into the rock properties database at Miningtek. The majority of the samples were prepared and measured by Jonathon Manganye. After excluding samples which were measured at a single frequency, 3797 records remained that had been measured at 7 frequencies from 1 MHz to 64 MHz. Many samples are described in the database only in terms of their borehole numbers and depth. I decided to ignore samples which did not have an identifiable rock type, further reducing the number of samples to 2151. These were processed to provide the data presented here.

For each sample, the loss tangent was calculated at each frequency and a line was fitted to the loss tangent as a function of frequency using the least mean square approach. An example for a single sample is shown in Figure 2.9.

If the loss tangent as a function of frequency for a sample is now

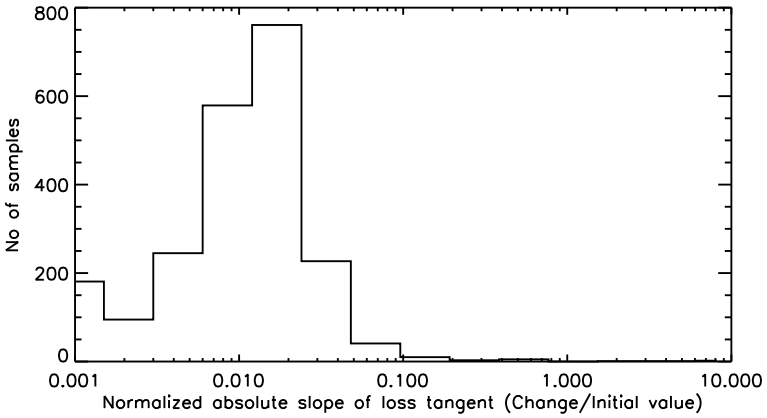

Figure 2.10: Loss tangent slope for 2151 samples.

characterized by a line, the line consists of two parameters: the slope and the x-intercept. If the slope is normalized by the x-intercept, the slopes can be compared directly. A histogram of the normalized absolute values of slope for all the samples analyzed is shown in Figure 2.10.

The graph shows that the majority of samples do not have constant loss tangents as a function of frequency, but loss tangents that do not vary from constant by more than a few percent. The small slopes of the majority of the samples show that the constant loss tangent model is a good first approximation for the behaviour of electrical properties of rocks as a function of frequency, supporting results reported in Turner (1993).

Another result is plotted in Figure 2.11. As a general trend, permittivity increases with increasing conductivity. This is likely to be a consequence of Maxwell–Wagner polarization: tiny conductive particles embedded in an insulating host have large polarizations, because the electrons in the particle are free to move to its edges under an applied force (Hasted, 1973). Many conductive ores consist of tiny conductive particles in a resistive host matrix.

2.4.3 RT *range/resolution estimation*

The initial problem of RT surveying is to determine the operating frequency that will provide an image between two boreholes, where

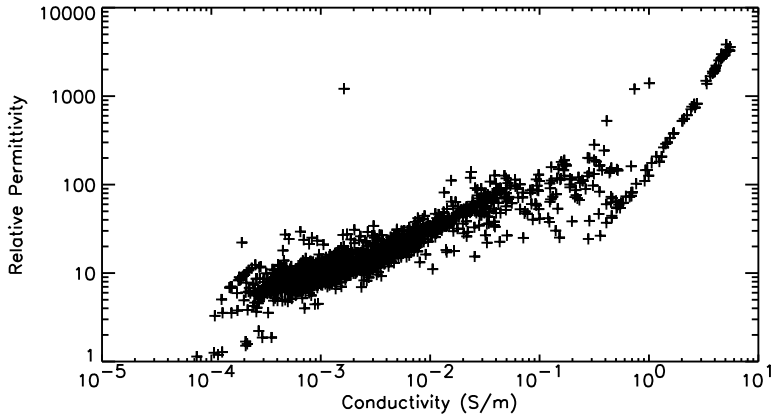

Figure 2.11: Conductivity against permittivity for all the samples in the database.

the distance between the boreholes is fixed. A constant loss tangent model can be used to estimate range as a function of frequency. In general, the aim is to use the highest frequency that will allow penetration between the two boreholes. The highest frequency corresponds to the shortest wavelength and the highest resolution.

Equation 2.13 on page 17 gives the basic RT equation in dB form. If the rock between the two boreholes is homogenous, then

$$\alpha^* R = C_u + P_{t_{dBW}} + S + A_p - V_{r_{\mathrm{dB}\mu\mathrm{V}}}. \tag{2.49}$$

To determine the maximum possible attenuation that can be tolerated, assume the range R is given and that all the system related figures within A_p are known, or can be replaced by worst case figures. The lowest received voltage that can be detected is determined by the system noise, $V_{r(\min)} \geq V_n$. The system noise is composed of two parts: the background noise of the rock around the receiver and any noise introduced by the receiver system. For the purposes of estimating range, it can be taken to be

$$V_n = \sqrt{\mathrm{k}TBR} \tag{2.50}$$

where k is Boltzman's constant, 1.38×10^{-23} J/K ,T is the temperature of the system in Kelvin, B is the bandwidth in Hz and R is the antenna impedance in ohms. If $R = 50\Omega$, $V_n \approx -67\mathrm{dB}\mu\mathrm{V} + 10\log_{10} B$. Equation 2.50 is a simplification, because it does not

consider how the antenna impedance changes as a function of frequency, but it is adequate as a first approximation.

The maximum voltage that can be received corresponds to the voltage at the receiver for maximum transmitted power, in the absence of path loss and assuming the best possible figures for gain.

$$V_{r(\max)} = C_u + P_{t_{\mathrm{dBW}}} + A_p. \tag{2.51}$$

The difference between the maximum possible received signal and the minimum detectable signal is the system performance figure, F_{sp}, where

$$F_{sp_{\max}} = V_{r(\max)} - V_n. \tag{2.52}$$

It must be stressed that the system performance figure will change in different environments, as the impedance and gain of the antenna change. Note that the expression for F_{sp} does not include the spreading factor, S.

If the RT equation for a homogenous medium is rewritten in terms of the system performance and the spreading term is expanded, the RT equation becomes

$$\alpha^* R = F_{sp_{\max}} - 10\log 4\pi R^2. \tag{2.53}$$

The maximum average attenuation that can be tolerated for a given set of equipment (F_{sp}) and a given required range (R) is

$$\alpha^* = \frac{F_{sp} - 10\log 4\pi R^2}{R}. \tag{2.54}$$

If the loss tangent is assumed to be constant as a function of frequency and if α^* is expressed in terms of the loss tangent,

$$\alpha^* = 8.686\omega\sqrt{\frac{\mu\varepsilon}{2}}\left[\sqrt{1+\tan^2\delta}-1\right]^{1/2} \tag{2.55}$$

the operating frequency can be determined:

$$\omega = \frac{F_{sp} - 10\log 4\pi R^2}{8.686R\sqrt{\frac{\mu\varepsilon}{2}}\left[\sqrt{1+\tan^2\delta}-1\right]^{1/2}}. \tag{2.56}$$

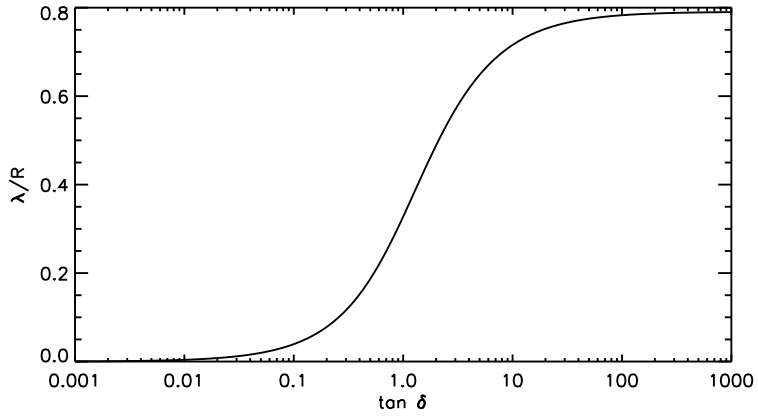

Figure 2.12: Resolution as a function of loss tangent for constant loss tangent background rocks (R=100 m, $F_{sp} = 120$ dB).

Resolution is a function of wavelength, which in turn is given by

$$\lambda = \frac{2\pi}{\beta} = \frac{2\pi}{\omega\sqrt{\frac{\mu\varepsilon}{2}}\left[\sqrt{1+\tan^2\delta}+1\right]^{1/2}} \tag{2.57}$$

but the operating frequency, ω, is given by equation 2.56, so

$$\frac{\lambda}{R} = \left[\frac{\sqrt{1+\tan^2\delta}-1}{\sqrt{1+\tan^2\delta}+1}\right]^{1/2} \frac{2\pi 8.686}{F_{sp} - 10\log 4\pi R^2}. \tag{2.58}$$

Equation 2.58 implies that there is a lower limit on the resolution that can be achieved using RT and that limit is a fraction of the borehole spacing. At high loss tangents, the operating frequency must be decreased substantially to achieve penetration, but at the same time, the velocity of propagation in conductive rocks is low and there is a corresponding drop in wavelength. For an example system performance figure of 120 dB, over a range of 100 m, the shortest wavelength at a high loss tangent is 80 m.

Equation 2.58 is illustrated graphically in Figure 2.12, for a specific value of range (100 m) and system performance figure (120 dB). The figure shows clearly that RT is best suited to environments where the majority of the rock between the two boreholes has a loss tangent lower than about 0.2, because reasonable resolutions are then possible. For higher loss tangents the resolution and operating frequency decrease rapidly.

2.4.4 A selection of measurements

In order to reduce the scope of the modelling problem, seven rocks have been selected from the database. The selection includes a wide range of loss tangents from among the lowest in the database to among the highest. The variation of conductivity, permittivity and loss tangent as a function of frequency are plotted in Figure 2.13. More detailed electrical properties for each of the selected samples are included in Appendix B.

Each sample is presented here as measured. There is no attempt to generalize from a single sample to the rock type as a whole. No error bars are presented on the plot, although the data presented in Appendix B does include error bars. Apart from measurement uncertainty, high variability of physical properties is normal for rocks in the field and has also been observed in the laboratory: rocks of the same type, taken from the same borehole, within centimetres of one another in the core, can have electrical properties varying by an order of magnitude or more.

Rock models separate naturally into two categories: lossy dielectrics and conductors. Lossy dielectrics have an effective conductivity that increases linearly with frequency. They can be considered to have a constant complex permittivity and a complex conductivity of zero. If

$$\hat{\varepsilon}(\omega) = k_1 + \mathrm{j}k_2 \tag{2.59}$$

$$\hat{\sigma}(\omega) = 0 \tag{2.60}$$

where k_i are arbitrary constants, then

$$\sigma_e(\omega) = k_2\omega \tag{2.61}$$

$$\tan\delta(\omega) = \frac{\sigma_e}{\omega\varepsilon_e} = \frac{\omega k_1}{\omega k_2} = k_3. \tag{2.62}$$

Quartzite, granite and dolerite are good examples of lossy dielectrics. Although their DC conductivity is not zero, it is very close to zero and their conductivity increases in proportion to frequency. Their loss tangents are also approximately constant with frequency.

The other dominant rock model is the conductor. In a conductive material, the complex conductivity has a large real part and often a

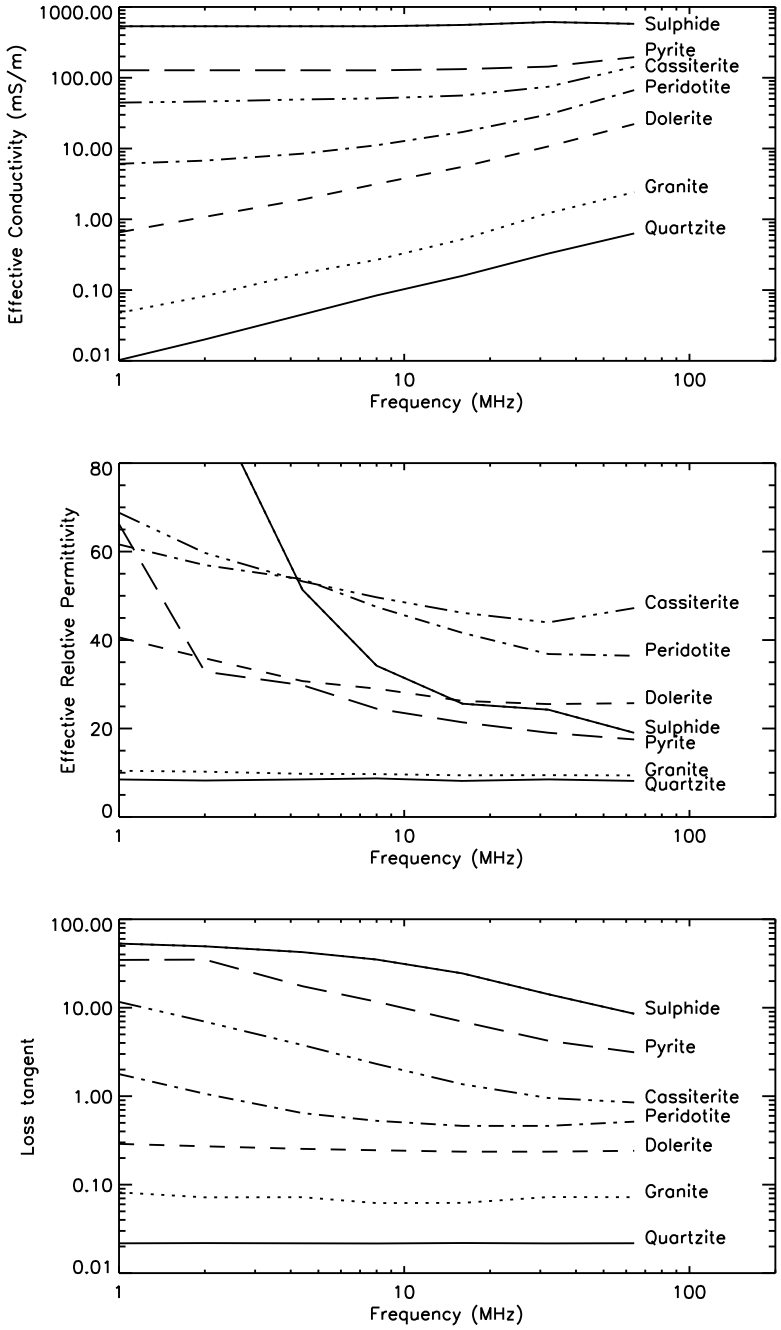

Figure 2.13: A selection of rocks across the electrical property spectrum from lossy dielectric to conductor.

negligible imaginary part. The complex permittivity may have real and imaginary parts, but the effective conductivity is dominated by the real part of the conductivity. In a material that fits the model perfectly, effective conductivity is constant with frequency, as is permittivity, so the loss tangent decreases with frequency.

Massive sulphide orebodies are close to ideal conductors, with almost constant conductivity across frequency, as shown in the conductivity plot in Figure 2.13. However, their permittivities are not constant, but fall rapidly from very large values at low frequencies. The high permittivity at low frequencies is probably a consequence of Maxwell–Wagner polarization, discussed earlier. The result is a loss tangent that is not inversely proportional to frequency, but that is nearly constant at both low and high frequencies.

Many rocks, including the remainder of the rocks plotted in Figure 2.13, fall between the lossy dielectric and the conductor: at low frequencies, their effective conductivity is dominated by the real part of the complex conductivity, while at higher frequencies the imaginary part of the complex permittivity starts to dominate.

The discussion is particularly valid in the RT regime: at lower or higher frequencies, other conceptual models can be applied. The plots of the rocks chosen here also show that while a constant loss tangent is a good first approximation for the change in electrical properties as a function of frequency, a loss tangent that decreases with frequency is more realistic. Fortunately, this implies that the tradeoff between range and resolution given in the previous section is conservative rather than optimistic.

2.5 MODELLING ROCK ELECTRICAL PROPERTIES

As shown above, it is possible to measure rock electrical properties across a frequency band and hence estimate the performance of various electromagnetic methods in that rock. It would be useful to reduce the variation of properties with frequency to simple relationships. Debye derived a relationship to describe the electrical properties of polar molecules with a single relaxation time (Daniel, 1967). The relaxation time is the time lag between applying an external field

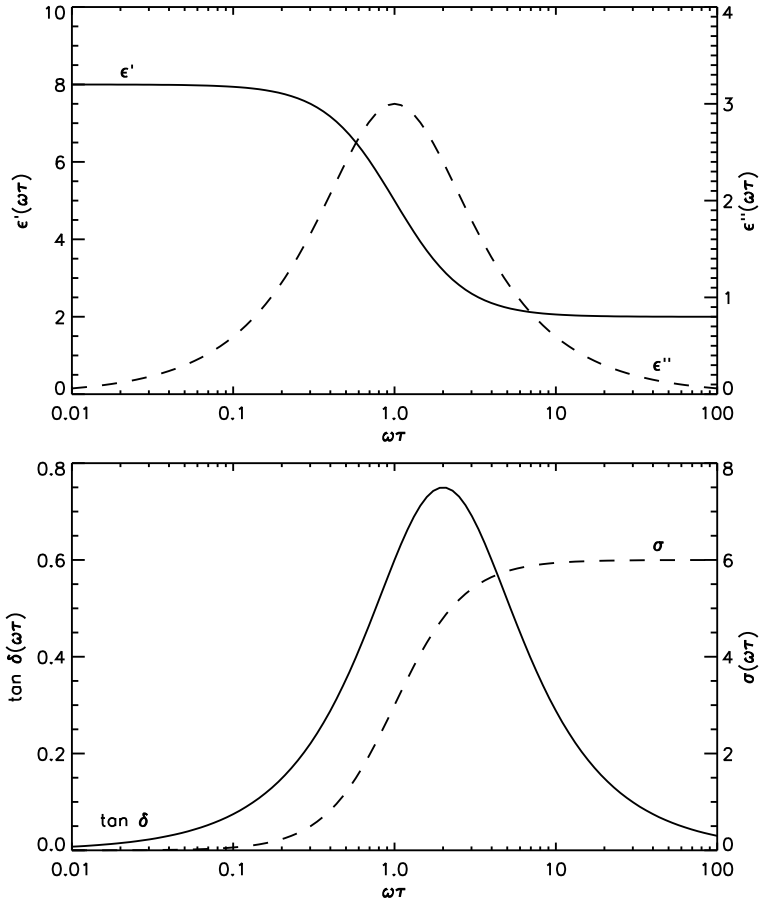

Figure 2.14: Characteristic variation of material properties for a Debye medium, after Daniel (1967). In the graphs $\varepsilon_s = 8$ and $\varepsilon_\infty = 2$.

and alignment of the molecule with the field. The Debye equation is

$$\varepsilon(\omega) = \varepsilon_\infty + \frac{\varepsilon_s - \varepsilon_\infty}{1 + \mathrm{j}\omega\tau} \tag{2.63}$$

where ε_s is the permittivity at $\omega = 0$, ε_∞ is the permittivity as $\omega \to \infty$ and τ is the relaxation time. The Debye equation is a solution to the differential equation that describes the polarization of a material with a single relaxation time, for example a polar liquid such as water:

$$\tau \frac{\mathrm{d}\boldsymbol{P}(t)}{\mathrm{d}t} + \boldsymbol{P}(t) = (\varepsilon_s - \varepsilon_\infty)\boldsymbol{E}(t). \tag{2.64}$$

The interpretation of τ as a relaxation time is now obvious.

The Debye relationship of equation 2.63 can be separated into real and imaginary components

$$\varepsilon_e(\omega) = \varepsilon'(\omega) = \varepsilon_\infty + \frac{\varepsilon_s - \varepsilon_\infty}{1 + \omega^2\tau^2}, \tag{2.65}$$

$$\varepsilon''(\omega) = \omega\tau\frac{\varepsilon_s - \varepsilon_\infty}{1 + \omega^2\tau^2}. \tag{2.66}$$

The conductivity and loss tangent are then described by

$$\sigma_e(\omega) = \omega^2\tau\frac{\varepsilon_s - \varepsilon_\infty}{1 + \omega^2\tau^2}, \tag{2.67}$$

$$\tan\delta = \frac{(\varepsilon_s - \varepsilon_\infty)\omega\tau}{\varepsilon_s + \varepsilon_\infty\omega^2\tau^2}. \tag{2.68}$$

Equations 2.67 and 2.68 only apply if the material has no DC conductivity, $\sigma' = 0$. The relationships in Equations 2.65 – 2.68 are shown graphically in Figure 2.14. Note that the loss tangent always peaks at the frequency corresponding to the relaxation time. As shown earlier, many real rocks have a nearly constant loss tangent over frequency, so the single term Debye equation is not a suitable model over a wide bandwidth.

The Cole-Cole equation (Daniel, 1967) is an alternative empirical expression used to model rock electrical properties. The equation is

$$\varepsilon(\omega) = \varepsilon_\infty + \frac{\varepsilon_s - \varepsilon_\infty}{1 + (\mathrm{j}\omega\tau)^{1-\alpha_{cc}}}, \tag{2.69}$$

where α_{cc}, the empirically derived Cole-Cole parameter, has the effect of broadening the loss tangent peak. The Cole-Cole equation can then be applied over a wider bandwidth than the Debye equation with a single relaxation time. It is widely used as a model for the electrical properties of material media (Turner, 1993).

The Jonscher parameterization (Hollender and Tillard, 1998) is also a good approximation for the frequency variation of the electrical properties of rock. It gives the effective permittivity as

$$\varepsilon_e(\omega) = \varepsilon_0\chi_r\left(\frac{\omega}{\omega_r}\right)^{n-1}\left[1 - \mathrm{j}\cot\left(\frac{n\pi}{2}\right)\right] + \varepsilon_\infty. \tag{2.70}$$

There are three real constant parameters to be fitted, n, χ_r and ε_∞. The frequency ω_r is arbitrary and cannot be compared to the Debye

relaxation frequency. The Jonscher parameterization offers an excellent fit to many sets of experimental data, but has not been pursued here because it does not integrate well into the time domain finite–difference approach of the FDTD method.

The Debye relationship was originally developed to explain the dielectric properties of a polar liquid (Debye, 1929). Rocks consist of mixtures of crystals of various minerals, so it is reasonable to approximate real rock electrical properties as the sum of Debye relaxations (Taflove, 1998):

$$\varepsilon(\omega) = \varepsilon_\infty + \frac{\varepsilon_{w_1}}{1 + \mathrm{j}\omega\tau_1} + \frac{\varepsilon_{w_2}}{1 + \mathrm{j}\omega\tau_2} + ... \qquad (2.71)$$

where $\varepsilon_{w_1} + \varepsilon_{w_2} + ... = \varepsilon_s - \varepsilon_\infty$. For any given material and frequency range of interest, it is often appropriate to consider only those terms with relaxation times close to the frequencies of interest.

It is possible to fit the experimental data shown in Figure 2.13 on page 31 within experimental error, to materials with between one and four relaxation times. The process of fitting the experimental data and the results for the samples are given in Appendix A.

2.6 CONCLUSION

The central problem examined in this thesis is the determination of the antenna parameter in the RT equation,

$$A_p = 10\log_{10}(R_{re}G_tG_r\lambda^2/4\pi) \qquad (2.72)$$

for an electric dipole antenna embedded in rock. The rock properties come from measurement and are modelled as Debye materials with multiple relaxation times.

Measurements show that it is reasonable to assume that rocks have a constant loss tangent with frequency as a first approximation. The assumption of constant loss tangent leads to a simple expression for the expected resolution from a survey, which is useful during initial survey design.

In the next chapter, various approaches are considered to determine R_r, G_r and G_t as functions of the design of the antenna and the rock in which it is embedded.

3

Modelling propagation in the earth

3.1 INTRODUCTION

The previous chapter introduced RT and showed that in order to improve the quality of RT images, it is necessary to have a good understanding of the antenna impedance and gain. In this chapter, some of the techniques for calculating the antenna parameters are discussed and the Finite-Difference Time-Domain (FDTD) technique is chosen for this thesis.

If the current distribution on the antenna is known, the rest of the antenna parameters can easily be calculated. In the case of an electric dipole antenna in air, sinusoidal current distribution is often assumed (Balanis, 1982). The assumption is based on the idea that from the feed point, the antenna acts as a pair of transmission lines, with open circuits at the end of each line. King and Smith (1981) go as far as to model an insulated antenna using a transmission line. If the end of the antenna is an open circuit, it reflects all arriving electromagnetic energy resulting in a sinusoidal standing wave for sinusoidal excitation.

A sinusoidal current distribution is a good first order estimate for an antenna in air. If the antenna is immersed in a conducting medium, the approximation breaks down as the conductivity increases (King and Smith, 1981). In addition, if an electrical structure is introduced near the antenna, the interaction of fields between the antenna

and currents induced on the structure also causes the current distribution to become non–sinusoidal. For simple cases, such as two dipole antennas in echelon, analytical solutions can be determined (King, 1957). Even for this case, the analytical expression is too complicated to easily improve our understanding of the factors affecting the problem.

For the general problem of modelling an RT antenna in a realistic rock environment, complete with different rock types and potential targets, a numerical solution is more appropriate. Computational electromagnetics (CEM) enables the user to do parametric analysis without having to build and test physical antennas in the difficult environment of a borehole.

Any grouping of techniques for antenna analysis tends to be arbitrary. In the sections that follow, I consider analytical techniques and then divide CEM techniques into "large scale" and "small scale" (Cloude, 1996):

- In large scale techniques, the structures to be modelled are divided into segments and the relationship between each segment and all the others is defined. The problem is then to determine the currents on conductive segments, given the interrelationships between the segments. The most common large scale techniques are finite element methods and the related method of moments.
- In small scale techniques, the space to be modelled is divided into elements, where each element depends only on those nearby. The current distribution is determined by applying a source voltage at some point in space and time stepping the space. The most common small scale techniques are the FDTD method and the Transmission Line Matrix (TLM) method.

Foster (2000) contains a good summary of various modelling techniques and discusses the advantages and shortcomings of all the dominant modelling methods. Foster divides CEM into methods that model current distributions on surfaces and those that model current distributions in volumes. The division is equivalent to that used here, where large scale techniques typically model current distributions on surfaces.

Techniques used to model electrically large conducting struc-

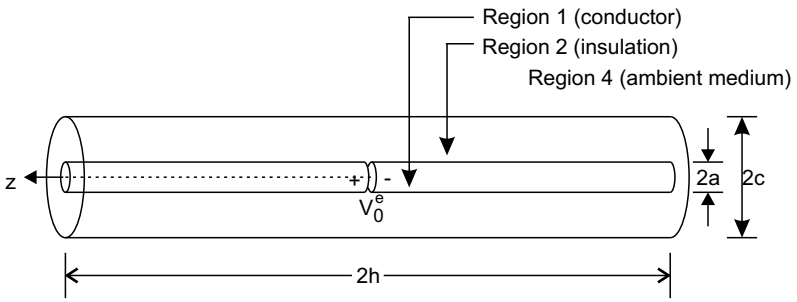

Figure 3.1: Geometry of the King-Smith insulated antenna (Casey and Bansal, 1986).

tures, such as the Physical Optics model, or the Geometric Theory of Diffraction are not considered, because in the RT problem, the conducting structure is relatively small.

3.2 ANALYTICAL METHODS

Although many electromagnetic problems do not have closed form analytical solutions there are approximate solutions available for a wide range of problems. Analytical solutions can give an insight into the physical processes occurring.

Two leading exponents of the analytical approach for antennas in the earth are King and Smith (1981). For an insulated electric dipole antenna embedded in a material, King and Smith propose equating the two arms of the antenna with two coaxial transmission lines, fed from their centre point. In each case, the antenna itself forms the inner conductor of the transmission line, the insulation forms the dielectric and the material medium forms the outer conductor, as shown in Figure 3.1.

In the classic King-Smith antenna configuration, the insulation consists of two layers, layers 2 and 3. If only one layer is used, the ambient medium is still referred to as layer 4. The wave number of the insulation is given by $k_2 = \omega(\mu_0\varepsilon_2')^{1/2}$, while the wave number of the ambient medium is $k_4 = \beta_4 + i\alpha_4 = \omega(\mu_0\varepsilon_4)^{1/2}$ where $\varepsilon_4 = \hat{\varepsilon}_4' + i\sigma_4''/\omega$.

For an insulated dipole that satisfies the following conditions

$$|k_4/k_2|^2 \gg 1 \tag{3.1}$$

$$(k_2 b)^2 \ll 1 \tag{3.2}$$

the distribution of current on the antenna can be approximated by equation 4.15 on page 509 of King and Smith (1981):

$$I(z) = -\frac{iV_0^e}{2Z_c}\frac{\sin k_L(h-|z|)}{\cos k_L h}, \tag{3.3}$$

where

$$Z_c = \frac{\zeta_2 k_L}{2\pi k_2}\left[\ln(b/a) + \frac{k_2^2}{k_4^2}\frac{H_0^{(1)}(k_4 b)}{k_4 b H_1^{(1)}(k_4 b)}\right] \tag{3.4}$$

and

$$k_L = k_2\left[\frac{k_4^2[H_0^{(1)}(k_4 b) + k_4 b\ln(b/a)H_1^{(1)}(k_4 b)]}{k_2^2 H_0^{(1)}(k_4 b) + k_4^2 k_4 b\ln(b/a)H_1^{(1)}(k_4 b)}\right]^{1/2}. \tag{3.5}$$

$H_0^{(1)}$ is the Hankel function of the first kind and order zero and ζ_2 is the wave impedance of the insulation, where $\zeta_2 = (\mu_2/\varepsilon_2)^{1/2}$.

Equations 3.4 and 3.5 correspond to equations 4.21 and 4.22 on Page 510 of King and Smith (1981), referred to in Sato and Thierbach (1991). These approximations of the characteristic impedance and the wave number are acceptable as long as $|k_4^2/k_2^2| \geq 2$. However, the current distribution on the antenna given in Equation 3.3 is only accurate under the more severe restriction that $|k_4^2/k_2^2| \gg 1$.

Casey and Bansal (1986) show weaknesses in the King approximation close to the antenna. In particular, King and Smith take an approximation to evaluate an integral that is only valid when

$$|k_4 c|^2 \ll 1. \tag{3.6}$$

Casey and Bansal (1986) use a numerical technique to evaluate the same integral and claim more accurate results in the near field, although their far field results correspond closely to those reported in King et al. (1983).

Analytical methods are not introduced here to propose an exact method of modelling RT antennas, but to extract what understanding

is available about the underlying physics from the analytical expressions. For example, Hansen (1999) offers a good detailed analysis of a somewhat unrealistic problem: the Hertzian dipole in a borehole. Although the problem is unrealistic, the insights gained are physically useful: how waves propagate along the interface between the borehole and the rock, and when that propagation is important.

The aim of this section is to introduce the idea of modelling one arm of an insulated dipole antenna as a coaxial cable, together with its effective wave number and effective wave impedance. These concepts are useful when normalizing the electrical length of insulated antennas.

3.3 FINITE ELEMENT METHODS

The first of the large scale numerical techniques discussed here is the Finite Element Method. The principle of the method is to break the problem space down into finite elements, often triangles, where properties within the elements are related to those of nearby elements. The whole system is then subject to boundary conditions and solved subject to a solution constraint; usually minimum energy (Silvester and Ferrari, 1996).

For static electromagnetic problems the finite elements are only related to immediately adjacent elements. The solution matrix is sparse so large matrices can be solved using sparse matrix solvers. However, for full Maxwell's equation solutions, each finite element is often related to all the others and the matrix becomes dense, limiting the problem size. For unbounded problems, there is also often the need to define absorbing boundary conditions. The method of moments represents an alternative formulation for solving finite element problems.

The finite element computational domain is finite, but the problem space may be unbounded. Some way of truncating the problem is required. Absorbing boundary conditions (ABCs) are implemented to simulate a boundary through which energy only passes in one direction, truncating the problem space. The development of ABCs is currently an active research area. The latest ABCs for the finite ele-

ment method are being developed from those for the FDTD method, for example those of Wu et al. (1997).

A variation on the finite element technique is the volume current method, detailed in Howard and Kretzschmar (1986). This code was used to generate the RT data in Van Schoor et al. (1997). It is not suitable for use as an antenna model, because it is 2D and assumes infinite line sources.

3.4 THE METHOD OF MOMENTS

Possibly the most popular large scale technique for modelling electromagnetic problems is the method of moments introduced by Harrington (1967). The electromagnetic problem is broken down into current carrying wires and surfaces and the interactions between all the elements.

The method of moments is a technique to solve general problems of the form

$$L(f) = g \tag{3.7}$$

where L is a linear operator, g is a known excitation or source function and f is the desired field response.

For example, Maxwell's equations for the time-harmonic case are

$$\nabla \times \boldsymbol{E} = -\mathrm{j}\omega\mu\boldsymbol{H} \tag{3.8}$$

$$\nabla \times \boldsymbol{H} = \mathrm{j}\omega\varepsilon\boldsymbol{E} + \boldsymbol{J}. \tag{3.9}$$

The two equations can be combined into a single equation for $\boldsymbol{E}$ as

$$\frac{-1}{\mathrm{j}\omega}\nabla \times (\mu^{-1}\nabla \times \boldsymbol{E}) - \mathrm{j}\omega\varepsilon\boldsymbol{E} = \boldsymbol{J}. \tag{3.10}$$

This is of the form

$$L(\boldsymbol{E}) = \boldsymbol{J} \tag{3.11}$$

and follows the form of Equation 3.7. Conditions need to be applied to Equation 3.10 to restrict the domain of L and boundary conditions are needed on $\boldsymbol{E}$, but once these are in place, Equation 3.11 can be

set up in matrix form and solved. Wire antennas are modelled in a similar manner, using a different set of basic equations.

The moment method has the advantage that it does not require boundaries to model antennas because the interactions are only between antenna elements. By the same token, modelling additional structure near antennas adds considerably to the cost, because the additional structure must be discretized.

There are two costs in solving a moment method problem: setting up the matrix L and solving the matrix. Setting up the matrix is not trivial as it involves numerical integration for typical antenna problems. The matrix is square, $N \times N$, where N is the number of unknowns, typically the number of segments in the problem. The computational cost of solving a moment method problem is proportional to N^3 and the memory requirement is proportional to N^2.

For the general problem of antennas in inhomogenous earth, the problem quickly becomes large because of the need to discretize the surfaces that represent changes in the earth material properties. For some specific geometries, the Green's functions used to create L can incorporate an inhomogenous earth structure, for example by assuming a layered earth (Van Tonder, 1995). In a similar way, new Green's functions can be derived to handle insulated coatings by introducing surface current densities (Richmond and Newman, 1976; Lee and Balmain, 1979). Iterative techniques can extend the moment method to model inhomogenous lossy dielectric objects (Sultan and Mittra, 1985).

In general, there are two problems with using the method of moments to model RT antennas: firstly, the method cannot handle inhomogenous earth and secondly, changing the method to incorporate novel elements, including insulated antennas, is a significant research effort in itself.

3.5 FINITE DIFFERENCE METHODS

The two small scale modelling techniques described here are both finite difference methods, that is, they break the volume to be modelled into a computational grid that maps the electromagnetic fields of the

problem spatially. They are also both time-domain methods, where a source waveform is introduced at a point or points in the grid and the electromagnetic field propagation is simulated by time-stepping the system. The two methods discretize space in fundamentally different ways.

3.5.1 The Finite-Difference Time-Domain method

Within the FDTD method, space is discretized directly. Yee (1966) proposed that Maxwell's equations be discretized as a set of finite difference equations, on a grid with electric fields offset both spatially and temporally from magnetic fields. Update equations express the present values of fields in terms of past values. Fields are updated in a leapfrog scheme, to incrementally march the $\boldsymbol{E}$ and $\boldsymbol{H}$ fields forward in time.

A source is implemented in FDTD by setting $\boldsymbol{E}$ or $\boldsymbol{H}$ fields to values of a function specified in the time-domain as the model is time stepped. Both point and wave sources can be modelled. If the source function contains many frequencies, a single run of the model will produce results for all the frequencies contained in the source waveform.

The technique did not attract much attention initially, partly because of its high computational cost. Since the mid 1980's, as computers have become ever cheaper and more powerful, the technique has attracted a great deal of interest (Schlager and Schneider, 1995, 1998).

The FDTD method cannot model radiation problems without modification, because the modelling space is finite. It is necessary to terminate the modelling space numerically in such a way that waves radiating out through the boundary appear to travel on infinitely. The boundary termination is often called an absorbing boundary condition (ABC). It can be implemented through one-way wave equations, or through the introduction of absorbing media.

The FDTD method can be used to model material media, including dispersive media, either by recursive convolution (Luebbers and Hunsberger, 1992) or by adding auxiliary differential equations

(ADEs)(Gandhi et al., 1993). This makes it ideal for modelling RT and it has been used to model GPR (Giannopoulos, 1997; Bourgeois and Smith, 1996).

The FDTD method can be expressed as a full three-dimensional model, or as a two-dimensional model, where the system is uniform in its third dimension. It can also be modelled for specific geometries such as cylinders, with body of revolution (BOR) symmetry (Maloney et al., 1990). The BOR model is numerically accurate in 3D, but has a 2D computational cost. Since RT antennas have cylindrical symmetry, BOR symmetry is appropriate to model a wide range of RT problems. One problem that cannot be modelled by a BOR code is an antenna close to a conductive body on one side. Such a problem requires full 3D modelling.

3.5.2 Transmission Line Matrix method

The Transmission Line Matrix (TLM) method (Christopoulos, 1995) is another differential time-domain technique. In TLM, the modelling space is simulated by a network of transmission lines. The voltages and currents on the transmission lines give information about electric and magnetic fields in the modelling space. Lines intersect at nodes. At each time step, voltage pulses are incident on each node from each transmission line connected to that node. The node voltage is calculated and the result is then scattered to produce a new set of pulses at each connected node at the next time step.

The characteristics of the transmission lines are set up to be consistent with Maxwell's equations. Transmission line stubs can be connected to each node to add different material properties. TLM is excellent for applications that are naturally expressed in terms of reflection coefficients. Shielding problems in EMC work are a good example, because shielding effectiveness is often measured in terms of S_{11} and S_{21} parameters, which can be applied easily within the TLM model.

Comparisons of TLM and FDTD tend to end inconclusively. For example, Giannopoulos and Tealby (1995) compare an ABC in the two techniques and conclude that performance is better in TLM, but

that TLM is also more computationally expensive. In general, features such as lossy dispersive media, or advanced ABCs are implemented first within FDTD models and only later in TLM. Efforts have been made recently to combine the two (Eswarappa and Hoefer, 1996; Chen and Xu, 1997), particularly to reap the benefits of new ABC techniques within TLM (Eswarappa and Hoefer, 1995). Krumpholz et al. (1995) argue that since TLM leads to some non-physical eigenvalues, as well as all the physical eigenvalues of FDTD, it contains redundant information, but they do not take a position on the superiority of either technique.

3.6 CHOICE OF MODELLING TECHNIQUE

Modelling RT presents an interesting challenge. Although RT images are created at a single frequency, the choice of frequency is the most important choice an operator can make, so modelling at different frequencies is a requirement. The model must be able to incorporate electric dipole antennas coated with a thin layer of insulation embedded in a lossy dispersive medium. It is an advantage if the modelling technique can incorporate targets in the earth medium that have different electrical characteristics.

Ideally, a commercial modelling package would be used. No available method of moments code could be found that implements antennas embedded in rock. The method of moments has been used to model GPR , notably in Turner (1993), but the code used is often NEC 3, a version of the Numerical Electromagnetics Code (Burke and Poggio, 1981) that can incorporate a lossy earth. However, in 1997, when this research was initiated, NEC 3 was only licensed by the US Government to specific military customers. A commercially available code, Concept (Singer et al., 1997) was also assessed, but again, its implementation of a lossy earth did not permit a general solution to the RT problem.

Certainly, it is possible to extend the method of moments to incorporate thin layers of insulation and generalized lossy media, but if a code is to be written or extended, the FDTD method offers a smaller, simpler kernel as a base to extend from, so the FDTD code was

chosen above the moment method. The time-domain formulation of FDTD gives results for many frequencies from a single run and the computational cost of a run does not go up substantially if the target becomes geometrically complex. Although simple geometries take longer to run than in a moment method code, the time is not substantial enough to present an obstacle to using the code.

Both finite elements and the method of moments require an excellent understanding of the electromagnetics of the problem and need to be set up in different terms for different problems. For example, adding a thin layer of insulation to a wire antenna changes the equations used to model the wire. By contrast, finite difference methods apply everywhere in space, although specific electromagnetic equations may be required to define subcell extensions. It can be argued that if a technique must be modified, as is the case for modelling RT, the correct choice of technique is the one that is easiest to modify.

Johns (1979) argues that there is some danger in using modelling techniques that are too far removed from the physical process, because of the loss of insight that occurs. He feels that the calculus approach of FDTD obscures the propagating nature of the wave, but I feel equally that TLM obscures the underlying field properties through its translation to transmission lines. Johns (1987) goes on to say that FDTD and TLM are complementary and that "Some engineers prefer to think of time-domain discretization through mathematical finite differencing; others prefer to model with transmission-line networks." I am one of the former and for that reason I have chosen FDTD over TLM as my tool of choice.

There have been several published FDTD models of the earth, including Bourgeois and Smith (1996); Debroux (1996); Teixeira et al. (1997); Holliger and Bergmann (1998); Liu (1999) and at least one including BOR symmetry (He and Liu, 1998), all of which support the choice of FDTD as a modelling methodology. Giannopoulos (1997) modelled GPR, a very similar problem to modelling RT, using both FDTD and TLM and concluded that FDTD was easier to apply. Maloney et al. (1990) claimed very good results modelling a simple antenna using a BOR code. The same group later published a study of radiation from a resistive monopole that was created using a thin-

layer approximation (Maloney and Smith, 1993). The authors compared their results with measurements and claimed "A survey of the literature for this antenna shows that no better agreement has been obtained." Although their claim is specific to their model, it does show the ability of an FDTD code with subcell extensions to model antennas accurately.

4

The RT FDTD model

4.1 INTRODUCTION

In the previous chapter, the FDTD method was chosen as suitable for modelling RT antennas and systems. A computer code for modelling RT has been written and is described in this chapter. The most important characteristics of the model are described together with the update equations for novel aspects of the model. The complete derivations of the update equations are included in Appendix A, collecting together in one algorithm several techniques that have not been published together before.

The problem is assumed to be rotationally symmetrical, so body–of–revolution (BOR) symmetry is applied. It is assumed that the antenna is thin enough that there are no circulating currents on the antenna. Even in a rock of high conductivity and dielectric constant, the antenna diameter of 44 mm is well below the 10 m wavelength of a 30 MHz radio wave. Because there are no circulating currents, and excitation is only of the $\boldsymbol{E}_z$ field, only a TM mode is propagated from the antenna so only the TM mode is modelled in the computational space. A cylindrical co-ordinate system is used and update equations are provided for $\boldsymbol{E}_z$, $\boldsymbol{E}_r$ and $\boldsymbol{H}_\phi$.

The antenna is placed on the axis of the modelling space as shown in Figure 4.1. The image line is a perfectly electrically conducting (PEC) plane that converts the monopole model into the effective di-

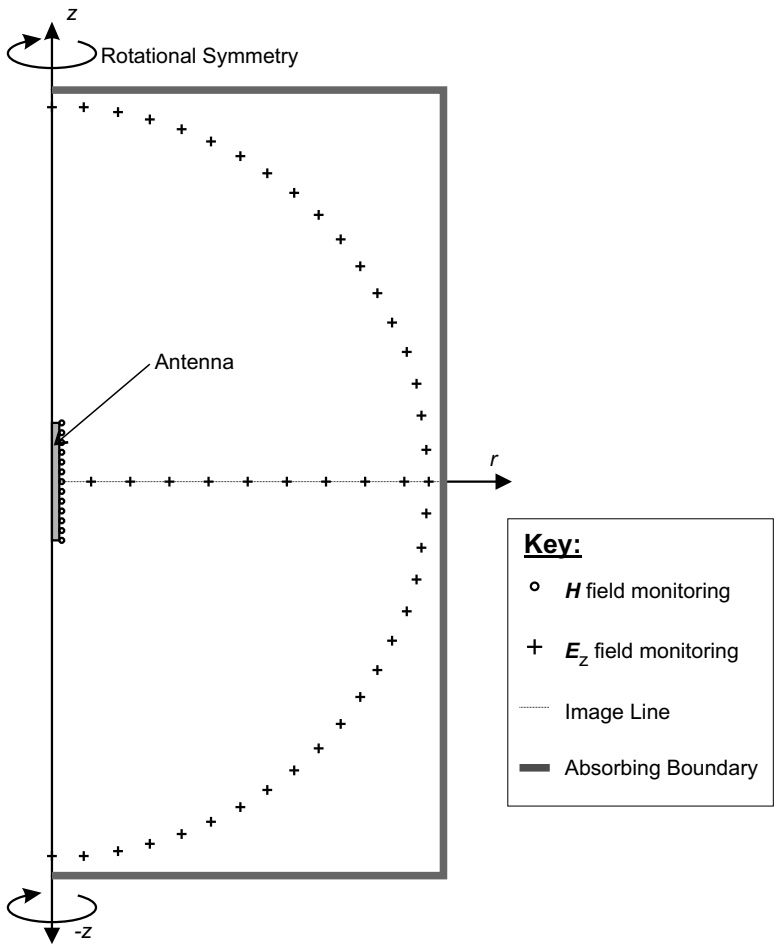

Figure 4.1: The geometry of the computational space.

pole shown. In general the code is capable of modelling a dipole, but the antenna is normally modelled as a monopole over a PEC ground plane. Image theory allows the performance to be equated to that of a dipole with twice the voltage across it.

The right and top of the modelling space are truncated in absorbing boundaries. The bottom boundary can be either a perfectly conducting ground plane or an absorbing boundary. Second order Higdon boundaries are used, because they offer adequate performance with a small computational burden. The antenna is modelled using a thin-wire approximation and is coated using a thin-layer approximation. Electrical properties can be varied with frequency in accordance with the Debye model. The combination of Debye model

and thin coated wire presented here is novel.

The antenna is driven by forcing the $\boldsymbol{E}_z$ field across the driving element. A more accurate driving method could be employed, but forced E fields have the benefits of extreme simplicity and great robustness. A bipolar, or differentiated, Gaussian pulse is used to excite the antenna, producing a range of frequencies from just above DC to a specified maximum frequency, normally between 20 MHz and 30 MHz. Results are obtained for discrete frequencies by taking the Fourier Transform of the time domain results.

No near-to-far field transformation is used. In an RT system, the observation points are usually sufficiently close to the transmitter to be included in the computational domain. Because the model is 2D, fields would have to be extrapolated into 3D to calculate the far fields. Although the near-to-far field transformation could reduce the size of the computational space, that advantage is outweighed by the extra computational cost of the extrapolation.

The modelling code was prototyped in IDL, a mathematics and visualization language (RSI, 1995). Once the model and visualization tools were working in IDL, the model itself was translated into C, to reduce run times. The modelling code was written to run on a PC but has also been compiled and executed on a workstation. As an example of execution speed, one run of a model consisting of 200 $\times$ 200 cells, modelled for 4096 time steps, takes approximately 400 seconds on a computer with a Pentium processor running at 166 MHz.

4.2 THE FDTD ALGORITHM

Yee (1966) proposed what came to be known as the FDTD technique. He substituted finite-difference equations for Maxwell's equations and made the crucial proposal that $\boldsymbol{E}$ and $\boldsymbol{H}$ fields be placed on grids offset from one another by half a grid space. The evaluation of $\boldsymbol{E}$ and $\boldsymbol{H}$ then also takes place half a time step apart. The system of equations is excited with a point or wave source and values of $\boldsymbol{E}$ and $\boldsymbol{H}$ are updated at each time step.

As an example, assume the electromagnetic field and the excit-

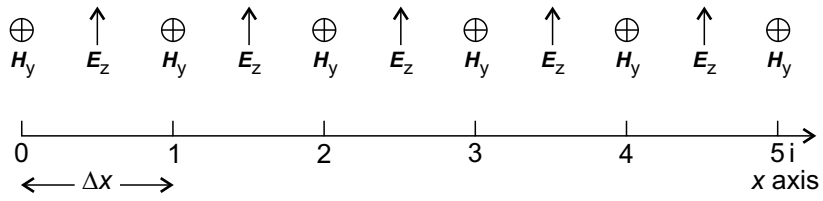

Figure 4.2: A 1D FDTD example.

ation have no variation in the y or z direction, as illustrated in Figure 4.2. In effect the medium is infinite in extent with possible layering in the x direction. Maxwell's equations for the TM mode then reduce to

$$\frac{\partial}{\partial t}\boldsymbol{E}_z = \frac{1}{\varepsilon}\left(\frac{\partial}{\partial x}\boldsymbol{H}_y - \sigma \boldsymbol{E}_z\right) \tag{4.1}$$

$$\frac{\partial}{\partial t}\boldsymbol{H}_y = \frac{1}{\mu}\left(\frac{\partial}{\partial x}\boldsymbol{E}_z - \rho' \boldsymbol{H}_y\right) \tag{4.2}$$

where ρ' is the equivalent magnetic resistivity, normally zero. The $\boldsymbol{E}_z$ field points are placed on a line, $\triangle x$ apart, with the $\boldsymbol{H}_y$ fields centred between each pair of $\boldsymbol{E}_z$ points. It is possible to derive a set of finite difference equations to update the $\boldsymbol{E}$ fields from the $\boldsymbol{H}$ fields at time step n and then update the $\boldsymbol{H}$ fields from the $\boldsymbol{E}$ fields at time step $n + 1/2$.

Yee chose to take derivatives as central differences. The idea of difference equations follows from the definition of the derivative as the limit of a difference (Spiegel, 1971)

$$\frac{\mathrm{d}x}{\mathrm{d}y} = \lim_{\triangle y \to 0} \frac{\triangle x}{\triangle y}. \tag{4.3}$$

Taflove (1995) uses a notation for describing vector fields at positions in a grid in space and time:

$$\boldsymbol{V}\big|^n_{i,j,k} \tag{4.4}$$

describes a vector $\boldsymbol{V}$ at a position defined by grid points i, j and k, at a time n. The subscripts and superscripts do not refer to the

actual position in time and space, but to the integer grid: $x = i\triangle x$, $y = j\triangle y$, $z = k\triangle z$ and $t = n\triangle t$.

Using Taflove's notation, derivatives with respect to time and space for an arbitrary vector $\boldsymbol{V}$ can be written as

$$\frac{\mathrm{d}\boldsymbol{V}}{\mathrm{d}t} = \frac{\boldsymbol{V}\big|_{i,j,k}^{n+1} - \boldsymbol{V}\big|_{i,j,k}^{n}}{\triangle t}, \tag{4.5}$$

$$\frac{\mathrm{d}\boldsymbol{V}}{\mathrm{d}x} = \frac{\boldsymbol{V}\big|_{i+1,j,k}^{n} - \boldsymbol{V}\big|_{i,j,k}^{n}}{\triangle x}. \tag{4.6}$$

Values not available at a particular time step can be estimated using a time average of the half steps before and after:

$$\boldsymbol{V}\big|_{i,j,k}^{n+1/2} = \frac{\boldsymbol{V}\big|_{i,j,k}^{n+1} + \boldsymbol{V}\big|_{i,j,k}^{n}}{2}. \tag{4.7}$$

Schuster et al. (2000) recommend the use of a different scheme, time forward. They show that time average is less stable than alternative formulations when modelling materials with high conductivity. Experimental results confirm their findings, but their paper only became available after the bulk of the modelling had been done for this thesis. Time averaging was used for all the modelling shown here.

Using Equations 4.5 – 4.7, the 1D Maxwell's equations (Equations 4.2 and 4.1) can now be expressed in difference form as

$$\begin{aligned}\frac{\boldsymbol{E}_z\big|_{i+1/2}^{n+1/2} - \boldsymbol{E}_z\big|_{i+1/2}^{n-1/2}}{\triangle t} = \frac{1}{\varepsilon}\Bigg[&\frac{\boldsymbol{H}_y\big|_{i+1}^{n} \boldsymbol{H}_y\big|_{i}^{n}}{\triangle x} \\ &- \sigma\frac{\boldsymbol{E}_z\big|_{i+1/2}^{n+1/2} - \boldsymbol{E}_z\big|_{i+1/2}^{n-1/2}}{2}\Bigg]\end{aligned} \tag{4.8}$$

$$\begin{aligned}\frac{\boldsymbol{H}_y\big|_{i}^{n+1} - \boldsymbol{H}_y\big|_{i}^{n}}{\triangle t} = \frac{1}{\mu}\Bigg[&\frac{\boldsymbol{E}_z\big|_{i+1/2}^{n+1/2} - \boldsymbol{E}_z\big|_{i-1/2}^{n+1/2}}{\triangle x} \\ &- \rho'\frac{1}{\mu}\frac{\boldsymbol{H}_y\big|_{i}^{n+1} - \boldsymbol{H}_y\big|_{i}^{n}}{2}\Bigg]\end{aligned} \tag{4.9}$$

Equations 4.8 and 4.9 can be manipulated into a pair of update equations for the $\boldsymbol{E}$ and $\boldsymbol{H}$ fields in a 1D simulation:

$$\begin{aligned}\boldsymbol{E}_z\big|_{i+1/2}^{n+1/2} &= \left[\frac{2\varepsilon - \sigma\triangle t}{2\varepsilon + \sigma\triangle t}\right]\boldsymbol{E}_z\big|_{i+1/2}^{n-1/2} \\ &+ \frac{2\triangle t}{\triangle x(2\varepsilon + \sigma\triangle t)}\left[\boldsymbol{H}_y\big|_{i+1}^{n} - \boldsymbol{H}_y\big|_{i}^{n}\right],\end{aligned} \tag{4.10}$$

$$\boldsymbol{H}_y\big|_i^{n+1} = \left[\frac{2\mu - \rho'\triangle t}{2\mu + \rho'\triangle t}\right]\boldsymbol{H}_y\big|_i^n + \frac{2\triangle t}{\triangle x(2\mu + \rho'\triangle t)}\left[\boldsymbol{E}_z\big|_{i+1/2}^{n+1/2} - \boldsymbol{E}_z\big|_{i-1/2}^{n+1/2}\right]. \quad (4.11)$$

To simulate propagation, Equation 4.10 is run to update all the $\boldsymbol{E}$ field vectors. Equation 4.11 is then run to update all the $\boldsymbol{H}$ field vectors. The process is then repeated, corresponding to the next time step of the model. Exactly the same process is followed in a three dimensional model. The grid is offset between $\boldsymbol{E}$ and $\boldsymbol{H}$ and the $\boldsymbol{E}$ and $\boldsymbol{H}$ field updates are separated in time by half a time step.

It is not possible to construct a grid of arbitrary size. The size of a single cell must be significantly less than a wavelength (Yee, 1966). A cell size of $\lambda/10$ is often used, although $\lambda/20$ gives a more accurate model. The time step needs to be such that a wave does not cross a cell in less than one time step. This is formally stated as the Courant stability criterion for a 3D model:

$$\triangle t \leq \frac{\triangle}{c_{\max}\sqrt{3}} \quad (4.12)$$

where $\triangle$ is the dimension of one side of the cell (where $\triangle x = \triangle y = \triangle z = \triangle$) and $c_{\max}$ is the maximum velocity of propagation in the model. The cube root comes about because of three dimensional geometry. In a 2D geometry, it is replaced by $\sqrt{2}$.

Note that in media where the velocity is not constant either across the modelling space or as a function of frequency, the size of the time step needs to be set according the highest velocity in the modelling space. In general, when the media become dispersive, it is difficult to formulate a simple criterion for stability (Taflove, 1995). Stability considerations are discussed in detail in Section 4.8 on Page 81.

4.3 FREQUENCY DEPENDANT ELECTRICAL PROPERTIES

In its basic form, the FDTD method does not allow for material properties to vary with frequency. However, as discussed in Chapter 2, real rock has electrical properties that vary with frequency. There are a number of ways of handling varying material properties. The simplest is to assume that material properties are constant with frequency and repeat the computation of the model with different fixed

properties for each frequency point. If results are required at ten frequency points, ten separate runs will be required.

Dispersive material properties can also be incorporated into the update equations through recursive convolution (Kunz and Luebbers, 1993; Luebbers and Hunsberger, 1992), auxiliary differential equations (Gandhi et al., 1993; Taflove, 1995) or Z transform techniques (Sullivan, 1992; Weedon and Rappaport, 1997). In this thesis, the FDTD formulation is extended by the auxiliary differential equation (ADE) method, from Gandhi et al. (1993) as outlined in Giannopoulos (1997).

Gandhi et al. (1993) base their ADE method on the frequency domain relationship,

$$\boldsymbol{D} = \hat{\varepsilon}\,(\omega)\boldsymbol{E}. \tag{4.13}$$

If a polarization vector $\boldsymbol{P}$ is defined as

$$\boldsymbol{P} = \varepsilon_0\chi(\omega)\boldsymbol{E} \tag{4.14}$$

(Balanis, 1989), Equation 4.13 can be extended to include any frequency dependant effects (Young, 1995). The frequency domain susceptibility, $\chi(\omega)$ can be made arbitrarily complex, allowing for the modelling of any material variation with frequency (Kunz and Luebbers, 1993). As discussed earlier, the Debye model forms the basis for a suitable model of the frequency dependence of the electrical properties of rock. The Debye model with a single relaxation time gives complex permittivity in terms of frequency as

$$\hat{\varepsilon}\,(\omega) = \varepsilon_\infty + \frac{\varepsilon_s - \varepsilon_\infty}{1 + \mathrm{j}\omega\tau} \tag{4.15}$$

where ε_s is the static permittivity when ω=0, ε_∞ is the permittivity as $\omega \to \infty$ and τ is the relaxation time. If

$$\chi(\omega) = \frac{\varepsilon_s - \varepsilon_\infty}{1 + \mathrm{j}\omega\tau} \tag{4.16}$$

then Equation 4.15 can also be written as

$$\hat{\varepsilon}(\omega) = \varepsilon_0\varepsilon_\infty + \varepsilon_0\chi(\omega) \tag{4.17}$$

Equation 4.14 can now be expanded for the specific case of a Debye medium to

$$\boldsymbol{P} = \varepsilon_0 \frac{\varepsilon_s - \varepsilon_\infty}{1 + \mathrm{j}\omega\tau} \boldsymbol{E}. \tag{4.18}$$

Equation 4.18 can then be transformed into the time domain, resulting in

$$\frac{\partial \boldsymbol{P}}{\partial t} = \frac{1}{\tau}[\varepsilon_0(\varepsilon_s - \varepsilon_\infty)\boldsymbol{E} - \boldsymbol{P}]. \tag{4.19}$$

Equation 4.19 is the auxiliary differential equation from which the technique gets its title. It is now possible to express Equation 4.13 in terms of known parameters for a Debye material. From Equations 4.13 and 4.17,

$$\boldsymbol{D} = (\varepsilon_0\varepsilon_\infty + \varepsilon_0\chi(\omega))\boldsymbol{E}, \tag{4.20}$$

but by including Equation 4.14 this becomes

$$\boldsymbol{D} = \varepsilon_0\varepsilon_\infty\boldsymbol{E} + \boldsymbol{P}. \tag{4.21}$$

Equation 4.21 can now be used with Ampère's law to relate $\boldsymbol{E}$ and $\boldsymbol{H}$ fields on a surface.

The choice of the Debye model over the Cole–Cole model or the Jonscher parameterization is now justified. Because the Debye model is the solution to a time domain differential equation, it is straightforward to implement in an FDTD scheme. It is far less straightforward to implement either of the other dispersion models into an FDTD scheme.

4.3.1 Debye media with multiple relaxation times

As shown in Chapter 2, many rocks require more than a single relaxation time to model their electrical properties accurately. Equation 4.18 can be replaced by one describing the polarization as a sum of Debye relaxations:

$$\boldsymbol{P} = \sum_{i=1}^{n} \frac{\varepsilon_{wi}}{1 + \mathrm{j}\omega\tau_i} \boldsymbol{E} \tag{4.22}$$

where

$$\sum_{i=1}^{n} \varepsilon_{wi} = \varepsilon_s - \varepsilon_\infty. \tag{4.23}$$

The total polarization in Equation 4.22 can be considered as a sum of a series of polarization components, so

$$\boldsymbol{P} = \sum_{i=1}^{n} \boldsymbol{P}_i \tag{4.24}$$

where

$$\boldsymbol{P}_i = \frac{\varepsilon_{wi}}{1 + \mathrm{j}\omega\tau_i}\boldsymbol{E}. \tag{4.25}$$

The derivation of update equations now follows that given earlier for a Debye medium with a single relaxation time. The differential equation for each component polarization is given by

$$\frac{\partial \boldsymbol{P}_i}{\partial t} = \frac{1}{\tau_i}[\varepsilon_0 \varepsilon_{wi}\boldsymbol{E} - \boldsymbol{P}_i]. \tag{4.26}$$

The total polarization is the sum of the components as given in Equation 4.24. The alternative formulation is to expand Equation 4.22 into a function with higher order time derivatives in $\boldsymbol{E}$ and $\boldsymbol{P}$. Implementing the higher order derivatives in the FDTD code requires storage of the recent time history of $\boldsymbol{E}$ and $\boldsymbol{P}$. This formulation requires all the component polarizations, $\boldsymbol{P}_i$ to be stored, so it does not offer an improvement in computer storage. However, I believe it is conceptually easier to understand.

Equation 4.24 can be converted to difference form, leading to an update equation for $\boldsymbol{P}_i$ of

$$\boldsymbol{P}_i\big|_{r,z}^{n+1/2} = p_{i,1}\boldsymbol{P}_i\big|_{r,z}^{n-1/2} + p_{i,2}\boldsymbol{E}\big|_{r,z}^{n} \tag{4.27}$$

where

$$p_{i,1} = \frac{2\tau_i - \triangle t}{2\tau_i + \triangle t} \tag{4.28}$$

$$p_{i,2} = \frac{2\triangle t \varepsilon_0 \varepsilon_{wi}}{2\tau_i + \triangle t} \tag{4.29}$$

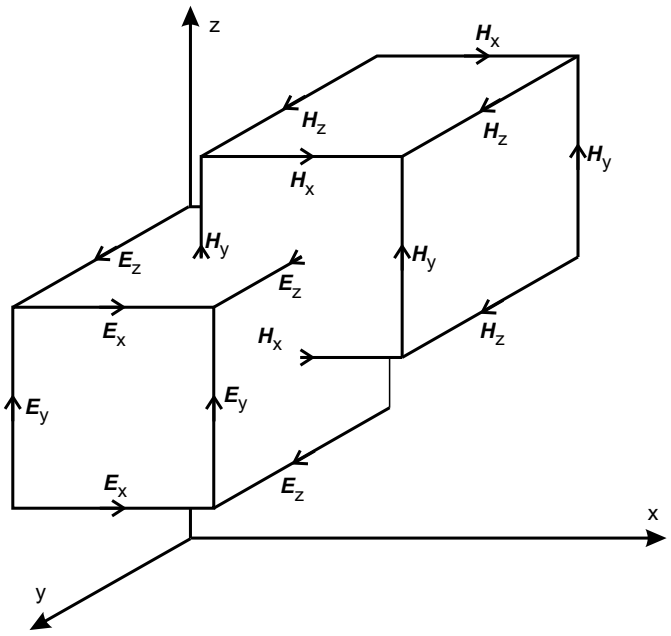

Figure 4.3: A conventional Yee grid in 3D.

4.4 THE BODY OF REVOLUTION MODEL

As discussed earlier, RT lends itself to being modelled using a code with BOR symmetry. The conventional FDTD model is derived on a rectangular 2D or 3D interlaced grid, shown in Figure 4.3, and is based on the differential form of Maxwell's equations applied at points in space.

The BOR model is based on applying the integral form of two of Maxwell's equations to patches that interlock in space. The surface integral of the field normal to the patch is then calculated in terms of the fields on the line integral around the patch. In each patch, the field normal to the surface is assumed to be constant over the whole patch and the fields along each side of the patch are assumed to be constant along each side. The complete derivation of the update equations is presented in Appendix A and follows the method presented in Jurgens and Saewert (1995). Total BOR symmetry is assumed, equivalent to the single Fourier mode $m = 0$ in Jurgens and Saewert.

The way the cells interlink and the exact cell numbering and geometry used are shown in Figure 4.4. In cylindrical geometry, TE and

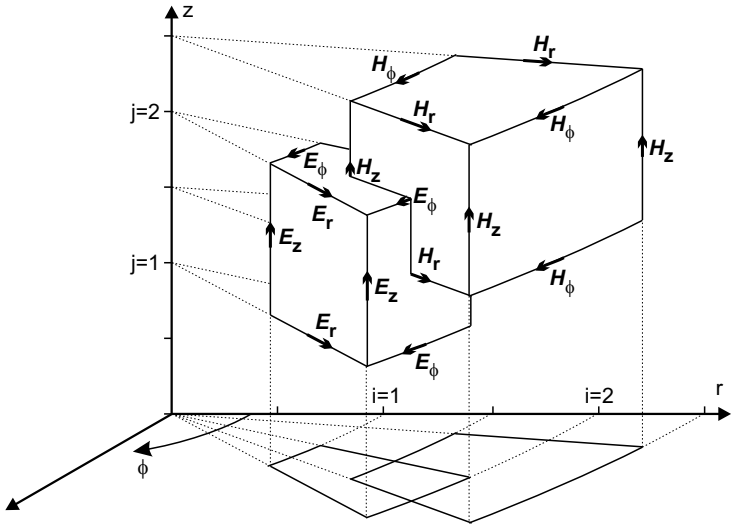

Figure 4.4: Spatial relationship of the field components for the FDTD unit cell in cylindrical coordinates.

TM modes are separable. Since the electric dipole antenna excites only $\boldsymbol{E}_z$, only the TM mode is modelled simplifying the FDTD algorithm from six components to three: $\boldsymbol{E}_r$, $\boldsymbol{E}_z$ and $\boldsymbol{H}_\phi$. The update equations for the three components are

$$
\begin{aligned}
\boldsymbol{E}_z\big|_{rr,z}^{n+1} &= c_1 \boldsymbol{E}_z\big|_{rr,z}^{n} \\
&+ \sum_{i=1}^{n} c_{2i} \boldsymbol{P}_{zi}\big|_{i,j+1/2}^{n+1/2} \\
&+ c_3 \frac{i+1/2}{i} \boldsymbol{H}_\phi\big|_{i+1/2,j+1/2}^{n+1/2} \\
&- c_3 \frac{i-1/2}{i} \boldsymbol{H}_\phi\big|_{i-1/2,j+1/2}^{n+1/2} \qquad (4.30) \\
\boldsymbol{E}_r\big|_{i,j+1/2}^{n+1} &= c_1 \boldsymbol{E}_r\big|_{i,j+1/2}^{n} \\
&+ \sum_{i=1}^{n} c_2 \boldsymbol{P}_{ri}\big|_{i,j+1/2}^{n+1/2} \\
&+ c_4 \left(\boldsymbol{H}_\phi\big|_{i+1/2,j+1/2}^{n+1/2} - \boldsymbol{H}_\phi\big|_{i+1/2,j-1/2}^{n+1/2} \right) \qquad (4.31) \\
\boldsymbol{H}_\phi\big|_{i+1/2,j+1/2}^{n+1/2} &= \boldsymbol{H}_\phi\big|_{i+1/2,j+1/2}^{n-1/2} \\
&+ m_1 \left(\boldsymbol{E}_z\big|_{i+1,j+1/2}^{n} - \boldsymbol{E}_z\big|_{i,j+1/2}^{n} \right) \\
&- m_2 \left(\boldsymbol{E}_r\big|_{i+1/2,j+1}^{n} - \boldsymbol{E}_r\big|_{i+1/2,j}^{n} \right) \qquad (4.32)
\end{aligned}
$$

where the coefficients are

$$c_1 = \frac{2\varepsilon_\infty - \triangle t \sum_{i=0}^{n} \frac{\varepsilon_{wi}}{\tau_i} - \sigma \triangle t}{2\varepsilon_\infty + \triangle t \sum_{i=0}^{n} \frac{\varepsilon_{wi}}{\tau_i} + \sigma \triangle t} \tag{4.33}$$

$$c_{2i} = \frac{2\triangle t/\tau_i}{2\varepsilon_\infty + \triangle t \sum_{i=0}^{n} \frac{\varepsilon_{wi}}{\tau_i} + \sigma \triangle t} \tag{4.34}$$

$$c_3 = \frac{2\triangle t/\triangle r}{2\varepsilon_\infty + \triangle t \sum_{i=0}^{n} \frac{\varepsilon_{wi}}{\tau_i} + \sigma \triangle t} \tag{4.35}$$

$$c_4 = \frac{2\triangle t/\triangle z}{2\varepsilon_\infty + \triangle t \sum_{i=1}^{n} \frac{\varepsilon_{wi}}{\tau_i} + \sigma \triangle t} \tag{4.36}$$

$$m_1 = \frac{\triangle t}{\mu_0 \triangle r} \tag{4.37}$$

$$m_2 = \frac{\triangle t}{\mu_0 \triangle z} \tag{4.38}$$

From the geometry illustrated in Figure 4.4, only one component occurs on the axis of rotation, namely $\boldsymbol{E}_z$. The update equation for $\boldsymbol{E}_z$ on the axis is given by

$$\begin{aligned} \boldsymbol{E}_z\big|_{n+1}^{0,j+1/2} &= c_1 \boldsymbol{E}_z\big|_{n+1}^{0,j+1/2} \\ &\quad + \sum_{i=1}^{n} c_{2i} \boldsymbol{P}_{zi}\big|_{n+1/2}^{0,j+1/2} + c_5 \boldsymbol{H}_\phi\big|_{n+1/2}^{1/2,j+1/2} \end{aligned} \tag{4.39}$$

where c_1 and c_{2i} are defined as above in equations 4.33 and 4.34 and

$$c_5 = \frac{8\triangle t/\triangle r}{2\varepsilon_\infty - \triangle t \sum_{i=0}^{n} \frac{\varepsilon_{wi}}{\tau_i} - \sigma \triangle t}. \tag{4.40}$$

4.5 ABSORBING BOUNDARY CONDITIONS

As the FDTD method is grid based, the computational space is finite and limited to the grid. As discussed in in Chapter 3, if the problem to be modelled is open, the grid has to be truncated in some way, usually with an ABC. The quest for an ABC that produces negligible reflections is one of the most active areas of FDTD research (Schlager and Schneider, 1998). Most of the popular ABCs fall into two categories: ABCs employing a material absorber and ABCs derived from differential equations.

4.5.1 Material based ABCs

One way to truncate the computational domain is to place lossy materials at the edge of the domain, in an attempt to damp waves reaching the boundary and reflections from the boundary. The method is analogous to placing absorbing foam in front of the walls of an anechoic chamber. However, real materials can only be impedance matched to the rest of the computational space for normal incidence.

Bérenger (1994) advanced the cause of material based ABCs by introducing the perfectly matched layer, or PML. He introduced a split-field formulation of Maxwell's equations, allowing boundaries to absorb the components of waves normal to the boundary. The major advantage of the PML method is that it is not affected by numerical accuracy problems at higher orders, unlike differential-equation based ABCs (Taflove, 1995).

Bérenger's paper lead to a flood of interpretations, improvements and design aids. Veihl and Mittra (1996) introduced a more efficient formulation by combining some elements. Sullivan (1996) proposed a different formulation by introducing fictitious conductivities associated with $\boldsymbol{H}$ and $\boldsymbol{D}$ instead of $\boldsymbol{H}$ and $\boldsymbol{E}$, but the formulation is more computationally expensive. Chew and Weedon (1994) and Rappaport (1995) reported PMLs based on coordinate stretching, where the field splitting occurs through an anisotropic stretching of the geometry. Sacks et al. (1995) proposed an alternative anisotropic mapping, based on expressing the permittivity and conductivity of the PML medium as complex diagonal tensors. Gedney (1996) extended the formulation and showed that it is more computationally efficient than the Bérenger PML. Ziolkowski (1997b,a) showed how the Bérenger PML is actually a passive lossy electrical and magnetic medium with Debye dispersion characteristics. He then went on on to propose a more general Maxwellian PML based on a time-derivative Lorentz material, as did Zhao and Cangellaris (1996).

Liu and He (1998) showed that a true Bérenger PML is not reflectionless at the boundary of a cylindrical FDTD computational space. They proposed a quasi-PML. Teixeira and Chew (1997) described a PML for cylindrical coordinates in terms of coordinate stretching.

Shen and Chen (2000) go further and define a generalized system for a cylindrical FDTD that includes a PML. However, their system is essentially a combination of previous work synthesized into a single algorithm. Several authors also reported adaptations of the PML to dispersive or lossy dispersive media, including Uno et al. (1997).

Gedney (1998) is an excellent overall reference on PML methods. He reviews the advances in the PML method, its application to lossy dispersive media and to non-Cartesian grids.

In the model reported in this thesis, a PML ABC is not used because it is computationally more complex and costly than a one-way wave equation PML. The extra performance it can deliver is not required because a traditional one-way wave equation ABC is sufficient for modelling RT antennas.

4.5.2 Analytical ABCs

Traditionally, ABCs have been based on factoring the wave equation into incoming and outgoing waves and allowing only outgoing waves at the boundary. The traditional ABCs are usually local in the sense that the field at a point on the boundary depends only on fields local to that point. Taflove (1995) describes a series of four stages that occurred in the development of analytical ABCs before the introduction of the PML.

The Bayliss–Turkel annihilating operator

Bayliss and Turkel (Taflove, 1995) proposed an ABC based on the expansion of the outward propagating solutions of the wave equation in spherical or cylindrical coordinates. The idea is to construct a weighted sum of three partial derivatives of the field: 1) the partial spatial derivative of the field in the direction of outgoing propagation, 2) the partial spatial derivative perpendicular to the direction of outgoing propagation and 3) the time partial derivative. By careful construction of the weighted sum, the operator “kills” or “annihilates” the outgoing wave.

The solution to the spherical wave equation

$$\frac{\partial^2 \boldsymbol{u}}{\partial t^2} = c^2 \nabla^2 \boldsymbol{u} \tag{4.41}$$

can be expanded as a convergent series and simplified in the limit as the radius, $R \to \infty$. If the partial derivative operator

$$L \equiv \frac{1}{c}\frac{\partial}{\partial t} + \frac{\partial}{\partial R} \tag{4.42}$$

is formed and applied to the convergent series emerging from Equation 4.41, it leads to

$$\frac{\partial \boldsymbol{u}}{\partial R} = -\frac{1}{c}\frac{\partial \boldsymbol{u}}{\partial t} + O(R^{-2}). \tag{4.43}$$

In principle, Equation 4.43 can be used to terminate the outer grid boundary, if the remainder term is neglected. However the remainder is not negligible, unless R is very large. Equation 4.42 is known as the Sommerfeld radiation condition (Taflove, 1995). Bayliss and Turkel sought to devise an operator similar to L with a remainder term that diminished more rapidly to zero and proposed

$$B_1 = L + \frac{1}{R} \tag{4.44}$$

which leads to a remainder term of the order of R^{-3}. Higher orders can be derived recursively. B_n annihilates the first n terms of the expansion of Equation 4.41.

The main problem with the Bayliss–Turkel operator is that it is expressed naturally in spherical coordinates. In Cartesian space, the boundary of the space is not at a constant distance R from the centre of the grid, leading to azimuthal spatial derivatives outside the grid. It is possible to create a Bayliss-Turkel annihilating operator for a 2D cylindrical geometry, but the geometry is 2D seen from above the cylinder, where structures are constant in z, rather than the 2D BOR symmetry being used here, where structures are constant in ϕ.

One-way wave equations

A partial differential equation that only permits wave propagation in certain directions is called a one-way wave equation. It can be used to

truncate the boundary of an FDTD grid. Consider a two-dimensional wave equation in Cartesian coordinates:

$$\frac{\partial^2 \boldsymbol{u}}{\partial x^2} + \frac{\partial^2 \boldsymbol{u}}{\partial x^y} - \frac{1}{c^2}\frac{\partial^2 \boldsymbol{u}}{\partial t^2} = 0. \tag{4.45}$$

It is possible to define a partial differential operator, so that

$$L \equiv \frac{\partial^2}{\partial x^2} + \frac{\partial^2}{\partial y^2} - \frac{1}{c^2}\frac{\partial^2}{\partial t^2} \equiv D_x^2 + D_y^2 - \frac{1}{c^2}D_t^2 \tag{4.46}$$

where D_x is the partial derivative with respect to x. The wave equation can then be compactly written as

$$L\boldsymbol{u} = 0. \tag{4.47}$$

The wave operator L can be factored as (Taflove, 1995)

$$L\boldsymbol{u} = L^+ L^- \boldsymbol{u} = 0, \tag{4.48}$$

where L^- is defined as

$$L^- \equiv D_x - \frac{D_t}{c}\sqrt{1 - S^2} \tag{4.49}$$

where

$$S \equiv \frac{D_y}{D_t/c}. \tag{4.50}$$

Engquist and Majda (Taflove, 1995) showed that at the left grid boundary, $x = 0$, the application of L^- to the wave function absorbs a plane wave propagating normally toward the boundary.

The problem with the one way wave equation method is the square-root function in Equation 4.49. If the square root is expanded as a Taylor series, a limited number of terms can be taken as an accurate approximation and those terms can then be used to create a differential equation suitable for use in a FDTD code. Mur (Taflove, 1995) created a scheme based on the Taylor series expansion, that became very popular. Trefethen and Halpern (Taflove, 1995) proposed a different scheme based on a polynomial expansion of the square root. They showed that different choices of the polynomial lead to perfect absorption for plane waves impinging on the boundary from different angles α. The design process for a Trefethen–Halpern ABC is not set up in terms of absorption angle.

The theoretical performance of both the Mur and Trefethen–Halpern ABCs can be improved by taking higher orders of the Taylor series. However, in numerical experiments, the actual performance typically converges to about 1% reflection (Taflove, 1995). The problem probably occurs because the formulations assume that waves propagate in the grid at the speed of light in free space, c, but in fact, numerical dispersion causes phase velocity variations of 0.1 to 1%.

Higdon (1986) took a different approach: rather than produce an analytical ABC (Equation 4.49) and then create a finite-difference form of the analytical ABC, he produced a finite-difference ABC directly and then calculated its equivalence to an analytical boundary condition. The ABC that resulted is different from those already discussed because it is expressed both in terms of its order and in terms of specific angles that are absorbed perfectly. For example, a second order Higdon ABC can perfectly absorb energy impinging on the outer boundary from two given angles.

The freedom to assign the angle for perfect absorption does improve the ability of the modeller to specify an appropriate boundary. Higdon (1987) also showed that the Higdon ABC is equivalent to the Mur and Trefethen–Halpern ABCs for specific values of α. Higdon's differential annihilator is given by (Higdon, 1987)

$$\left(\prod_{j=1}^{p}\left((\cos\alpha_j)\frac{\partial}{\partial t}-c\frac{\partial}{\partial x}+\varepsilon_j\right)\right)u=0. \tag{4.51}$$

The discretization scheme for Equation 4.51 is given by (Giannopoulos, 1997)

$$\begin{aligned}\prod_{j=1}^{p}[&\frac{\mathbf{I}-\mathbf{Z}^{-1}}{\triangle l}((1-b)\mathbf{I}+b\mathbf{K}^{-1})+\\ &\frac{\cos\theta_j}{u}\frac{\mathbf{I}-\mathbf{K}^{-1}}{\triangle t}((1-a)\mathbf{I}+a\mathbf{Z}^{-1})]\boldsymbol{U}=0\end{aligned} \tag{4.52}$$

where $\mathbf{I}$, $\mathbf{K}$ and $\mathbf{Z}$ are defined as

$$\mathbf{I}\boldsymbol{U}\big|_{i,j}^{n} = \boldsymbol{U}\big|_{i,j}^{n} \tag{4.53}$$

$$\mathbf{K}\boldsymbol{U}\big|_{i,j}^{n} = \boldsymbol{U}\big|_{i,j}^{n+1} \tag{4.54}$$

$$\mathbf{Z}\boldsymbol{U}\big|_{i,j}^{n} = \boldsymbol{U}\big|_{i+1,j}^{n} \tag{4.55}$$

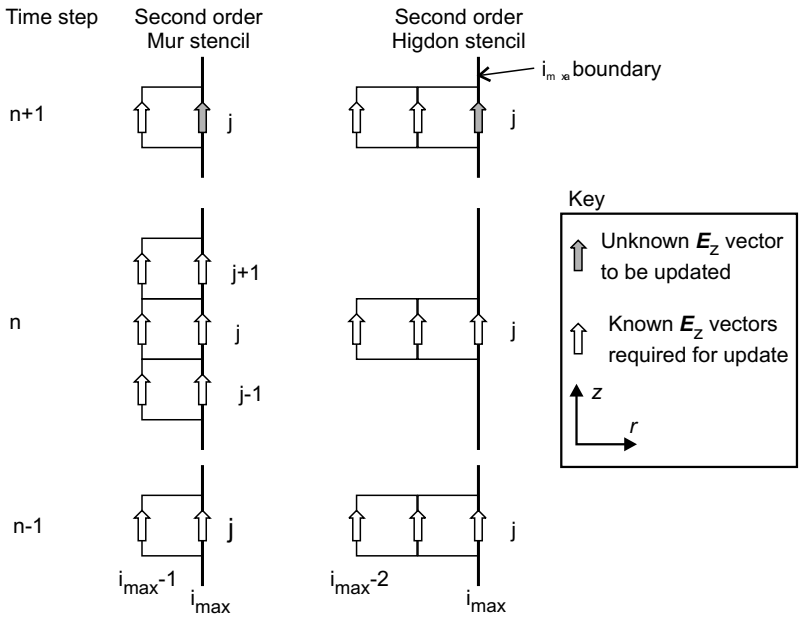

Figure 4.5: The stencils for the Mur and Higdon ABCs.

and the coefficients a and b are weighted space and time averages of the space and time derivatives. Higdon examined some specific sets of a and b, but the most popular and the one used in this thesis, is the box scheme, $a = 0.5$ and $b = 0.5$. The first order Higdon ABC applied at the boundary $x = x_{\max} = M$ of a 2D Cartesian mesh is then

$$\boldsymbol{E}_y\big|_{M,j}^{n} = \boldsymbol{E}_y\big|_{M-1,j}^{n-1} + h(\boldsymbol{E}_y\big|_{M-1,j}^{n} - \boldsymbol{E}_y\big|_{I,j}^{n-1}) \tag{4.56}$$

where

$$h = \frac{u\triangle t - \cos(\theta)\triangle l}{u\triangle t + \cos(\theta)\triangle l} \tag{4.57}$$

In Equations 4.52 and 4.57, θ is the angle of incidence for which zero reflection is required. In the event that higher order boundaries are applied, several values of θ_j can be used to prevent reflections in specific directions.

Higher order Higdon boundaries can be created by expressing the Higdon operator in a matrix form and applying it iteratively, as discussed in Randhawa (1996).

The Higdon ABC has a number of properties that make it ideal for RT modelling:

- Equation 4.56 is easy to apply, as are the higher order expressions of Equation 4.56.
- The Higdon ABC only requires knowledge of field values perpendicular to the boundary, as shown in Figure 4.5. The Mur ABC, requires knowledge of fields in adjacent rows so it needs special treatment in corner regions.
- The angle of total absorption can be specified for each point on the boundary. If the source position is known, the ABC can be optimized for each point on the boundary by calculating the expected angle of incidence of the outgoing wave.
- The velocity is required to set up the Higdon ABC, but velocities other than the velocity of light in free space can be used. Fortunately, low loss rocks, as shown in Appendix B, have relatively constant velocities as a function of frequency. In rocks with higher loss the performance of the ABC is less important because reflections are highly attenuated.

The Liao ABC

Liao et al. (1984) introduced an alternative formulation for an ABC that is not based on a wave equation. In the Liao ABC, the value of the field on the boundary is determined by using a space-time extrapolation from known fields along the line perpendicular to the boundary. The extrapolation is given by (Giannopoulos, 1997)

$$x - ut = \text{constant}. \tag{4.58}$$

The Liao ABC is (Liao et al., 1984)

$$U\big|_x^{n+1} = \sum_{m=1}^{N} (-1)^{m+1} C_m^N U\big|_{x-m\alpha c\triangle t}^{n-(m-1)} \tag{4.59}$$

where the binomial coefficient, C_m^N is

$$C_m^N = \frac{N!}{(N-m)!m!}. \tag{4.60}$$

Liao introduces a factor, c_A, the artificial transmitting velocity, where

$$c_A = \alpha c. \tag{4.61}$$

Values for α can be between 0.5 and 2 (Liao et al., 1984). Note that α here is not the angle of incidence, as it is in other ABCs. The Liao method is a Newton backward-difference polynomial used to extrapolate the field value on the boundary. If α can take any value between 0.5 and 2, it makes sense to choose values of α that will place $x - m\alpha c\triangle t$ at known grid points. For meshes abiding by the stability criterion, $c\triangle t = \triangle/2$, then for $\alpha = 2$, $m\alpha c\triangle t = m\triangle$ which is on the standard FDTD mesh. The update equation for a boundary point at $x = x_{\max} = M$ is then given by

$$U\big|_X^{n+1} = \sum_{m=1}^{N} (-1)^{m+1} C_m^N U\big|_{M-m}^{n-(m-1)}. \tag{4.62}$$

The Liao ABC has some advantages and some problems:

- The nature of the wave propagation is not referred to anywhere in the derivation of the ABC. The method appears to be very robust and the wide range of permissible values for α implies that a Liao boundary will work within a model where propagation is dispersive.
- Like the Higdon and other earlier ABCs, higher order Liao boundaries have better performance than lower order boundaries. However, unlike the earlier ABCs, the performance of the Liao boundary does increase for higher orders in real problems. This is probably because the Liao ABC is robust and is not based on any assumptions about velocity or angle of incidence of the outgoing waves (Taflove, 1995).
- The Liao ABC, like the Higdon ABC, uses a stencil of field values that are perpendicular to the boundary, as shown in Figure 4.5.
- The Liao boundary is reported to be unstable when run on computers using single-precision arithmetic(Taflove, 1995). Taflove cites Moghaddam (1990) who explains this instability as a consequence of a pole close to the unit circle. With an accumulation of error as a consequence of single-precision arithmetic, the pole can be moved out of the unit circle. The problem can be solved by using double precision arithmetic. Moghaddam recommends subtracting an adiabatic loss term of about 0.5% from each interpolation coefficient. Even with the loss term, performance of a second order Liao boundary is still better than second-order Mur.

The Liao ABC has been implemented in the RT model and can be used as an alternative to the Higdon ABC. In practice, there is a

problem with the Liao ABC, because of the limits on α: Parts of the RT FDTD model sometimes require the time step to be made considerably smaller than $\triangle t = \triangle/\sqrt{2}$ dictated by the Courant stability criterion. The Liao ABC cannot then be adjusted to fit existing grid values through judicious choice of α because α is restricted to values between 0.5 and 2. For example, if $\triangle t = \triangle/16$ the Liao ABC can become ineffective and may also be unstable.

Superabsorption and the complementary operators method

The final analytical ABCs discussed here use the concept of complementary solutions. The first of these is superabsorption, introduced by Mei and Fang (Taflove, 1995). Any ABC introduces some error, compared to the fields that would be calculated at the position of the ABC if the computational area were infinite. However, with some manipulation, the error can be substantially reduced.

Consider an outer grid boundary, $x_{\max} = M\triangle$ where the field component $\boldsymbol{E}_z^{\mathrm{ABC}}\big|_{M,j}^{n}$ has been calculated using some local ABC. The error in the ABC is

$$\mathrm{Error}_1 = \boldsymbol{E}_z^{\mathrm{ABC}}\big|_{M,j}^{n} - \boldsymbol{E}_z^{\infty-\mathrm{grid}}\big|_{M,j}^{n} \tag{4.63}$$

where $\boldsymbol{E}_z^{\infty-\mathrm{grid}}\big|_{M,j}^{n}$ is the ideal FDTD solution that would be obtained in an infinitely large grid. If Equation 4.63 is used to calculate the adjacent magnetic field, that field will also have an associated error:

$$\boldsymbol{H}_y^{(1)}\big|_{M-1/2,j}^{n+1/2} = \boldsymbol{H}_y^{(1)}\big|_{M-1/2,j}^{n+1/2} + \frac{\triangle t}{\mu_0 \triangle} \cdot \mathrm{Error}_1. \tag{4.64}$$

We can obtain a second estimate for the adjacent magnetic field by applying the same ABC used on the electric field to the magnetic field, at the plane $x = (M - 1/2)\triangle$:

$$\boldsymbol{H}_y^{\mathrm{ABC}}\big|_{M-1/2,j}^{n+1/2} \equiv \boldsymbol{H}_y^{(2)}\big|_{M-1/2,j}^{n+1/2} = \boldsymbol{H}_y^{\infty-\mathrm{grid}}\big|_{M-1/2,j}^{n+1/2} + \mathrm{Error}_2. \tag{4.65}$$

The key observation is that Error_1 and Error_2 are not independent. By assuming an outward propagating wave, Mei and Fang related the two errors and used the relationship to cancel the error in $\boldsymbol{H}_y\big|_{M-1/2,j}^{n+1/2}$.

Taflove (1995) concludes that superabsorption was well worth applying before the PML was developed, but doubts that it will achieve the overall performance of the PML.

The complementary operators method (COM) (Ramahi, 1997a) is similar to superabsorption, except that instead of deriving two expressions for the same error, it strives to develop two ABCs with complementary errors. Ramahi achieves this by using a Higdon ABC and its derivative with respect to the direction of propagation, which has the same reflection coefficient but is 180° out of phase.

Initially, the COM required two runs of the FDTD code, but it was later improved to operate in a single run and also to remove second-order reflections in both 2D and 3D models (Ramahi, 1997b, 1998). Ramahi and Schneider (1998) show that the complementary COM can outperform the PML for certain very difficult ABC problems.

Although the COM provides excellent performance, it is a costly technique to implement; certainly of the same order as the PML for ABCs with similar performance. It is not used for RT modelling because the additional performance is not required.

4.6 SOURCES

The nature of the source is determined by the type of problem being modelled. For a receiving antenna, or a scattering problem, a wave is introduced at the boundary of the numeric model and allowed to propagate across the model. For a transmitting antenna, a voltage wave can be introduced at the terminals of the antenna.

Yee (1966) provided the original plane wave source condition by inserting $\boldsymbol{E}$ and $\boldsymbol{H}$ fields for a wave into the model as an initial condition. If the $\boldsymbol{H}$ fields that are inserted are calculated offset by half a time step from the $\boldsymbol{E}$ fields, then when modelling is started the wave will continue to propagate in the desired direction and will scatter off any structure in the grid.

There are two problems with inserting the incident wave as an initial condition (Taflove, 1995): if long duration pulses are used, the physical space required to contain them may be quite large; and plane waves in 2D or 3D grids, at oblique angles to the grid, undergo

wavefront distortion. For these reasons, the initial condition wave source is usually applied only in specialized models, primarily 1D FDTD simulations.

The simplest source to implement is the "hard source" (Taflove, 1995). The hard source is implemented by assigning a desired time function to a specific electric or magnetic field component in the FDTD space lattice. For example, if a wire antenna in the z direction is modelled as a series of cell boundaries where $\boldsymbol{E}_z = 0$, then a source voltage can be introduced at the feed point of the wire, by setting the value of that electric field vector at each time step.

Many different voltage waveforms can be used. For single frequency simulations, a sinusoidal source waveform may be appropriate. However, since the FDTD method is inherently broadband, a source waveform that contains a range of frequencies is more suited to its abilities. The Gaussian is a common hard source pulse that contains DC. Its general form is (Taflove, 1995),

$$\boldsymbol{E}_z\big|_{i_s}^{n} = E_0 \mathrm{e}^{-[(t-t_0)/t_{\mathrm{decay}}]^2}. \tag{4.66}$$

The pulse is centred at time step n_0 and has a 1/e characteristic decay of n_{decay}.

When designing an FDTD simulation, the source pulse is usually specified in terms of the required bandwidth. If a Gaussian source pulse is used, its bandwidth is simply the inverse of the width of the pulse, measured at 50% of its maximum value. This width is called the full width half maximum, or FWHM,

$$\mathrm{FWHM} = 1/f_{\mathrm{max}}. \tag{4.67}$$

The decay time used in the modelling code described in this thesis is then

$$t_{\mathrm{decay}} = \mathrm{FWHM}/1.667. \tag{4.68}$$

where f_{max} is the desired bandwidth, or in this case the desired maximum frequency. The factor 1.667 implies that the frequency response will be 30 dB down from its maximum value at the specified maximum frequency. The value of 30 dB is a compromise based on

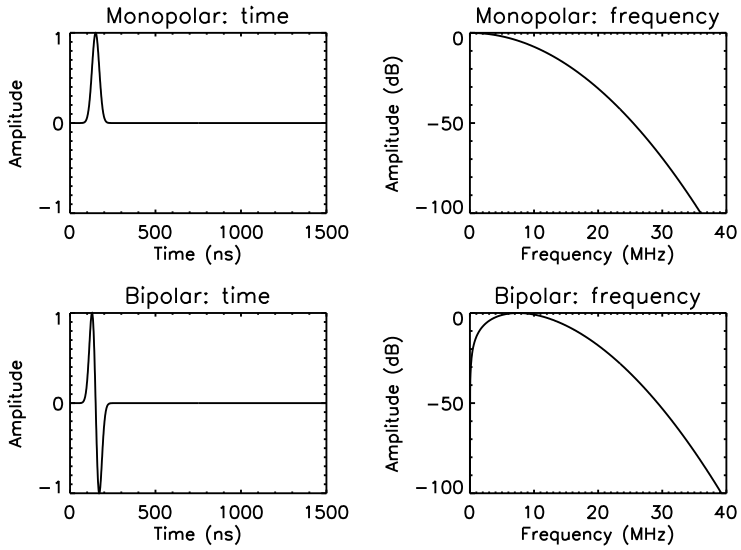

Figure 4.6: Monopolar and bipolar Gaussian source pulses, in the time and frequency domain, with a bandwidth of 20 MHz.

the need to have as much energy as possible at the maximum frequency, but as little energy as possible above it. In practice, the value works well.

From Equation 4.66 $\boldsymbol{E}_z$ is not zero at time step $n = 0$. In order to avoid truncation error when converting to the frequency domain, the value of the pulse at time step $n = 0$ has to be small, so the pulse centre needs to be delayed by some factor. The recommended value is three times the pulse width (Taflove, 1995), so

$$n_0 = 3\text{FWHM}. \tag{4.69}$$

The value of the pulse at truncation depends on both the decay time and the delay. From the values in Equations 4.68 and 4.69, the pulse is truncated at e^{-25}, or more than 217 dB down on the maximum amplitude of the pulse. This value is smaller than the dynamic range available from typical implementations of single precision real numbers (Kunz and Luebbers, 1993).

The complete expression of the monopolar Gaussian source pulse used in the RT modelling code is

$$\boldsymbol{E}_z\big|_{i_s}^n = \frac{1}{\triangle z}\mathrm{e}^{-[1.667 f_{\max}(n\triangle t - 3/f_{\max})]^2}. \tag{4.70}$$

The amplitude of the electric field is fixed to a maximum of 1 V/m.

For modelling conductive materials, it is useful to use a source pulse that has no energy at DC because the velocity of propagation of a pulse, v is given by

$$v = \frac{2}{\mu\varepsilon\left[\left(\sqrt{1+\frac{\sigma^2}{\omega^2\varepsilon^2}}+1\right)\right]^{1/2}}. \tag{4.71}$$

If there is any conductivity at low frequencies, the term containing the conductivity increases rapidly as $\omega \rightarrow 0$ leading to a decreasing propagation velocity. In practice, a pulse develops a long tail as it propagates across the modelling space. The pulse cannot be transformed into the frequency domain until the tail has settled, so modelling has to continue for a large number of steps. If the low frequencies are removed from the source pulse, the tail settles more quickly and modelling can be terminated after fewer steps.

The source pulse used in the RT modelling software is the time derivative of Equation 4.70, scaled to have a peak amplitude of 1 V/m. In this thesis, it is called a bipolar Gaussian. It is defined in the modelling code as

$$\boldsymbol{E}_z\big|_{i_s}^n = -\frac{3.886 f_{\max}}{\triangle z}(n\triangle t - 3/f_{\max})\mathrm{e}^{-[1.667 f_{\max}(n\triangle t - 3/f_{\max})]^2}. \tag{4.72}$$

The monopolar and bipolar Gaussian source waveforms are illustrated in Figure 4.6.

4.7 SUBCELL EXTENSIONS

Earlier, in the introduction to the FDTD method, I mentioned that it is not possible to construct a grid of arbitrary size and suggested that grids of between $\lambda/10$ and $\lambda/20$ offer acceptable results. In fact, in order to model physically small features, the grid must be sufficiently fine to resolve the features of interest, in addition to being small compared to the wavelength. There is no point in using a 1.0 m grid if the antenna being modelled is 0.5 m high, even if the grid can resolve the wavelength being used.

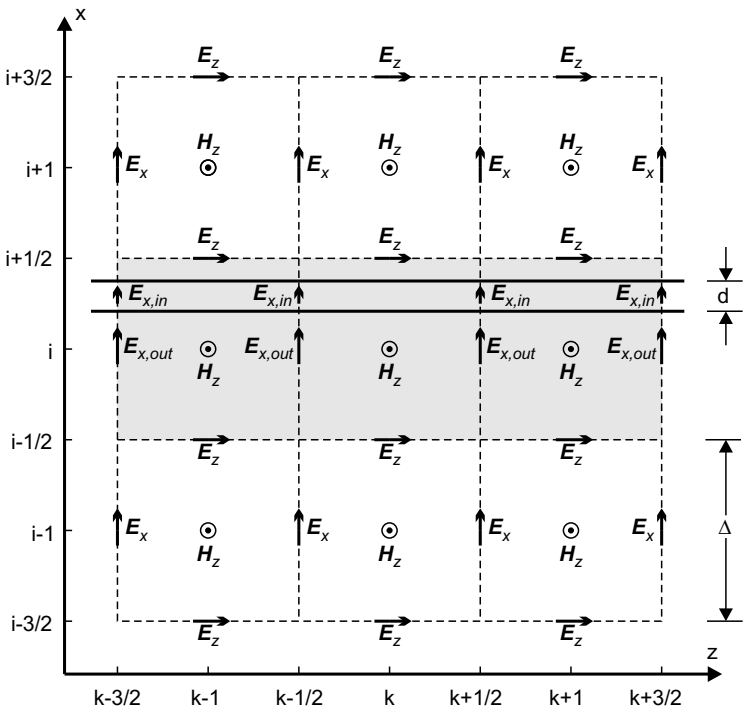

Figure 4.7: A slice through the rectangular FDTD grid at $j - 1/2$ plane showing the locations of field components. The shaded cells are modified using the special cell update equations. From Maloney and Smith (1992).

The need to reduce grid size to model fine features can be overcome by introducing subcell extensions — modified update equations in cells that contain features smaller than the grid size. Several extensions have been introduced (Taflove, 1995), but two are of particular interest to RT modelling: thin layers and thin wires. Antennas for use in RT are always thin compared to the wavelength and may be coated in a thin layer of insulation.

4.7.1 The thin layer

Maloney and Smith (1992) proposed a thin layer approximation for layers thinner than a cell. The geometry is illustrated in Figure 4.7. In cells containing the thin layer, the $\boldsymbol{E}_x$ component is divided into two, a component within the layer, $\boldsymbol{E}_{x,in}$ and a component in the existing cell, $\boldsymbol{E}_{x,out}$. Maxwell's equations in integral form are applied around

the boundary of the cell to derive the update equations. $\boldsymbol{E}_{x,in}$ and $\boldsymbol{E}_{x,out}$ are updated in the conventional way, as is $\boldsymbol{H}_x$. At the $\boldsymbol{E}_z$ and $\boldsymbol{E}_y$ field nodes the integration creates an effective conductivity and permittivity equal to the average of those of the background and the thin layer. The $\boldsymbol{H}$ fields tangential to the thin layer, $\boldsymbol{H}_y$ and $\boldsymbol{H}_z$ are updated taking both $\boldsymbol{E}_{x,in}$ and $\boldsymbol{E}_{x,out}$ into account.

Maloney and Smith assume that the $\boldsymbol{E}$ field in the thin layer is constant, which implies that the thickness of the thin layer is small compared to the skin depth of material comprising the layer. Van Den Berghe et al. (1998) model the thin layer including the skin depth.

4.7.2 The thin wire

The earliest thin wire extension was accomplished by introducing the current and charge on the wire as separate parameters into the FDTD update equations, coupled to the fields around the wire (Holland and Simpson, 1981). The approach is accurate but computationally complex to apply (Douglas et al., 1999).

The general approach of using Maxwell's equations in integral form can incorporate near field physics to yield special purpose time stepping expressions that are not obvious from the pure finite-difference perspective (Taflove, 1995). A good example is the thin-wire subcell extension introduced in Umashankar et al. (1987). The geometry of the thin-wire subcell is shown in Figure 4.8. The approximation is based on the near field assumptions that the circumferential magnetic field and the radial electric field vary as $1/r$ near the wire, where r is the distance from the centre of the wire. In 3D rectangular coordinates,

$$\boldsymbol{E}_x(r) = \frac{\triangle}{2r}\boldsymbol{E}_x(\triangle/2), \tag{4.73}$$

$$\boldsymbol{H}_y(r) = \frac{\triangle}{2r}\boldsymbol{H}_y(\triangle/2). \tag{4.74}$$

There is no variation of any of the other properties across the cell. There is also no variation in $\boldsymbol{E}_x$ and $\boldsymbol{H}_y$ as z varies across one cell. Faraday's law can now be applied around contour C. The $1/x$ variations yield natural logarithms. The following expression relates the

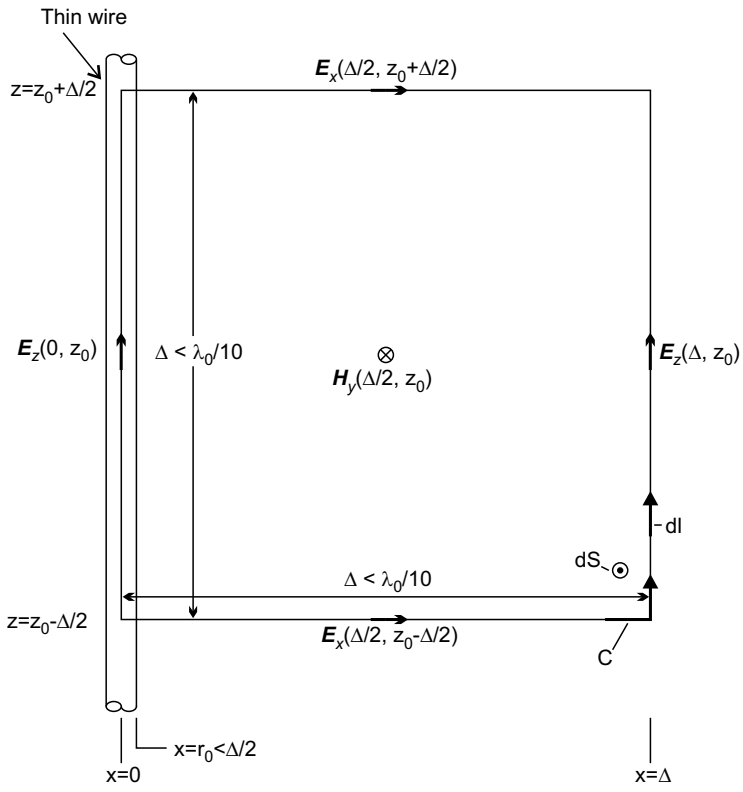

Figure 4.8: Faraday's law contour path for a thin wire model. From Umashankar et al. (1987)

two components:

$$\frac{\boldsymbol{H}_y\big|_{\triangle/2,z_0}^{n+1/2} - \boldsymbol{H}_y\big|_{\triangle/2,z_0}^{n-1/2}}{\triangle t} \simeq \frac{\boldsymbol{E}_x\big|_{\triangle/2,z_0-\triangle/2}^{n} - \boldsymbol{E}_x\big|_{\triangle/2,z_0+\triangle/2}^{n} \cdot \frac{1}{2}\ln\left(\frac{\triangle}{r_0}\right) + \boldsymbol{E}_z\big|_{\triangle,z_0}^{n}}{\mu_0 \frac{\triangle}{2}\ln\left(\frac{\triangle}{r_0}\right)}. \quad (4.75)$$

In Equation 4.75, r_0 is the wire radius, and it is assumed to be less than half the cell size, $\triangle$. Isolating $\boldsymbol{H}_y\big|_{\triangle/2,z_0}^{n+1/2}$ on the left hand side, yields the required modified time stepping relation. The equation can be generalized to obtain time stepping relations for the other circumferential magnetic field components adjacent to the wire. Note that no other update equations need to be modified to use the thin-wire subcell extension.

The methods of Umashankar et al. (1987) or Holland and Simpson

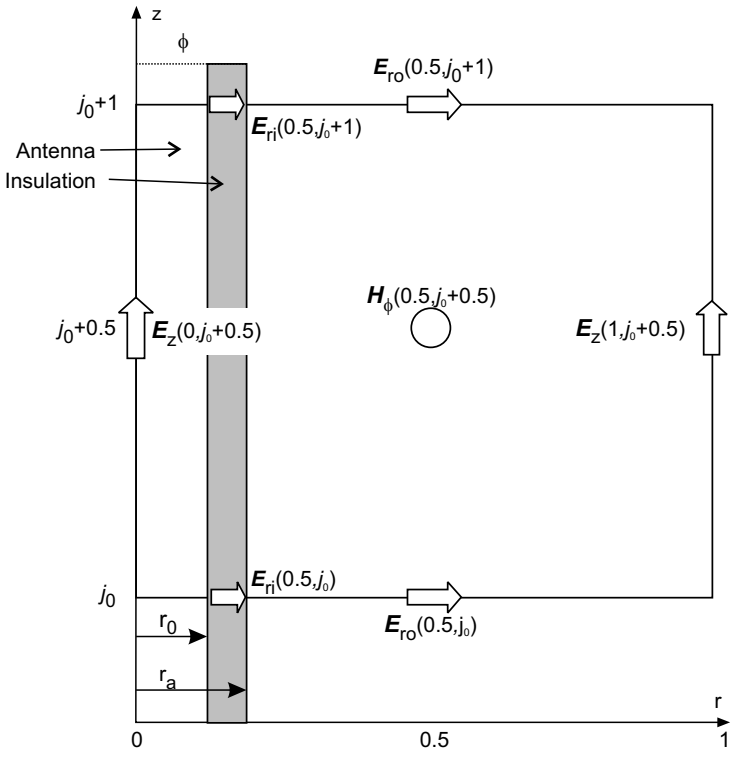

Figure 4.9: The Faraday's law contour path for a generalized thin wire model, including a lossy dispersive coating.

(1981) improve the performance of thin wires in free space by modifying the circumferential magnetic fields adjacent to the conductor. The FDTD assumption of constant fields across each cell is also inaccurate in the volume at the end of the antenna. Douglas et al. (1999) assume a particular charge density distribution at the end of the antenna to revise the update equations for the axial electric field from the end of the antenna and the circumferential magnetic field surrounding it. They claim improvement in accuracy particularly in determining the input impedance.

4.7.3 The coated thin wire

The thin-wire and the thin layer subcell extensions are useful additions to the FDTD technique. To model an RT antenna, a subcell extension is required that can model a thin wire coated with a thin layer

and do so accurately when the coated wire is enclosed in a dispersive lossy medium. Boonzaaier and Pistorius (1992) reported a thin-wire subcell extension for wires coated with non-dispersive dielectrics. They developed the technique further to incorporate lossy coatings, but neither the coating nor the medium can be dispersive (Boonzaaier and Pistorius, 1994).

A novel coated thin-wire subcell extension has been developed specifically for RT and its derivation is now presented. It incorporates both the thin-wire and thin layer techniques discussed above. The combination is simplified because both of those techniques are derived from the integral form of Maxwell's equations, applied to the boundaries of the cell. The cell geometry is defined in Figure 4.9. As the subcell extension is designed to fit into the BOR FDTD code, it is expressed in the coordinate system of that code.

The radial $\boldsymbol{E}$ field at the surface of the antenna is split into two: $\boldsymbol{E}_{rin}$ within the insulation and $\boldsymbol{E}_{ro}$ outside the insulation. Both the radial $\boldsymbol{E}$ field and the circumferential $\boldsymbol{H}$ field are assumed to vary as $1/r$, according to the quasi-static approximation:

$$\boldsymbol{E}_{rin}\big|_{r,j}^{n} = \boldsymbol{E}_{rin}\big|_{(r_a+r_0)/2,j}^{n} \frac{r_a + r_0}{2r}, \tag{4.76}$$

$$\boldsymbol{E}_{ro}\big|_{r,j}^{n} = \boldsymbol{E}_{ro}\big|_{1/2,j}^{n} \frac{\triangle r}{2r}, \tag{4.77}$$

$$\boldsymbol{H}_{\phi}\big|_{r,j}^{n} = \boldsymbol{H}_{\phi}\big|_{1/2,j}^{n} \frac{\triangle r}{2r}. \tag{4.78}$$

Note that in each case, the position of the vector has the continuous index r, rather than the discrete index i.

I modelled this geometry in two ways. The first is described in Vogt et al. (1999) and relies on continuity of the electric flux density across the boundary between the insulation and the surrounding medium,

$$\boldsymbol{D}_{ri}\big|_{r_0^-,j} = \boldsymbol{D}_{ro}\big|_{r_0^+,j} \tag{4.79}$$

where

$$\boldsymbol{D}_r = \varepsilon_\infty \boldsymbol{E}_r + \boldsymbol{P}_r. \tag{4.80}$$

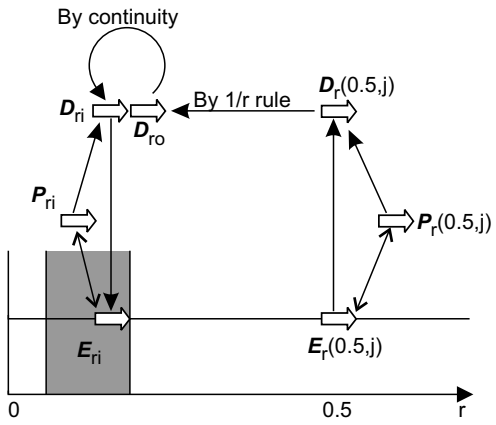

Figure 4.10: One process for deriving the subcell extension of a coated thin wire.

The $\boldsymbol{H}_\phi$ component can be determined by applying Faraday's law around the boundary of the cell illustrated in Figure 4.9, but $\boldsymbol{E}_{ro}$ and $\boldsymbol{E}_{rin}$ are required to perform the necessary integrations.

Following Vogt et al. (1999), $\boldsymbol{E}_{ro}$ and $\boldsymbol{P}_{ro}$ are known, because they are available from the FDTD grid. $\boldsymbol{D}_{ro}$ follows from $\boldsymbol{E}_{ro}$, by equation 4.80. From the $1/r$ dependence, $\boldsymbol{D}_{ro}\big|_{r_0^+,j}$ just outside the boundary of the insulation can be determined. By continuity $\boldsymbol{D}_{rin}\big|_{r_0^-,j}$ follows. $\boldsymbol{E}_{rin}$ at the boundary can be determined by applying equation 4.80 again. Both the $\boldsymbol{E}_r$ vectors are now known so $\boldsymbol{E}$ fields can be integrated around the contour. The process is illustrated graphically in Figure 4.10. $\boldsymbol{P}_{rin}$ has to be determined and stored between steps to update $\boldsymbol{E}_{rin}$.

The method works well if the two materials do not have large polarization contributions. It has been verified in Vogt et al. (1999). However, when the polarization contributions are large, the time offset between $\boldsymbol{P}_{rin}$ and $\boldsymbol{P}_{ro}$ leads to inaccuracies. A different, simpler extension is now proposed:

To determine $\boldsymbol{E}_{rin}$ just inside the insulation/background boundary, make use of the fact that $\boldsymbol{H}_\phi$ varies as $1/r$ in the radial direction and does not vary over the cell in the z direction. Calculate the value of $\boldsymbol{H}_\phi$ at the desired radius by

$$\boldsymbol{H}_\phi\big|_{r_a,j}^n = \boldsymbol{H}_\phi\big|_{1/2,j}^n \frac{\triangle r}{2r_a}. \tag{4.81}$$

Use the new value of $\boldsymbol{H}_\phi$ to update $\boldsymbol{E}_{rin}$. $\boldsymbol{E}_{ro}$ is updated normally as part of the FDTD algorithm. $\boldsymbol{H}_\phi$ can now be updated using the two values from $\boldsymbol{E}_{rin}$ and $\boldsymbol{E}_{ro}$. The update for $\boldsymbol{E}_{rin}$ follows that given in equation 4.32 for $\boldsymbol{E}_r$, altered to take account of equation 4.81,

$$\begin{aligned}\boldsymbol{E}_{rin}\big|^{n+1}_{r_a,j+1/2} &= c_1\boldsymbol{E}_{rin}\big|^{n}_{r_a,j+1/2} \\ &+ \sum_{i=1}^{n} c_{2i}\boldsymbol{P}_{rin}\big|^{n+1/2}_{r_a,j+1/2} \\ &+ c_4\frac{\triangle r}{2r_a}\left(\boldsymbol{H}_\phi\big|^{n+1/2}_{1/2,j+1/2} - \boldsymbol{H}_\phi\big|^{n+1/2}_{1/2,j-1/2}\right) \end{aligned} \quad (4.82)$$

where the coefficients c_1, $c_2 i$ and c_4 are as before (Equations 4.33, 4.34 and 4.36), except that they are calculated using the electrical properties of the insulation rather than those of the surrounding medium.

The update equation for $\boldsymbol{E}_{ro}$ does not change, it is simply that for $\boldsymbol{E}_r\big|_{1/2,j}$. The update equation for $\boldsymbol{H}_\phi$ can be derived by integrating Faraday's law,

$$\oint_C \boldsymbol{E}\cdot \mathrm{d}\boldsymbol{l} = -\frac{\partial}{\partial t}\iint_{\mathrm{S}} \boldsymbol{B}\cdot \mathrm{d}\boldsymbol{S} \quad (4.83)$$

around the contour shown in Figure 4.9 giving

$$\begin{aligned}-\mu_0\frac{\partial}{\partial t}\int_{r_0}^{\triangle r}\int_{j}^{j+1} \boldsymbol{H}_\phi\big|_{1/2,j+1/2}\frac{\triangle r}{2r}\partial z\partial r& \\ = \int_{j}^{j+1}\boldsymbol{E}_z\big|_{0,j+1/2}\,\mathrm{d}z + \int_{j+1}^{j}\boldsymbol{E}_z\big|_{1,j+1/2}\,\mathrm{d}z& \\ + \int_{r_0}^{r_a}\boldsymbol{E}_{rin}\big|_{j+1}\frac{r_a}{r}\,\mathrm{d}r + \int_{r_a}^{r_0}\boldsymbol{E}_{rin}\big|_{j}\frac{r_a}{r}\,\mathrm{d}r& \\ + \int_{r_a}^{\triangle r}\boldsymbol{E}_r\big|_{1/2,j+1}\frac{\triangle r}{2r}\,\mathrm{d}r + \int_{\triangle r}^{r_a}\boldsymbol{E}_r\big|_{1/2,j}\frac{\triangle r}{2r}\,\mathrm{d}r.& \end{aligned} \quad (4.84)$$

Evaluating the integrals,

$$\begin{aligned} -\mu_0 \triangle z \frac{\triangle r}{2} \ln\left[\frac{\triangle r}{r_0}\right] \frac{\partial}{\partial t} \boldsymbol{H}_\phi\big|_{1/2,j+1/2} & \\ = -\triangle z \boldsymbol{E}_z\big|_{1,j+1/2} & \\ + r_a \ln\left[\frac{r_a}{r_0}\right] \left(\boldsymbol{E}_{rin}\big|_{j+1} - \boldsymbol{E}_{rin}\big|_j\right) & \\ + \frac{\triangle r}{2} \ln\left[\frac{\triangle r}{r_a}\right] \left(\boldsymbol{E}_r\big|_{1/2,j+1} - \boldsymbol{E}_r\big|_{1/2,j}\right) & \end{aligned} \tag{4.85}$$

which leads directly to the update equation

$$\begin{aligned} \boldsymbol{H}_\phi\big|_{1/2,j+1/2}^{n+1/2} = & \boldsymbol{H}_\phi\big|_{1/2,j+1/2}^{n-1/2} \\ & + m_3 \, \boldsymbol{E}_z\big|_{1,j+1/2}^{n} \\ & + m_4 \left(\boldsymbol{E}_r\big|_{1/2,j}^{n} - \boldsymbol{E}_r\big|_{1/2,j+1}^{n}\right) \\ & + m_5 \left(\boldsymbol{E}_{rin}\big|_{j}^{n} - \boldsymbol{E}_{rin}\big|_{j+1}^{n}\right) \end{aligned} \tag{4.86}$$

where

$$m_3 = \frac{2\triangle t}{\mu_0 \triangle r \ln\left[\frac{\triangle r}{r_0}\right]}, \tag{4.87}$$

$$m_4 = \frac{\triangle t \ln\left[\frac{\triangle r}{r_a}\right]}{\mu_0 \triangle z \ln\left[\frac{\triangle r}{r_0}\right]}, \tag{4.88}$$

$$m_5 = \frac{2 r_a \triangle t \ln\left[\frac{r_a}{r_0}\right]}{\mu_0 \triangle z \triangle r \ln\left[\frac{\triangle r}{r_0}\right]}. \tag{4.89}$$

If there is no insulation, then $r_a = r_0$, $\ln(r_a/r_0) = 0$, and equations 4.86–4.89 simplify to those given in Umashankar et al. (1987).

This second formulation for a coated thin wire has been tested for materials with large polarization. Verification is presented later in this chapter.

4.8 STABILITY

The generalized Courant stability criterion for a lossless homogeneous FDTD grid determines the largest time step that can be used before the grid is *guaranteed* to be unstable. The stability criterion

implies that the time step must be less than the time it takes a wave propagating in the grid to cross a grid cell. For a 2D FDTD grid, if $\triangle x = \triangle y = \triangle$, then the time step is given by

$$\triangle t \leq \frac{\triangle}{c\sqrt{2}}. \tag{4.90}$$

However, the general problem of stability in an FDTD model extends beyond the grid itself. The absorbing boundaries contribute to the problem of stability, as does the use of lossy dispersive media in the grid. The BOR algorithm itself also introduces stability problems (Taflove, 1995). In general, a properly chosen time step allows models to be stable for many thousands of steps, if not indefinitely (Taflove, 1995), but very small time steps lead to very long run times.

4.8.1 The BOR algorithm

Taflove (1995), gives an empirical stability criterion for a BOR FDTD code:

$$\triangle t \leq \triangle x/\sqrt{2}c \tag{4.91}$$

but also notes "It has been observed that the stability of the algorithm is very sensitive to the way the field components near the axis are computed".

4.8.2 Absorbing boundary conditions

Giannopoulos (1997) investigated ABCs for lossy media in both FDTD and TLM and discussed their stability. At zero frequency, both the Higdon and Liao ABCs have a marginally stable pole located on the unit circle $|R| = 1$ irrespective of the angle of incidence. Instabilities arise from the unavoidable use of finite precision arithmetic in the numerical algorithms.

One way to make the ABCs stable is to include loss into their formulation. Higdon (1987) recommends the addition of a small loss term. As discussed in Section 4.5.2, the Liao ABC can be made stable by using double precision arithmetic, or by adding a small loss term. Both ABCs that can be used with the RT modelling code are stable when the model itself is stable.

Table 4.1: The Debye model of a dolomite sample.

$\sigma_0 =$	0	$\varepsilon_\infty =$	10.15
$\varepsilon_{w1} =$	0.34	$\tau_1 =$	7.3×10^{-12}
$\varepsilon_{w2} =$	0.37	$\tau_2 =$	2.20×10^{-9}
$\varepsilon_{w3} =$	0.27	$\tau_3 =$	1.88×10^{-8}
$\varepsilon_{w4} =$	0.35	$\tau_4 =$	1.51×10^{-7}
$\varepsilon_{w5} =$	0.34	$\tau_5 =$	5.11×10^{-12}
$\varepsilon_{w6} =$	0.34	$\tau_6 =$	0.0027
$\varepsilon_{w7} =$	0.34	$\tau_7 =$	0.139

4.8.3 Lossy media

Pereda et al. (1998) show that the time–average scheme used in this thesis has the same stability criterion as the standard FDTD algorithm for lossless media, $\triangle t \leq \triangle/\sqrt{2}$ for a 2D model. They point out that the time–forward scheme allows larger time steps to be used at the cost of increased dispersion. They recommend remaining with time–average, while Schuster et al. (2000) recommend time–forward. Computer run time has not been a major problem with the RT FDTD code, so at the moment it remains a time–average code.

4.8.4 Dispersive media

When the FDTD model contains Debye media, the smallest time step must obey the Courant criterion, but it must also resolve the smallest relaxation time of the medium (Petropoulos, 1994a,b). This is confirmed here by numerical experiment:

A particular dolomite sample can be approximated by a seven term Debye medium with the electrical properties listed in Table 4.1. A bare 0.7 m long monopole, 2 mm in diameter is modelled immersed in a dolomite medium and modelled from DC to 50 MHz. The modelling space is 50×50 cells, with each cell 0.1×0.1 m in size. The highest velocity in the model leads to a Courant time step of 0.54 ns. If the model is run including all seven terms of the Debye model, it is unstable and requires the time step to be reduced to 1/8th of its original value.

The only relaxation time faster than 0.54 ns is the first, at 7.3 ps. If that term is removed from the Debye medium, the model runs without reducing the time step size. It also runs without instability if the 2 mm diameter antenna is insulated with 20 mm of PTFE insulation. It is reasonable to remove Debye terms with relaxation times smaller than the FDTD time step because they only influence the permittivity of the material at frequencies outside the bandwidth of the model.

4.8.5 Subcell extensions

Douglas et al. (1999) discuss the stability of their thin-wire subcell extension and propose an experimentally determined stability coefficient, $S_{\max}$. Their stability coefficient is proportional to $\ln(r_0)$, the log of the radius of the wire being modelled, but also contains other factors.

Grando et al. (1993) offer a stability analysis for an alternative thin-wire formulation, based on an introduction of in-cell inductance. Their calculations show that for wires with a radius of less than $0.06\times$ the cell radius, the system should be stable if it abides by the general FDTD stability criteria. For wires of larger radius, they propose an alternative stability criterion. However, their stability criterion is specific to their thin-wire model and does not apply to the thin-wire model reported here.

4.8.6 The general problem

The basic Courant stability criterion, modifications necessary for the ABC, and modifications for dispersive media all lead to a figure for the largest time step before the grid is guaranteed to be unstable. Under certain circumstances, models with time step sizes set by the criterion and its modifications may still be unstable, because it is difficult to determine the stability of algorithms such as the coated thin wire subcell extension.

In general, the stability criteria give a guideline as to what time step size can be expected to work, but exact values for $\triangle t$ may need

to be determined empirically.

4.9 MODEL VERIFICATION

4.9.1 Introduction

The FDTD model presented here can only be accepted as an accurate model of the physical processes after it has been verified. The ultimate verification is comparison against a real antenna in a real rock situation. Unfortunately, rock is not homogeneous, so it is not possible to build a realistic test site at full scale with a volume of rock suitable for testing against.

Another option for testing is to compare the numerical model against a scale model (Smith and Scott, 1989). The scale model is a real physical environment, so it can be used to verify that aspects of the numerical model accurately reflect the real situation. I have tested the numerical model against a model that is physically small, but a reasonable electrical size compared to the wavelength used. It is not a scale model, but rather a manageably sized physical model.

The alternative to scale model testing, is to test numerically, against analytical solutions or against alternative computational models. It is difficult to test against analytical solutions, because closed form solutions are not available for most problems of antennas in rock. Also, there are not many numerical codes that can model thin wire antennas with a thin layer of insulation, buried in rock, but it is possible to compare simpler cases and confirm that the FDTD model accurately represents those cases.

Here, the model will be verified in stages. In the first stage, it will be compared with an alternative numerical model for thin wire antennas. The second stage will confirm the dispersive media model by comparing a single run of a model using Debye dispersion to several runs of various models using fixed values of σ_e and ε_e . In the third stage, the thin-layer subcell extension will be modelled within the FDTD model by comparing it to a thin layer modelled using a very fine grid. The comparison will confirm that the thin-layer subcell extension is functioning correctly. Finally, the model will be compared

with an experimental scale model using salt water at frequencies of up to 450 MHz to confirm that the whole system is working and can model real antennas.

4.9.2 Verification against a moment method code

A 6.4 m dipole in air is modelled using the FDTD code and the Numerical Electromagnetics Code, NEC , a well known moment method code considered to be a benchmark standard. The FDTD antenna is modelled as a dipole. The modelling space is 120×240 cells, each $0.4\,\text{m} \times 0.4\,\text{m}$. The antenna is 15 segments long fed in the centre. The model uses second order Higdon ABCs and is run for 16384 steps each of 0.67 ns. The FDTD model is stimulated with a bipolar Gaussian pulse, containing frequency components of up to 50 MHz.

The NEC antenna is 6.4 m long. This is to account for the fact that FDTD creates an antenna that is effectively 1 segment longer than the modelled length, unless some correction for the end of the wire is applied (Douglas et al., 1999). The NEC model is run for frequencies from 1 MHz to 51 MHz in 0.5 MHz steps. Fields at 40 m are extracted using the NEC near field card.

The models are run twice, once for antennas 44 mm in diameter, and once for antennas 2 mm in diameter. All the antennas have no insulation and are in air. Field strength is measured 40 m away from the feed point of the antenna in the direction normal to the antenna axis.

The field strengths predicted by both models at 40 m are plotted in Figure 4.11. The match is so close that the plots of one technique obscure those of the other. The input impedance predictions are also good, as shown in Figure 4.12. If the antenna is reduced from 44 m to 2 mm in diameter there is a small change in the bandwidth of the antenna, shown in Figure 4.11, but a marked change in the input impedance, shown in Figure 4.12.

This first stage of verifying the FDTD code confirms that it is capable of modelling an antenna in air and suggests that the thin-wire subcell extension is working. The verification implies that the BOR model, source model and ABCs are working correctly.

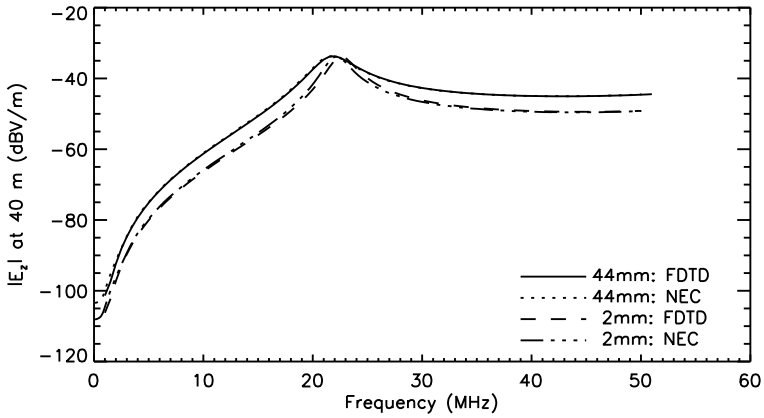

Figure 4.11: NEC vs FDTD: $|E_z|$ fields at 40 m.

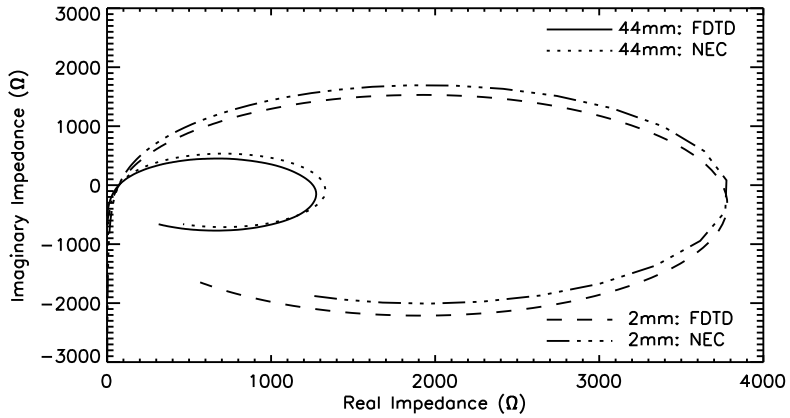

Figure 4.12: Input impedance calculated by NEC and FDTD.

4.9.3 Verifying the Debye model

The implementation of the Debye model in the FDTD code is verified by first running a single model including the Debye estimate for a material. Then a series of models are run, using different fixed electrical properties, corresponding to the electrical properties predicted by the Debye model for various frequencies.

The antenna that is modelled here for verification is a 3.4 m long 44 mm diameter bare monopole on a ground plane, embedded in a dolerite background. The dolerite was chosen because its Debye model is fourth order. The electrical properties of the sample are

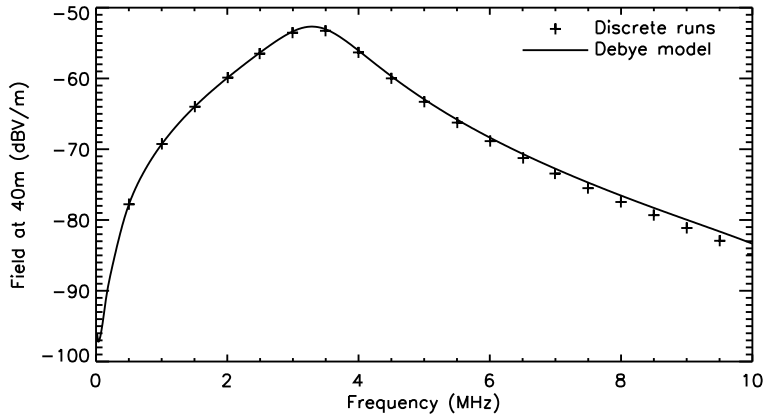

Figure 4.13: A comparison of field predictions for Debye and fixed material models.

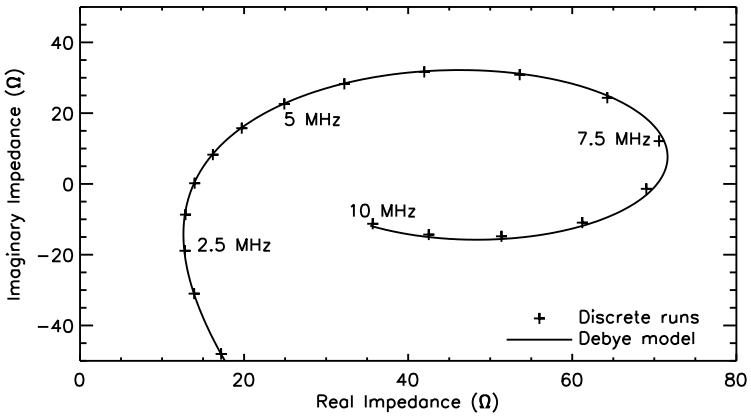

Figure 4.14: A comparison of input impedance predictions for Debye and fixed material models.

illustrated in Appendix B. The model consists of 120×120 cells, each 0.4 m square. It is run for 32768 steps of 3.65 ns. The electric field is monitored 40 m away from the antenna immediately above the ground plane. Second order Higdon ABCs are used to terminate the model on the two open sides. A bipolar Guassian source pulse is used, with a bandwidth up to 10 MHz.

From the Debye model, the estimated conductivities and permittivities are extracted at approximately 0.5 MHz intervals, from 0.5 MHz to 10 MHz. The exact frequencies are a product of the time step size and the number of steps. Rather than fix the time step size,

Table 4.2: Parameters used in small cell and large cell models.

	Small cell model	Large cell model (subcell extension)
Cell size	0.025 m	0.25 m
Modelling space	500 × 500	60 × 60
Steps	32768	8192
Time step	0.06 ns	0.6 ns
Frequency resolution	505 kHz	202 kHz
Observation point to $r_{\max}$ boundary	20 cells	12 cells
Machine	Pentium III, 750 MHz	Pentium, 166 MHz
Run time	11639 s	222 s

the recommended time step for stability has been used and the frequencies chosen for plotting have been calculated accordingly.

A model is then run for each fixed set of electrical properties and the response at the chosen frequency is extracted. The model runs with a fixed material are done using the same time step and number of steps as the full Debye model, so that the response is available at exactly the same frequency as the response in the full Debye model.

The results are presented in Figures 4.13 and 4.14. Correspondence in the field at 40 m from the antenna between the Debye model and the discrete models becomes poorer at higher frequencies. This is caused by imperfect ABCs, because the correspondence is better closer to the antenna. In general the comparison between the single Debye model run and the twenty discrete runs is good, confirming that the implementation of Debye materials within the FDTD model is working.

4.9.4 Verifying the thin-layer subcell extension

The thin-layer subcell extension is verified by comparing it to a model consisting of finer cells. The antenna that is modelled is a 3.25 m long monopole, operating from 1–30 MHz. Fields are observed 12 m away from the antenna immediately above the ground

plane. The antenna is 2 mm in diameter and is surrounded by 24 mm of insulation.

Parameters for the two models are listed in Table 4.2. The cells in the small cell model are 1/10th of the size of those in the subcell model. In order to reduce the computation time, the run time of the small cell model is not $10\times$ that of the large cell model. Acceptable results were achieved within 32768 steps. Both models use second order Higdon ABCs on the two open sides of the model.

The execution times listed in Table 4.2 should be regarded as guidelines, as both machines are time-shared, although the models ran with highest priority in both cases. The small cell model is expected to take 278 times as long to run as the large cell model.

The results are illustrated in Figure 4.15 for the antenna embedded in peridotite. Correspondence between the two models is fair. The small cell model results are not as smooth as those for the large cell, because the small model was not run for the correctly scaled number of time steps. As a result, the frequency resolution is not as good in the small cell model.

Inaccuracies in the comparison come about because the fine cell model is not equivalent to the large cell model with the subcell extension. In the large cell model, $\boldsymbol{E}_r$ and $\boldsymbol{H}_\phi$ are assumed to vary as $1/r$ from the antenna out to 0.25 m. In the fine cell model they only vary as $1/r$ out to 0.025 m. The insulation thickness is comparable between the two models, but fields outside the insulation are slightly different, and that difference is apparent in the comparison.

If the same set of comparisons are generated for the antenna embedded in granite the correspondence between the fine cell model and the large cell model with the subcell extension is closer Figure 4.16. The lower loss tangent of the granite reduces the extent of the differences caused by the implementation of the quasi-static approximation.

Even in the peridotite, the difference in field strength between the two models is 6 dB at worst. Considering the method of comparison, the thin-wire, thin-layer subcell method is working correctly.

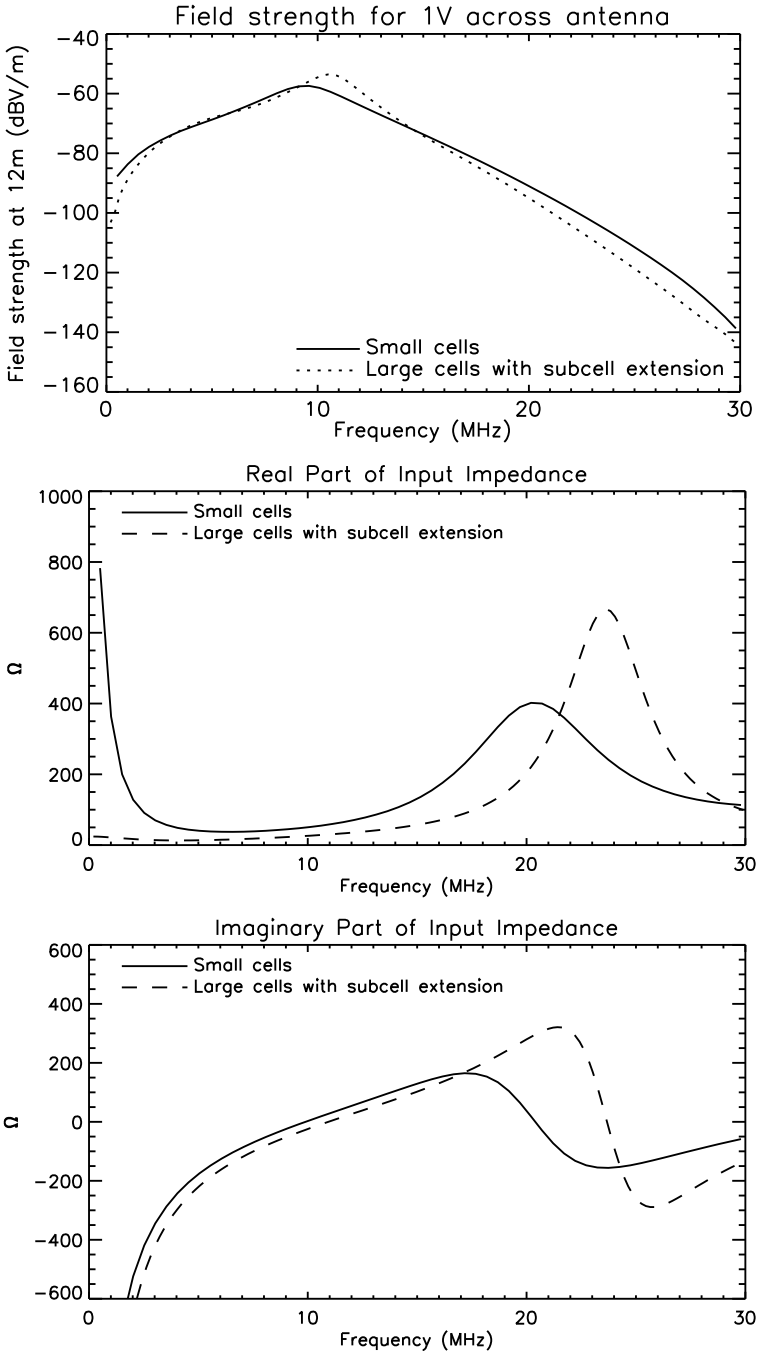

Figure 4.15: Comparison of the thin subcell extension and a model consisting of small cells embedded in peridotite.

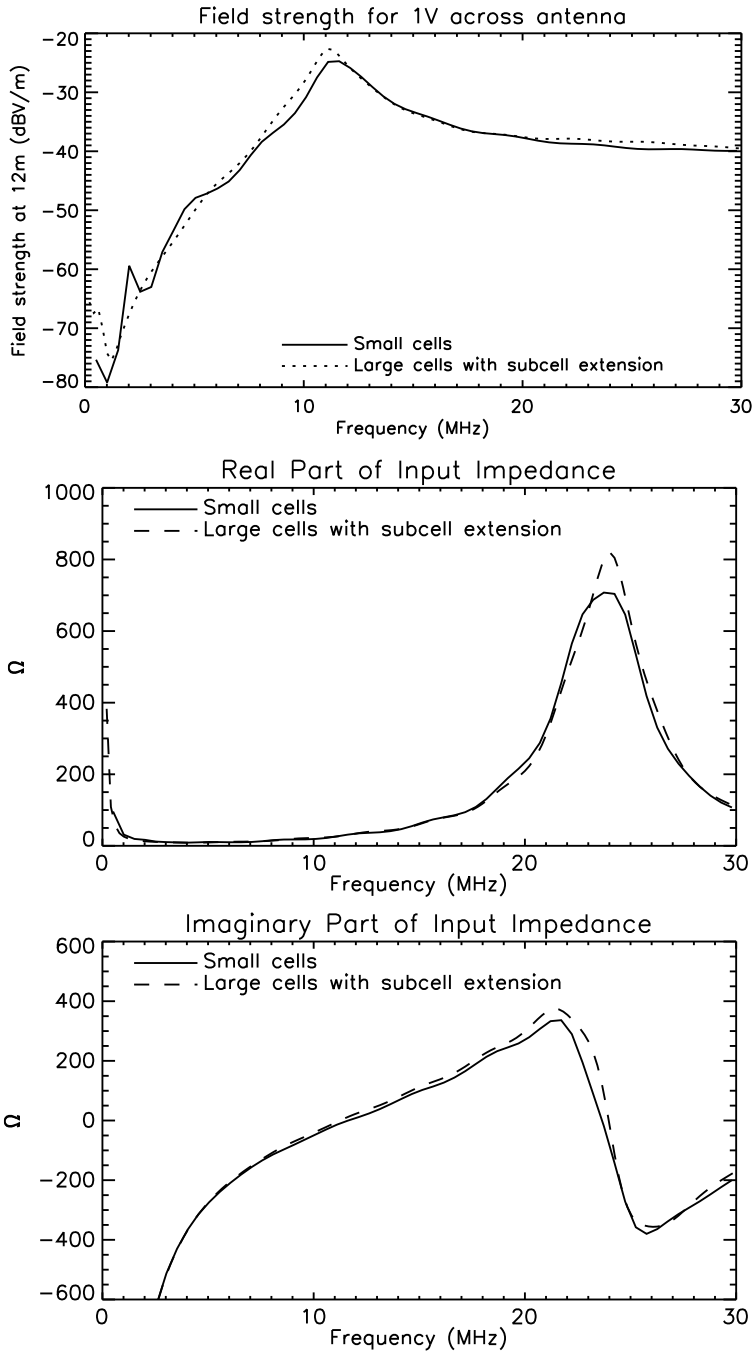

Figure 4.16: The same comparison as that shown in Figure 4.15 for an antenna embedded in granite.

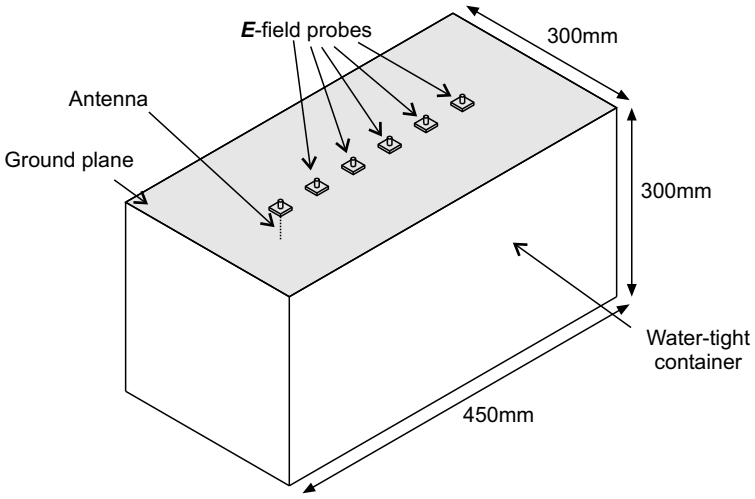

Figure 4.17: The configuration of the physical model.

4.9.5 Experimental verification

Modelling philosophy

The physical model described here is meant to confirm that the FDTD model works correctly. In particular, it is meant to verify the thin-wire, thin-layer subcell extension. However, it is not a scale model of a real RT situation. It includes the elements that are to be modelled, but no attempt is made to scale the elements in every respect, compared to an HF antenna in rock.

Physical model description

The physical model is illustrated in Figure 4.17. It consists of a thin wire monopole that is mounted pointing vertically downward from a ground plane, into a tank of water. The tank is approximately 300 mm wide, 450 mm long and 300 mm deep. The ground plane covers the top of the tank. The monopole is 50 mm long and 0.5 mm in diameter. Two monopoles have been constructed: one is a bare wire, the other is a wire coated with 0.5 mm of PTFE insulation. Only one antenna is used in a particular model, then comparisons are drawn between the two antennas.

Five electric field sensors are mounted in a line running away from the monopole at 50 mm intervals. The electric field sensors are

SMA connectors, with their central pins and surrounding insulation cut to protrude 1.6 mm below the ground plane. The ground plane itself is a brass plate, 2 mm thick.

Experiments were originally undertaken using a double sided printed circuit board (PCB) instead of a brass plate for the ground plane. Although PCB can make a good ground plane, in this case propagation between the two layers of the board severely compromised the measurements. Even the small amount of propagation that can occur between the two layers of the PCB is large by comparison to the small signal propagating through the water.

The tank is filled with salt water. From King and Smith (1981), the electrical properties of saline solutions are easy to approximate for low values of salinity. The complex permittivity is given by a Debye equation with $\varepsilon_{rs} = 80.4$, $\varepsilon_{r\infty} = 5.5$ and a relaxation time of $\tau = 9.5 \times 10^{-12}$, at 20° C. The effective permittivity is then estimated as

$$\sigma_e = \sigma_0 + \omega\varepsilon'' \tag{4.92}$$

where σ_0 is the DC conductivity.

The aim of the experiment is to determine the difference in field strength at each field measurement point for the case of the bare antenna compared to the insulated antenna. Because the system is identical for both measurements, it is not necessary to have absolute calibration of the field measurement system. The E-field probes have very low gain so the experiment cannot be run with high values of conductivity. In practice, two experiments were undertaken, with conductivities of 1 S/m and 2 S/m.

Ideally, the experiment would be conducted in an environment where reflections from the walls of the vessel could be eliminated. In practice, the reflections were substantially attenuated because of the high conductivity of the water. The numerical model was also run with and without absorbing boundaries and there was no notable difference between the two sets of results.

Measurements on the physical model were undertaken with an HP8753A network analyser. S_{21} measurements were taken and corrected for input reflection coefficient, giving a relative field strength

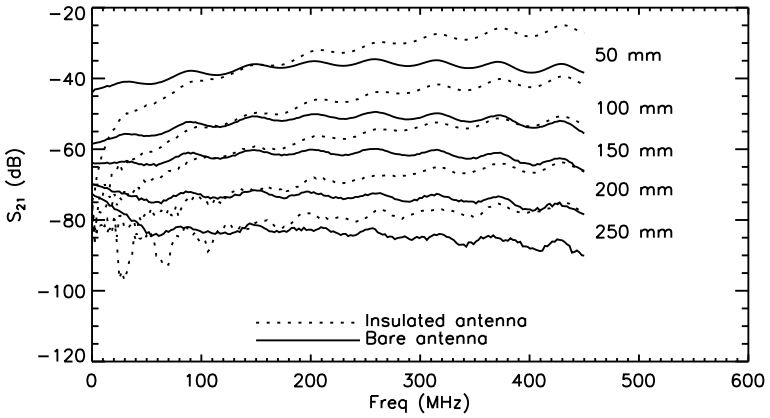

Figure 4.18: Field fall off observed at five observation points in a 1 S/m salt water medium.

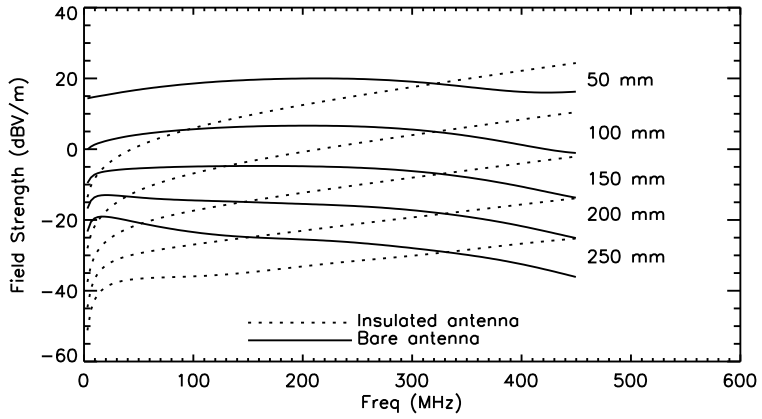

Figure 4.19: Field fall off computed at five observation points in a 1 S/m salt water medium.

at each measurement point. The results for water with a conductivity of 1S/m, at each of the measurement points are shown in Figure 4.18. The data is presented as a set of ten graphs, two for each field observation point. The first measurement is for the bare monopole and the second is for the insulated monopole.

When the numerical data is presented in a similar form to the measured data, in Figure 4.19, the correspondence is visible. The numerical model does not simulate field observation antennas; it measures the field strength directly. The field observation antennas

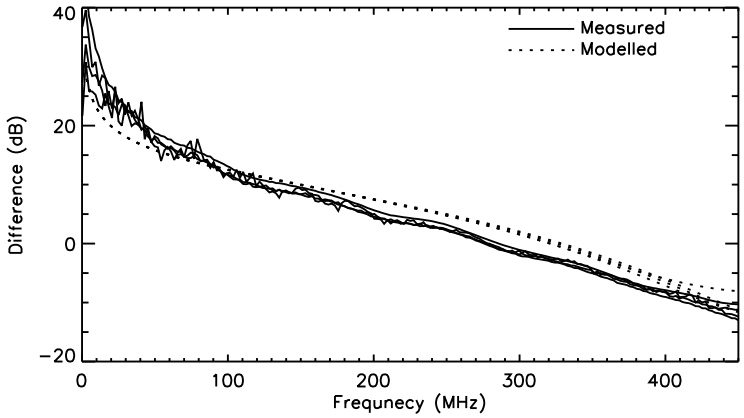

Figure 4.20: Comparison between the differences measured and those computed at each of the five observation points in a 1 S/m salt water medium.

in the physical model are relatively insensitive, so the absolute field strengths in the two graphs are different.

At each observation point, the difference between the fields radiated by the bare antenna and those radiated by the insulated antenna can be measured. If those measurements are plotted on a single graph, all the difference plots have a very similar shape. The result is to be expected, as antenna effects are unlikely to vary markedly as a function of distance. In Figure 4.20 there is good correspondence between the group of differences measured from the physical model and the group of differences predicted by the numerical model. Only results from the first four field measurement points are plotted, because the signal from the fifth was below the noise floor.

If the water salinity is increased to 2 S/m, the results for measured and modelled differences are as shown in Figure 4.21. Only the fields from the first three field measurement points are plotted, as the high water conductivity in the experimental model results in very little energy reaching the more distant field probes. Signal strength at the fourth and fifth probes is below the noise floor and even the third probe shows some noise. Again, correspondence between measured and computed fields is good.

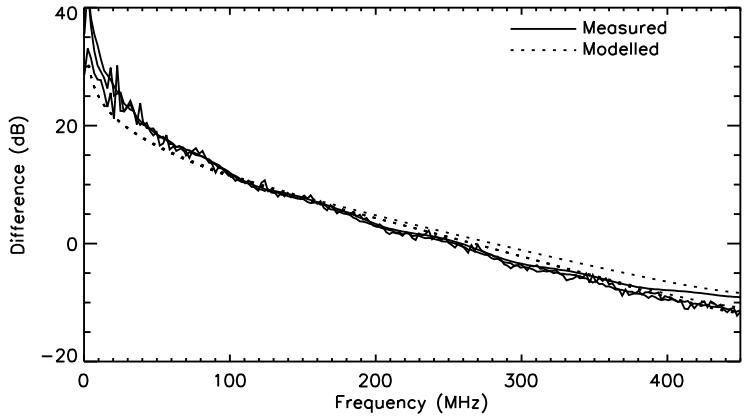

Figure 4.21: Comparison between the differences measured and those computed at each of the five observation points in a 2 S/m salt water medium.

4.10 CONCLUSION

In this chapter, a FDTD code that is suitable for modelling RT systems has been developed and verified. The code uses BOR symmetry because an RT antenna is rotationally symmetrical. The BOR model can produce a 3D result in the time of a 2D computation, although it cannot model geometries that are not symmetrical. The shorter run time of a 2D is desired because it is hoped to use the model eventually as part of an iterative inversion process. During inversion the model will be run many times, and a short run time is essential.

The frequency dependant electrical properties of the rock are modelled by a Debye equation with multiple relaxation times. Each relaxation time corresponds to a separate component of the polarization vector and is implemented using a separate auxiliary differential equation.

The FDTD computational space is terminated using either Higdon or Liao ABCs. Boundaries with higher performance were considered, but the computational cost is not warranted because the conductive rock attenuates any unwanted reflections. The antenna is fed directly by a hard source.

RT antennas are electric dipoles that may have a thin layer of insulation. To efficiently model the fine structure of an RT antenna, the

published thin-wire and thin-layer subcell extensions have been combined in a novel thin-wire, thin-layer subcell extension. The subcell extension allows both the insulation layer and the surrounding rock to be modelled as Debye materials.

The code has been verified using a variety of numerical comparisons, and has been compared against a physical scale model. In every case, the results from the FDTD model are in good agreement with alternative numerical codes or approaches and are also in good agreement with comparison to a physical model.

5

Antenna modelling and design

In the previous chapter, the FDTD code used to model RT antennas was described in detail. In this chapter the code is used to investigate how RT antennas perform in various environments. The definitions of input impedance, gain and directivity as they apply to lossy media are reviewed. The techniques used for extracting performance figures from the FDTD model results are also discussed. The BOR FDTD model can only be used to model transmit antennas. To model receive antennas, plane waves are required, and plane waves violate BOR symmetry. Can the performance figures from the BOR model be applied to receive antennas? A comparison with a 3D FDTD model shows that they can.

The performance of bare antennas is examined in detail to illustrate the importance of electrical length. The performance of insulated antennas is then discussed to show how insulation isolates the antenna from its environment.

Insulated antennas are physically longer than bare antennas that are resonant at the same frequency, because the relative permittivity of insulation is typically between 2 and 3, whereas the permittivity of rock is usually greater than 9. Modelling shows how longer antennas affect tomographic imaging. The compromise of insulation against length and practicality is incorporated into a proposal for a new RT antenna. That proposal is used as the basis for a novel receiver probe, to replace the existing probe on the Miningtek Pluto-6 RT system.

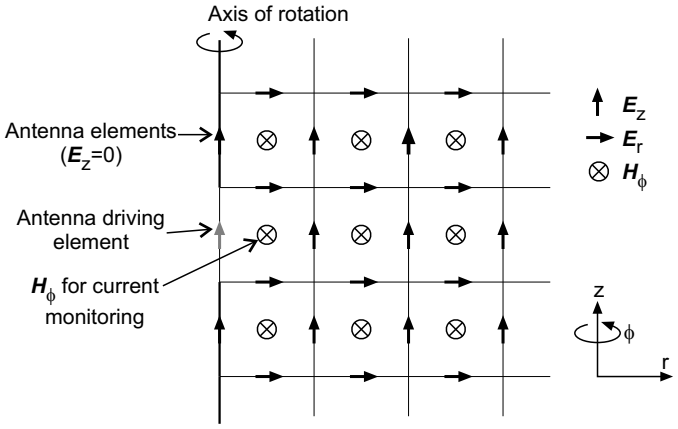

Figure 5.1: Measuring impedance in the FDTD code.

The design of the new receiver probe is a natural outcome of the modelling earlier in the chapter.

5.1 BASIC ANTENNA PARAMETERS

5.1.1 Antenna impedance

The impedance of an antenna is a very useful measurement to a system designer, because it defines the interface between the antenna and the equipment connected to it. The impedance of the antenna in the RT FDTD code is extracted by measuring the $\boldsymbol{E}$ field across the driven element of the antenna and the $\boldsymbol{H}$ field adjacent to it. The locations of the specific vectors are shown in Figure 5.1.

The voltage across the antenna is defined by the hard source, where

$$V\Big|^n = \triangle z \boldsymbol{E}_z\Big|^n_{0,j}. \tag{5.1}$$

The current flowing in the source can be determined by using Faraday's law and is

$$I\Big|^{n+1/2} = 2\pi\frac{\triangle r}{2}\boldsymbol{H}_\phi\Big|^{n+1/2}_{1/2,j}. \tag{5.2}$$

Note that the current is determined half a time step later than the voltage and $\triangle r/2$ away from the position where the voltage is determined. In a rectangular grid, the spatial offset can be compensated

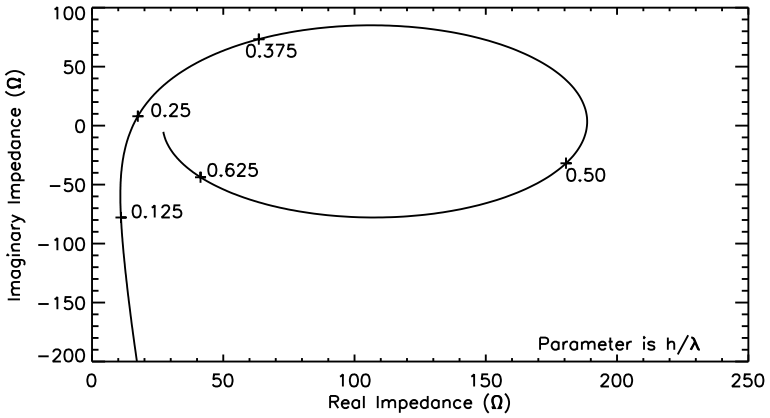

Figure 5.2: Input impedance of a bare monopole in granite.

for by averaging currents on either side of the voltage (Fang and Xeu, 1995). In a grid with BOR symmetry, averaging is not necessary because the magnetic field around the axis is assumed to be uniform and equal to the value at $\triangle r/2$.

The offset in time is corrected by averaging currents half a time step before and after the voltage value:

$$I\Big|^n = 2\pi\frac{\triangle r}{2}\frac{\boldsymbol{H}_\phi\Big|^{n-1/2}_{1/2,j} + \boldsymbol{H}_\phi\Big|^{n+1/2}_{1/2,j}}{2}. \tag{5.3}$$

In the BOR FDTD code the average is taken in the time domain, rather than in the frequency domain as suggested by Fang and Xeu (1995). Although the time offset is small, if it is not accounted for it can lead to a non-physical input impedance, with a negative real part. After correcting for the time offset, the input impedance in the time domain is

$$Z\Big|^n = \frac{V\Big|^n}{I\Big|^n}, \tag{5.4}$$

which is converted to the frequency domain by using a Fast Fourier Transform.

FDTD codes can generally model input impedance accurately, (Maloney et al., 1990). However, over the very broad band from DC to triple the operating frequency of an RT antenna, some inaccuracies can be expected. A typical antenna impedance spiral is shown in Figure 5.2, which is similar in form to those reported in King and

Smith (1981, p. 478). The antenna is a monopole, embedded in granite, which has a loss tangent of 0.06. Imaginary impedance is large and negative at low frequencies, rises to zero continues to rise to a maximum between the first resonance at approximately $h/\lambda = 0.25$ and the first anti-resonance at $h/\lambda = 0.5$. The real part of the impedance rises with frequency up to the anti-resonance then falls.

The behaviour of the real part of the impedance at very low frequencies is interesting, because it differs from that of an antenna in free space. In Figure 5.2 the real part of the antenna impedance is increasing as frequency approaches zero: $R \rightarrow R_{\mathrm{DC}}$ as $h/\lambda \rightarrow 0$, where R_{DC} is the DC value of the input impedance. This low frequency behaviour only becomes apparent as the surrounding medium becomes lossy, otherwise $R_{\mathrm{DC}} = 0$.

5.1.2 Gain

Possibly the most useful measurement of the performance of an RT antenna is its gain. Gain is normally defined as the ratio of radiation intensity in a particular direction to the uniform radiation intensity that would exist if the total power supplied to the antenna were radiated isotropically (Ramo et al., 1993):

$$G = \frac{K(\theta, \phi)}{P_{\mathrm{t}}/4\pi} \tag{5.5}$$

where K is the radiation intensity and P_{t} is the power transmitted by the antenna.

For antennas embedded in rock, radiation intensity is not a good measure of performance, because the radiation intensity decreases with distance from the antenna, as the signal is attenuated. Gain in a particular direction is defined in this thesis after Moore (1963) as the ratio of the power density at a distance R, to the power density that would exist at that distance if the total power supplied to the antenna were radiated isotropically. If no direction is specified, the gain is assumed to be in the normal, or boresight direction. Then

$$G = \frac{W(\theta, \phi, R)}{P_{\mathrm{t}} \mathrm{e}^{-2\alpha R}/4\pi R^2} \tag{5.6}$$

where W is the power density.

The power density at a distance R is the real part of the radial component of the Poynting Vector. For the BOR FDTD code, the power density in the boresight direction depends only on the $\boldsymbol{E}_z$ and $\boldsymbol{H}_\phi$ vectors. The power density is

$$W_{\text{obs}} = \Re(\boldsymbol{E}_z \boldsymbol{H}_\phi^*) \tag{5.7}$$

where $\boldsymbol{H}_\phi^*$ is the complex conjugate of the magnetic field. The gain in Equation 5.6 can now be expressed as

$$G = \frac{\Re(\boldsymbol{E}_z \boldsymbol{H}_\phi^*) 4\pi R^2}{P_{\text{t}} \text{e}^{-2\alpha R}}. \tag{5.8}$$

Gain is dimensionless and lends itself to expression in decibels.

5.1.3 Directivity

Directivity is defined as the ratio of the radiation intensity from the antenna in a given direction to the uniform radiation intensity from an isotropic radiator with the same total radiation power (Ramo et al., 1993). If a direction is not specified, the direction normal to the antenna is assumed:

$$D = \frac{K(\theta, \phi, R)}{(P/4\pi)}, \tag{5.9}$$

where P is the total power by the antenna, rather than the power fed to the antenna. The relationship between gain and directivity is

$$G = \eta D \tag{5.10}$$

where η is the efficiency of the antenna.

Again, for an antenna in rock, the definition of directivity is modified to introduce a distance from the antenna. Consider the antenna to be surrounded at a distance, R, by a sphere, S, centred on the feed point of the antenna. The total power crossing the sphere is then

$$P_{tot} = \oint_S W(R, \theta, \phi) \, \mathrm{d}S \tag{5.11}$$

and the average power density is

$$W_{ave} = \frac{1}{4\pi R^2} \oint_S W(R, \theta, \phi) \, \mathrm{d}S. \tag{5.12}$$

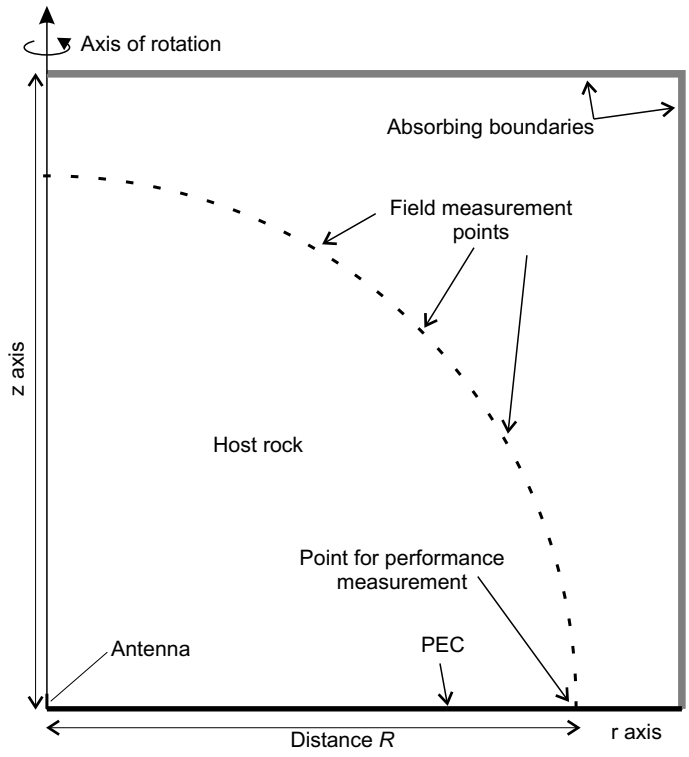

Figure 5.3: Geometry for calculating directivity in the 2D BOR model.

The directivity in the boresight direction is then

$$D(0,0) = \frac{4\pi R^2 W(R,0,0)}{\oint_S W(R,\theta,\phi)\,\mathrm{d}S}. \tag{5.13}$$

Equation 5.13 is implemented numerically by observing the field in an arc around the antenna using the geometry shown in Figure 5.3. At each observation point the $\boldsymbol{H}_\phi$, $\boldsymbol{E}_z$ and $\boldsymbol{E}_r$ fields are observed. The power density in the direction radial to the feed point of the antenna is calculated as $\boldsymbol{E} \times \boldsymbol{H}^*$. It is combined in a weighted sum over the surface of the sphere to determine the total radiated power and hence average power density. The directivity is the ratio of the power density in the boresight direction to the average power density.

Figure 5.4 shows computed numerical results for the directivity and gain of a 3.2 m monopole antenna in air. The directivity is calculated on an arc 40 m from the antenna. Directivity and gain are measured in the boresight direction. For a perfectly conducting an-

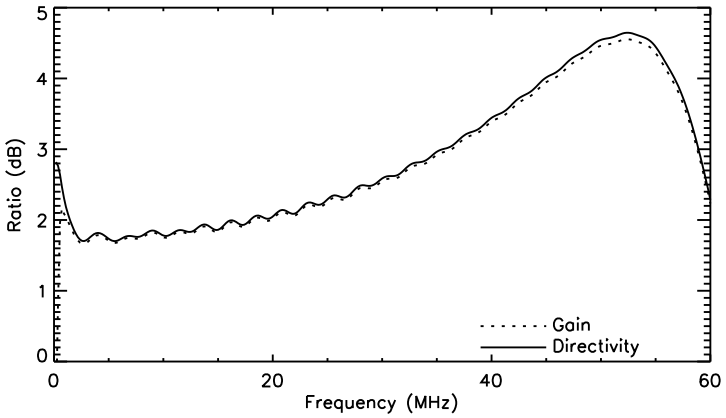

Figure 5.4: Directivity and gain of a perfectly conducting monopole antenna in air.

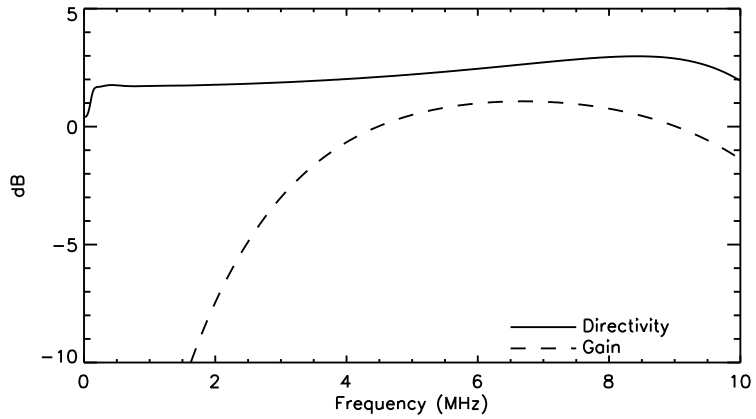

Figure 5.5: An example of the difference between directivity and gain: a wire antenna embedded in dolerite.

tenna in a lossless medium, gain and directivity should be equivalent. The correspondence in Figure 5.4 is good, confirming the calculations used to extract both parameters. However, the correspondence is not perfect, because there are computational inaccuracies, both in the FDTD model and in the techniques used to extract gain and directivity. From analytical calculations, the gain of the antenna should be 1.76 dB at low frequencies. The sharp rise in directivity and gain as $\omega \rightarrow 0$ and the ripple in the directivity and gain plots are both artifacts of the FDTD model.

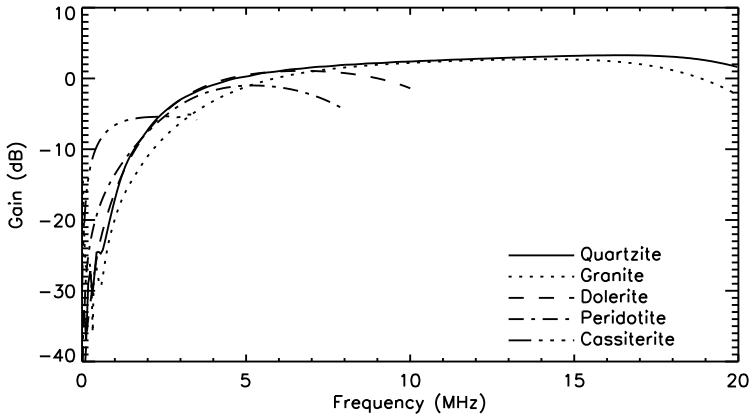

Figure 5.6: Gain of a bare antenna for a variety of rock types.

Figure 5.5 shows how a surrounding rock affects the gain. In this example, the antenna is embedded in dolerite. The antenna is still assumed to be perfectly conducting. The directivity is similar to that for the antenna in free space, but the gain is considerably reduced by losses in the surrounding rock. Directivity is calculated using an arc 40 m from the antenna. Directivity and gain are both measured in the boresight direction. The gain is expected to drop because rock in the vicinity of the antenna reduces the efficiency of the antenna.

5.2 A BARE ANTENNA IN ROCK

RT is conducted in boreholes with a minimum diameter of 48 mm, so the maximum diameter of a practical antenna is 44 mm. This figure constrains the size of the bare and the insulated antennas. The bare antenna considered here is modelled as a monopole and is 44 mm in diameter.

5.2.1 Gain

In Figure 5.6 gain is plotted for a bare wire antenna embedded in a selection of different rock types. In each case the antenna is a 3.2 m monopole. The model consists of 120×120 cells, each 0.4 m square. The runs normally take 16384 time steps, of $\triangle t = \triangle / 4c$, where c is the maximum speed in the model. The time step is half the normal

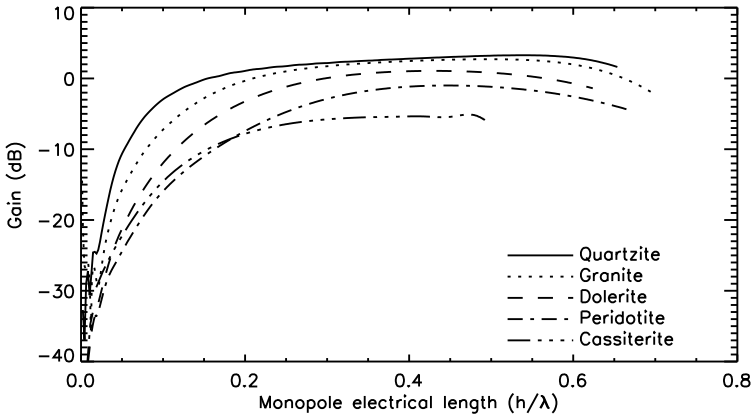

Figure 5.7: Gain of a bare antenna measured at 40 m for a variety of rock types and normalized for electrical length in the host rock.

time step to ensure stability.

The gain is measured at 40 m for the quartzite, granite, dolerite and peridotite and at 20 m for the remaining rocks. All of the rocks fill the whole modelling space. Each rock is modelled using a suitable Debye model, as detailed in Appendix B, with between 1 and 4 Debye terms. In every case, the source is a bipolar Gaussian pulse and second order Higdon ABCs are used to terminate the two open sides of the model.

All of the results follow the same general pattern: gain increases with increasing frequency, maintains a constant value, then falls gently. The maximum corresponds to the resonant length of the antenna. The results in Figure 5.6 become more uniform when they are normalized to the electrical length of the antenna in the background rock.

Normalized results are plotted in Figure 5.7 and show that all the antennas have gains within a few decibels of one another when at $\lambda/4$. Generally, the higher the loss tangent, the poorer the gain.

5.2.2 Directivity

The directivity in absolute figures, plotted in Figure 5.8, is less influenced by rock type, indicating that rock type affects the shape of the antenna pattern less than it does the efficiency of the antenna.

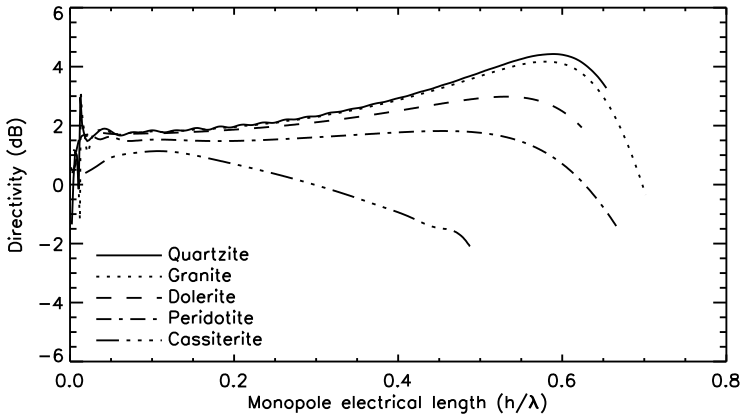

Figure 5.8: Directivity of a bare antenna in a variety of rock types.

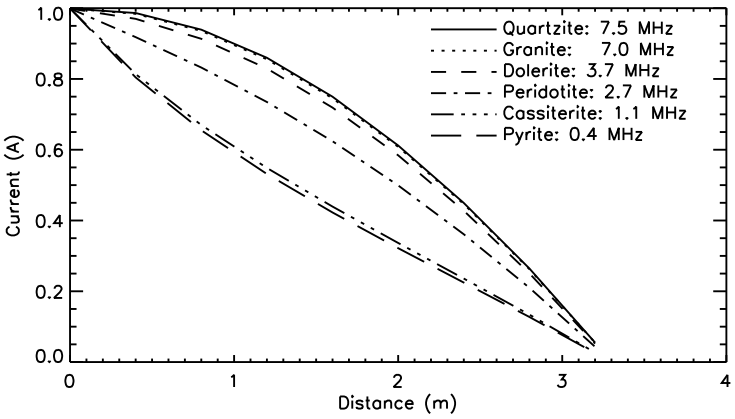

Figure 5.9: Normalized current distribution on the bare antenna.

5.2.3 Antenna currents

In Figure 5.9, the current distribution on the bare antenna is plotted for the antenna embedded in six different rock types. In each rock, the current distribution is plotted for the frequency at which the monopole is a quarter of a wavelength long in the surrounding medium. The current is normalized to 1 A at the feed point.

The current distribution explains the changes in directivity as a function of rock type: as the loss tangent of the rock increases, the current distribution at resonance becomes less sinusoidal, which affects the pattern and the directivity of the antenna in the boresight

direction.

5.2.4 Antenna impedance

The surrounding rock has a marked influence on the input impedance of a bare antenna. Plots of the antenna input impedance in six rocks are shown in Figure 5.10. The impedance is plotted against the electrical length of the antenna in the host rock. Both the real and imaginary part of the input impedance decrease as the loss tangent of the surrounding rock increases. In the case of the highly conductive pyrite, both the real and imaginary parts are no more than one or two ohms.

The rise in the real impedance of the antenna at low frequencies is unusual, compared to a typical antenna in air. Unlike the earlier plot of directivity and gain of an antenna in air on Page 105, the rise illustrated in Figure 5.10 is not a modelling artifact. It is confirmed by both King and Smith (1981) and by Burke et al. (1983).

5.2.5 Pattern

The antenna pattern for a bare antenna in granite is shown in Figure 5.11. The pattern is typical of a dipole antenna: at frequencies below resonance there is a single main lobe in the boresight direction. As the frequency passes resonance (about 11 MHz for a 3.2 m monopole in granite), a lobe starts to develop at a large angle away from boresight. With increasing frequency the lobe develops further and starts to move towards the boresight direction. Although it is not shown on the plot, when the monopole antenna length is $3/4\lambda$, there is a single lobe at about 45°to boresight and a null in the boresight direction.

The pattern of an antenna embedded in a lossy medium often depends on the geometry of material structures around the antenna and is examined in more detail in the next chapter.

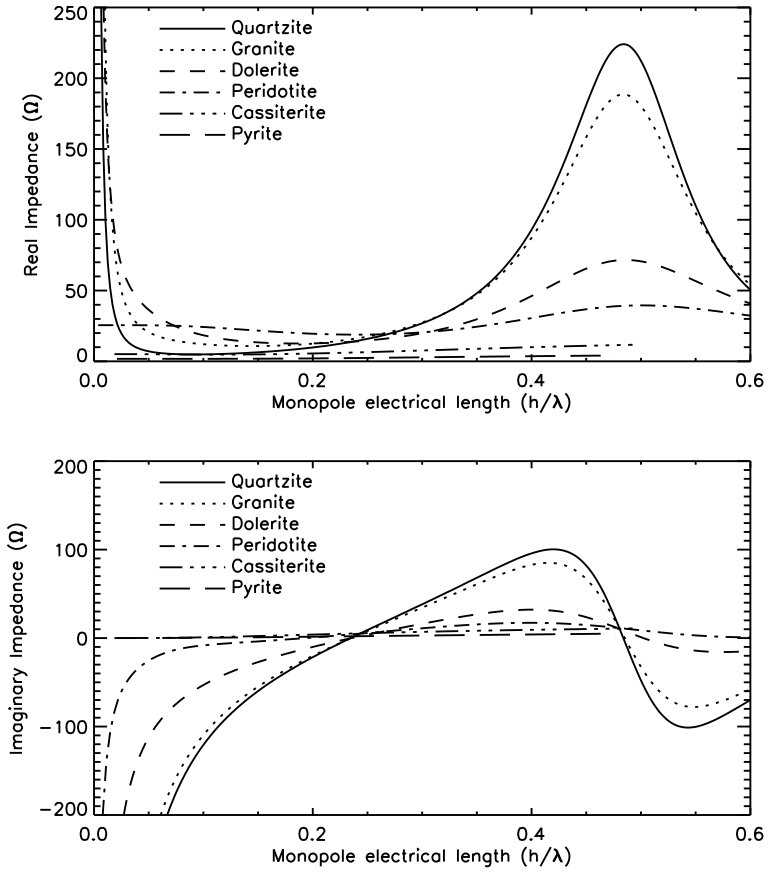

Figure 5.10: Input impedance of a bare monopole in six different rock types.

5.2.6 Discussion

The electrical characteristics of a bare antenna change considerably from rock to rock. For example, a 6.4 m dipole, operating at resonance at 0.4 MHz in pyrite will have a gain of approximately -10 dB. Its gain will drop to less than -30 dB in quartzite at the same frequency. At the same time, the impedance will change from small and almost purely resistive in the pyrite to large and almost purely capacitive in the quartzite, leading to problems matching both transmitter and receiver.

Bare antennas have to be considered as broadband: they cannot be optimized for a specific frequency across a wide range of rock

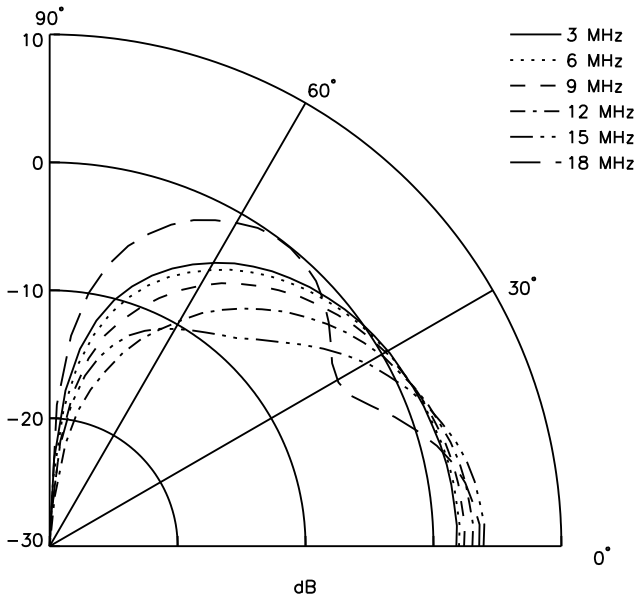

Figure 5.11: The directivity of a bare monopole antenna embedded in granite as a function of frequency.

types. If a bare antenna is considered as a poor, but broadband antenna, it can be used at frequencies that are different from its design frequency. In an RT survey, a frequency will be chosen based on estimates of rock properties and geology. The choice of frequency cannot be confirmed until the survey has begun. If penetration cannot be achieved at the chosen frequency, the operator will attempt to use a lower frequency. If the same antennas are used, gain is likely to fall. If there is a mechanism to correct for antenna parameters in different rock types, the survey can continue and the operator can correct the measured data afterwards. Such a correction mechanism is essential to any application of bare antennas in RT and can be provided by the FDTD model presented in this thesis. An example of such a correction is presented in the next chapter.

5.3 AN INSULATED ANTENNA IN ROCK

As discussed in the introduction to the previous section, RT antennas are constrained to fit into a borehole with a diameter of 48 mm, so

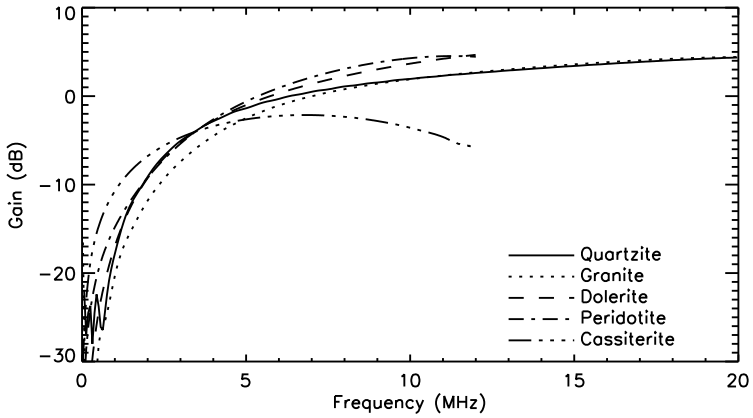

Figure 5.12: Gain of an insulated antenna for a variety of rock types.

must be 44 mm in diameter or less. In this section, an insulated antenna is discussed. The insulated antenna consists of a 4 mm diameter conductor surrounded by a layer of insulation 20 mm thick. The insulated antenna has the greatest ratio of conductor radius to insulation thickness that is practical within a 44 mm diameter. The insulation assumed in the models is lossless with a permittivity of 2.1, the same as that of PTFE.

The bare antenna of the previous section and the insulated antenna of this section can be considered as the two ends of a continuum. The electrical properties of antennas with different thicknesses of insulation will lie somewhere between the limits of the two example antennas.

5.3.1 Gain

A 3.2 m monopole antenna, 4 mm thick, surrounded by a 20 mm thickness of PVC insulation is modelled using the FDTD code. The model has 120×120 cells, each 0.4 m square. The runs normally take 16384 time steps, of $\triangle t = \triangle / 4c$, where c is the highest velocity of propagation in the model.

The gain is measured at 40 m for the quartzite, granite, dolerite and peridotite and at 20 m for the remaining rocks. All of the rocks fill the whole modelling space. Each rock is modelled using a suit-

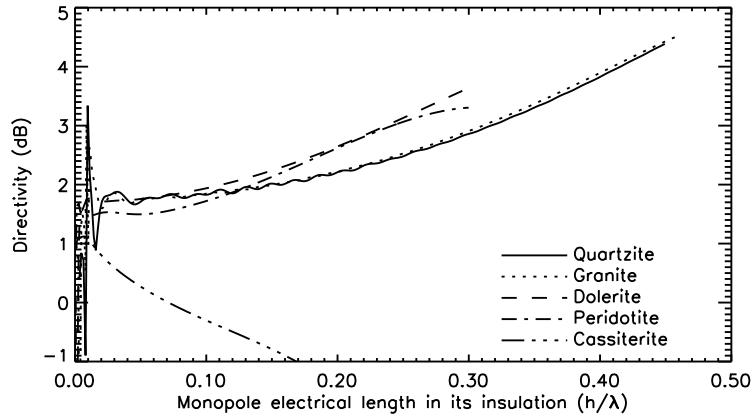

Figure 5.13: Directivity of an insulated antenna measured at 40 m for a variety of rock types.

able Debye model, as detailed in Appendix B, with between 1 and 4 Debye terms. In every case, the source is a bipolar Gaussian pulse and second order Higdon ABCs are used to terminate the two open sides of the model.

The results are presented in Figure 5.12 as a function of frequency. Note that compared to the bare antenna, the insulated antenna has roughly the same electrical length in all of the five rock types plotted. The overall gain is slightly higher than that of the bare antenna. All of the gains apart from that of cassiterite follow the same form. Cassiterite is discussed in more detail in the next section.

5.3.2 Directivity

The directivity of an insulated antenna as a function of rock type shown in Figure 5.13 is consistent as rock type changes, except for the directivity of the cassiterite. The directivity of the cassiterite is not comparable to the directivity of the other rocks because of the conceptual difficulty in defining the directivity of an antenna in lossy media. The results calculated here for cassiterite are a perfect example of the breakdown of the classic concepts of directivity and gain for antennas in conductive materials (Moore, 1963).

Directivity was defined earlier as the ratio of power density in one direction to the average power density crossing a sphere of ra-

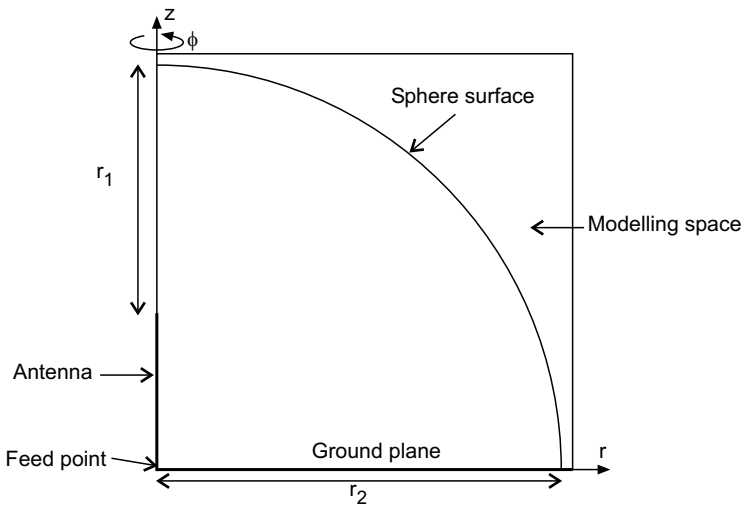

Figure 5.14: Calculating directivity in high loss rocks.

dius R from the antenna. A difficulty arises in rocks with a high loss tangent: the sphere cannot be made large relative to the length of the antenna because the power density will fall to below the noise level at the surface of the sphere. If the sphere is made smaller, then the minimum distance between the antenna and the sphere in the boresight direction is substantially larger than the minimum distance between the antenna and the sphere along the antenna axis.

The situation is illustrated with some exaggeration in Figure 5.14. Because the conductive rock attenuates signals so rapidly, the shorter path, r_1, leads to higher power density at the surface of the sphere than the longer path, r_2. The distortion is worse in insulated antennas than in bare antennas because the antenna current in insulated antennas is higher near the end of the antenna relative to the feed point than in a bare antenna.

5.3.3 Antenna currents

In Figure 5.15, the current distribution on the insulated antenna is plotted, with the antenna embedded in five different rock types. In each rock, the result is shown at the frequency that corresponds to a quarter wave monopole in the insulation. The current is normalized to 1 A at the feed point.

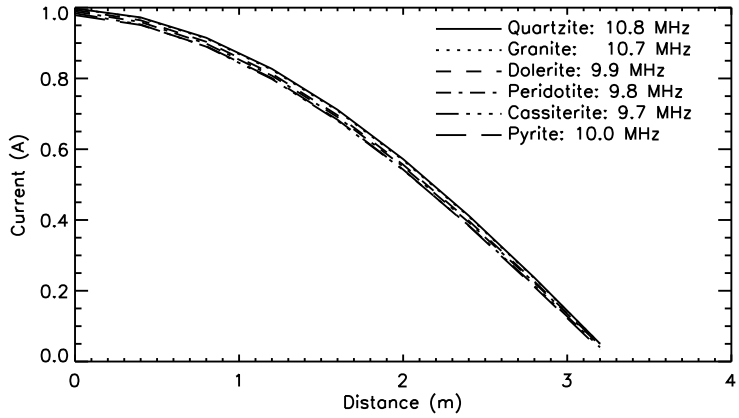

Figure 5.15: Normalized current distribution on an insulated antenna.

The resonant frequency of the antenna is determined using the King and Smith approximation for the wave number in the insulation of an insulated antenna, Equation 3.5 in Chapter 3.

The current on an insulated antenna is different to that of the bare antenna in two respects, both directly a consequence of the insulation. Firstly, there is less difference between the current distributions in the most and least conductive rocks. Secondly, the frequency at which the antenna is resonant shows far less variation as a function of rock type.

If an insulated antenna is viewed as a coaxial transmission line, then the results are as expected: the insulation becomes the medium for carrying the fields, so the current does not change as the external medium changes. The electrical length of the antenna does not change as the external medium changes because the velocity of propagation along the antenna is very close to that of the insulation medium.

5.3.4 Antenna impedance

While the only form of the impedance function is similar for a bare wire antenna in various media, for insulated antennas the actual impedance is very similar, as shown in Figure 5.16. Once again, the impedance of the coaxial line made up of the antenna conductor, the

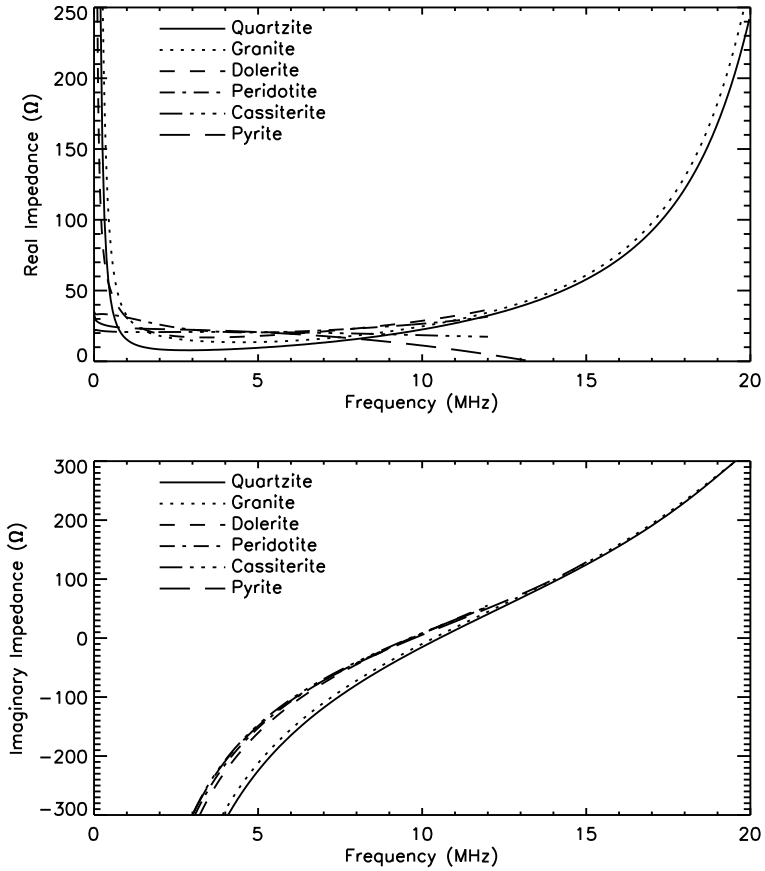

Figure 5.16: Input impedance of an insulated antenna in six different rock types.

insulation and the surrounding conducting rock dominates the antenna impedance, hence the impedance for all five rocks shown here is approximately the same at the design frequency of 10 MHz.

5.3.5 Antenna pattern

The pattern for an insulated antenna in granite is shown in Figure 5.17 and reflects the same general characteristics as the bare dipole. However, the 6 m antenna is now electrically shorter, so the main lobe has not broken into two by the time the highest frequency on the plot is reached.

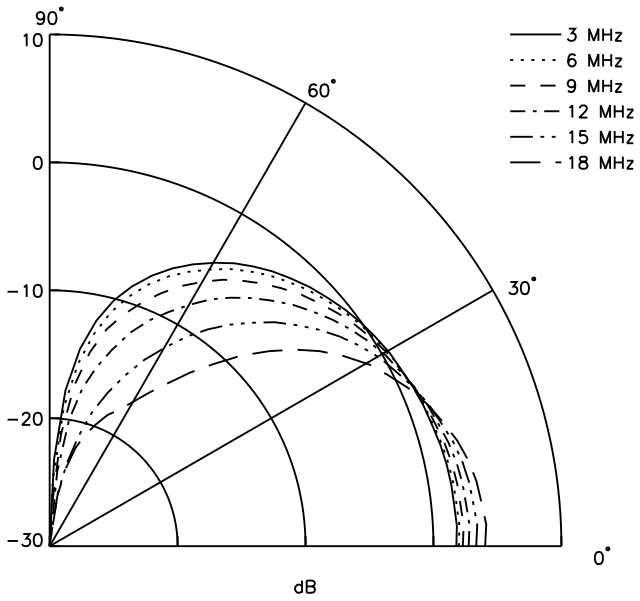

Figure 5.17: How the directivity of an insulated monopole antenna embedded in granite changes as a function of frequency and angle.

5.3.6 Discussion

A 4 mm diameter antenna insulated by 20 mm of PVC is effectively isolated from the surrounding rock. It has almost the same gain, antenna current and antenna impedance regardless of the surrounding rock. However it must be considered as a narrowband antenna. Whereas the operational frequency of a bare antenna can be changed to achieve performance advantages in particular rocks, using an insulated antenna at any frequency other than its design frequency bestows no such advantage.

The insulated antenna is theoretically ideal for RT because of its reasonable gain and excellent isolation from the surrounding rock. In practice, the operator may not be prepared to compromise on the inability to use the antenna at any frequency for which it is not designed as well as its long physical length.

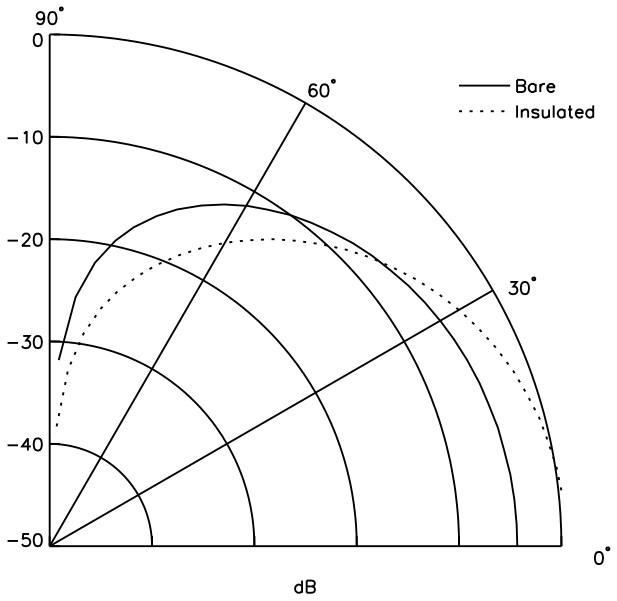

Figure 5.18: The effect of physical length on the pattern of two antennas resonant at 3.9 MHz in dolerite.

5.4.1 Noise

The real part of the antenna impedance increases at very low frequencies in both the insulated and bare antennas, in contrast to an antenna in air which is purely capacitive at low frequencies. The minimum resistance is then typically achieved when the monopole antenna is between 0.10 and 0.25 of a wavelength in length. As the frequency increases above this, the resistance also increases. Since noise is related to the resistance of the antenna, the lowest system noise can be achieved in the range already mentioned.

5.4.2 Physical length

Figure 5.18 is a plot of the directivity for two antennas, both operating in dolerite at 3.9 MHz. The bare antenna is a 6.4 m dipole, which is resonant at 3.9 MHz. The insulated antenna has a 4 mm diameter conductor surrounded by 20 mm of insulation. Because the velocity of propagation in the insulation is so much higher than in the surrounding rock, the insulated antenna must be much longer to

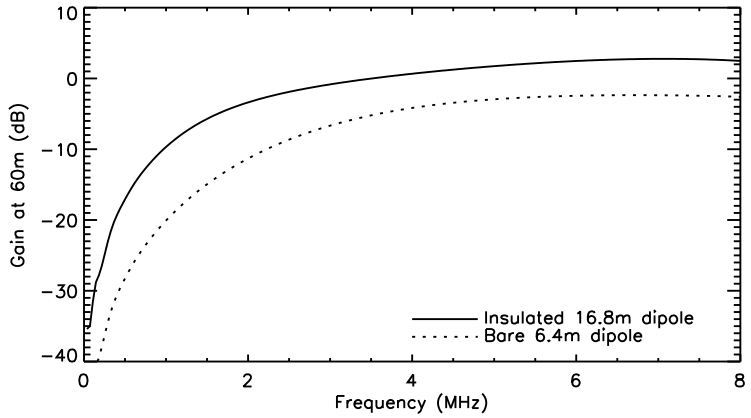

Figure 5.19: The effect of physical length on the gain of two antennas resonant at 3.9 MHz in dolerite.

be resonant at the same frequency. The resultant antenna is 16.8 m long. Both antennas are electrically a quarter of a wavelength long and both are operating in the same rock, yet the physically longer antenna has a more directive pattern.

The physically longer insulated antenna also has higher gain, illustrated in Figure 5.19. The higher gain and directivity are expected, because the physically longer antenna has a larger aperture and the low loss insulation surrounding the antenna isolates it from the surrounding rock.

5.5 TOMOGRAPHIC RESOLUTION

Insulated antennas are physically longer than bare antennas operating at the same wavelength in the rock. Does this extra length affect imaging resolution? Van Schoor et al. (1997) report that the resolution of the RT imaging process is between a quarter and half of a wavelength, but the experiments leading to this conclusion used a 2D modelling code (Howard and Kretzschmar, 1986) and did not include antenna effects. Here, I use the FDTD code to create two full tomographic models. In one, the transmit antenna is bare, in the other it is insulated.

The two models consist of 290×170 cells, each 0.4 m square. The background rock is dolerite and the target is a $20\,\text{m} \times 20\,\text{m}$ area

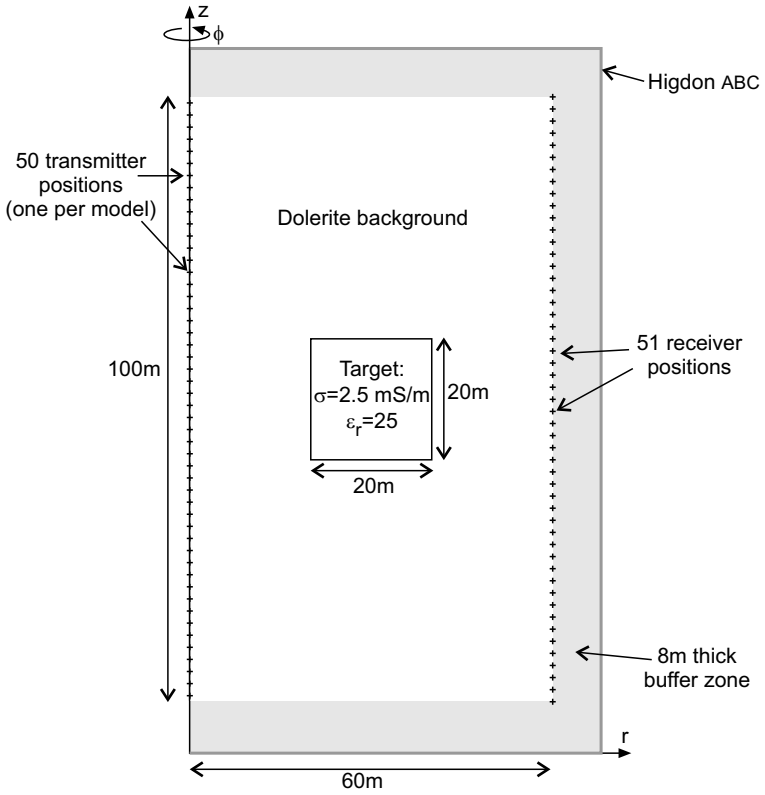

Figure 5.20: The geometry for creating tomographic forward models.

with fixed electrical properties of $\sigma = 2.5$ mS/m and $\varepsilon_r = 25$. The geometry is illustrated in Figure 5.20. Each antenna model is run 50 times, once for the transmit antenna at each source position. For each run, the $\boldsymbol{E}_z$ at each of the 51 receiver positions is extracted, at a frequency of 3.9 MHz. The field is simply measured: there is no attempt to simulate a receive antenna, because the two models will be directly compared.

In the first model, the antenna is 22 mm diameter bare wire, 6.4 m long. It resonates at 3.9 MHz in the dolerite. In the second model, an insulated antenna is used, with a conductor diameter of 4 mm, surrounded by 20 mm of insulation. In order to resonate the insulated antenna at the same frequency, it is 16.8 m long.

After the fifty runs of each model are completed, all the received data at 3.9 MHz is converted into a form suitable for tomographic inversion. The data is inverted using the same Maximum Entropy

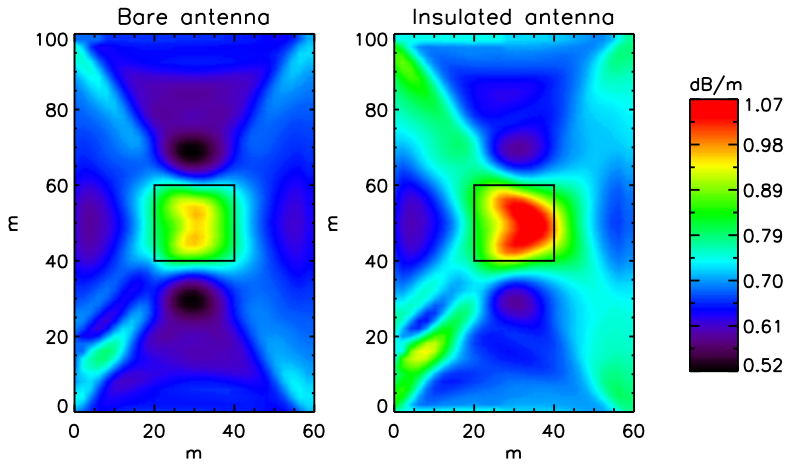

Figure 5.21: RT images of two synthetic data sets created for a $\sigma = 2.5\,\text{mS/m}$, $\varepsilon_r = 25$ target in a dolerite background. The image on the left is created using a bare antenna. The image on the right is created using an insulated antenna.

code and inversion parameters used by Van Schoor et al. (1997). The images produced for each model are compared in Figure 5.21. The data is corrected for the different gain of the two antennas.

The insulated antenna has slightly degraded resolution, particularly in the horizontal direction, because of the longer antenna length. There is also a distinct shift of the image to the right for the insulated antenna, caused by the geometry of the physically longer antenna and the point receivers. Comparison of the two images highlights one disadvantage of using a longer antenna for RT data collection. The slight loss in resolution has to be balanced against the increased gain and isolation from the surrounding rock. The images were produced modelling only the transmit antenna. If the receive antenna was also modelled, a more emphatic result would be expected.

5.6 EFFECTIVE APERTURE AND GAIN

The 2D BOR RT model can only model an antenna in transmitting mode, because the symmetry of the system limits it to radially symmetrical fields. To model a receiving antenna, a 3D model is required to implement a plane wave impinging on the receiving antenna. In

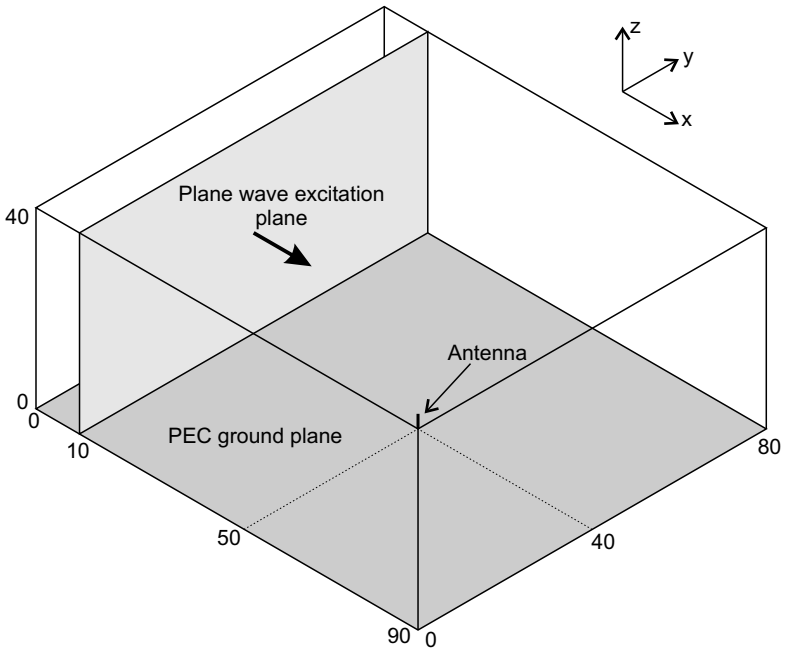

Figure 5.22: Geometry used in reciprocity experiments. Dimensions are given in cells.

this section I show that reciprocity allows measurements made on the 2D transmission model to be used to predict performance of the antenna as a receive antenna. A basic 3D FDTD code is used to produce the results shown here. It includes Debye media and a thin-wire subcell extension, but does not include a thin-layer subcell extension.

The geometry of the 3D model is illustrated in Figure 5.22. The modelling space has $90\times80\times40$ cells, each 0.4 m cubed. The antenna is a monopole over the ground plane and is 8 cells long including the driving element. All boundaries apart from the PEC ground plane are calculated using second order Higdon ABCs. The system can be used to model receiving antennas by including plane wave excitation, as shown in the figure. Alternatively, the antenna can function as a transmitter, driven by a hard source at the element directly above the ground plane. It is then possible to compare the same antenna functioning either as a transmit or receive antenna.

The antenna input impedance can be determined from the model of the antenna as a transmitter. Transmitter characteristics such as gain and directivity can also be measured, in the same way as they are

measured using the 2D BOR model. In receive mode the antenna is modelled as being short circuited to ground and the current in the feed element is determined by measuring the radial magnetic field around the wire. Physically, a transmit antenna driven by a hard voltage source becomes short circuited when the transmit pulse has ended. The short circuited receive antenna is a good physical analogue of the transmit antenna and also performs well numerically.

The effective length is used here as the indicator of antenna performance. The effective length is defined as

$$V_{oc} = \boldsymbol{E} L_e \tag{5.14}$$

where L_e is the effective length and V_{oc} is the open circuit voltage across the terminals of the antenna when the antenna is illuminated by a uniform field of $\boldsymbol{E}$.

The open circuit voltage is related to the short circuit current by the antenna impedance. The effective length for the receiving model is

$$L_{e,Rx} = \left| \frac{I_{sc} Z}{\boldsymbol{E}_i} \right| \tag{5.15}$$

where $\boldsymbol{E}_i$ is the incident field in the absence of the antenna. $\boldsymbol{E}_i$ is measured by running a model without an antenna present.

Deriving the effective length from the transmitting antenna is somewhat more involved. The effective aperture of an antenna is related to the gain by

$$A_e = G \frac{\lambda^2}{4\pi}. \tag{5.16}$$

Equation 5.16 is only valid when the antenna is feeding a conjugate matched load. If a 1 V/m incident field is assumed the power density of the incident field is

$$W_i = \frac{\boldsymbol{E}_i^2}{\zeta} = \frac{1}{\zeta}, \tag{5.17}$$

where η is the impedance of the background material in the model. The power received by a conjugate matched load is then given by

$$P_r = A_e W_i \tag{5.18}$$

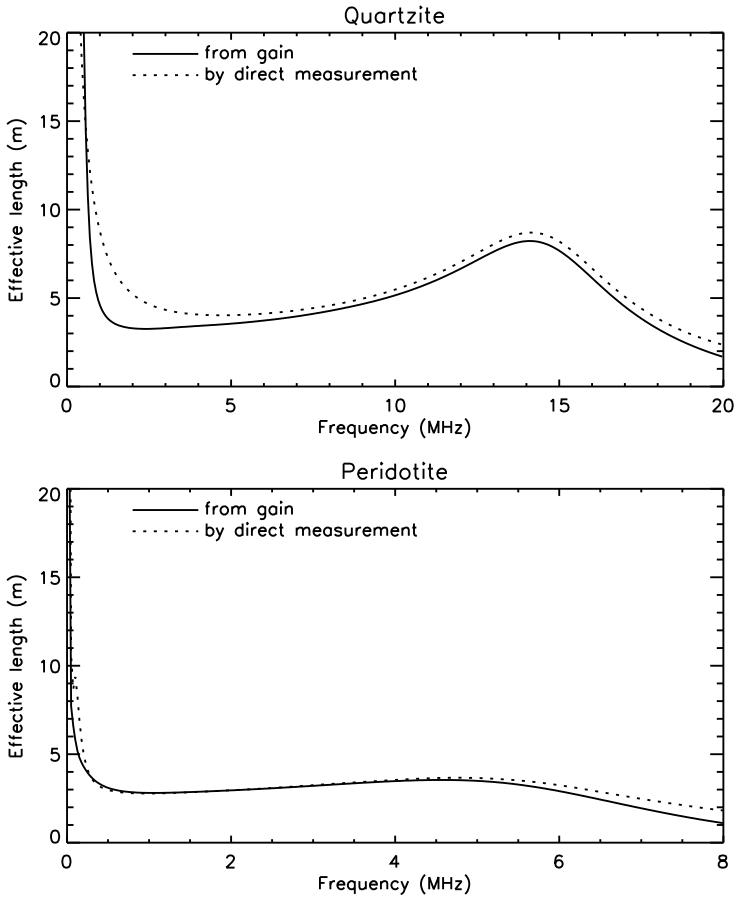

Figure 5.23: The effective length of a bare antenna measured directly from a 3D receive antenna model compared to that calculated from the gain measured in a 3D transmit antenna model.

and the open circuit voltage for that received power is

$$V_{oc} = \sqrt{P_r \Re(Z)}. \tag{5.19}$$

The effective length is equal to the open circuit voltage, because the incident field strength is 1 V/m.

The various elements of the effective length calculation can be combined to give

$$L_{e,Tx} = \sqrt{\frac{1}{\zeta} G \frac{\lambda^2}{4\pi} \Re(Z)}. \tag{5.20}$$

Results for antennas embedded in two rock types are presented in Figure 5.23. Correspondence between the two methods of determ-

ining effective length is good, with only slight errors at low and high frequencies. Reciprocity does apply for antennas within the earth modelled using FDTD, as expected, so the 2D BOR model can be used to derive receive antenna parameters.

5.7 ANTENNA DESIGN

5.7.1 Requirements for an RT antenna system

Unity gain or better at the operating frequency

The various graphs show that almost all the antennas modelled have approximately unity gain from the frequency at which the dipole antenna is electrically half a wavelength long. Lower frequencies lead to poor gain as do specific higher frequencies. This requirement is not difficult to achieve.

Gain does not change with rock type

For a bare antenna the gain at a given frequency changes with rock type and the change cannot be avoided. As insulation is added, the electrical length of the antenna becomes determined by the insulation rather than the surrounding rock, creating an antenna that has constant gain with rock type.

Real part of antenna impedance as low as possible

The noise of an antenna functioning as a receiver is determined by its impedance. A low impedance is preferred for better noise performance. In the transmitter, the desired impedance is a compromise between high current with on low impedance antenna and high voltage on a high impedance antenna. In general, a lower impedance is preferred.

Imaginary part of antenna impedance near zero

If the transmitter is required to deliver power into a highly reactive antenna, then it must be designed to run at a higher voltage than otherwise necessary. For example, consider an antenna of $10 + \mathrm{j}100\,\Omega$.

Without a matching network, an amplifier must supply 31.6 V at a current of 316 mA to achieve a real power output of 1 W. If the load is now reduced to $10 + j10\,\Omega$ a voltage of only 4.46 V is required to achieve an output power of 1 W. An amplifier capable of delivering 1 W into both loads must be able to supply 31.6 V. When it is feeding the load with the smaller imaginary part, it still has to supply 316 mA and its efficiency drops from 100 % to approximately 14 %. The problem is exacerbated if the imaginary part of the impedance is even larger.

Physically short

The antenna needs to be as short as possible for two reasons: the RT inversion algorithm assumes a point source and is not as accurate with a long antenna; and the boreholes used for RT must be drilled past the target by about half the borehole spacing plus half the antenna length. If the antenna is very long, the additional drilling cost may be considerable.

The effect of antenna length on RT image quality is has been discussed and illustrated in Section 5.5 on page 119.

5.7.2 Proposed implementation

In Figures 5.24 and 5.25, the design requirements are superimposed on a series of graphs of bare and insulated antennas in various rock types. Gain is required to be greater than -10 dB. The input impedance must have a magnitude of less than 140 Ω and a phase of less than $\pm 45°$. For each parameter, the graph is thicker where the parameter falls within the desired range.

In Figure 5.24, gain is not defined for the more conductive materials at the higher frequencies, because there isn't penetration at those frequencies.

From Figure 5.24 the bare antenna can only meet the requirements for gain and input impedance for a limited frequency range in each rock type. In general, the frequency ranges do not overlap for different rock types. The bare antenna operates optimally if the frequency of operation is changed as the antenna moves through various

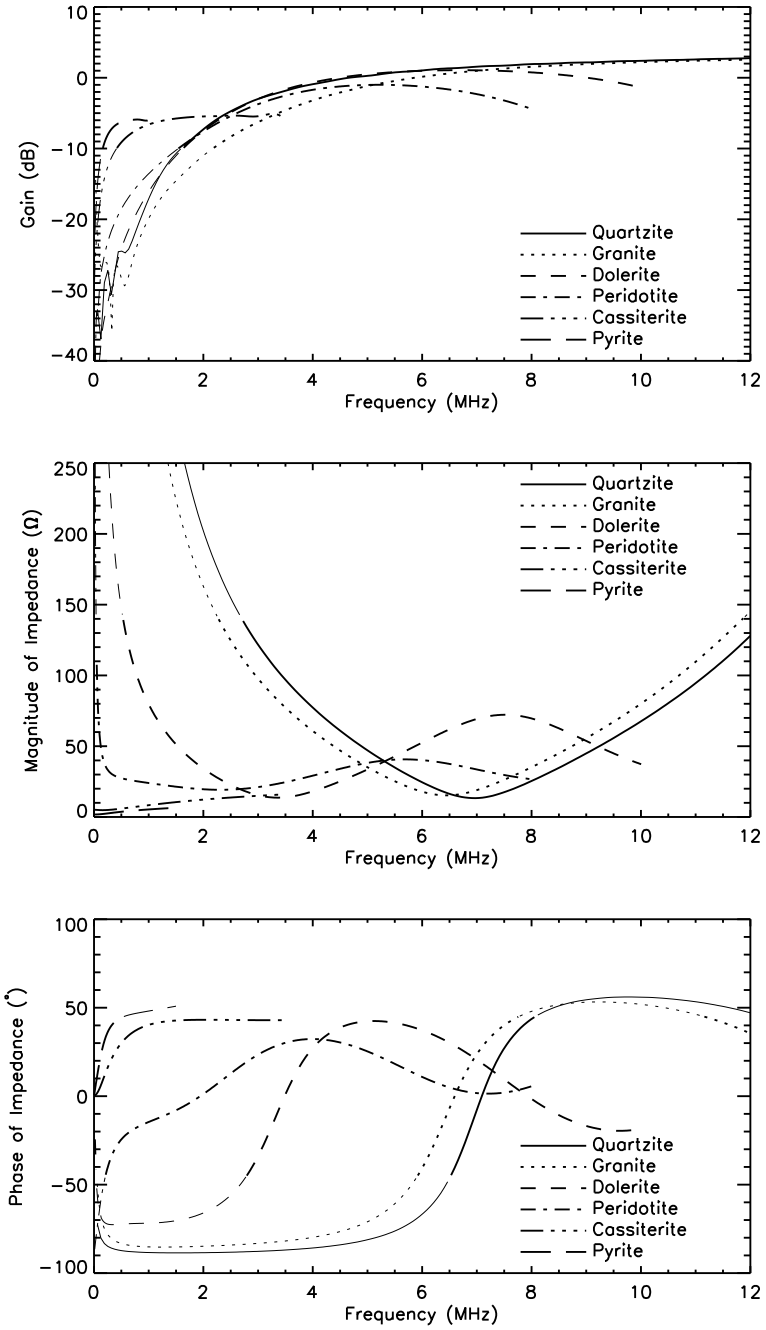

Figure 5.24: Gain and input impedance for bare antennas in a variety of rock types. The thicker lines are explained in the text.

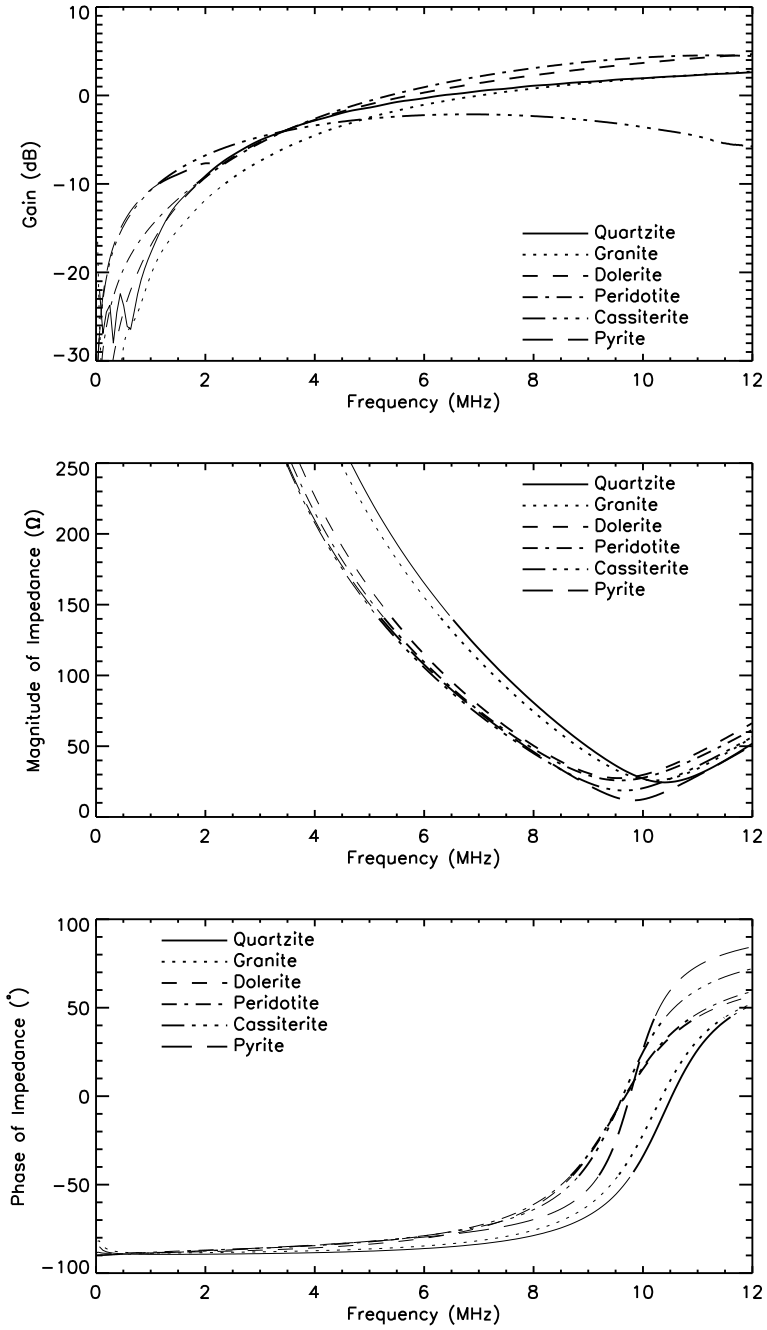

Figure 5.25: Gain and input impedance for insulated antennas in a variety of rock types. The thicker lines are explained in the text.

rock types. It is feasible as an RT antenna if performance changes in various rock types can be accounted for in the inversion. An example of such a correction is presented in the next chapter.

From Figure 5.25 an antenna with 20 mm of insulation can match all the requirements in all six rock types simultaneously. It meets all the requirements for a perfect RT antenna apart from physical length. The 6 m antenna illustrated would operate at 10 MHz and could be matched with reasonable efficiency in any of the six rock types. For operation at lower frequencies, a proportionally longer antenna would be required.

Note that 20 mm or more of insulation is required. A similar set of results for a conductor diameter of 14 mm and 15 mm of insulation would not match all the design requirements in all six rock types. From experiment, the insulated antenna requires a ratio of conductor radius to insulation thickness of at least 1:10. The requirement for thick insulation leads to a practical problem: if the probe electronics are housed within the antenna, the conductor has a minimum radius defined by the batteries used. If C-sized cells are used, the minimum radius of the conductor is 13 mm, allowing for only 9 mm of insulation.

To overcome the two disadvantages of a thickly insulated antenna, namely physical length and space for electronics, a hybrid antenna is proposed. The antenna is insulated over its centre section, but bare for a length at each end. The bare sections act electrically as end loads to the antenna and also provide two volumes for electronics and batteries. The bare sections are each 0.8 m long, leaving 4.4 m of insulated section. The insulated section is left as thick as possible. Other configurations of antenna were not considered due to the limited space available in the borehole.

The antenna is modelled as a monopole and its input impedance is presented in Figure 5.26. The input impedance is still largely characterized by the insulated section of the antenna. Resonance occurs at a slightly lower frequency than in the pure insulated antenna. Gain is plotted in Figure 5.27 and is very similar to that of the insulated antenna.

Adding bare sections to the ends of the insulated antenna has not

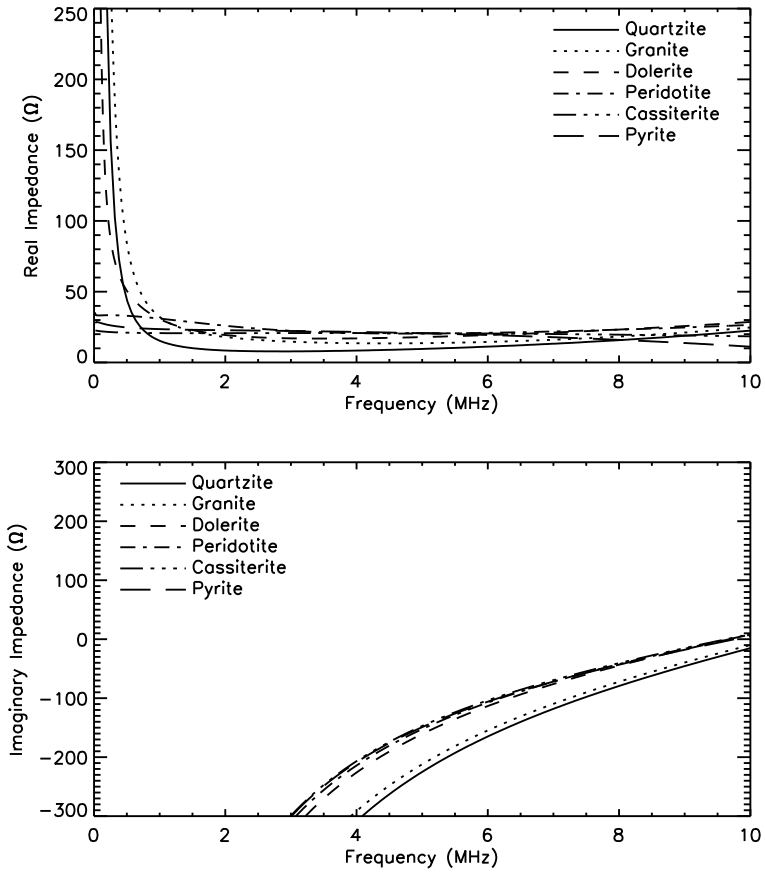

Figure 5.26: The input impedance of a novel antenna in six different rock types.

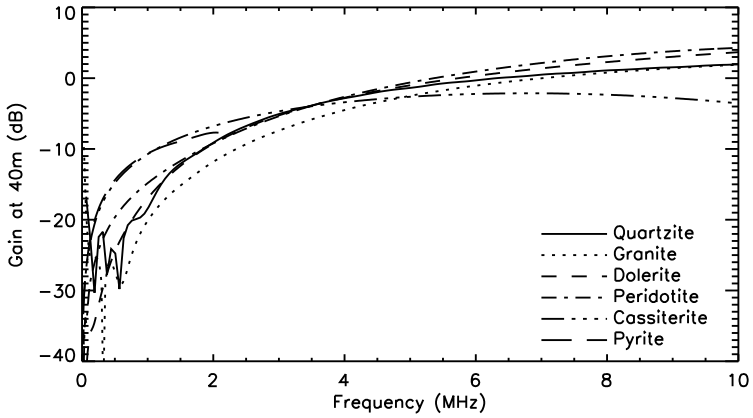

Figure 5.27: Gain of proposed novel antenna.

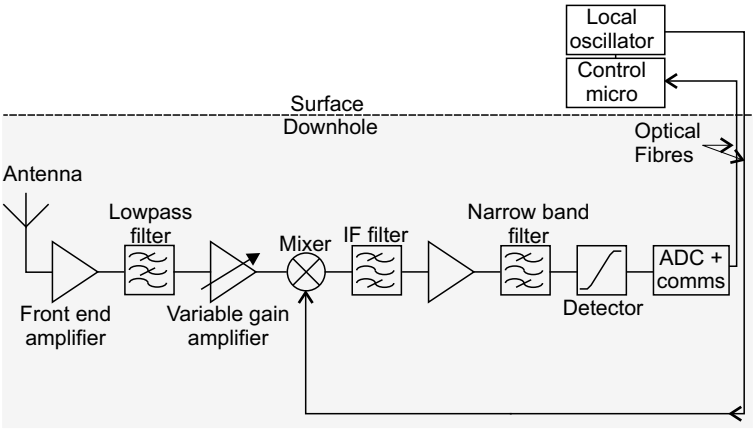

Figure 5.28: Receiver system diagram.

altered the impedance characteristics substantially but it has electrically lengthened the antenna. If further electrical length is required, the insulation can be made thinner at the cost of poorer electrical characteristics. The new configuration promises to perform well and is physically realizable within a working RT system.

5.8 ENHANCEMENTS TO THE PLUTO-6 RT SYSTEM RECEIVER

In Chapter 2, the Miningtek Pluto-6 RT system was described as part of the background to the modelling work that has been undertaken in this thesis. There are performance problems with the receiver probe of the Pluto system. With the benefit of modelling and improved understanding of the characteristics of an RT antenna, the probe has been redesigned.

5.8.1 Electronic design

It was determined by experiment that the poor noise performance of the existing probe is largely due to the noise associated with generating the local oscillator. A new circuit configuration is proposed where the local oscillator is moved to surface and the frequency that it generates is sent down the optical fibre link. The system design is illustrated in Figure 5.28. The probe contains a mixer, amplifiers and filters, a detector, an ADC and a microcontroller that continuously

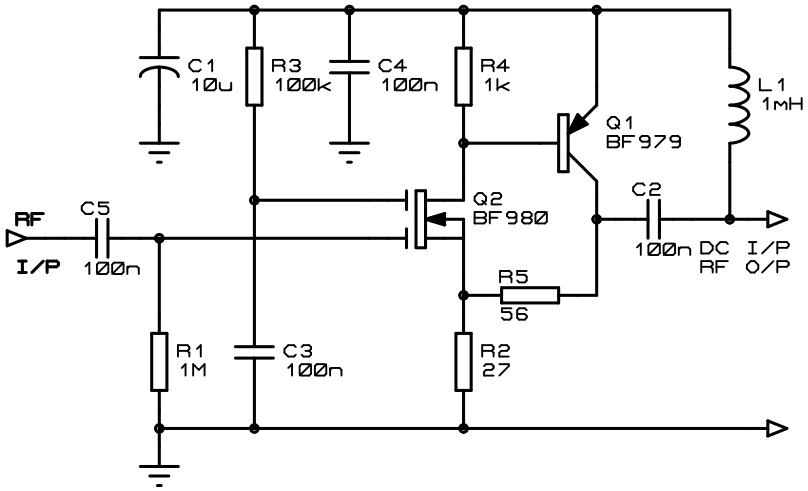

Figure 5.29: High impedance front-end amplifier.

streams the measured signal strength to surface. On surface, the receiver controller controls the LO generation, processes measurements from the down hole receiver and interfaces with the control computer.

A front-end with a fixed low impedance would unnecessarily limit the antenna design. While insulated antennas can be designed to match a fixed impedance, any bare antennas that are used with the system cannot be matched to a single impedance. If perfect matching cannot be achieved, a high impedance input is a good alternative and has been chosen here for that reason. The front-end amplifier is based around a dual-gate MOSFET and delivers sufficient gain to overcome its own noise contribution while providing a response that is flat as a function of frequency. The circuit is shown in Figure 5.29.

5.8.2 Mechanical design

Earlier in this chapter, it was shown that there are only slight differences in gain between bare and insulated antennas in rock. In the previous section, a hybrid insulated/bare antenna is proposed as a compromise between predictable electrical characteristics and practical mechanical considerations.

A new receiver probe design has been built, following the general principles of the proposal in the previous section. For practical reasons, it was not possible to implement a central section with thick

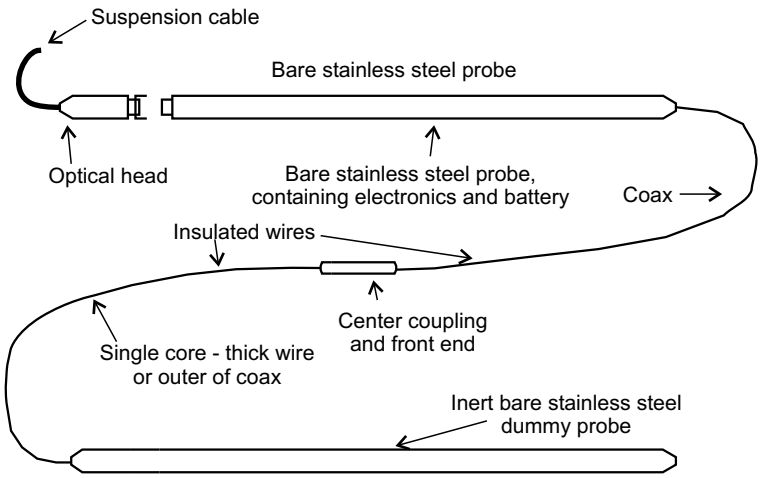

Figure 5.30: Mechanical configuration of the receiver probe.

insulation. A section with thinner insulation was tested to prove the general concept of a hybrid antenna.

The antenna design is illustrated in Figure 5.30. The antenna is a dipole, with the two arms meeting in the center coupling. From the feed point outwards, each arm consists of a length of insulated material, followed by a section of bare metal. The upper metal section is the container for the electronics and the battery, while the lower section is inert and is used as a weight to ensure that the wire elements of the antenna are pulled down the borehole. The receiver front end is at the center of the antenna, separated from the rest of the electronics to lower its susceptibility to noise.

Electrically, the antenna is a sleeve dipole (Milligan, 1985), driven from within one arm. A schematic of the structure is illustrated in Figure 5.31a. The configuration shown is for a transmitter, but the principles apply equally for a receiver. The current flow is illustrated in Figure 5.31b. Because the the two currents I^+ and I^- must be equal at the feed point of the antenna, it is automatically balanced. Any unbalanced current running on the outside of the feed coax, I_u, is forced to return along the inside of the sleeve cancelling any radiation that would otherwise have resulted.

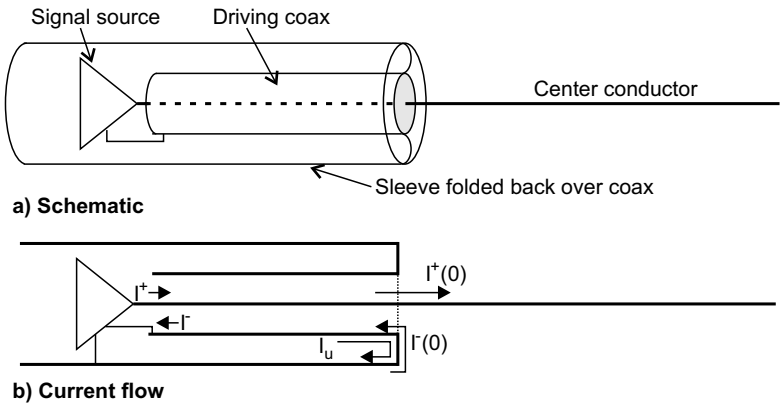

Figure 5.31: The sleeve dipole.

5.8.3 Tests

Unfortunately, during initial testing of the antenna the connection between the center section and the lower coaxial cable and dummy probe section failed mechanically and the dummy probe was lost down a borehole. To continue the tests within the time available, a new lower dipole section was made up from a single piece of RG213 coaxial cable. The bare inert probe section was simulated by removing the insulation from the coax for a distance from its end.

The tests were carried out in boreholes drilled in the car park at Miningtek in Johannesburg, illustrated on Page 11. Geologically, the site lies in the lower part of the Parktown Shales, within the Central Rand Group and Witwatersrand Supergroup. The shales are conductive in general, but contain bands of resistive quartzites (Kent, 1980; Maré and Oosthuizen, 1999). From RT measurement, the site has high conductivity zones near the top and bottom of the boreholes, with a lower conductivity zone in between.

Noise floor

The noise floor of the new receiver was determined by measuring the received signal without a transmitter present. It is difficult to determine the noise floor in a laboratory, because the measurement depends on a good quality screened room at low frequencies. Placing the receiver probe down a borehole ensures that no external noise

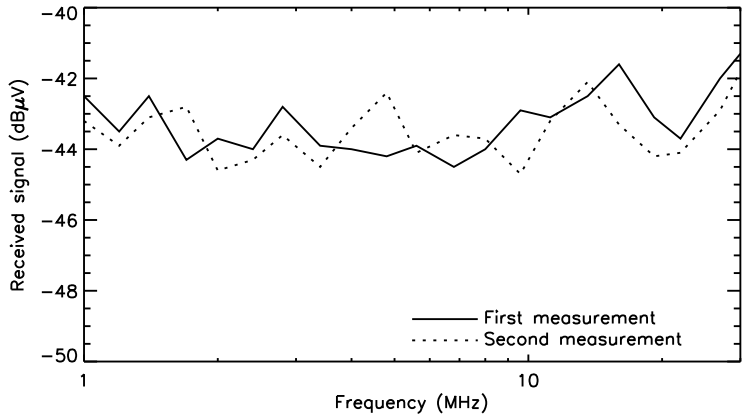

Figure 5.32: Noise floor of new RT receiver down a borehole.

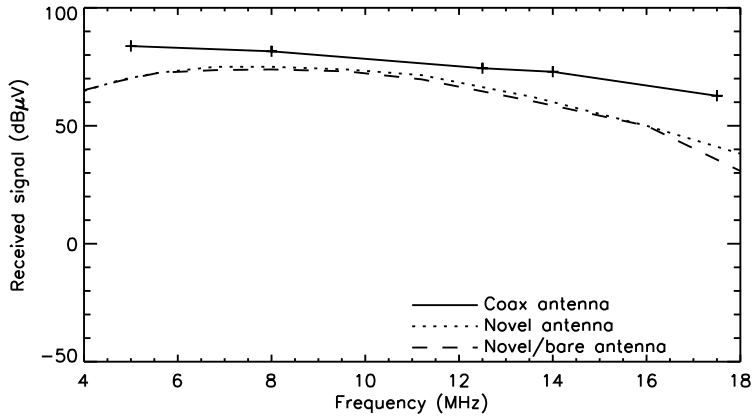

Figure 5.33: Comparison of the signal strength received by three antennas at the same position in the borehole, as a function of frequency.

reaches the receiver. At a depth of 18 m, two frequency scans were undertaken, with results plotted in Figure 5.32. The measured results are excellent, with a noise floor of better than -40 dBμV across the frequency band from 1 MHz to 30 MHz.

Functional comparison

The signal strength received by three antennas is compared in Figure 5.33. In each case, the receiver and transmitter are both at 24 m

in their respective boreholes. The first antenna is a sleeve dipole feeding a coaxial cable to the surface where the signal is measured using a Rhode & Schwartz ESHS10 test receiver. The second and third antennas are the two antennas described above: the new receiver with a lower arm that is insulated and with a bare lower arm. The two novel antennas agree well, but are some decibels below the sleeve dipole.

The sleeve dipole is different in several respects from the new receiver probe: it is heavily insulated, it is a different length and it is suspended on a coaxial cable. All three factors contribute towards the discrepancies seen in Figure 5.33. The plot is more remarkable for the similarity between the graphs: the new receivers perform comparably with the coaxial antenna.

It was not possible to test the high-impedance front end to the receiver, because a failure in the seal around the unit caused it to be flooded. Subsequent electrolytic damage could not be repaired within the time available. Bench tests of the front end on its own showed excellent gain characteristics against frequency. Gain was flat to within 0.1 dB from 1 MHz to 30 MHz.

5.8.4 Conclusion

The receiver probe that has been described has good electronic performance and it has been used to test the concept of using a hybrid insulated/bare antenna. Although it has not been adequately assessed, due to mechanical problems and time constraints during the test program, initial results are promising.

5.9 CONCLUSION

In this chapter, the FDTD modelling code developed in the previous chapter has been applied to model RT antennas, both bare and insulated in a range of rock types. The results show that antenna behaviour is relatively predictable for both antenna types. Behaviour is dominated by the electrical length of the antenna. For RT, bare antennas should be used only in conjunction with antenna corrections although they can be used across a range of frequencies, albeit inef-

ficiently. Antennas with sufficient insulation are more efficient and are effectively isolated from the surrounding rock, but they can only be used at a single frequency.

It has been shown that tomographic resolution is dependent on antenna length, but that the image is not degraded substantially by using a physically longer insulated antenna. It has also been confirmed that the BOR FDTD code can be used to determine the parameters that characterize both transmit and receive antennas.

A novel antenna has been proposed which takes advantage of insulation, while allowing for bare sections at each end to contain the required electronics. The antenna is a compromise between the conflicting requirements of a physically short antenna and one that does not vary with surrounding rock type. The concept of a hybrid insulated/bare antenna has been tested in a new receiver probe. Although the tests were marred by mechanical problems the initial results are promising.

6

RT case studies

In the previous chapters, an FDTD model of an RT system was developed and typical results were presented. In this chapter, the modelling code is applied to problems of significance to an RT operator, to develop understanding of how the antenna interacts with the rock around it.

6.1 Two antennas in one borehole

6.1.1 Analysis

The time taken to collect RT data could be reduced if more than one receive antenna could be placed in a single borehole, in the same way that seismic surveys usually use one source but an array of receiver geophones (Waters, 1978). However, closely spaced antennas will interact with one another. Arrays of antennas will not be viable unless that interaction is sufficiently small.

In a system with two antennas, the relationship between the voltage on the terminals of one antenna and the current in both antennas, is

$$V_1 = Z_{11} I_1 + Z_{12} I_2. \tag{6.1}$$

Z_{12} is the mutual impedance between antennas 1 and 2 and is given

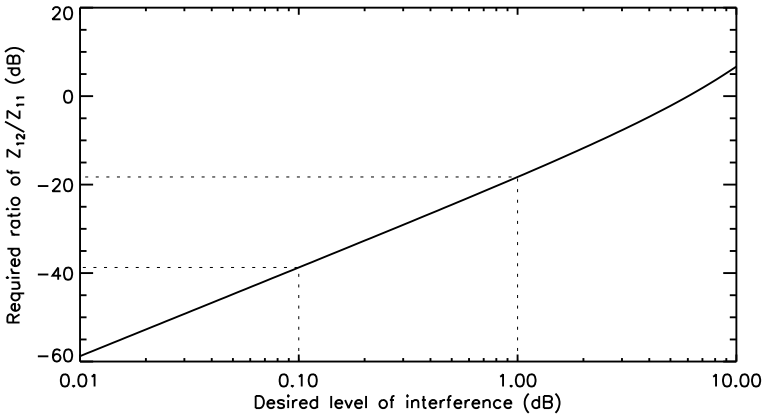

Figure 6.1: Determining the permissible coupling between two antennas in a single borehole.

by

$$Z_{12} = \frac{(V_1)_{\text{oc}}}{I_2(0)}, \tag{6.2}$$

the ratio of the open circuit voltage across antenna 1, to the terminal current flowing in antenna 2 (Balanis, 1982).

If the two antennas are identical, coplanar and illuminated by a normally incident plane wave, $I_1 = I_2$ and the second antenna acts to affect the voltage measured across the first because

$$V_1 = (Z_{11} + Z_{12})I. \tag{6.3}$$

The input impedance of one antenna is then

$$Z_i = Z_{11} + Z_{12}. \tag{6.4}$$

In an RT system, the change in measured voltage caused by the presence of the second antenna is tolerable if it is below a certain level. If Z_{12} is allowed to alter the measured voltage by an amount C in dBs, then the ratio of Z_{12} to Z_{11} is given by

$$\frac{Z_{12}}{Z_{11}} = 20\log_{10}(10^{C/20} - 1). \tag{6.5}$$

The relationship described by Equation 6.5 is illustrated in Figure 6.1 and two significant interference levels are plotted. If a change in measured voltage of 1 dB is permissible, then the mutual impedance

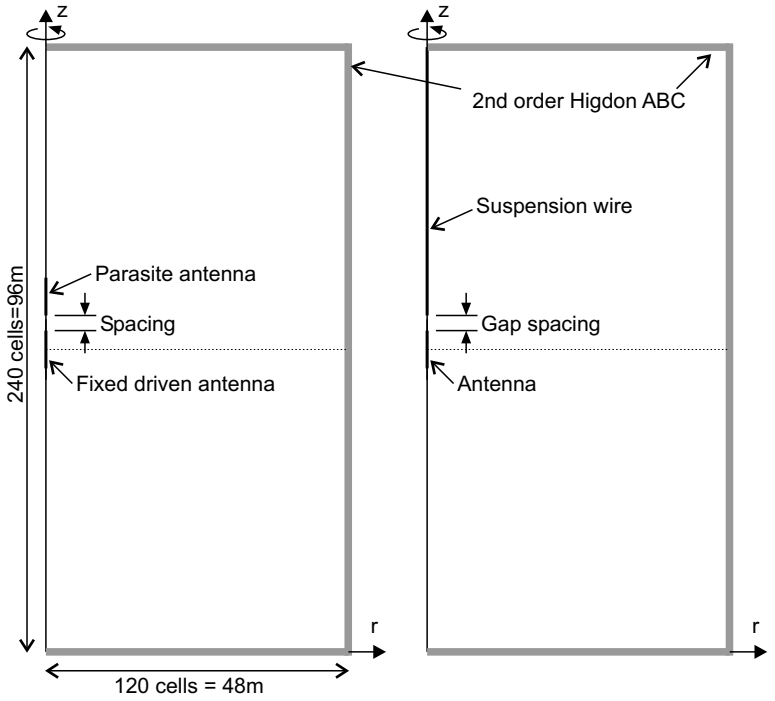

Figure 6.2: Modelling geometries to investigate the interaction of two antennas in one borehole and to investigate the interaction between an antenna and its support wire.

between the antennas should be more than 20 dB below the self impedance of the antenna. For a change in measured voltage of 0.1 dB, the mutual impedance must be at least 40 dB below the self impedance.

6.1.2 Modelling

The problem is investigated by creating a model with two antennas. One is driven and the second is left open circuited, at various distances from the first, as illustrated in Figure 6.2a. The parasite antenna corresponds to antenna 1 in the previous section. It is left open circuit to determine Z_{21} from Equation 6.2. Both antennas are 6.4 m long. The self and mutual impedances are determined from the model and the ratio is calculated.

An example set of results is plotted in Figure 6.3. The ratio of

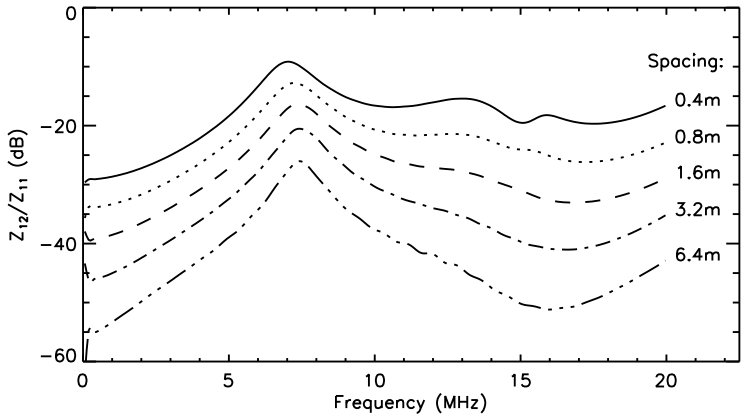

Figure 6.3: The effect of antenna spacing on measured signal in quartzite.

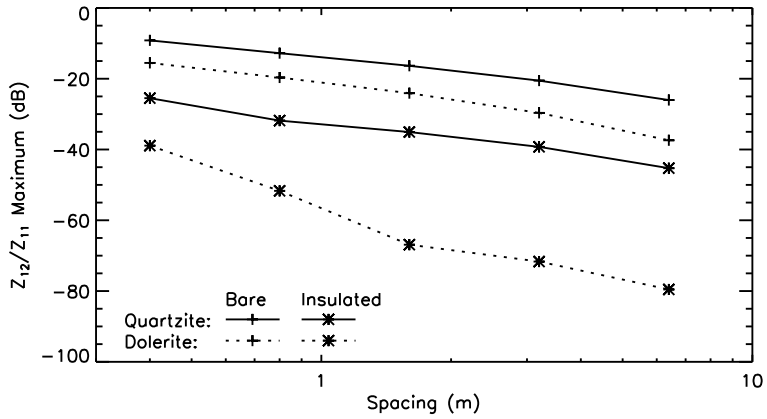

Figure 6.4: The effect of antenna spacing on maximum coupling ratio for two different types of antenna in two different rocks.

mutual to self impedance is calculated for a pair of bare antennas embedded in quartzite, as a function of frequency. Five graphs are plotted for increased spacings from 0.4 m to 6.4 m. Coupling decreases with increased spacing and the maximum coupling occurs roughly at the resonant frequency of the antenna.

In Figure 6.4, the maximum coupling is plotted as a function of antenna spacing for two antennas in two different environments. The two antennas are a bare wire, 44 mm in diameter, and a 4 mm diameter wire coated with 20 mm of insulation. The two rocks are highly

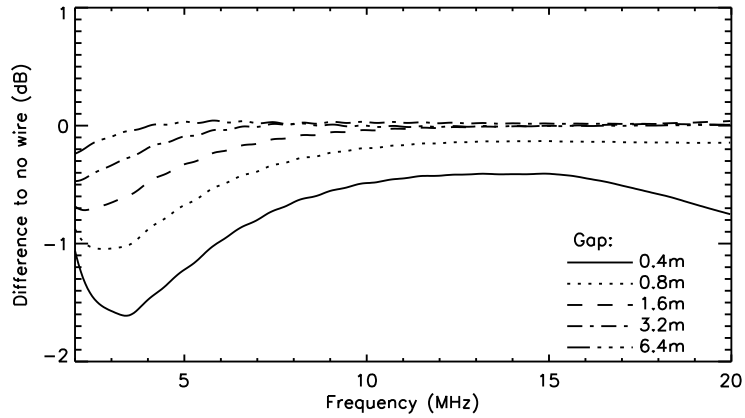

Figure 6.5: The gain variation of a 6 m bare wire antenna embedded in quartzite, suspended from a bare wire cable with various lengths of damped gap.

resistive quartzite, with a loss tangent of 0.02 and moderately lossy dolerite, with a loss tangent of 0.24. Coupling decreases as spacing increases, as expected and coupling is lower in more conductive rock. Insulating the antenna reduces coupling.

Coupling can be kept below -20 dB by leaving a space between the antennas that is at least long as the antennas themselves. To decrease coupling further, considerably larger spacings may be required, especially if the host rock has a low loss tangent.

6.2 SUSPENDING AN ANTENNA ON A WIRE

A pure dipole antenna in a borehole can be created by suspending the antenna using optical fibre and placing the electronics within the antenna. It is cheaper to suspend the antenna on coaxial cable and place the receiver on surface but the cable becomes a parasitic element, distorting both gain and pattern.

In this case study, the coaxial cable is approximated by a wire that is separated from the antenna by a gap in which no surface current flows on the wire. In practice, the gap would be achieved by placing ferrite beads around the wire (Grubb et al., 1976). Surface current can be caused by a poor balun within the antenna, or by coupling to the cable outside of the antenna. It causes radiation that alters the

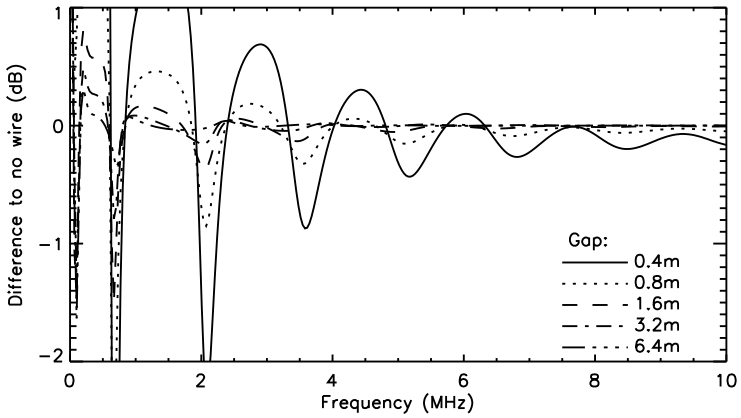

Figure 6.6: The gain variation of a 6 m insulated antenna embedded in dolerite, suspended from an insulated wire cable with various lengths of damped gap.

overall performance of the antenna.

The geometry for the study is very similar to that used for antenna arrays and is shown in Figure 6.2b. Two results are plotted in detail in Figures 6.5 and 6.6: a bare antenna embedded in quartzite with a loss tangent of 0.02 and an insulated antenna embedded in dolerite with a loss tangent of 0.24. The gain of antennas suspended below wire with varying gaps is compared to the gain of a free antenna. The gain is measured 40 m away from the 6 m dipole and is plotted as a function of frequency.

In common with the results for an antenna array, a gap of the same length as the antenna leads to almost negligible change in the gain at the designed operating frequency. The peak coupling is not at the antenna resonance frequency but is at low frequencies. Low frequency coupling can be very large because the wire acts as an excellent radiator for low frequencies, better than the antenna itself. Rock conductivity does not affect the coupling to the same extent as it did in the case of two antennas in one borehole.

The results also show how the insulated antenna supported on the insulated wire creates a series of gain peaks and troughs caused by standing waves on the insulated suspension wire. If the insulated antenna is suspended from a bare wire, the peaks and troughs are not present.

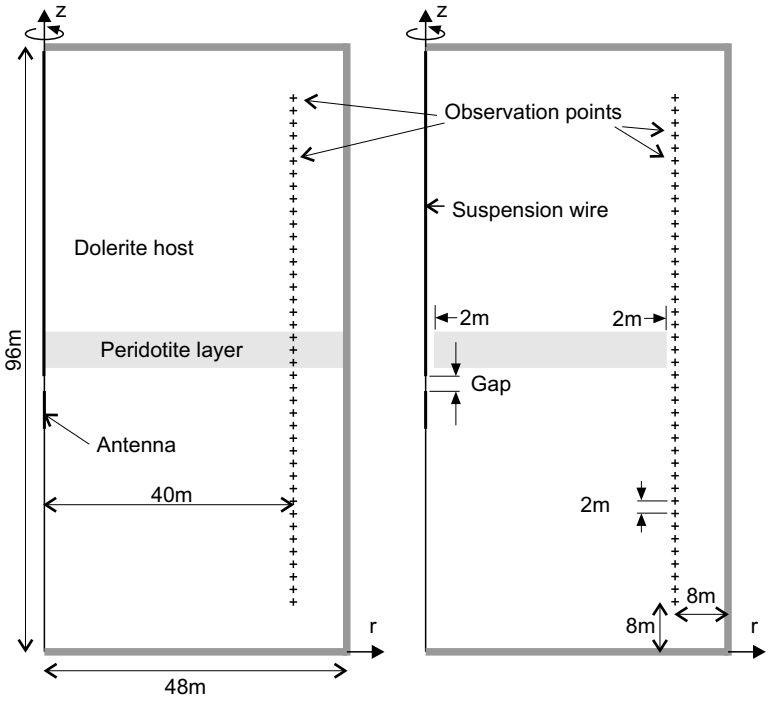

Figure 6.7: Geometry to test the effect of a suspension wire under RT data acquisition conditions.

6.2.1 Real geometry

For RT, the real concern about antennas suspended on wire is not a systematic change in the pattern as a function of rock type. Such a change can be removed in processing. The real concern is the effect of the suspension wire on the straight raypath approximation.

Two models have been constructed as illustrated in Figure 6.7. Tomographic data is collected between two boreholes with the transmitter antenna placed just below a layer of conductive material. In practice, the receive antenna is profiled in a parallel borehole. In the numerical model, the vertical electric field, $\boldsymbol{E}_z$, is observed at 2 m intervals along a vertical line 40 m from the transmit antenna.

The model presented here consists of a moderately conductive dolerite background, with a loss tangent of 0.24 and a more conductive peridotite target with a loss tangent of 0.76. The data is collected at a frequency of 4 MHz, close to the resonance of the 6 m dipole an-

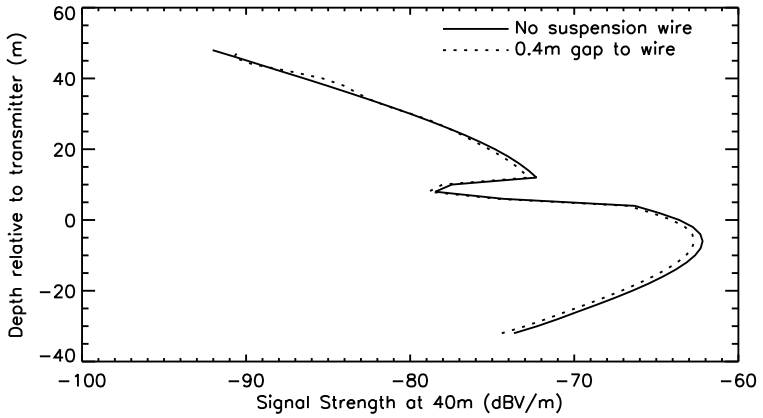

Figure 6.8: Field strength at 40 m due to an insulated dipole antenna below a continuous conductive block. Results are plotted for 4 MHz.

tenna in the dolerite host. The antenna is suspended on a wire, with a gap of 0.4 m between the antenna and the wire.

Figure 6.8 illustrates that in homogenous rock, wire suspension does not affect measured fields. The depth of the received field strength measurement point is presented on the vertical axis, matching the geometry of the system. The measured field strength is presented on the horizontal axis. For both antennas, starting at the bottom of the receiver borehole, the signal strength increases as the receiver positions approach the transmit antenna. The signal then decays dramatically through the peridotite layer. There is only a slight difference between the free and suspended antennas.

If the conductive layer does not intersect the boreholes, as shown in Figure 6.7b, the effect of a suspension wire is more pronounced. Figure 6.9 compares results for bare and insulated antennas with and without wire suspension. There are differences between the free antenna and the suspended antenna for both types of antenna, especially for receiver positions above the conductive layer. The absolute magnitudes of field strength are different for the two antenna types because both antennas are excited by 1 V sources but have different input impedances.

Numerical results not plotted show that the nature of the wire is immaterial: insulated and bare suspension wires have the same effect on performance. For both geometries, the wire acts as a guide for

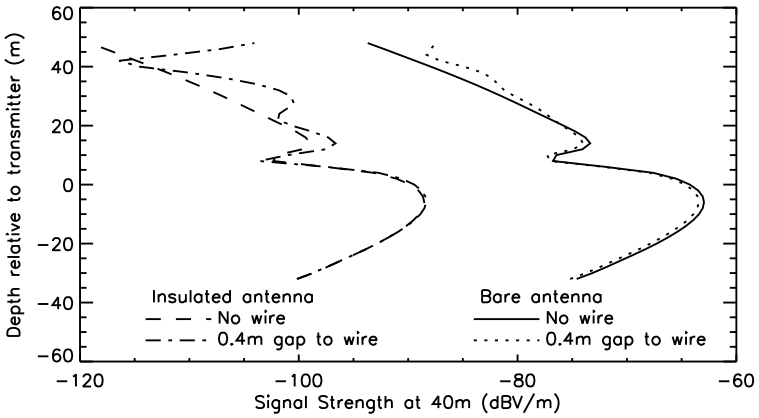

Figure 6.9: Field strength at 40 m for two antennas suspended freely or below a wire, for the geometry shown in Figure 6.7b. Results are plotted for 4 MHz.

energy to travel through the more conductive layer. When the layer doesn't intersect the wire, more energy can be guided past the layer.

The case study shows that wire suspension causes a breakdown in the straight raypath approximation. It may still be possible to use the FDTD code to incorporate the effects of wire suspension within the RT inversion but in the short term, wire suspension should not be used because it provides a guide for radio energy around conductive bodies and distorts the resultant RT images.

6.3 WATER FILLED BOREHOLES

The modelling presented thus far has concentrated exclusively on antennas embedded directly in the host rock. In fact, RT antennas are always in boreholes, which are usually filled with water. In the unusual case where the borehole is dry, the air in the borehole can be thought of as adding to the antenna insulation.

Here, I model a series of antennas surrounded by a layer of water, to determine how water influences the performance of a dipole antenna in rock. The real problem is more complicated because the antenna is almost always in contact with the rock on one side of the borehole, with a varying thickness of water between the antenna and the borehole in other directions.

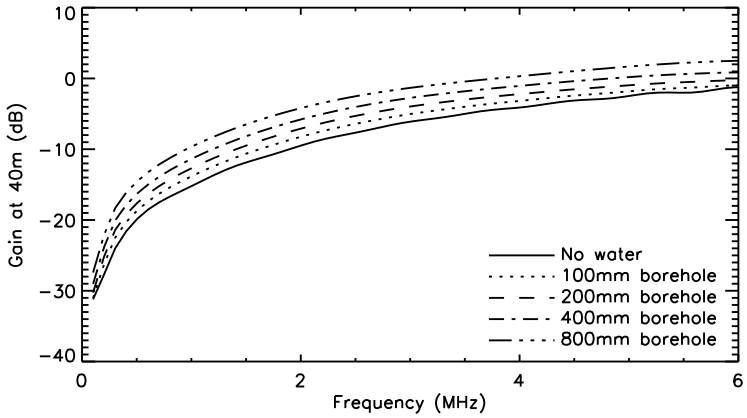

a) Bare antenna

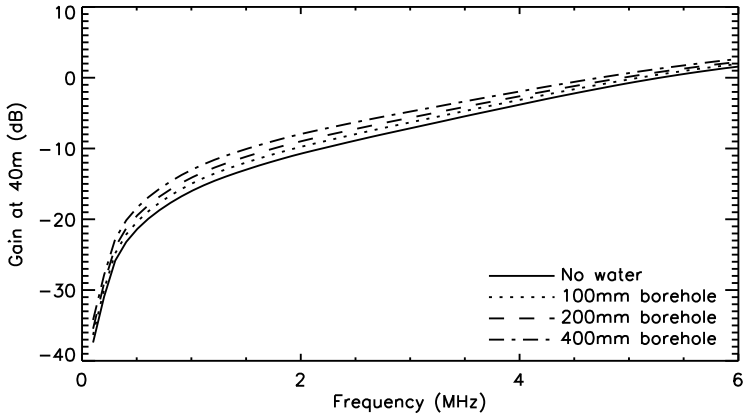

b) Insulated antenna

Figure 6.10: The effect of borehole water on the gain of 3.2 m monopole antennas in peridotite.

In a perfectly vertical borehole the horizontal antenna position in the borehole may be random and can change as the antenna swings like a pendulum. In practice, boreholes are very rarely vertical and even in vertical boreholes, the antenna is normally suspended against one wall. The performance of the antenna is fixed for a fixed position in the borehole and lies somewhere between the predicted performance of the antenna embedded in the rock and the antenna embedded in a symmetrical water filled borehole.

Figure 6.10 illustrates the effect of water surrounding two antennas in peridotite, with a loss tangent of 0.76. The water is assumed to

be non-dispersive in the frequency range of interest, with a conductivity of 0 S/m and a relative permittivity of 81. The bare 3.2 m monopole antenna is expected to be resonant at approximately 3.3 MHz. The model has 820×220 cells and each cell is 0.05 m square.

Water does increase the gain of both antennas slightly, but at realistic borehole diameters of 45–70 mm it does not alter the gain sufficiently to be a concern. The performance of the insulated antenna is affected less than that of the bare antenna. If the operator wishes to ensure that the effect of water is constant at all points in the borehole, she will have to ensure that the antenna remains centralized by using a fin or spring mechanism.

Water does not have the same effect as lossless insulation – it does not provide a coaxial structure for wave propagation. King and Smith (1981) limit their coaxial approximation to the general condition that

$$|k_4^2| = |\omega^2 \mu(\varepsilon_{e4} + \mathrm{j}\sigma_{e4}/\omega)| \gg |k_2^2| = |\omega^2 \mu(\varepsilon_{e2} + \mathrm{j}\sigma_{e2}/\omega)| \tag{6.6}$$

where k_4 is the wave number in the surrounding medium and k_2 is the wave number in the insulation. In effect, the ambient region 4 must be electrically relatively dense compared to the insulating region 2. Normally, the surrounding region is more dense than the insulation because it is more conductive. In this instance the water, acting as the insulation, is more dense than the surrounding region due to its high dielectric constant.

In Figure 6.11, a bare monopole antenna is modelled embedded in granite surrounded by a varying thickness of water. Superficially, there is a larger change in gain than in the peridotite example shown earlier. In fact, the magnitude of the gain remains similar as a function of electrical length but the frequency of maximum gain becomes lower as the thickness of the layer of water surrounding the antenna increases.

The decrease in the frequency of unity gain in the granite is caused by the high permittivity of water compared to the permittivity of the granite, which is about 9. It is not as evident in the peridotite example, because peridotite has a higher permittivity, about 57 at

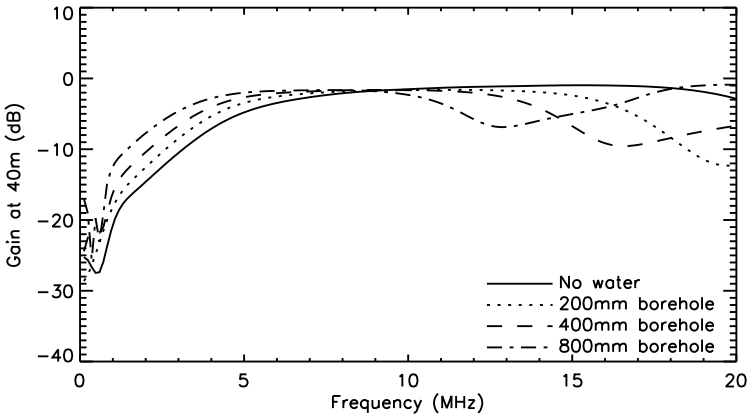

Figure 6.11: The effect of borehole water on the gain of a 3 m bare monopole antenna in granite.

4 MHz. The increase in gain in the peridotite is caused by highly resistive water around the antenna allowing larger antenna currents to flow.

The two examples show how water can be thought of as another medium surrounding the antenna, rather than as a special medium, like lossless insulation. In a real situation the water is likely to be made more conductive by dissolved salts, becoming even less like lossless insulation. The examples show that in narrow exploration boreholes, where the thickness of the water layer is a very small fraction of a wavelength, water does not appear to affect the performance of RT antennas. In large diameter boreholes the FDTD model can be used to investigate the effect of water on the antenna.

6.4 UNBALANCED ANTENNAS

The operator and the designer of an RT system both have an interest in the performance of antennas that are not fed in the center. The operator wishes to determine whether a break has occurred in an arm of the antenna by looking at parameters that he is recording, especially antenna impedance and signal strength. He also wants to know if a given failure is critical to system performance. The designer wants to ascertain if some performance advantage is available by moving the feed point.

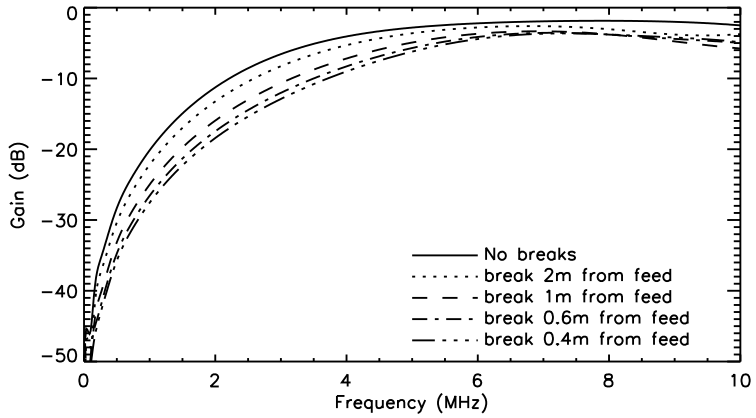

Figure 6.12: The variation in the gain of a dipole antenna that is broken at different points.

6.4.1 Detecting broken antennas

Will a broken antenna influence the final RT image? Can an operator detect a broken antenna? In Figures 6.12 – 6.14 a break has been introduced into one arm of a dipole antenna. The dipole is modelled in a space consisting of 220×440 pixels, each 0.2 m square. The dipole itself is bare, center fed and 31 segments long. The antenna is embedded in dolerite, and is expected to resonate at about 4 MHz.

A break is introduced into the antenna by removing a segment from one arm of the dipole antenna to simulate a bad contact between one part of the dipole antenna and another. The break is moved from 0.4 m from the feed point to 2 m from the feed point.

At the operating frequency, the effect of the break on gain is evident, but it is also small. The worst difference in gain occurs when the break is close to the feed point. Gain becomes approximately equal to the gain of the unbroken antenna as the break moves closer to the end of the antenna.

The effect on pattern is illustrated in Figure 6.13. At the operating frequency, the pattern does not vary significantly as the break is moved away from the feed. At double the operating frequency, 8 MHz, the effect of the break is marked. The unbroken antenna has a vertically symmetrical pattern, but all of the antennas with missing segments have a main lobe directed downwards by about 15°.

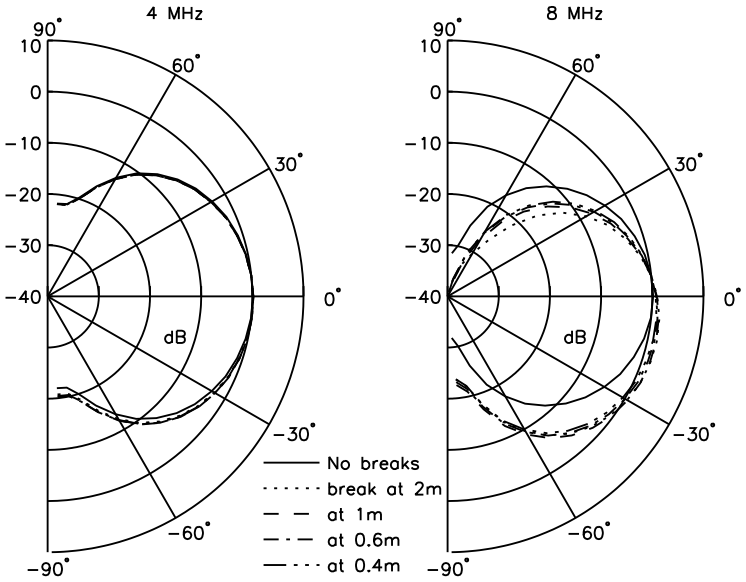

Figure 6.13: The variation in the pattern of a dipole antenna that is broken at different points. Results are presented for 4 MHz and 8 MHz.

The performance figures illustrate that an operator probably can live with a broken antenna as long as she is working with the antenna at its resonant frequency. Away from the resonant frequency, performance may not be as predictable.

From Figure 6.14 the operator will have no difficulty in detecting a break that occurs during a survey. Although the real part of the antenna impedance hardly changes at 4 MHz, the antenna goes from being resonant to being capacitive. If the antenna impedance is monitored during a survey, the operator will notice the change in impedance when a break occurs in the antenna. If the breakage is recorded, the FDTD model can be used to subsequently correct the effect of the broken antenna on the data.

6.4.2 Designing with unbalanced antennas

In Figures 6.16 – 6.17 the effect of changing the feed point on one antenna in one rock type can be seen. The antenna is a bare 6.4 m dipole, embedded in dolerite. It is modelled in a space 120×240

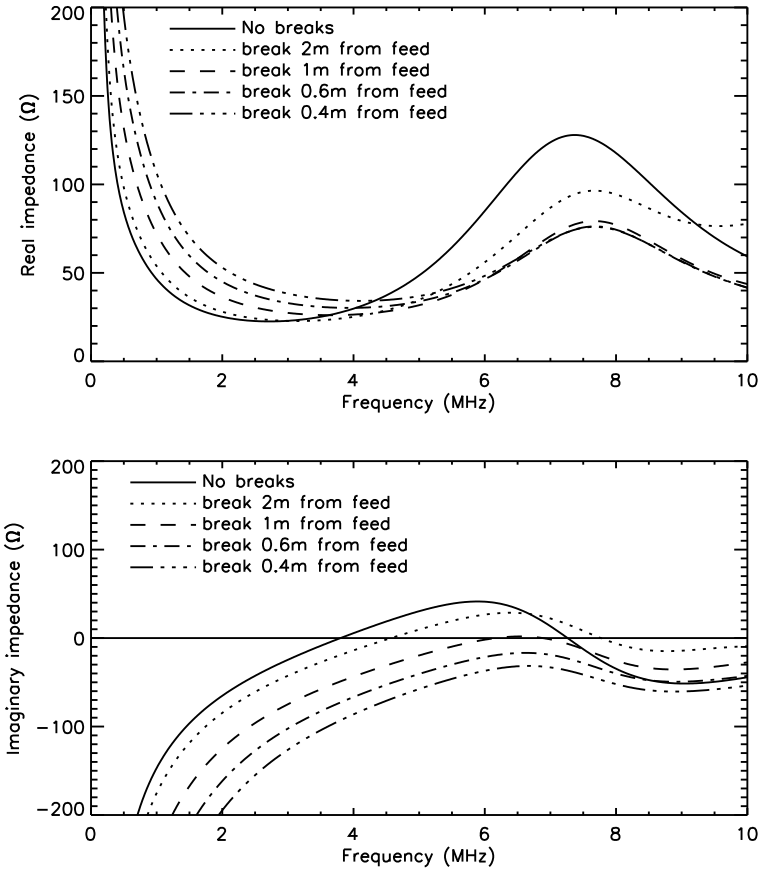

Figure 6.14: The variation in the input impedance of a dipole antenna that is broken at different points.

cells, with each cell 0.4 m square. The 6.4 m antenna is 15 cells long. In the symmetrical case, the antenna consists of 7 cells either side of the $\boldsymbol{E}_z$ hard source. The source is then offset by 3 cells, so that the source is 4 cells from one end. Finally, the antenna is offset by 5 cells, with the source 2 cells from one end. The design frequency of a 6.4 m long bare dipole in dolerite is approximately 4.2 MHz.

At the design frequency, all three antennas have very similar characteristics. The gain, illustrated in Figure 6.15 remains unchanged up to the operating frequency, but does suffer at higher frequencies.

The effect of offset feed on pattern, illustrated in Figure 6.16, is not as dramatic as a break in one arm of the dipole . Offset feed leads to a slight offset in pattern both at the design frequency and at a

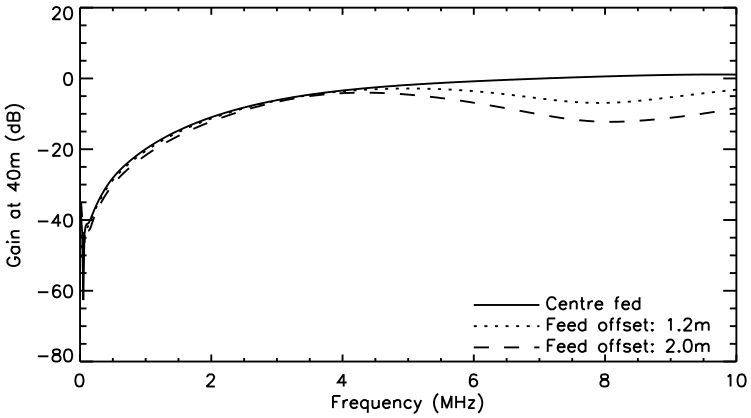

Figure 6.15: Gain of a bare dipole antenna in dolerite for three different feed points.

higher frequency of 8 MHz, but the amplitude of the offset is almost negligible.

The most notable change in antenna characteristics is in the input impedance, illustrated in Figure 6.17. At the operating frequency, the antenna becomes capacitive, and the real part of the impedance increases. From the point of view of the designer, neither change is desirable. However, if an antenna must be driven in an offset manner for practical reasons, performance is acceptable for small offsets.

6.5 SYSTEM PERFORMANCE ESTIMATION

In Chapter 2, the RT equation was introduced in Equation 2.12:

$$\begin{aligned}\int_0^R \alpha^* . \, \mathrm{d}r &= 126 \\ &+ P_{t_{\mathrm{dBW}}} \\ &+ 10 \log_{10} \left(\frac{1}{4\pi R^2} \right) \\ &+ 10 \log_{10} \left(\frac{R_r G_t G_r \lambda^2}{4\pi} \right) \\ &- V_{r_{\mathrm{dB}\mu\mathrm{V}}} . \end{aligned} \tag{6.7}$$

The antenna parameters vary as a function of the rock surrounding the antenna. With the assistance of the FDTD model, it is possible to

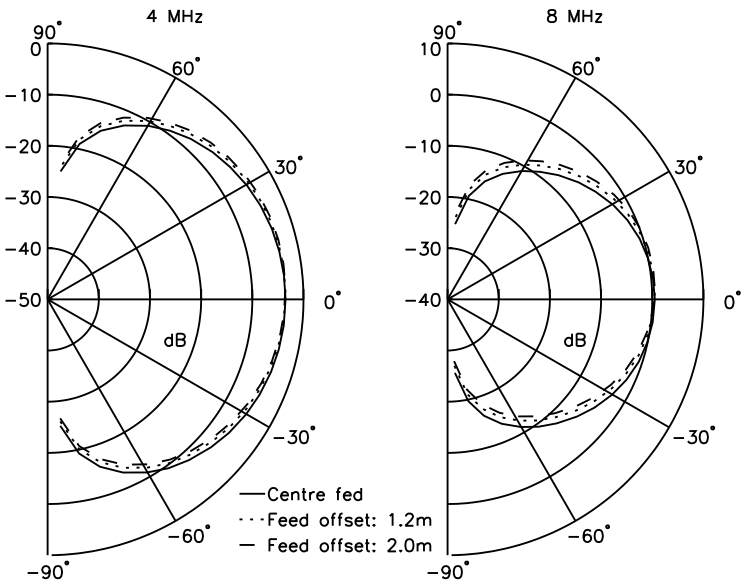

Figure 6.16: Pattern of a bare dipole antenna in dolerite for three different feed points.

determine all the parameters in the equation that apply to the transmitter and receiver antennas.

To calculate the parameters for an antenna in a single rock type, a model is created containing an accurate representation of the physical antenna, surrounded by the rock. The antenna resistance can be obtained directly from the model. The wavelength can be determined from the electrical properties of the rock. The gain can be calculated using both the electrical properties and the model results. The transmitted power and the received voltage are measured.

The RT equation for a particular transmit and receive pair can be written as

$$\begin{aligned}\int_0^R \alpha^*.\,\mathrm{d}r &= P_{t_{\mathrm{dBW}}} \\ &+ 10\log_{10}\left(\frac{1}{4\pi R^2}\right) \\ &+ 126 + 10\log_{10} G_t(\theta_1) \\ &+ 10\log_{10}\left(\frac{R_r G_r(\theta_2)\lambda^2}{4\pi}\right) \\ &- V_{r_{\mathrm{dB}\mu\mathrm{V}}} \end{aligned} \tag{6.8}$$

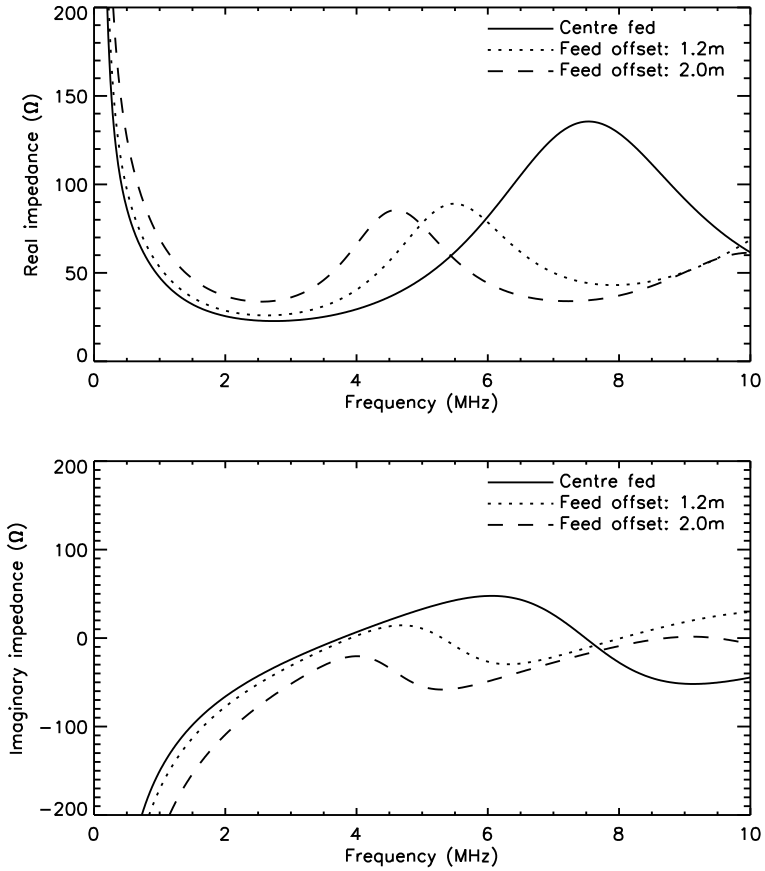

Figure 6.17: Input impedance of a bare dipole antenna in dolerite for three different feed points.

separating transmit and receive antenna characteristics. The correct characteristics can be inserted depending on the rock types at the transmitter and receiver locations. The transmitter coefficient as a function of the angle between the normal to the antenna and the raypath is

$$C_{\mathrm{Tx}} = 126 + 10\log_{10} G_t(\theta_1). \tag{6.9}$$

The receiver coefficient is

$$C_{\mathrm{Rx}} = 10\log_{10}\left(\frac{R_r G_r(\theta_2)\lambda^2}{4\pi}\right). \tag{6.10}$$

Later in the chapter, modelling results will be applied to correct field RT data for antenna effects as the rock type changes in the borehole.

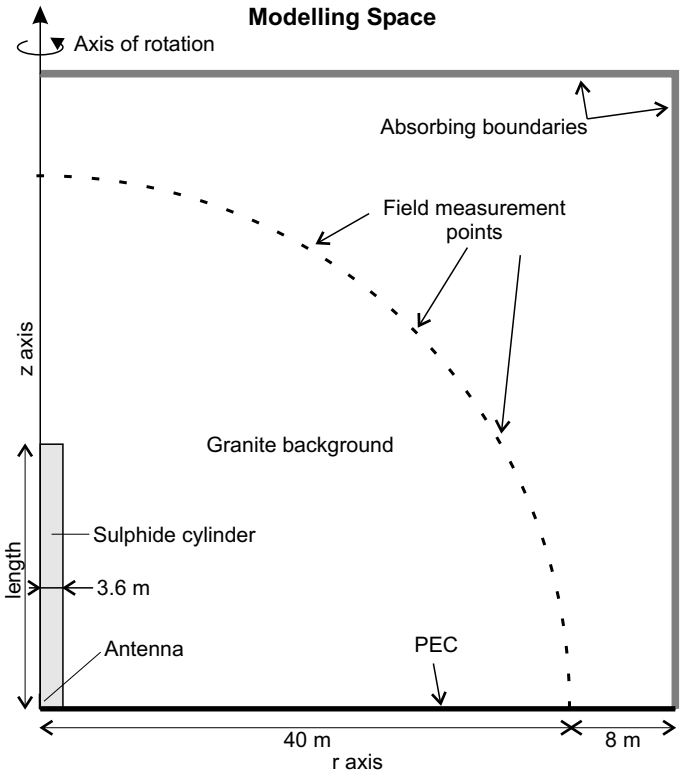

Figure 6.18: Geometry for modelling an antenna embedded in a massive sulphide body.

6.6 ANTENNAS IN VERY LOSSY ENVIRONMENTS

It is not possible to model the performance of an antenna in a very lossy rock by completely filling the modelling space with the rock. The attenuation in the rock is so high that all the transmitted energy is dissipated before it reaches the measuring point. The high attenuation rate also means that pattern measurements cannot be interpreted in the usual manner.

An antenna has been modelled embedded in a cylinder of sulphide, which is in turn embedded in granite, a low loss rock. The geometry of the model is shown in Figure 6.18. In each case, the antenna is a bare monopole, 3.2 m long and 44 mm in diameter.

The gain of an antenna embedded in sulphide cylinders of five different lengths is illustrated in Figure 6.19. The gain resembles that expected for five antennas of different lengths because the sulphide

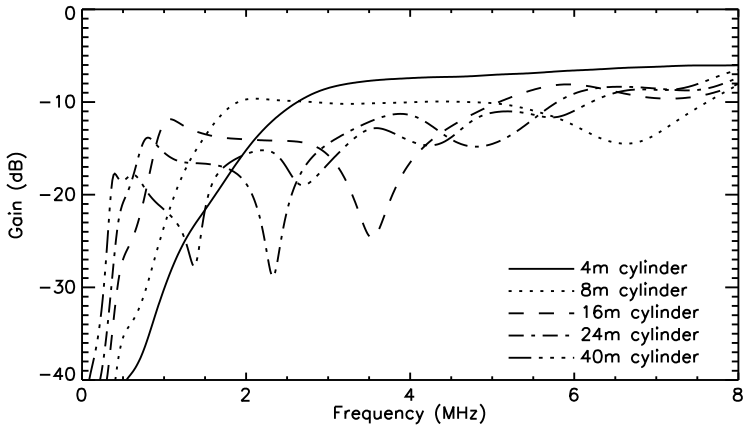

Figure 6.19: The effect of sulphide cylinder length on gain.

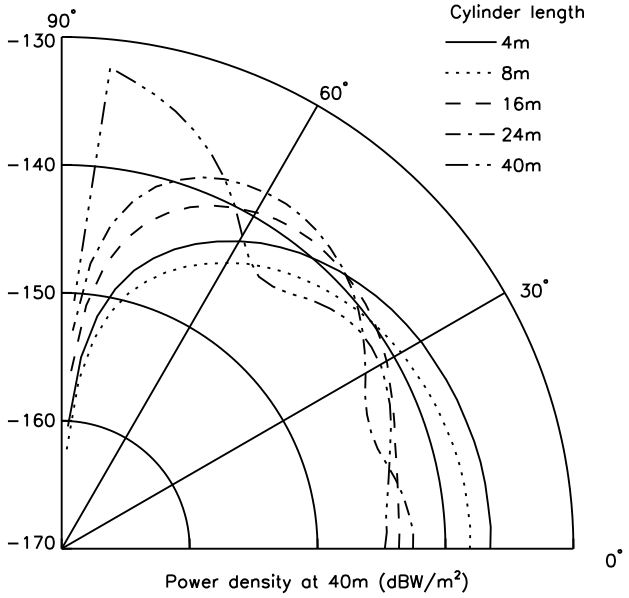

Figure 6.20: Power density at 3 MHz 40 m from the feedpoint of the antenna as a function of the length of the sulphide cylinder.

cylinder supports an antenna-like current distribution.

In Figure 6.20 the pattern for the short sulphide cylinder resembles that expected from a dipole antenna: similar to the cosine pattern of a dipole antenna in air. From the earlier result for gain, as the sulphide cylinder is lengthened, its pattern should resemble that of a longer antenna at the same frequency. Superficially, the patterns in Figure 6.20 do resemble those of longer antennas but they also have a lobe developing at a high angle to boresight. The lobe comes about purely through the proximity to the measurement surface, as discussed on Page 114.

This case study serves as another warning that as rock becomes more conductive, the concepts of gain and pattern become less meaningful. For RT inversion, a straight raypath model with correction for pattern and gain is insufficient. The full FDTD model needs to be incorporated into the inversion to completely account for the effects of highly conductive rock.

6.7 A TOMOGRAPHY EXAMPLE

The RT modelling code can be used to estimate the performance of antennas used in field surveys. Estimates of gain, pattern and impedance can then be used to enhance the inversion. A field survey reported by Van Schoor and Duvenhage (1999) is processed here with information added about the performance of the antennas used. I would like to thank the authors for granting their permission to use their data here.

An RT survey was conducted at a disseminated sulphide test site in Mpumalanga Province, South Africa. The geological situation is illustrated in Figure 6.21. Information from three boreholes was available. Two of the boreholes are shown with their geological logs and the major and minor ore intersections are shown on all three. The geological interpretation is overlaid, based purely on the evidence of core sampled from the three boreholes.

After the RT data was acquired, it was processed assuming that the antenna performance of both antennas was constant as a function of depth and that the antenna pattern was cosinusoidal. The RT

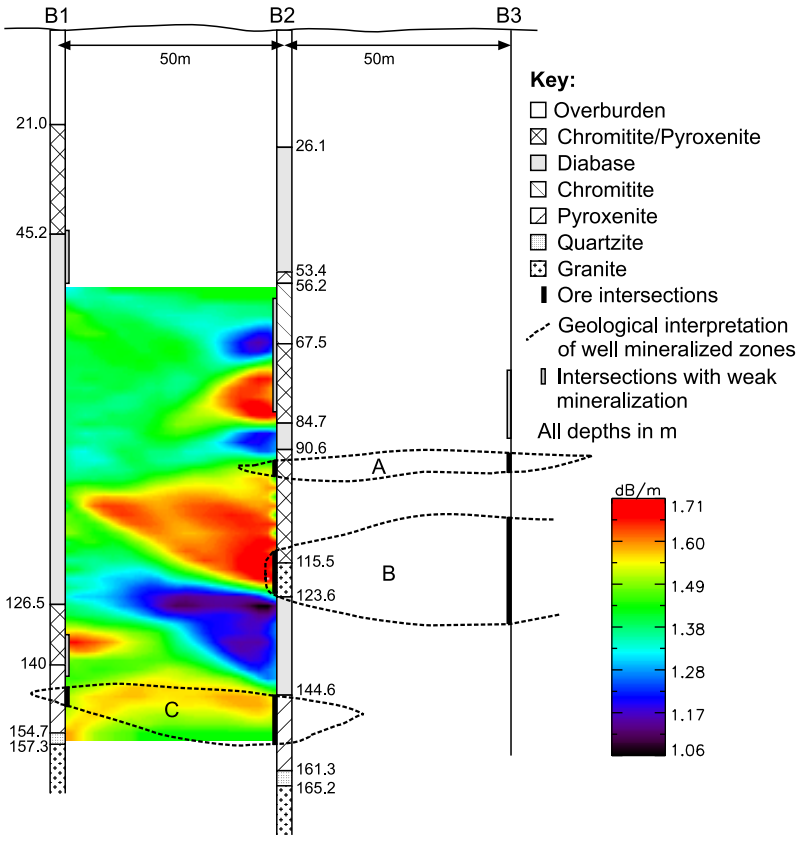

Figure 6.21: RT survey results as originally processed.

equation applied was

$$\begin{aligned}\int_0^R \alpha^*.\,\mathrm{d}r &= 125 \\ &+ P_{t_{\mathrm{dBW}}} \\ &+ 10\log_{10}\left(\frac{1}{4\pi R^2}\right) \\ &+ 10\log_{10}(cos^2(\theta)) \\ &- V_{r_{\mathrm{dB}\mu\mathrm{V}}}\end{aligned} \tag{6.11}$$

for each transmitter and receiver position. The resulting data was inverted using a maximum entropy algorithm, assuming straight raypath propagation.

In Figure 6.21 the resultant image is shown, placed under the original geological interpretation. There are clear discrepancies between the image and the geological interpretation. The proposed interpret-

Table 6.1: Rock properties of case study at 12.5 MHz.

Rock	Conductivity (mS/m)	Relative Permittivity
Diabase	0.5	12
Pyroxenite	1.5	40
Chromitite/Pyroxenite	2.5	15
Chromitite	1.5	25
Quartz	0.25	8
Granite	0.25	8

ation suggests that there is very little ore between boreholes B1 and B2, while the image suggests a large mineralized zone.

To improve the image, rock dependant antenna parameters can be calculated using the FDTD model. The antenna parameters were determined by running one numerical model for each rock type in the survey. Information was only required from the models at the frequency used in the RT survey, 12.5 MHz, so the electrical properties used in the model were fixed. Electrical properties were estimated from measurements made in similar rocks in nearby boreholes. The five rock types present in the borehole logs as well as the electrical property estimates that were used are summarized in Table 6.2.

The antenna used in the field and modelled here, is an electric dipole. The dipole is centre fed, with two sections 1.5 m long, 36 mm in diameter coated with 4 mm of insulation. The lower dipole section is extended by 0.5 m with a wire 8 mm in diameter coated with 11 mm of insulation, while the upper dipole section is extended by 2.5 m with a wire 4 mm in diameter coated with 2 mm of insulation. The dipole is thus asymmetrical, as it has 4 m above the feed point and 2 m below the feed point. The dipole geometry was chosen for operational rather than electrical reasons.

The gain, pattern and impedance of the antennas are determined from the FDTD models. The transmitter and receiver coefficients for each rock type in the model are tabulated in Table 6.2. Note that the difference between the most favourable and the least favourable pair of coefficients is greater than 20 dB.

Table 6.2: Antenna performance of the various rocks in the case study at 12.5 MHz.

Rock	C_{Tx} (dB)	C_{Rx} (dB)
Diabase	120.2	11.7
Pyroxenite	110.6	-0.9
Chromitite/Pyroxenite	114.4	5.9
Chromitite	111.8	1.4
Quartz & Granite	118.6	11.8

The attenuation calculated at each transmitter and receiver position can be adjusted for the antenna pattern in the rock types at those positions. The data is then inverted again to create a new attenuation image. In Figure 6.22 the left hand image has been corrected including only pattern correction. The right hand image has been corrected only including transmitter and receiver correction without pattern correction. In Figure 6.23 the two corrections shown in Figure 6.22 are both applied and the image produced is compared to the original image with no correction.

In this example, in all cases where processing is applied the effect on the output image is not significant. The final processed image suggests that the resistive zone between about 120 m and 140 m does not extend as far towards the left hand borehole as originally suggested. There are also some detail changes within the main conductive zone at approximately 105 m depth and the main conductive zone is slightly better resolved when all corrections have been applied.

In this case, correcting antenna performance for the different rocks in the boreholes has not lead to a significant change in the resultant tomographic image. Greater improvements are likely to be seen when the contrast between the conductivity of the target and that of the host is greater. The case study leaves open the question of whether RT imaging using the straight raypath approximation and the maximum entropy inversion can benefit from rock dependent antenna corrections.

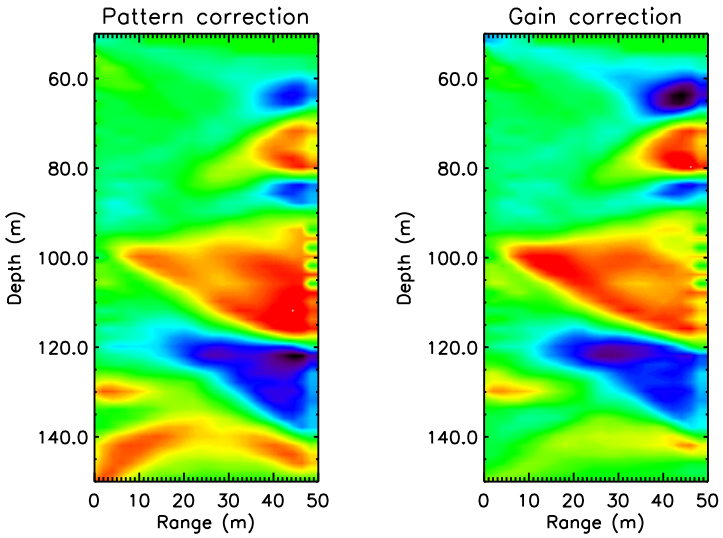

Figure 6.22: The tomographic image corrected for rock dependant pattern on the left and for rock dependant gain and impedance on the right.

6.8 CONCLUSION

In this chapter, the computer model of Chapter 4 and the techniques of the last chapter are applied to real RT scenarios. Case studies show that more than one receive antenna can be used in a single borehole, as long as the spacing between the antennas is at least as great as the antenna length. The influence of wire on an antenna has been illustrated, highlighting the potential danger of wire suspension in particular environments.

The effect of water in the borehole has been investigated and found not to affect performance significantly, especially if realistically small quantities of water are considered. Unbalanced antennas are investigated to determine how a break in an antenna would effect its electrical performance. A break will cause a discernible change in input impedance. If the position of the break is accurately known, it should be possible to correct for it using an antenna model from the FDTD code.

A series of models shows how antennas in very lossy environments deviate from the straight raypath approximation. The models

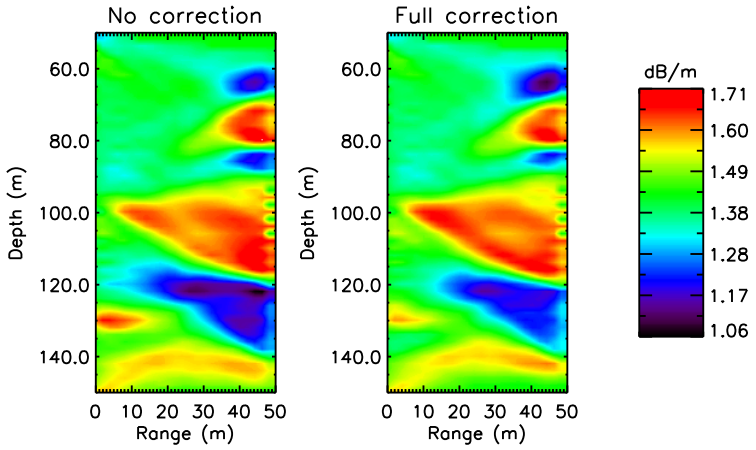

Figure 6.23: The tomographic image with no corrections on the left and with both corrections applied on the right.

of antennas in a lossy environment show how the environment becomes part of the antenna for performance estimation purposes and therefore limits the correction that can be applied to antenna parameters. To take full advantage of the capabilities of the FDTD model, the model itself must be introduced into the RT inversion, replacing of the straight raypath model.

An antenna correction can be derived from FDTD modelling and applied to data as a first order correction for the behaviour of antennas in various rock types. The correction was applied to an example of field data but did not have a significant effect on the image in that case. A greater effect is expected when the electrical contrast between the host and the target rocks is greater.

7

Conclusions and recommendations

7.1 INTRODUCTION

Radio Tomography is a geophysical imaging technique that uses single frequency HF radio waves to determine the attenuation of the rock between two boreholes. By conducting measurements between many different transmitter and receiver positions it is possible to build up an image of the attenuation between the boreholes. Attenuation corresponds to rock conductivity and hence to geology.

One of the most important problems in RT imaging is the conversion from measured signal strength to attenuation. If the inversion used for RT data includes the antenna as part of its forward model, then no explicit conversion is required. If the straight raypath approximation is used as the forward model, measured data must be converted to attenuation before inversion. The conversion depends on accurate figures for the gain and impedance of the antenna as a function of the surrounding rock type. This thesis describes the development, testing and application of a numerical model that can be used to determine the performance of RT antennas in rock.

7.2 NUMERICAL MODELS

Rock is often modelled in the literature by assuming a constant loss tangent as a function of frequency across the HF band. The assump-

tion is tested by examining the electrical properties of 2151 rock samples and it is found to be a good first approximation. The constant loss tangent model leads to an equation to estimate the resolution that can be achieved by an RT system over a given range in a given rock type. The equation shows that resolution is a proportion of borehole spacing. Resolution decreases with increasing loss tangent until it reaches a lower limit beyond which there is no further decrease in resolution.

The antenna model developed in this thesis is based on the FDTD technique. It has been implemented assuming rotational symmetry and models only the TM mode. The model is terminated using second order Higdon absorbing boundaries. The electric field across the antenna feed point is directly driven.

The constant loss tangent model of rock properties is difficult to incorporate into a FDTD antenna model. For more accurate numerical modelling, a Debye equation is fitted to individual rock sample measurements. Modelling can be extended across an arbitrarily large bandwidth by increasing the number of Debye relaxation times.

To efficiently model insulated RT antennas, published thin-wire and thin-layer subcell extensions to the FDTD technique have been combined in a novel thin-wire, thin-layer subcell extension. The subcell extension allows both the insulation layer and the surrounding rock to be modelled as Debye materials. The novel subcell extension greatly reduces the size of the model required to accurately characterize an electric dipole antenna with a thin insulating layer.

The code has been verified using a variety of numerical comparisons, and has also been compared against a physical scale model. In every case, the results from the FDTD model are in good agreement with alternative numerical codes or approaches and with the physical model.

The combination of the Debye model for material properties with the thin-wire, thin-layer subcell extension provides a useful tool for modelling both RT antennas and propagation. A realistic antenna in a realistic RT environment can be modelled across a broad frequency band in less than twenty minutes on a 750 MHz Pentium computer. Modelling time does not increase if the rock geometry becomes more

complex, or if another antenna is introduced. Broad band results are particularly useful because frequency is the easiest variable for an RT operator to change.

7.3 ANTENNAS IN ROCK

Input impedance, gain and directivity of an antenna can all be extracted from the FDTD model. Gain and directivity measure how efficiently the antenna couples energy into the rock. High gain is desirable to maximize the range that can be achieved in a given rock type. The antenna impedance controls how efficiently energy it transferred between the antenna and surrounding electronics. Without a matching network, a wholly real impedance of tens of ohms is desirable as the best compromise between high voltages and high currents in the transmitter output stage. A low real impedance will also have the best noise performance in the receiver.

Gain is a simple function of electrical length for all the antennas modelled. An acceptable gain of close to unity is achieved when the electric dipole antenna is electrically half a wavelength long. If the antenna is bare, its electrical length is determined by the wavelength in the surrounding rock and changes as the rock changes along the borehole. If the antenna is sufficiently well insulated its electrical length is entirely determined by the characteristics of the insulation and becomes independent of the surrounding rock.

In a bare antenna, antenna impedance varies as a function of the surrounding rock. The antenna can be considered to be broad band because it can be used at different frequencies to improve performance in different rocks. For any given frequency, overall performance in an RT survey will be a compromise: high gain in one rock type may have to be sacrificed in order to achieve penetration in another rock type. Changes in performance as a function of rock type can be accounted for in the RT inversion by modelling the antenna in each rock type using the FDTD code.

Electrically, the insulated antenna is perhaps a perfect RT antenna: its parameters are not affected by the surrounding rock. It is narrow band because there is no performance advantage to be gained

from operating the antenna at any frequency other than its design frequency.

The problems with the insulated antenna are mechanical and operational: it is difficult to manufacture because a thick layer of insulation limits the space available within the conductor for electronics; it is physically long, making it difficult to handle in the field; it requires longer boreholes; it reduces tomographic resolution slightly; if a different frequency is required the antenna must be changed.

A hybrid insulated/bare antenna solves some of the practical problems of an insulated antenna. Modelling results show that it is possible to design a practical antenna having bare end sections without losing the benefits of insulation. Hardware has been developed to test the hybrid antenna approach. Preliminary results indicate that the technique is viable.

7.4 ANTENNA CASE STUDIES

RT data acquisition could be considerably speeded up if there were more than one receive antenna in the receive borehole. The presence of a second antenna in the same borehole as the receive antenna will cause a change in received signal of less than 1 dB if the spacing between antennas is larger than the length of the antennas themselves. Much larger spacings may be necessary if more isolation is required.

Mechanically, it would be convenient to suspend an RT antenna on a wire rather than on an optical cable. The wire will not influence the antenna characteristics if a sufficient gap can be interposed between the antenna and the wire. The gap could be implemented in practice using ferrite beads. There is a danger in using wire suspension: it offers a route to guide radio waves around conductive obstacles. The guiding effect breaks the straight raypath approximation used in inversion leading to artifacts in the final image.

Real boreholes are usually filled with water. For narrow boreholes the water has a negligible effect on the antenna parameters. If the boreholes are greater than 200 mm in diameter, water can be considered as a lossy dielectric material, in the same way as rock. It is not analogous to insulation because of its high dielectric constant.

RT antennas can become unbalanced if there is mechanical failure of electrical contacts. The change in antenna performance is small at the design frequency but can be become larger at other frequencies. The input impedance offers a clear diagnostic: in the event of a break the input impedance becomes more capacitive. The designer of an RT antenna may be forced to used an unbalanced dipole for practical reasons. Performance is similar to a balanced dipole of the same length at the design frequency. The pattern is only slightly skewed. Both the real and imaginary parts of the antenna impedance are increased, which is undesirable.

7.5 ANTENNAS AND IMAGING

RT will not work where the rock is uniformly very conductive, as energy will not propagate from one borehole to another. Where smaller volumes of very conductive rock are interspersed within more resistive rock, RT may work, depending on the geometry of the situation. Where small volumes of conductive rock are close to, or surrounding, the antenna, it ceases to act as a simple antenna and becomes a compound structure, including the nearby conductive rock. The straight raypath approximation is violated.

Antenna parameters derived from the FDTD model can be substituted into the RT equation to correct field data for changes in antenna parameters as the rock surrounding the antennas changes. The rock immediately surrounding the borehole is known from drilling. The technique has been applied to a case study of a massive sulphide orebody hosted in diabase, quartzite and granite. The calculated RT correction coefficients have a variation of more than 20 dB between different rock types. In the case study, applying the corrections did not alter the RT image significantly. It is not known whether the result is general to all RT applications.

7.6 RECOMMENDATIONS FOR FURTHER WORK

1 The numerical model developed here is only quasi-3D: it delivers a 3D solution using a 2D model for the specific case of rotational sym-

metry. For problems with a more general geometry, the model has to be extended to 3D. The main area of research that will be necessary is the implementation of an efficient thin-wire thin-layer subcell extension in 3D. Two specific problem requiring 3D modelling are the effect of out of plane conductors on the RT image and the effect of asymmetrical conducting bodies on the antenna performance.

2 It is not clear from the single case study whether an RT inversion can be improved by incorporating a model of the antenna performance as a function of rock type. Further work is necessary to determine whether antenna corrections can improve the quality of RT images. It is possible that alternative approaches to improved image quality, including different inversion techniques, may offer greater benefits.

3 Application of the FDTD to several problems has shown that the straight raypath approximation used in the forward model of the tomographic inversion can be violated. In environments that contain rocks with contrasting conductivity, the geometry of the conductive rocks plays an important part in how the energy propagates from one borehole to the other. If there is a wire in the borehole above the antenna, that wire can act as a guide for radio waves.

One way to account for the interrelationship between the antenna and the structure of the rock around it is to incorporate the antenna model into the inversion. The FDTD code can be used as the forward model in preference to a straight raypath model. The concept will become particularly attractive as computing power becomes ever more affordable and forward models can be run in seconds rather than minutes or hours.

4 Although data has been obtained using hardware developed from the modelling results, there is still considerable scope for improvement in the probe design. Mechanical improvements are necessary to make the probes more reliable. Electrically, the performance of a completely insulated antenna should be confirmed in a borehole.

5 There is also scope for developing a methodology for survey design using results obtained in this thesis. The methodology should guide an operator in antenna selection and frequency selection. The numerical model provides an excellent tool for testing a survey design before attempting to apply it in the field.

A

Derivation of update equations

In this appendix, the complete derivation of the update equations for the basic BOR FDTD algorithm are presented. The equations contain elements from a variety of sources and the derivations are presented here as a single reference.

A.1 THE E_z PATCH

Given *Ampère's Law*

$$\oint_C \boldsymbol{H} \cdot \mathrm{d}\boldsymbol{l} = \int\int_S \sigma \boldsymbol{E} \cdot \mathrm{d}\boldsymbol{S} + \frac{\partial}{\partial t} \int\int_S \sigma \boldsymbol{D} \cdot \mathrm{d}\boldsymbol{S}, \tag{A.1}$$

and integrating around the $\boldsymbol{E}_z$ patch illustrated in Figure A.1, we get

$$\begin{aligned} \frac{\partial}{\partial t} \int_{\phi_1}^{\phi_2} \int_{r_1}^{r_2} \boldsymbol{D}_z r \, \mathrm{d}r \, \mathrm{d}\phi \quad &+ \quad \sigma \int_{\phi_1}^{\phi_2} \int_{r_1}^{r_2} \boldsymbol{E}_z r \, \mathrm{d}r \, \mathrm{d}\phi \\ &= \int_{r_1}^{r_2} \boldsymbol{H}_r \, \mathrm{d}r + \int_{\phi_1}^{\phi_2} \boldsymbol{H}_\phi \, r \, \mathrm{d}\phi \\ &+ \int_{r_2}^{r_1} \boldsymbol{H}_r \, \mathrm{d}r + \int_{\phi_2}^{\phi_1} \boldsymbol{H}_\phi \, r \, \mathrm{d}\phi. \end{aligned} \tag{A.2}$$

Evaluating the integrals gives:

$$\begin{aligned} \frac{1}{2}\left(r_2^2 - r_1^2\right) \triangle\phi \, (\boldsymbol{D} + \sigma \boldsymbol{E}_z) = \triangle r \boldsymbol{H}_r(\phi_2) + r_2 \triangle\phi \boldsymbol{H}_\phi(r_2) \\ - \triangle r \boldsymbol{H}_r(\phi_1) - r_1 \triangle\phi \boldsymbol{H}_\phi(r_1) \end{aligned} \tag{A.3}$$

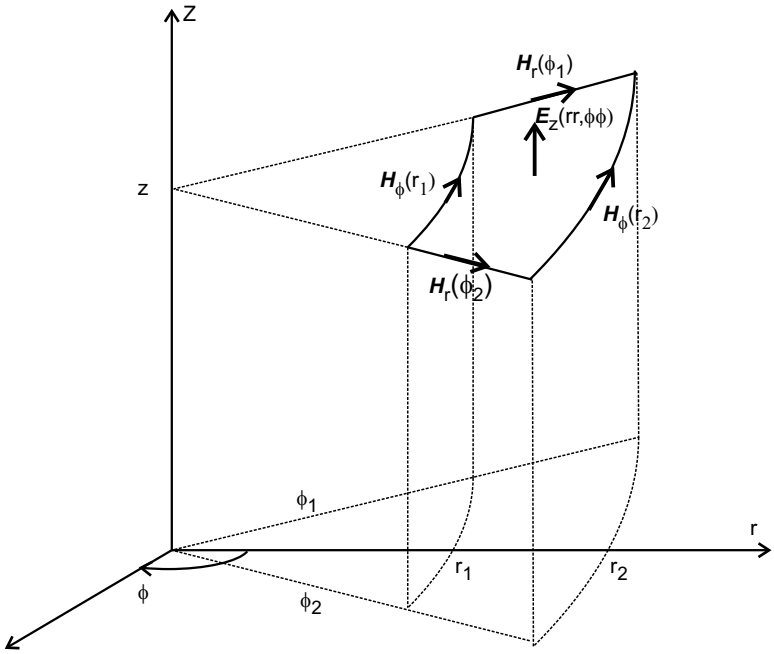

Figure A.1: The $\boldsymbol{E}_z$ patch.

Because there is no dependence on ϕ, $\boldsymbol{H}_r(\phi_2) = \boldsymbol{H}_r(\phi_1)$. Remember that $\boldsymbol{D} = \varepsilon_\infty \boldsymbol{E} + \boldsymbol{P}$. Then

$$\varepsilon_\infty \frac{\partial}{\partial t}\boldsymbol{E}_z + \frac{\partial}{\partial t}\boldsymbol{P}_z + \sigma \boldsymbol{E}_z = \frac{2}{r_2^2 - r_1^2}\left[r_2 \boldsymbol{H}_\phi(r_2) - r_1 \boldsymbol{H}_\phi(r_1)\right]. \tag{A.4}$$

But from Equation 4.24, $\boldsymbol{P} = \sum \boldsymbol{P}_i$, so

$$\frac{\partial \boldsymbol{P}}{\partial t} = \sum_{i=1}^{n} \frac{\partial \boldsymbol{P}_i}{\partial t} \tag{A.5}$$

Substituting in Equation A.4 and expanding the time derivatives of $\boldsymbol{P}_{zi}$,

$$\begin{aligned} \varepsilon_\infty \frac{\partial}{\partial t}\boldsymbol{E}_z + \sum_{i=1}^{n} \frac{1}{\tau_i}\left[\varepsilon_{wi}\boldsymbol{E}_z - \boldsymbol{P}_{zi}\right] + \sigma \boldsymbol{E}_z = \\ \frac{2}{r_2^2 - r_1^2}\left[r_2 \boldsymbol{H}_\phi(r_2) - r_1 \boldsymbol{H}_\phi(r_1)\right]. \end{aligned} \tag{A.6}$$

and rearranging gives

$$\left[\sum_{i=1}^{n}\frac{\varepsilon_{wi}}{\tau_i}+\sigma\right]\boldsymbol{E}_z+\varepsilon_\infty\frac{\partial}{\partial t}\boldsymbol{E}_z = \sum_{i=1}^{n}\frac{1}{\tau_i}\boldsymbol{P}_{zi} + \frac{2}{(r_1+\triangle r)^2-r_1^2}\left[r_2\boldsymbol{H}_\phi(r_2)-r_1\boldsymbol{H}_\phi(r_1)\right]. \tag{A.7}$$

The differential equation can now be discretized,

$$\frac{\boldsymbol{E}|_{rr,j}^{n+1}-\boldsymbol{E}|_{rr,j}^{n}}{\triangle t}+\frac{\boldsymbol{E}|_{rr,j}^{n+1}+\boldsymbol{E}|_{rr,j}^{n}}{2}\frac{1}{\varepsilon_\infty}\left[\sum_{i=1}^{n}\frac{\varepsilon_{wi}}{\tau_i}+\sigma\right] = \frac{1}{\varepsilon_\infty}\sum_{i=1}^{n}\frac{1}{\tau_i}\boldsymbol{P}_{zi} + \frac{2}{\varepsilon_\infty\triangle r(2r_1+\triangle r)}\left[r_2\boldsymbol{H}_\phi(r_2)-r_1\boldsymbol{H}_\phi(r_1)\right]. \tag{A.8}$$

If Equation A.8 is rearranged, then for the chosen grid, $r_1=\triangle r(i-0.5)$ and $r_2=\triangle r(i+0.5)$

$$\begin{aligned}\boldsymbol{E}_z|_{rr,z}^{n+1}&\left[2\varepsilon_\infty+\triangle t\sum_{i=0}^{n}\frac{\varepsilon_{wi}}{\tau_i}+\sigma\triangle t\right]\\ &=\boldsymbol{E}_z|_{rr,z}^{n}\left[2\varepsilon_\infty-\triangle t\sum_{i=0}^{n}\frac{\varepsilon_{wi}}{\tau_i}-\sigma\triangle t\right]\\ &+2\triangle t\sum_{i=1}^{n}\frac{1}{\tau_i}\boldsymbol{P}_z\\ &+\frac{4\triangle t}{\triangle r2(r_1+\triangle r/2)}\left[r_2\boldsymbol{H}_\phi(r_2)-r_1\boldsymbol{H}_\phi(r_1)\right].\end{aligned} \tag{A.9}$$

The update equation for $\boldsymbol{E}_z$ is

$$\begin{aligned}\boldsymbol{E}_z\big|_{rr,z}^{n+1}&=c_1\boldsymbol{E}_z\big|_{rr,z}^{n}\\ &+\sum_{i=1}^{n}c_{2i}\boldsymbol{P}_{zi}\big|_{i,j+0.5}^{n+0.5}\\ &+c_3\left[\frac{i+0.5}{i}\boldsymbol{H}_\phi\big|_{i+0.5,j+0.5}^{n+0.5}-\frac{i-0.5}{i}\boldsymbol{H}_\phi\big|_{i-1/2,j+1/2}^{n+0.5}\right]\end{aligned} \tag{A.10}$$

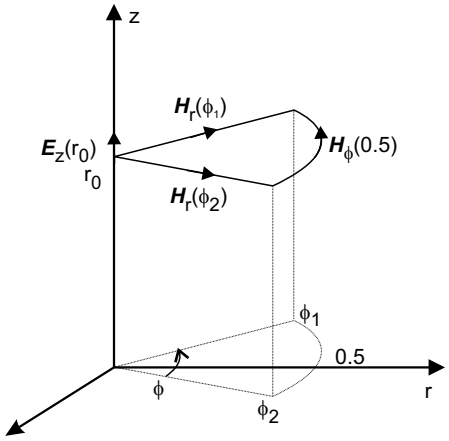

Figure A.2: The $\boldsymbol{E}_z$ patch on the axis.

where

$$c_1 = \frac{2\varepsilon_\infty - \triangle t \sum_{i=0}^{n} \frac{\varepsilon_{wi}}{\tau_i} - \sigma \triangle t}{2\varepsilon_\infty + \triangle t \sum_{i=0}^{n} \frac{\varepsilon_{wi}}{\tau_i} + \sigma \triangle t}, \tag{A.11}$$

$$c_{2i} = \frac{2\triangle t/\tau_i}{2\varepsilon_\infty + \triangle t \sum_{i=0}^{n} \frac{\varepsilon_{wi}}{\tau_i} + \sigma \triangle t}, \tag{A.12}$$

$$c_3 = \frac{2\triangle t/\triangle r}{2\varepsilon_\infty + \triangle t \sum_{i=0}^{n} \frac{\varepsilon_{wi}}{\tau_i} + \sigma \triangle t}. \tag{A.13}$$

A.2 THE $\boldsymbol{E}_z$ PATCH ON THE AXIS

From the definition of the coordinate system the only component that occurs on the axis is $\boldsymbol{E}_z$. The geometry necessary to determine the update equation for $\boldsymbol{E}_z$ is shown in Figure A.2. Only the previous value of $\boldsymbol{E}_z$ and the value of $\boldsymbol{H}_\phi$ in the cell adjacent to the axis are necessary to calculate the present value of $\boldsymbol{E}_z$. From Ampère's Law,

equation Equation A.1,

$$\begin{aligned}\frac{\partial}{\partial t}\int_{\phi_1}^{\phi_2}\int_{r_1}^{r_2}\boldsymbol{D}_z r\,\mathrm{d}r\,\mathrm{d}\phi \;&+\; \sigma\int_{\phi_1}^{\phi_2}\int_{r_1}^{r_2}\boldsymbol{E}_z r\,\mathrm{d}r\,\mathrm{d}\phi \\ &= \int_0^{r_0}\boldsymbol{H}_r(\phi_1)\,\mathrm{d}r+\int_{r_0}^{0}\boldsymbol{H}_r(\phi_2)\,\mathrm{d}r \\ &+ \int_{\phi_1}^{\phi_2}\boldsymbol{H}_\phi\, r\,\mathrm{d}\phi. \qquad (A.14)\end{aligned}$$

Evaluating the integrals gives

$$\frac{r_0^2}{2}\triangle\phi\left[\sigma\boldsymbol{E}_z+\frac{\partial}{\partial t}\boldsymbol{D}_z\right]=r_0\triangle\phi\boldsymbol{H}_\phi. \qquad (A.15)$$

Once again, because $\boldsymbol{D}=\varepsilon_\infty\boldsymbol{E}+\boldsymbol{P}$ and $\boldsymbol{P}=\sum\boldsymbol{P}_i$,

$$\frac{r_0}{2}\left[\sigma\boldsymbol{E}_z+\varepsilon_\infty\frac{\partial}{\partial t}\boldsymbol{E}_z+\sum_{i=1}^{n}\frac{\partial}{\partial t}\boldsymbol{P}_{zi}\right]=\boldsymbol{H}_\phi. \qquad (A.16)$$

Expanding the derivative of $\boldsymbol{P}_z$ using Equation 4.19 yields

$$\frac{r_0}{2}\left[\sigma\boldsymbol{E}_z+\varepsilon_\infty\frac{\partial}{\partial t}\boldsymbol{E}_z+\sum_{i=1}^{n}\frac{1}{\tau_i}\left[\varepsilon_{wi}\boldsymbol{E}_z-\boldsymbol{P}_{zi}\right]\right]=\boldsymbol{H}_\phi. \qquad (A.17)$$

Regrouping gives

$$\left[\sigma+\sum_{i=1}^{n}\frac{\varepsilon_{wi}}{\tau_i}\right]\boldsymbol{E}_z+\varepsilon_\infty\frac{\partial}{\partial t}\boldsymbol{E}_z=\sum_{i=1}^{n}\frac{1}{\tau_i}\boldsymbol{P}_{zi}+\frac{2}{r_0}\boldsymbol{H}_\phi. \qquad (A.18)$$

Note that $r_0=\triangle r/2$. If Equation A.18 is rearranged in difference form,

$$\begin{aligned}\left[2\varepsilon_\infty+\triangle t\sum_{i=0}^{n}\frac{\varepsilon_{wi}}{\tau_i}+\sigma\triangle t\right]\boldsymbol{E}_z\Big|_{0,j}^{n+1} \\ = \left[2\varepsilon_\infty-\triangle t\sum_{i=0}^{n}\frac{\varepsilon_{wi}}{\tau_i}-\sigma\triangle t\right]\boldsymbol{E}_z\Big|_{0,j}^{n} \qquad (A.19)\\ +2\triangle t\sum_{i=0}^{n}\frac{1}{\tau_i}\boldsymbol{P}_i\Big|_{n+1/2}^{0,j}+\frac{8\triangle t}{\triangle r}\boldsymbol{H}_\phi\Big|_{n+1/2}^{1/2,j}\end{aligned}$$

then the update equation for $\boldsymbol{E}_z$ on the axis is

$$\begin{aligned}\boldsymbol{E}_z\Big|_{n+1}^{0,j+1/2} &= c_1\boldsymbol{E}_z\Big|_{n+1}^{0,j+1/2} \\ &+\sum_{i=1}^{n}c_{2i}\boldsymbol{P}_{zi}\Big|_{n+1/2}^{0,j+1/2}+c_5\boldsymbol{H}_\phi\Big|_{n+1/2}^{1/2,j+1/2}\end{aligned} \qquad (A.20)$$

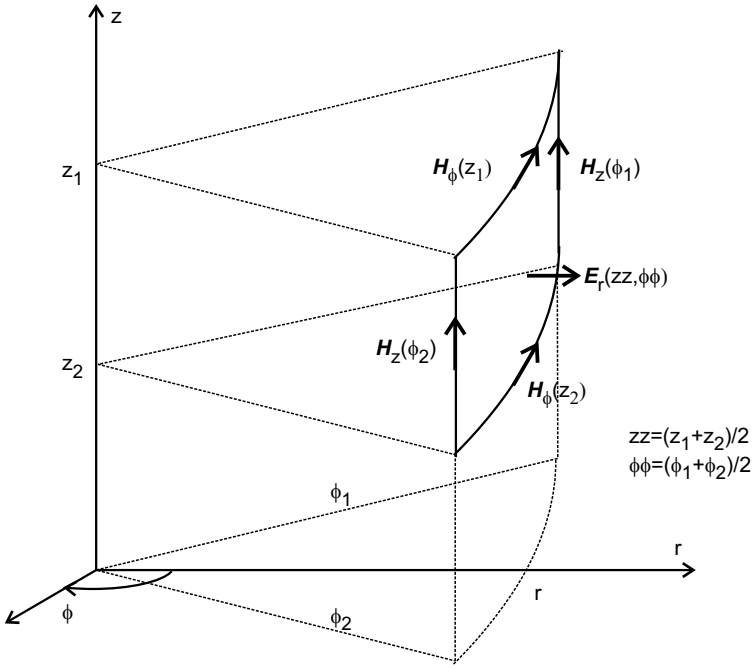

Figure A.3: The $\boldsymbol{E}_r$ patch.

where c_1 and c_{2i} are defined as above in equations Equation A.11 and Equation A.12 and c_5 is

$$c_5 = \frac{8\triangle t/\triangle r}{2\varepsilon_\infty - \triangle t \sum_{i=0}^{n} \frac{\varepsilon_{wi}}{\tau_i} - \sigma\triangle t}. \tag{A.21}$$

A.3 THE $\boldsymbol{E}_r$ PATCH

Using Ampère's law, equation Equation A.1, around the patch shown in Figure A.3 gives

$$\begin{aligned}\int_{\phi_1}^{\phi_2}\int_{r_1}^{r_2}[\frac{\partial}{\partial t}\boldsymbol{D}_r + \sigma\boldsymbol{E}_r].r\ \mathrm{d}\phi\,\mathrm{d}z \quad &= \int_{z_1}^{z_2}\boldsymbol{H}_z\,\mathrm{d}z + \int_{\phi_1}^{\phi_2}\boldsymbol{H}_\phi r\,\mathrm{d}\phi \\ &+ \int_{z_2}^{z_1}\boldsymbol{H}_z\,\mathrm{d}z + \int_{\phi_2}^{\phi_1}\boldsymbol{H}_\phi r\,\mathrm{d}\phi \end{aligned} \tag{A.22}$$

Evaluating the integrals and simplifying gives

$$r\triangle\phi\triangle z\left(\frac{\partial}{\partial t}\boldsymbol{D}_r + \sigma\boldsymbol{E}_r\right) = r\triangle\phi\left(\boldsymbol{H}_\phi(z_2) - \boldsymbol{H}_\phi(z_1)\right). \tag{A.23}$$

Because $\boldsymbol{D}_r = \varepsilon_\infty \boldsymbol{E}_r + \boldsymbol{P}_r$ and $\boldsymbol{P}_r = \sum \boldsymbol{P}_{ri}$

$$\varepsilon_\infty \frac{\partial}{\partial t}\boldsymbol{E}_r + \sum_{i=1}^{n} \frac{\partial}{\partial t}\boldsymbol{P}_{ri} + \sigma \boldsymbol{E}_r = \frac{1}{\triangle z}\left(\boldsymbol{H}_\phi(z_2) - \boldsymbol{H}_\phi(z_1)\right). \quad \text{(A.24)}$$

The time derivative of $\boldsymbol{P}_{ri}$ can be expanded, giving

$$\begin{aligned} \sigma \boldsymbol{E}_r + \varepsilon_\infty \frac{\partial}{\partial t}\boldsymbol{E}_r &+ \sum_{i=1}^{n} \frac{1}{\tau_i}\left[\varepsilon_{wi}\boldsymbol{E}_r - \boldsymbol{P}_{ri}\right] \\ &= \frac{1}{\triangle z}\left(\boldsymbol{H}_\phi(z_2) - \boldsymbol{H}_\phi(z_1)\right). \quad \text{(A.25)} \end{aligned}$$

Rearranging gives

$$\begin{aligned} \varepsilon_\infty \frac{\partial}{\partial t}\boldsymbol{E}_r &+ \left[\sigma + \sum_{i=1}^{n} \frac{\varepsilon_{wi}}{\tau_i}\right]\boldsymbol{E}_r \\ &= \sum_{i=1}^{n} \frac{1}{\tau_i}\boldsymbol{P}_{ri} + \frac{1}{\triangle z}\left(\boldsymbol{H}_\phi(z_2) - \right. \quad \text{(A.26)} \\ &\quad \left. - \boldsymbol{H}_\phi(z_1)\right) \quad \text{(A.27)} \end{aligned}$$

The differential equation can now be discretized, using central differencing, for the position shown in Figure A.3:

$$\begin{aligned} \frac{\boldsymbol{E}_r\big|_{i+1/2,j}^{n+1} - \boldsymbol{E}_r\big|_{i+1/2,j}^{n}}{\triangle t} &+ \frac{1}{\varepsilon_\infty}\left[\sigma + \sum_{i=1}^{n} \frac{\varepsilon_{wi}}{\tau_i}\right] \frac{\boldsymbol{E}_r\big|_{i+1/2,j}^{n+1} + \boldsymbol{E}_r\big|_{i+1/2,j}^{n}}{2} \\ &= \sum_{i=1}^{n} \frac{1}{\tau_i}\boldsymbol{P}\big|_{i+1/2,j}^{n+1/2} \\ &+ \frac{1}{\triangle z}\left(\boldsymbol{H}_\phi\big|_{i+1/2,j+1/2}^{n+1/2}\right. \\ &\quad \left. - \boldsymbol{H}_\phi\big|_{i+1/2,j-1/2}^{n+1/2}\right) \quad \text{(A.28)} \end{aligned}$$

which leads to an update equation for $\boldsymbol{E}_r$:

$$\begin{aligned} \boldsymbol{E}_r\big|_{i,j+1/2}^{n+1} &= c_1 \boldsymbol{E}_r\big|_{i,j+1/2}^{n} \\ &+ \sum_{i=1}^{n} c_2 \boldsymbol{P}_{ri}\big|_{i,j+1/2}^{n+1/2} \\ &+ c_4\left(\boldsymbol{H}_\phi\big|_{i+1/2,j+1/2}^{n+1/2} - \boldsymbol{H}_\phi\big|_{i+1/2,j-1/2}^{n+1/2}\right) \quad \text{(A.29)} \end{aligned}$$

where c_1 and c_{2i} are as defined earlier and

$$c_4 = \frac{2\triangle t/\triangle z}{2\varepsilon_\infty + \triangle t \sum_{i=1}^{n} \frac{\varepsilon_{wi}}{\tau_i} + \sigma \triangle t}. \quad \text{(A.30)}$$

The polarization vector components $\boldsymbol{P}_{ri}$ are updated in exactly the same way as the components $\boldsymbol{P}_{zi}$ presented earlier.

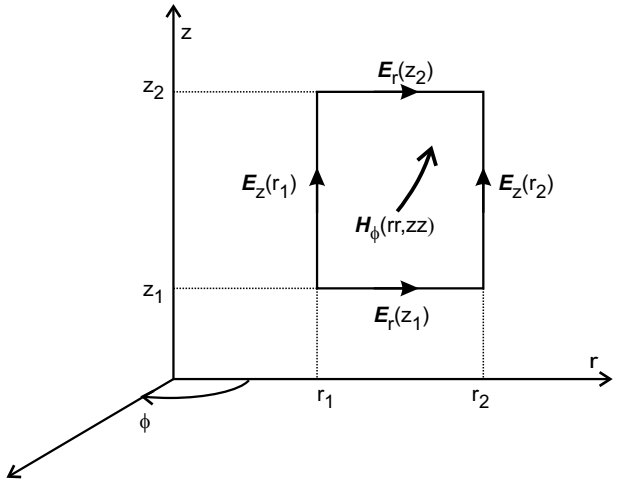

Figure A.4: The $\boldsymbol{H}_\phi$ patch.

A.4 THE $\boldsymbol{H}_\phi$ PATCH

The update equations for $\boldsymbol{H}_\phi$ are derived using Faraday's law,

$$\oint_C \boldsymbol{E} \cdot \mathrm{d}\boldsymbol{l} = -\frac{\partial}{\partial t} \iint_S \boldsymbol{B} \cdot \mathrm{d}\boldsymbol{S} \tag{A.31}$$

Faraday's law is applied on the patch shown in Figure A.4. The derivation is simpler than that for the E-field update equations, because the permeability is assumed to be constant, $\mu = \mu_0$, there are no losses and there is no frequency dependence.

$$\begin{aligned} -\frac{\partial}{\partial t} \int_{z_1}^{z_2} \int_{r_1}^{r_2} \boldsymbol{B}_\phi \,\mathrm{d}r\,\mathrm{d}z = & \int_{r_1}^{r_2} \boldsymbol{E}_r(z_2)\,\mathrm{d}r + \int_{z_2}^{z_1} \boldsymbol{E}_z(r_2)\,\mathrm{d}z \\ & + \int_{r_2}^{r_1} \boldsymbol{E}_r(z_1)\,\mathrm{d}r + \int_{z_1}^{z_2} \boldsymbol{E}_z(r_1)\,\mathrm{d}z \end{aligned} \tag{A.32}$$

If $\boldsymbol{B} = \mu_0 \boldsymbol{H}$ and all the fields are assumed constant along their respective edges and across the surface of the patch, then the integrals evaluate to

$$\begin{aligned} -\mu_0 \triangle r \triangle z \frac{\partial}{\partial t} \boldsymbol{H}_\phi &= \triangle r \left(\boldsymbol{E}_z(r_2) - \boldsymbol{E}_z(r_1) \right) \\ &+ \triangle r \left(\boldsymbol{E}_r(z_2) - \boldsymbol{E}_z(z_1) \right) \end{aligned} \tag{A.33}$$

which translates simply into the finite difference update equation,

$$\begin{aligned} \boldsymbol{H}_\phi\big|^{n+1/2}_{i+1/2,j+1/2} &= \boldsymbol{H}_\phi\big|^{n-1/2}_{i+1/2,j+1/2} \\ &+ m_1\left(\boldsymbol{E}_z\big|^{n}_{i+1,j+1/2} - \boldsymbol{E}_z\big|^{n}_{i,j+1/2}\right) \\ &- m_2\left(\boldsymbol{E}_r\big|^{n}_{i+1/2,j+1} - \boldsymbol{E}_r\big|^{n}_{i+1/2,j}\right) \end{aligned} \tag{A.34}$$

where

$$m_1 = \frac{\triangle t}{\mu_0 \triangle r}, \tag{A.35}$$

$$m_2 = \frac{\triangle t}{\mu_0 \triangle z}. \tag{A.36}$$

B

Rock properties

This appendix contains a catalogue of the electrical properties of the seven rock types used throughout this thesis. For each rock, a series of graphs are plotted showing the basic electrical property behaviour with frequency, from 1 MHz to 64 MHz. Superimposed on each graph is the response of a Debye material designed to replicate the electrical properties of the sample. Error bars are also plotted on the material properties graphs to indicate the uncertainty of measurements made with the HP4815A Vector Impedance Meter.

The seven rocks chosen from the Miningtek rock properties database have all been given single word titles, although the titles refer to considerably more complex geological names. The rocks are

1 Quartzite: The sample is an example of a high quality massive quartzite with very little contamination by other minerals, almost pure silica (SiO_2), with a low conductivity.

2 Granite: A coarse grained igneous intrusive rock consisting of quartz, feldspar and biotite mica.

3 Dolerite: A fine grained igneous intrusive rock of more mafic composition than the granite.

4 Peridotite: A coarse grained ultramafic rock with a low silica content. This particular sample has also undergone weathering and contains clay minerals.

5 Cassiterite: The sample contains cassiterite, a tin ore, hosted in chlorite. It is referred to in this thesis only by the name of its ore mineral.

6 Pyrite: The sample is a quartzite that contains over 25% of pyrite mineralization. Again, it is referred to only by the name of its ore mineral.

7 Sulphide: The sample is an example of massive sulphide mineralization and contains a variety of metallic sulphides, including those of copper, lead and zinc.

B.1 FITTING THE DEBYE MODEL

To model rocks using the FDTD technique, the rock electrical properties as a function of frequency must be approximated by a Debye model. The experimental rock property data at seven frequencies is fitted to Debye models with one or more relaxation times, using a genetic algorithm (GA) implemented in IDL. Fitting experimental data to a Debye model is difficult for a number of reasons: two parameters must be fitted, the permittivity and the conductivity; the Debye model is not an ideal model for rock electrical properties, but it is well suited to the FDTD method; and the Debye equation for conductivity is non-linear.

The GA avoids difficulties with the non-linear nature of the Debye equations by making no assumptions about the form of the function that it is fitting (Goldberg, 1989). It is also ideal for optimizing complex systems, including the design of antennas (Lee et al., 2000a).

The Debye equation requires $n_t = 2 + 2n$ terms to be fitted for n relaxation times. The GA starts with an initial population of a number of sets of random values for the n_t terms. For fitting the Debye equations a constant population size of 30 was used, although the number of terms to be fitted varied.

In GA nomenclature, each value to be fitted is a *string* and the whole set of strings that make up one Debye equation is a *structure*. The structure can be decoded to form a solution point. In this implementation of the GA as a decimal GA (Lee et al., 2000b), the decoding is a simple 1:1 mapping of strings to Debye equation parameters.

The GA is implemented using scaling: strings in the GA always have values between 0 and 1, which are scaled to represent the parameters of the Debye equation. Values for ε are restricted to lie

Table B.1: An example population with four strings.

No.	String	Fitness	% of Total
1	0.45	169	14.4
2	0.98	576	49.2
3	0.16	64	5.5
4	0.29	361	30.9
Total		1170	100.0

between 0.01 to 1000. The value for τ is limited to lie between 1.0^{-5} and 1.0^{-9} and is mapped to its string logarithmically.

A simple genetic algorithm (Goldberg, 1989) consists of three steps:

1 Reproduction,

2 Crossover,

3 Mutation.

Initially a population is created by filling a number of structures with random strings. In reproduction, each structure is evaluated by a fitness function. The fitness function used for fitting rock properties data is

$$\begin{aligned} F = & \sum_{i=1}^{7} \left(\frac{\varepsilon_{fi} - \varepsilon_{mi}}{\varepsilon_{mi}} \right)^2 \\ & + 100 \sum_{i=1}^{7} \left(\frac{\sigma_{fi} - \sigma_{mi}}{\sigma_{mi}} \right)^2 \\ & + \sum_{i=1}^{7} \left(\frac{\tan \delta_{fi} - \tan \delta_{mi}}{\tan \delta_{mi}} \right)^2 \end{aligned} \tag{B.1}$$

where ε_{mi} is the i'th measured value and ε_{fi} is the i'th fitted value. Seven measured and fitted values are compared for each rock sample, one for each frequency at which the sample is measured. The fitness is made up of three parameters: the permittivity, ε, the conductivity, σ and the loss tangent, $\tan \delta$. The factor of 100 in the conductivity term was empirically determined to provide the best overall fit of the three parameters.

Once the fitness of each member of the population is determined, a new population is created by copying the existing population ran-

domly, weighted by the fitness of each element. For example, consider a structure of one string and a population with four members, as shown in Table B.1. When creating the new population, the first entry has a 49.2% chance of being string 2, and a 5.5% chance of being string 3. The same is true for each other entry in the new population. Fitter members of the population come to dominate the new population selected for reproduction, but there is a chance that less fit members may survive.

The next stage is crossover: each string of each child is made up of a combination of the same string from each of its two parents. In the decimal GA crossover is a linear combination of the same string in each parent (Lee et al., 2000b).

The population chosen for reproduction is paired off at random and each pair of parents produces two children. If f_1 is the string to be fitted, then the new value of f_1 for the two children is created with

$$\begin{aligned} f_{1_{c1}} &= r f_{1_{p1}} + (1-r) f_{1_{p2}} \\ f_{1_{c2}} &= r f_{1_{p2}} + (1-r) f_{1_{p1}} \end{aligned} \tag{B.2}$$

where r is a random value between -0.5 and 1.5, and the subscipts $p1$, $p2$, $c1$ and $c2$ represent the two parents and two children, respectively. All strings have values between 0 and 1 and values are wrapped around. For example, if crossover leads to a string having a value of 1.1, then the value will be wrapped around to 0.1. Using a random value from -0.5 and 1.5 increases the range of the search and empirically performs better than a true GA which uses random values between 0 and 1.

Most of the new population are created by reproduction and crossover. However, the top 10% of the population is transferred directly into the new population, an elitist approach that guarantees that the fittest members of the population always survive.

A small proportion, 0.5%, of the new population are mutated, by randomly adding or subtracting a fraction, 10%, to one of the strings making up the member of the population.

The new population is then tested for fitness and subsequently undergoes reproduction, crossover and mutation. For fitting the RT Debye equations, the process continued until the fitness function varied by less than 0.02% in 10 generations, or until 1200 generations

Table B.2: Rock properties of all the chosen samples for a wavelength of 12 m.

Rock	Frequency (MHz)	Loss tangent	Attenuation (dB/m)
Quartzite	8.59	0.02	0.05
Granite	7.98	0.06	0.14
Dolerite	4.26	0.24	0.54
Peridotite	3.29	0.76	1.57
Cassiterite	1.33	9.48	4.10
Pyrite	0.53	31.6	4.40
Sulphide	0.13	262	4.53

had passed. The GA is run 8 times for each rock and the best result is selected.

The GA was used to fit models with 1 to 4 Debye relaxation times to the measured data and the model that fitted the data best was then chosen by hand. If a lower order model fitted the data nearly as well, it would be chosen in preference to a higher order model with a slightly better fit. The results for each rock are presented in the catalogue that follows.

B.2 SUMMARY OF PROPERTIES

In Table B.2 all the rocks are listed, together with the frequency at which the wavelength in the rock is 12 m. The loss tangent and attenuation at that frequency are also listed.

The attenuation rates of the three most conductive rocks for a wavelength of 12 m are all approximately equal, but occur at different frequencies. This supports the relationship plotted in Figure 2.12 in Chapter 2: for a given attenuation rate, the resolution becomes constant above a loss tangent of about 20-30. Table B.2 shows a constant loss for a constant wavelength, and hence a fixed relationship between attenuation and resolution.

B.3 INDIVIDUAL ROCKS

Over the next pages, the properties of each of the seven rocks are plotted. For each rock, the effective conductivity and permittivity are presented, together with four derived parameters. For each parameter, the measured value is plotted at each of seven frequencies, together with error bars. The error bars represent a rectangular distribution of error, derived from the error specification of the HP4815A Vector Impedance Meter given in Chapter 2. Where only one horizontal line is plotted, the error values have converged.

For each rock, a table presents the Debye model used to approximate that rock in all work in this thesis. The Debye model is also plotted on the electrical property graphs as a line.

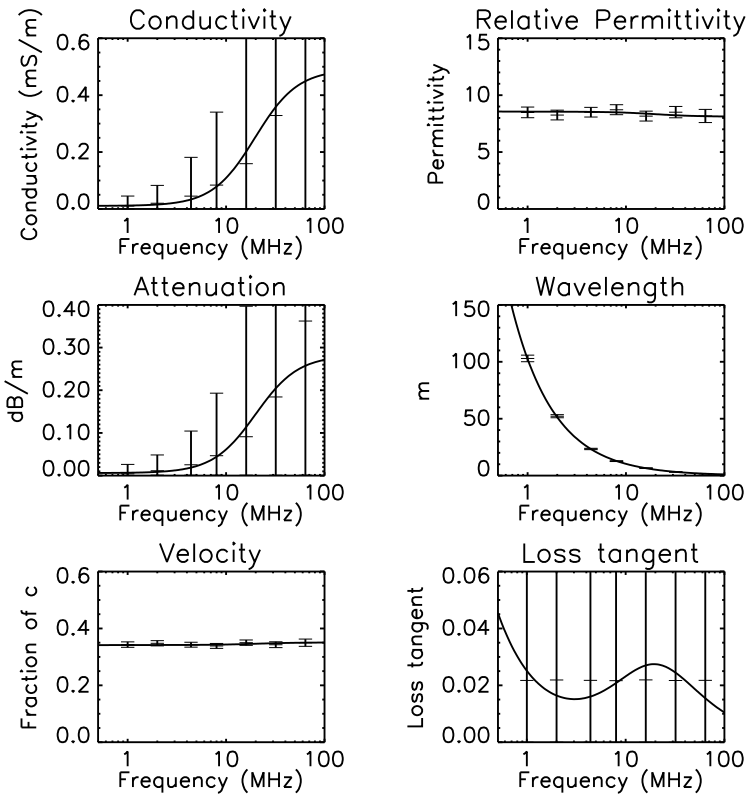

Figure B.1: Electrical properties of the quartzite sample.

Table B.3: The Debye model for quartzite.

$\sigma_0 =$	1.48×10^{-6}		
$\varepsilon_\infty =$	8.11		
$\varepsilon_{w1} =$	10.21	$\tau_1 =$	9.79×10^{-6}
$\varepsilon_{w2} =$	0.44	$\tau_2 =$	8.08×10^{-9}

B.3.1 Quartzite

This quartzite sample has almost the lowest conductivity or loss tangent of any sample in the Miningtek database. It is almost perfectly characterized by a constant loss tangent and is correspondingly difficult to fit to a Debye model with a small number of relaxation times. The poor fit here is considered acceptable because the very low loss tangent means that even poor loss tangent estimation is unlikely to affect model performance.

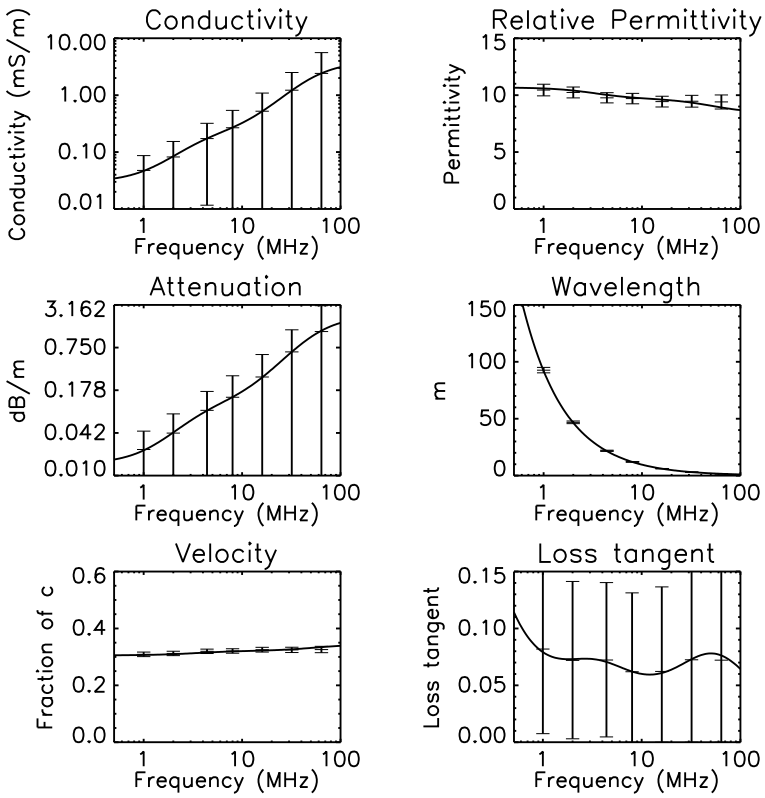

Figure B.2: Electrical properties of the granite sample.

Table B.4: The Debye model for granite.

$\sigma_0 =$	2.99×10^{-5}		
$\varepsilon_\infty =$	8.41		
$\varepsilon_{w1} =$	1.00	$\tau_1 =$	4.82×10^{-8}
$\varepsilon_{w2} =$	1.27	$\tau_2 =$	3.03×10^{-9}

B.3.2 Granite

The granite is highly resistive, so its resistivity is subject to high uncertainty.

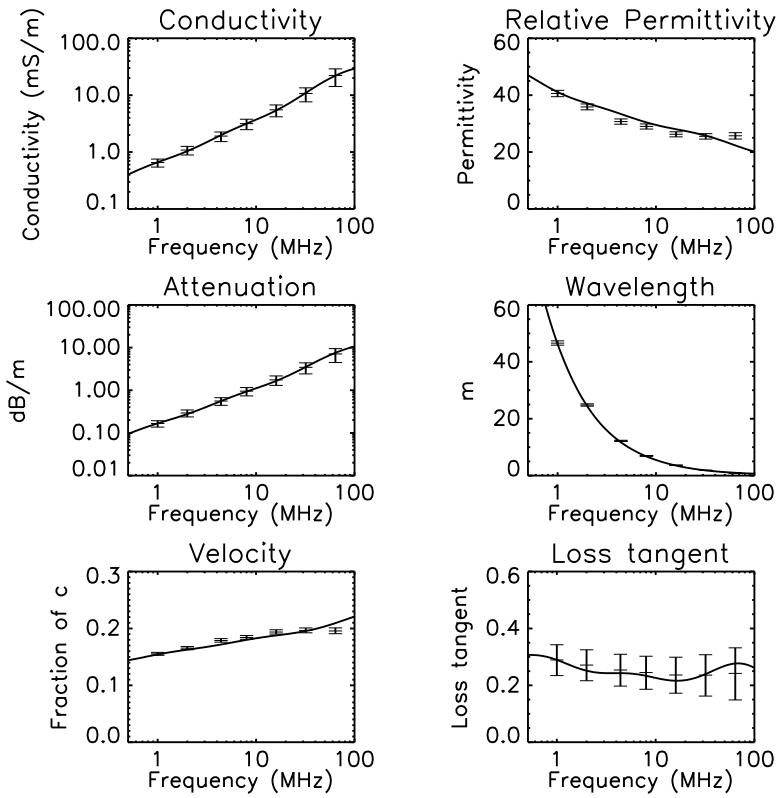

Figure B.3: Electrical properties of the dolerite sample.

Table B.5: The Debye model for the dolerite sample.

$\sigma_0 =$	1.17×10^{-4}	$\varepsilon_\infty =$	17.30
$\varepsilon_{w1} =$	16.53	$\tau_1 =$	2.65×10^{-7}
$\varepsilon_{w2} =$	3.77	$\tau_2 =$	9.18×10^{-7}
$\varepsilon_{w3} =$	9.13	$\tau_3 =$	3.07×10^{-8}
$\varepsilon_{w4} =$	10.52	$\tau_4 =$	2.62×10^{-9}

B.3.3 Dolerite

Dolerite is a good example of a lossy dielectric with a relatively high effective conductivity and loss tangent.

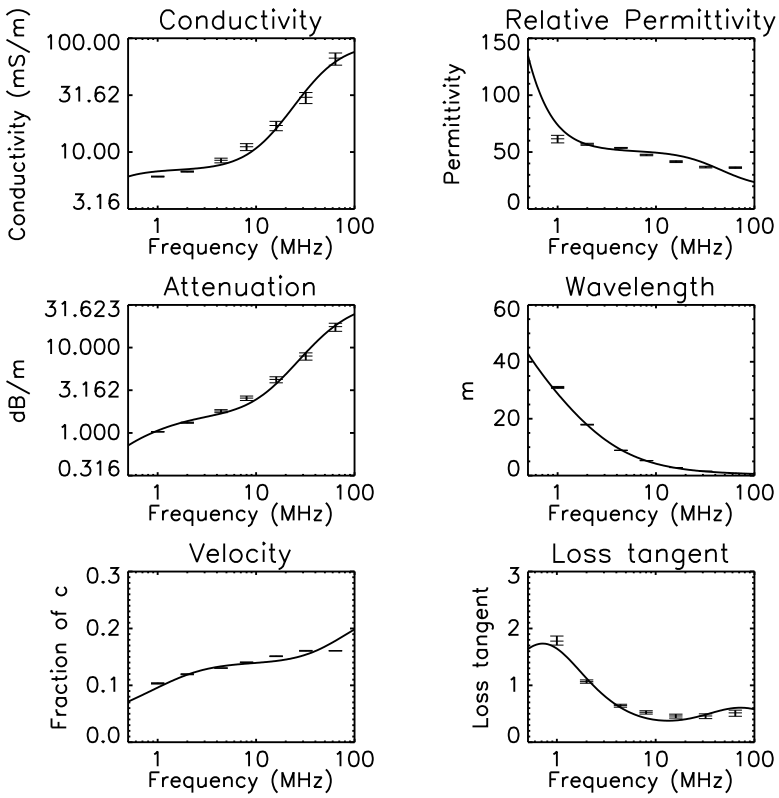

Figure B.4: Electrical properties of the peridotite sample.

Table B.6: The Debye model for the peridotite sample.

$\sigma_0 =$	3.74×10^{-9}		
$\varepsilon_\infty =$	17.93		
$\varepsilon_{w1} =$	653.5	$\tau_1 =$	8.29×10^{-7}
$\varepsilon_{w2} =$	32.84	$\tau_2 =$	3.50×10^{-9}

B.3.4 Peridotite

The peridotite is the first sample where the conductivity is dominated by DC conductivity, rather than effective conductivity caused by complex permittivity.

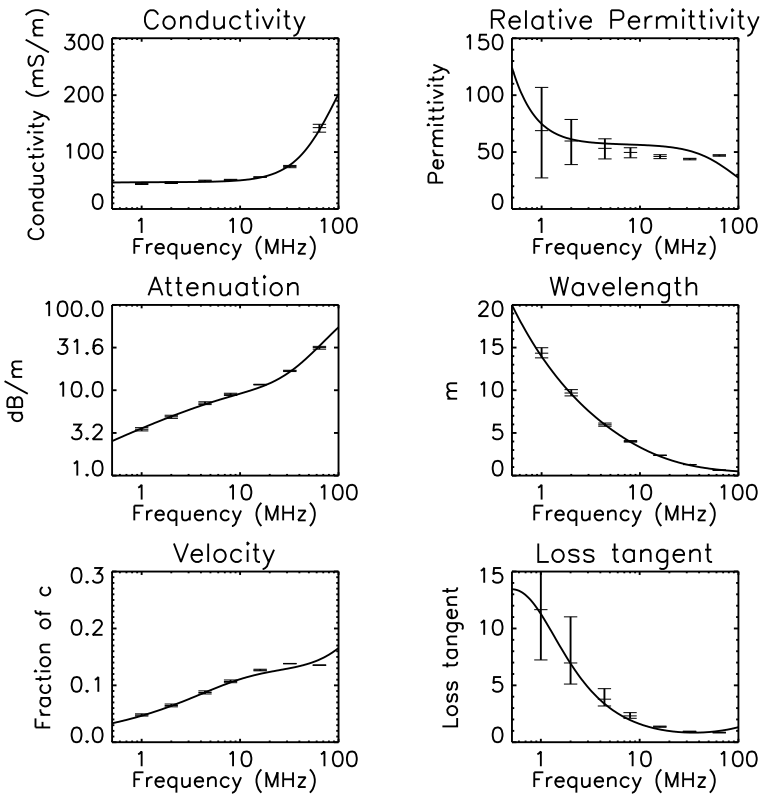

Figure B.5: Electrical properties of the cassiterite sample.

Table B.7: The Debye model for the cassiterite sample.

$\sigma_0 =$	0.041		
$\varepsilon_\infty =$	1.00		
$\varepsilon_{w1} =$	732.7	$\tau_1 =$	9.98×10^{-7}
$\varepsilon_{w2} =$	55.69	$\tau_2 =$	1.68×10^{-9}

B.3.5 Cassiterite

The electrical properties of the cassiterite sample are dominated by the high DC conductivity.

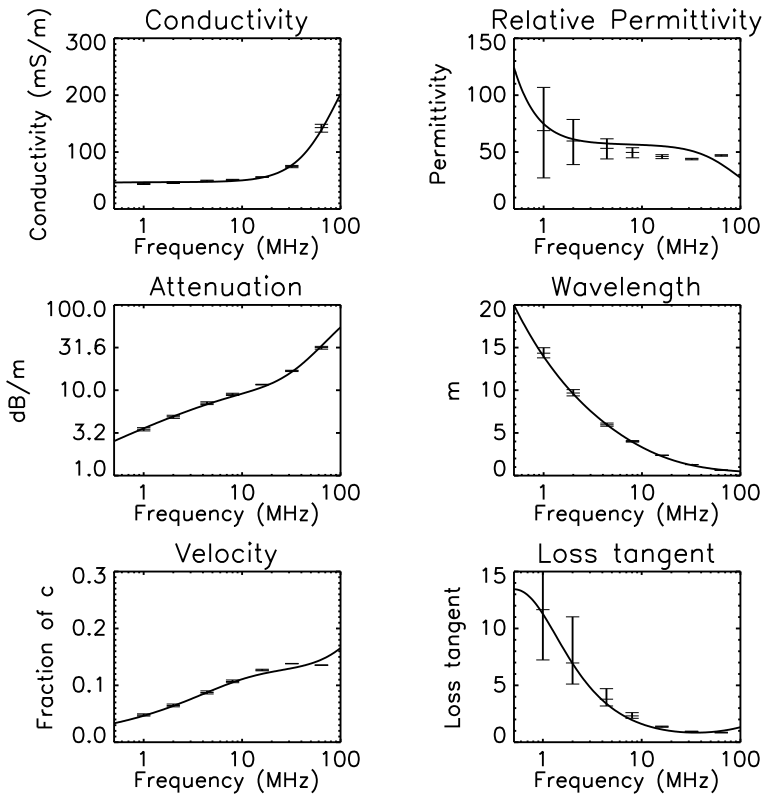

Figure B.6: Electrical properties of the sample containing pyrite mineralization.

Table B.8: The Debye model for the sample containing pyrite mineralization.

$\sigma_0 =$	0.117		
$\varepsilon_\infty =$	1.006		
$\varepsilon_{w1} =$	1284	$\tau_1 =$	9.99×10^{-7}
$\varepsilon_{w2} =$	28.95	$\tau_2 =$	2.38×10^{-9}

B.3.6 Pyrite

The pyrite sample is a good example of a rock dominated by its conductivity, but where complex permittivity comes affect the conductivity at high frequencies.

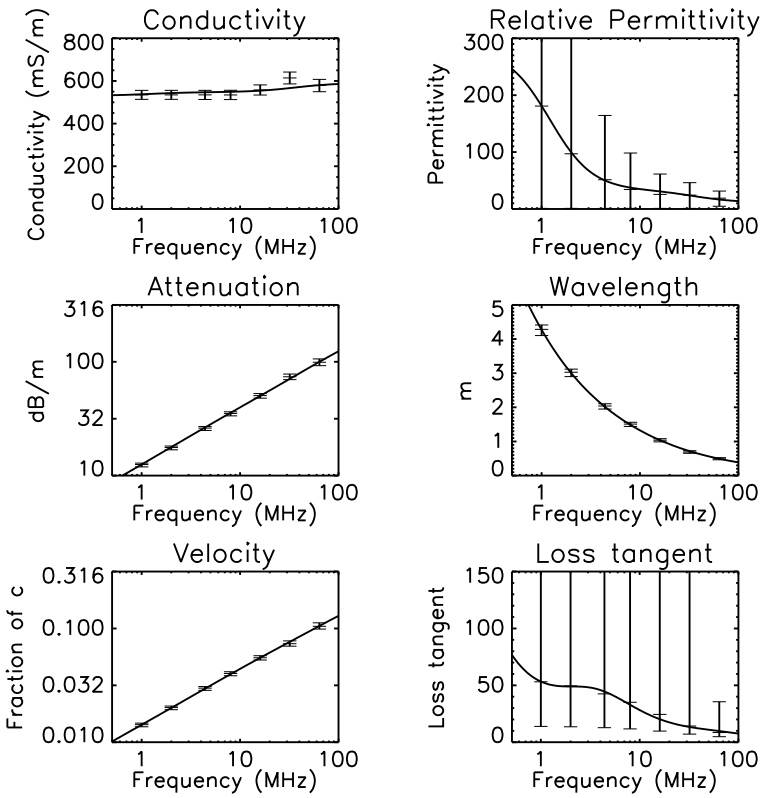

Figure B.7: Electrical properties of the sample containing massive sulphide mineralization.

Table B.9: The Debye model for the sample containing massive sulphide mineralization.

$\sigma_0 =$	0.531		
$\varepsilon_\infty =$	11.31		
$\varepsilon_{w1} =$	249.7	$\tau_1 =$	1.38×10^{-7}
$\varepsilon_{w2} =$	21.62	$\tau_2 =$	4.42×10^{-9}

B.3.7 Sulphide

The sulphide is an example of a very good conductor. Effective conductivity is high and remains roughly constant with frequency.

Symbols and nomenclature

NOMENCLATURE

$\boldsymbol{V}$	Vector V
$\boldsymbol{V}_x$	Component of vector V in the x direction
$\boldsymbol{V}_x\big\|_{i,j}^{n}$	x component of vector V evaluated at time $t = n\triangle t$ and position $r = i\triangle r$ and $z = j\triangle z$
r, z, ϕ	Components of cylindrical coordinate system
x, y, z	Components of Cartesian coordinate system
$\hat{c}$	Complex number
$\hat{c}^*$	Complex conjugate
c'	Real part of complex number
c''	Imaginary part of complex number
$\Re$	Real operator

SYMBOLS

α	angle of incidence in ABCs
α	fraction of transmitting velocity in Liao ABC
α	Attenuation constant in Np/m (8.686 Np = 1 dB)
α^*	Attenuation constant in dB/m
β	Wave number
$\triangle$	Cell size if $\triangle r = \triangle z$, m
ε	Permittivity or dielectric constant, F/m

ε_r	Permittivity relative to free space
ε_s	Permittivity of Debye medium as $\omega \to 0$
ε_{wi}	Weighted permittivity of Debye medium
ε_0	Permittivity of free space, 8.854×10^{-12} F/m
ε_∞	Permittivity of Debye medium as $\omega \to \infty$
ζ	Wave impedance, Ω
η	Efficiency, dimensionless
θ	Elevation angle
λ	Wavelength, m
μ	Permeability, H/m
μ_0	Permeability of free space, $4\pi \times 10^{-7}$ H/m
ρ	Resistivity, $= 1/\sigma$, Ω m
ρ'	Equivalent magnetic resistivity, Ω/m
σ	Conductivity, Si/m
τ	Relaxation time of a Debye medium, s
ϕ	Azimuth angle
χ	Electric susceptibility
ω	Rotational frequency, rad/s
a_{tot}	Total attenuation, dimensionless
c	Speed of light in free space, 3×10^8 m/s
c	Velocity of propagation in FDTD model, m/s
c_A	Artifical transmitting velocity, m/s
f	Frequency, Hz
f	String, in GA
h	Dipole antenna half length, m
i	Index of x or r direction
j	Index of y or z direction
j	$\sqrt{-1}$
k	Index of z or ϕ direction
k	Boltzman's constant, 1.38×10^{-23} J/K
k	Complex wavenumber $= \alpha + \mathrm{j}\beta$
m	Limit of i in r
n	Limit of j in z
n	Index of time
r	Distance along path in tomographic equation, m
r	Radius in cylindrical coordinate system, m

t	Time, s
$\tan\delta$	Loss tangent, dimensionless
A_e	Effective aperture, m^2
A_p	Antenna parameters in RT equation, dimensionless
B	Bandwidth, Hz
B_i	Bayliss-Turkel operator of order i
$\boldsymbol{B}$	Magnetic flux density, T
C	Capacitance, F
C_u	Conversion of units in RT equation, dimensionless
C_{Rx}	RT transmitter antenna coefficient, dimensionless
C_{Tx}	RT receiver antenna coefficient, dimensionless
C_n^m	Binomial coefficient
$\boldsymbol{D}$	Electric flux density, C/m^2
D	Directivity, dimensionless
$\boldsymbol{E}$	Electric field, V/m
G	Gain, dimensionless
$H_0^{(1)}$	Hankel function of first kind, order zero
$\boldsymbol{H}$	Magnetic field, A/m
I	Current, A
$\boldsymbol{J}$	Current density, A/m^2
K	Radiation intensity, W/sr
L	Differential equation operator
L_e	Effective length, m
$\boldsymbol{M}$	Magnetic polarization, A/m
$\boldsymbol{P}$	Electric polarization, C/m^2
P	Power, W
P_n	Noise power, W
R	Resistance, Ω
R	Range, m
Rx	Receiver
S	Spherical spreading in RT equation, dimensionless
T	Temperature, K
Tx	Transmitter
V	Voltage, V
W	Power density, W/m^2
X	Reactive impedance, Ω

Z	Complex impedance, $Z = R + \mathrm{j}X$

ABBREVIATIONS

ABC	Absorbing boundary condition
ADC	Analog to digital converter
ADE	Auxiliary differential equation
BOR	Body of revolution
CEM	Computational electromagnetics
COM	Complimentary operator method
CT	Computed tomography
DC	Direct current
EMC	Electromagnetic compatibility
FDTD	Finite-Difference Time-Domain
FWHM	Full wave, half maximum
FET	Field Effect Transistor
GA	Genetic algorithm
GPR	Ground penetrating radar
HF	High frequency (3–30 MHz)
IDL	Interactive Data Language
LO	Local oscillator
NEC	Numerical Electromagnetics Code
PC	Personal computer
PCB	Printed circuit board
PEC	Perfect electrical conductor
PTFE	Polytetrafluoroethylene (Teflon)
PML	Perfectly matched layer
PVC	Polyvinyl chloride
RF	Radio frequency
RIM	Radio imaging method
RT	Radio Tomography
SIRT	Simultaneous iterative reconstruction technique
TLM	Transmission line matrix
TE	Transverse electric
TM	Transverse magnetic
UHF	Ultra high frequency (300 MHz – 3 GHz)

References

Balanis, C. A. (1982). *Antenna Theory, Analysis and Design*. John Wiley and Sons, New York.

Balanis, C. A. (1989). *Advanced Engineering Electromagnetics*. John Wiley and Sons, New York.

Bérenger, J.-P. (1994). A perfectly matched layer for the absorption of electromagnetic waves. *Journal of Computational Physics*, 114:185–200.

Boonzaaier, J. J. and Pistorius, C. W. I. (1992). Radiation and scattering by thin wires with a dielectric coating - a Finite-Difference Time-Domain approach. *Microwave and Optical Technology Letters*, 5(6):288–291.

Boonzaaier, J. J. and Pistorius, C. W. I. (1994). Finite-Difference Time-Domain field approximations for thin wires with a lossy coating. *IEE Proceedings on Microwaves, Antennas and Propagation*, 141(2):107–113.

Bourgeois, J. M. and Smith, G. S. (1996). A fully three-dimensional simulation of a ground-penetrating radar: FDTD theory compared with experiment. *IEEE Transactions on Geoscience and Remote Sensing*, 34(1):36–44.

Burke, G. J., A., J. W., and K., M. E. (1983). Modeling of simple antennas near to and penetrating an interface. *Proceedings of the IEEE*, 71(1):174–175.

Burke, G. J. and Poggio, A. J. (1981). *Numerical Electromagnetics Code (NEC) – Method of Moments*. Lawrence Livermore Laboratory.

Buselli, G. (1980). Electrical geophysics in the USSR. *Geophysics*, 45:1551–1562.

Casey, J. P. and Bansal, R. (1986). The near field of an insulated dipole in a dissipative dielectric medium. *IEEE Transactions on Microwave Theory and Techniques*, 34:459–463.

Chen, Z. and Xu, J. (1997). The generalized TLM-based FDTD—Summary of recent progress. *IEEE Microwave and Guided Wave Letters*, 7(1):12–14.

Chew, W. C. and Weedon, W. H. (1994). A 3D perfectly matched medium from modified Maxwell's equations with stretched coordinates. *Microwave and Optical Technology Letters*, 7(13):599–604.

Christopoulos, C. (1995). *The Transmission–Line Modelling Method TLM*. IEEE, New York.

Cloude, S. R. (1996). *CEM: Computational electromagnetics*, chapter 1, pages 1.1–1.9. University of York.

Côte, P., Degauque, P., Lagabrielle, R., and Levent, N. (1995). Detection of underground cavities with monofrequency electromagnetic tomography between boreholes in the frequency range 100 MHz to 1 GHz. *Geophysical Prospecting*, 43:1083–1107.

Daly, W. (1984). Underground oil-shale retort monitoring using geotomography. *Geophysics*, 49(10):1701–1707.

Daniel, V. V. (1967). *Dielectric Relaxation*. Academic Press, London.

Debroux, P. S. (1996). 3D modelling of the electromagnetic response of geophysical targets using the FDTD method. *Geophysical Prospecting*, 44(3):457–468.

Debye, P. (1929). *Polar Molecules*. The Chemical Catalog Company, Dover Publications edition.

Degauque, P., Côte, P., and Lagabrielle, R. (1992). Monofrequency electromagnetic tomography. In *Proceedings of the 54th Meeting of the European Association of Exploration Geophysicists*. Paris, France.

Douglas, M., Okoniewski, M., and Stuchly, M. A. (1999). Accurate modeling of thin-wire antennas in the FDTD method. *Microwave and Optical Technology Letters*, 21(4):261–265.

Eswarappa, C. and Hoefer, W. J. R. (1995). Implementation of Berenger absorbing boundary conditions in TLM by interfacing FDTD perfectly matched layers. *Electron. Lett.*, 31(15):1264–1266.

Eswarappa, C. and Hoefer, W. J. R. (1996). Bridging the gap between TLM and FDTD. *IEEE Microwave and Guided Wave Letters*, 6(1):4–6.

Fang, J. and Xeu, D. (1995). Numerical errors in the computation of impedances by FDTD method and ways to eliminate them. *IEEE Microwave and Guided Wave Letters*, 5(1):6–8.

Foster, P. R. (2000). CAD for antenna systems. *Electronics and Communications Engineering Journal*, 12(1):3–14.

Fullagar, P., Zhang, P., Wu, Y., and Bertrand, M.-J. (1996). Application of radio frequency tomography to delineation of nickel sulphides in the Sudbury Basin. In *SEG 66th International Meeting & Exhibition, Extended Abstracts*, pages 2065–2068. Denver.

Gandhi, O. P., Gao, B.-Q., and Chen, J. (1993). A Frequency-Dependant Finite-Difference Time-Domain formulation for

general dispersive media. *IEEE Transactions on Microwave Theory and Techniques*, 41(4):658–665.

Gedney, S. D. (1996). An anisotropic perfectly matched layer-absorbing medium for the truncation of FDTD lattices. *IEEE Transactions on Antennas and Propagation*, 44(12):1630–1639.

Gedney, S. D. (1998). The perfectly matched layer absorbing medium. In *Advances in Computational Electrodynamics: the Finite-Difference Time-Domain Method*, chapter 5. Artech House.

Giannopoulos, A. (1997). *The Investigation of Transmission-Line Matrix and Finite-Difference Time-Domain Methods for the Forward Problem of Ground Probing Radar*. PhD thesis, University of York.

Giannopoulos, A. and Tealby, J. M. (1995). Comparison of performance of absorbing boundary conditions in TLM and FDTD. *Electron. Lett.*, 31(9):1639–1640.

Goldberg, D. E. (1989). *Genetic Algorithms in Search, Optimization & Machine Learning*. Addison–Wesley, Reading, Masschusetts.

Grando, J., Issac, F., Lemistre, M., and Alliot, J. C. (1993). Stability analysis including wires of arbitrary radius in FD-TD code. In *IEEE Antennas and Propagation International Symposium*, volume 1, pages 18–21.

Grant, F. S. and West, G. F. (1965). *Interpretation Theory in Applied Geophysics*. McGraw-Hill Book Company, New York.

Greenfield, R. J. and Wu, S. T. (1991). Electromagnetic wave propagation in disrupted coal seams. *Geophysics*, 56(10):1571–1577.

Grodner, M. (1998). Fracturing around a preconditioned deep level gold mine stope. In *GGM98 - International conference on*

Geomechanics/Ground Control in Mining and Underground Construction. Wollongong, Australia.

Grubb, R. N., Orswell, P. L., and Taylor, J. H. (1976). Borehole measurements of conductivity and dielectric constant in the 300 kHz to 25 MHz frequency range. *Radio Science*, 11(4):275–283.

Hamran, S.-E., Gjessing, D. T., Helmstad, J., and Aarholt, E. (1995). Ground penetrating synthetic pulse radar: Dynamic range and modes of operation. *Journal of Applied Geophysics*, 33(1–3):7–14.

Hansen, T. B. (1999). The far field of a borehole radar and its reflection at a planar interface. *IEEE Transactions on Geoscience and Remote Sensing*, 37(4):1940–1950.

Harrington, R. F. (1967). Matrix methods for field problems. *Proceedings of the IRE*, 55(2):136–149.

Hasted, J. B. (1973). *Aqueous Dielectrics*. Chapman and Hall, London.

He, J.-Q. and Liu, Q. H. (1998). A nonuniform cylindrical FDTD algorithm with PML for borehole radar modeling. In *IGARSS '98. Int. Geoscience and Remote Sensing Symp.*, volume 1, pages 285–287, Seattle, WA.

Heinz, W. F. (1985). *Diamond Drilling Handbook*. South African Drilling Association, Johannesburg.

Hewlett-Packard (1966). *HP 4815A RF Vector Impedance Meter Operating Manual*. Manual part no: 04815-90011.

Higdon, R. L. (1986). Absorbing boundary conditions for difference approximations to the multi-dimensional wave equation. *Mathematics of Computation*, 47(176):437–459.

Higdon, R. L. (1987). Numerical absorbing boundary conditions for the wave equation. *Mathematics of Computation*, 49(179):65–90.

Holland, R. and Simpson, L. (1981). Finite-difference analysis of EMP coupling to thin struts and wires. *IEEE Transactions on Electromagnetic Compatibility*, 23(2):88–97.

Hollender, F. and Tillard, S. (1998). Modelling ground–penetrating radar wave propagation and reflection with the Jonscher parameterization. *Geophysics*, 63(6):1933–1942.

Holliger, K. and Bergmann, T. (1998). Accurate and efficient FDTD modeling of ground-penetrating radar antenna radiation. *Geophysical Research Letters*, 25(20):3883–3886.

Howard, A. Q. and Kretzschmar, J. L. (1986). Synthesis of EM geophysical tomographic data. *Proceedings of the IEEE*, 74(2):353–360.

Johns, P. B. (1979). The art of modelling. *Electronics and Power*.

Johns, P. B. (1987). Reply to comments on "On the relationship between TLM and finite-difference methods for Maxwell's equations". *IEEE Transactions on Microwave Theory and Techniques*, 35(9):872–873.

Jurgens, T. G. and Saewert, G. W. (1995). The body of revolution FD-TD algorithm. In *Computational Electrodynamics: The Finite-Difference Time-Domain Method*, chapter 12, pages 397–430. Artech House.

Kent, L. E. (1980). South African Committee for Stratigraphy (SACS) Stratigraphy of South Africa. Part 1: Lithostratigraphy of the Republic of South Africa, South West Africa/Namibia and the Republics of Bophuthatswana, Transkei and Venda. In *Handbook of the Geolical Survey of South Africa, Volume 8*, Pretoria. Government Printer.

King, H. E. (1957). Mutual impedance of unequal length antennas in echelon. *IRE Transactions on Antennas and Propagation*, pages 306–313.

King, R. W. P. and Smith, G. S. (1981). *Antennas in Matter*. The MIT Press, Cambridge, Massachusetts.

King, R. W. P., Trembly, B. S., and Strohbehn, J. W. (1983). The electromagnetic field of an insulated antenna in a conducting or dielectric medium. *IEEE Transactions on Microwave Theory and Techniques*, 31:574–583.

Kong, J. A. (1986). *Electromagnetic Wave Theory*. John Wiley and Sons, New York.

Krumpholz, M., Huber, C., and Russer, P. (1995). A field theoretical comparison of FDTD and TLM. *IEEE Trans. Microwave Theory Tech.*, 43(8):1935–1950.

Kunz, K. S. and Luebbers, R. J. (1993). *The Finite Difference Time Domain Method for Electromagnetics*. CRC Press, Boca Raton, Florida.

Lager, D. L. and Lytle, R. J. (1977). Determining a subsurface electromagnetic profile from high-frequency measurements by applying reconstruction technique algorithms. *Radio Science*, 12(2):249–260.

Lee, J. P. Y. and Balmain, K. G. (1979). Wire antennas coated with magnetically and electrically lossy material. *Radio Science*, 14(3):437–445.

Lee, Y. H., Porter, S. J., and Marvin, A. C. (2000a). Genetic algorithms using real parameters for efficient antenna design optimisation. In *Millennium Conference on Antennas & Propagation*. ESA, Conference publication SP–444.

Lee, Y. H., Porter, S. J., and Marvin, A. C. (2000b). A statistical intercomparison of binary and decimal genetic algorithms. *16th Annual Review of Progress in Applied Computational Electromagnetics*, 1:70–77.

Liao, Z. P., Wong, H. L., Baipo, Y., and Yifan, Y. (1984). A transmitting boundary for transient wave analyses. *Scientia Sinica*, 27(10):1063–1076.

Liu, Q. H. (1999). Simulation of GPR in dispersive media using a frequency-dependent PSTD algorithm. *IEEE Transactions on Geoscience and Remote Sensing*, 37(5):2317–2324.

Liu, Q. H. and He, J. Q. (1998). Quasi-PML for waves in cylindrical coordinates. *Microwave and Optical Technology Letters*, 19(2):107–111.

Luebbers, R. J. and Hunsberger, F. (1992). FDTD for Nth–order dispersive media. *IEEE Transactions on Antennas and Propagation*, 40(11):1297–1301.

Maloney, J. G. and Smith, G. S. (1992). The efficient modeling of thin material sheets in the Finite-Difference Time-Domain (FDTD) method. *IEEE Transactions on Antennas and Propagation*, 40(3):323–330.

Maloney, J. G. and Smith, G. S. (1993). A study of transient radiation from the Wu–King resistive monopole — FDTD analysis and experimental measurements. *IEEE Transactions on Antennas and Propagation*, 41(5):668–675.

Maloney, J. G., Smith, G. S., and Scott, Jr, W. R. (1990). Accurate computation of the radiation from simple antennas using the Finite-Difference Time-Domain method. *IEEE Transactions on Antennas and Propagation*, 38(7):1059–1068.

Maré, L. P. and Oosthuizen, B. P. (1999). South African Geophysical Atlas, Volume IV: Physical properties of South African rocks. Technical report, Council for Geoscience.

Milligan, T. (1985). *Modern Antenna Design*. McGraw–Hill, New York.

Moghaddam, M. (1990). *Modeling of the Subsurface Interface Radar*. PhD thesis, Dept of Electrical and Computer Engineering, University of Illinois at Urbana-Champaign.

Mohorovičić, A. (1910). Earthquake of 8th of October, 1909 (Potres od 8.x.1909). *Jahrbuch des Meteorologischen Obsevatoriums in Zagreb (Agram) für das Jahr 1909*, 4(1):1–63.

Moore, R. K. (1963). Effects of a surrounding conducting medium on antenna analysis. *IEEE Transactions on Antennas and Propagation*, 11:216–225.

Nickel, H. and Cerny, I. (1989). More effective underground exploration for ores using radio waves. *Exploration Geophysics*, 20:371–377.

Noon, D. A. (1996). *Stepped-Frequency Radar Design and Signal Processing Enhances Ground Penetrating Radar Performance*. PhD thesis, The University of Queensland.

Pereda, J. A., García, O., Vegas, A., and Prieto, A. (1998). Numerical dispersion and stability analysis of the FDTD technique in lossy dielectrics. *IEEE Microwave and Guided Wave Letters*, 8(7):245–247.

Petropoulos, P. G. (1994a). Modelling propagation and scattering in dispersive dielectrics with FD-TD. In *Proceedings of the 10th Annual Review of Progress in Applied Computational Electromagnetics*. Monterey, California.

Petropoulos, P. G. (1994b). Stability and phase error analysis of FD-TD methods in dispersive media. *IEEE Transactions on Antennas and Propagation*.

Pitts, B. E. and Kramers, A. P. (1995). The application of high resolution geophysics to base metal mining. In *Extended Abstracts, 4th Technical Meeting*, pages 170–173. Victoria Falls.

Ramahi, O. M. (1997a). Complementary boundary operators for wave propagation problems. *Journal of Computational Physics*, 133:113–128.

Ramahi, O. M. (1997b). Concurrent implementation of the complementary operators method in 2-D space. *IEEE Microwave and Guided Wave Letters*, 7(6):165–167.

Ramahi, O. M. (1998). The concurrent complementary operators method for FDTD mesh truncation. *IEEE Transactions on Antennas and Propagation*, 46(10):1475–1482.

Ramahi, O. M. and Schneider, J. B. (1998). Comparitive study of the PML and C-COM mesh-truncation techniques. *IEEE Microwave and Guided Wave Letters*, 8(2):55–57.

Ramo, S., Whinnery, J. R., and Van Duzer, T. (1993). *Fields and Waves in Communication Electronics*. John Wiley & Sons, New York.

Randhawa, B. S. (1996). *Electromagnetic Modelling of Curved Structures Using a Hybrid Finite-Volume Finite Difference Time-Domain Method*. PhD thesis, University of York.

Rao, V. M. and Rao, I. B. R. (1983). The radio wave absorption technique in Mailaram Copper Mines, India. *Geophysics*, 48(3):391–395.

Rappaport, C. M. (1995). Perfectly matched absorbing boundary conditions based on anisotropic lossy mapping of space. *IEEE Microwave and Guided Wave Letters*, 5(3):90–92.

Richmond, J. H. and Newman, E. H. (1976). Dielectric coated wire antennas. *Radio Science*, 11(1):13–20.

RSI (1995). *Using IDL*. Research Systems, Inc., Boulder, Colorado.

Sacks, Z. S., Kingsland, D. M., Lee, R., and Lee, J.-F. (1995). A perfectly matched anisotropic absorber for use as an absorbing boundary condition. *IEEE Transactions on Antennas and Propagation*, 43(12):1460–1463.

Saito, H., Shima, H., Toshioka, T., Kaino, S.-I., and Ohtomo, H. (1990). A case study of geotomography applied to a detailed investigation of a highway bridge foundation. In *Geophysical Applications for Geotechnical Investigations, ASTM STP 1101*, pages 17–34. American Society for Testing and Materials, Philadelphia.

Sato, M. and Thierbach, R. (1991). Analysis of a borehole radar in cross-hole mode. *IEEE Transactions on Geoscience and Remote Sensing*, 29(6):899–904.

Schlager, K. L. and Schneider, J. B. (1995). A selective survey of the finite-difference time-domain literature. *IEEE Antennas and Propagation Magazine*, 37(4):39–57.

Schlager, K. L. and Schneider, J. B. (1998). A survey of the finite-difference time-domain literature. In *Advances in Computational Electrodynamics: The Finite-Difference Time-Domain Method*, chapter 1, pages 1–62. Artech House, Boston.

Schuster, C., Christ, A., and Fichtner, W. (2000). Review of FDTD time-stepping schemes for efficient simulation of electric conductive media. *Microwave and Optical Technology Letters*, 25(1):16–21.

Shen, G. and Chen, Y. (2000). A nonuniform cylindrical FDTD algorithm for analysis of generalized cylindrical electromagnetic problems. *Microwave and Optical Technology Letters*, 24(1):46–51.

Silvester, P. P. and Ferrari, R. L. (1996). *Finite Elements for Electrical Engineers*. Cambridge University Press, third edition.

Singer, H., Brühns, H. D., Mader, T., Freiberg, A., and Bürger, G. (1997). *Concept II: Manual of the program system*. Universtät Hamburg-Harburg, Hamburg.

Smith, G. S. and Scott, W. R. (1989). A scale model for studying ground penetrating radars. *IEEE Transactions on Geoscience and Remote Sensing*, 27(4):358–363.

Somerstein, S. F., Berg, M., Chang, D., Chung, H., Johnson, H., Richardson, B., Pizzicara, J., and Salisbury, W. W. (1984). Radio-frequency Geotomography for remotely probing the interiors of operating mini- and commercial-sized oil-shale retorts. *Geophysics*, 49(8):1288–1300.

Spiegel, M. R. (1971). *Advanced Mathematics for Engineers and Scientists*. Schaum Series. McGraw–Hill, London, SI (Metric) edition.

Stolarczyk, L. G. (1992). Definition imaging of an orebody with the radio imaging method (RIM). *IEEE Transactions on Industry Applications*, 28(5):1141–1147.

Sullivan, D. M. (1992). Frequency-dependant FDTD methods using Z transforms. *IEEE Transactions on Antennas and Propagation*, 40(10):1223–1230.

Sullivan, D. M. (1996). A simplified PML for use with the FDTD method. *IEEE Microwave and Guided Wave Letters*, 6(2):97–99.

Sultan, M. F. and Mittra, R. (1985). An iterative moment method for analyzing the electromagnetic field distribution inside inhomogenous lossy dielectric objects. *IEEE Transactions on Microwave Theory and Techniques*, 33(2):163–168.

Taflove, A. (1995). *Computational Electrodynamics, The Finite-Difference Time-Domain Method*. Artech House, Boston.

Taflove, A. (1998). *Advances in Computational Electrodynamics, The Finite-Difference Time-Domain Method.* Artech House, Boston.

Tai, C. T. (1999). Teaching electrodynamics without magnetism. *IEEE Antennas and Propagation Magazine*, 41(5):60–67.

Takasugi, S., Miura, Y., and Arai, E. (1996). Conceptual design of an electromagnetic tomography system. *Journal of Applied Geophysics*, 35:199–207.

Teixeira, F. L. and Chew, W. C. (1997). PML-FDTD in cylindrical and spherical grids. *IEEE Microwave and Guided Wave Letters*, 7(9):285–287.

Teixeira, F. L., Chew, W. C., Straka, M., Oristaglio, M. L., and Wang, T. (1997). 3D PML-FDTD simulation of ground penetrating radar on dispersive earth media. In *IGARSS '97. Int. Geoscience and Remote Sensing Symp.*, volume 2, pages 945–947, Singapore.

Turner, G. (1993). *The Influence of Subsurface Properties on Ground Penetrating Radar Pulses*. PhD thesis, Macquarie University.

Umashankar, K. R., Taflove, A., and Beker, B. (1987). Calculation and experimental validation of induced currents on coupled wires in an arbitrary shaped cavity. *IEEE Transactions on Antennas and Propagation*, 35(11):1248–1257.

Uno, T., He, Y., and Adachi, S. (1997). Perfectly Matched Layer absorbing boundary condition for dispersive medium. *IEEE Microwave and Guided Wave Letters*, 7(9):264–266.

Van Den Berghe, S., Olyslager, F., and De Zutter, D. (1998). Accurate modeling of thin conducting layers in FDTD. *IEEE Microwave and Guided Wave Letters*, 8(2):75–77.

Van Schoor, M. and Duvenhage, D. (1999). Comparison of crosshole radio imaging and electrical resistivity tomography for mapping out disseminated sulphide mineralisation at a surface test site in Mpumalanga, South Africa. *Exploration Geophysics*, 30:135–139.

Van Schoor, M., Wedepohl, E. C., and Vogt, D. R. (1997). An assessment of the current Radio Tomography imaging capabilities – results of a 2D computer simulation study. In *Extended Abstracts, 5th Technical Meeting*. Swakopmund.

Van Tonder, J. J. (1995). *Electromagnetic Radiation by Planar Antennas Buried in Layered Media*. PhD thesis, University of Stellenbosch.

Vasco, D. W., Peterson Jr., J. E., and Lee, K. H. (1997). Ground–penetrating radar velocity tomography in heterogenous and anisotropic media. *Geophysics*, 62(6):1758–1773.

Veihl, J. C. and Mittra, R. (1996). An efficient implementation of Berenger's perfectly matched layer (PLML) for Finite-Difference Time-Domain mesh truncation. *IEEE Microwave and Guided Wave Letters*, 6(2):94–96.

Vogt, D. R. (1995). Radiowave tomography: a case study of reliable, redeployable distributed control underground. In *Proceedings of the 8th IFAC international symposium on automation in mining, mineral and metal processing*. Sun City, South Africa.

Vogt, D. R., Tealby, J. M., and Marvin, A. C. (1999). Modelling of radio tomography antennas using the Finite-Difference Time-Domain technique. In *IEE Conference Publication 461*, pages 225–229.

Waters, K. H. (1978). *Reflection Seismology*. John Wiley & Sons, New York.

Wedepohl, E. C. (1993). Radio Wave Tomography: Imaging ore bodies using radio waves. In *Extended Abstracts, 3rd Technical Meeting*. Cape Town.

Wedepohl, E. C. (1996). The importance of being honest: What can we really do with high resolution geophysics? (with apologies to Oscar Wilde). In *Extended Abstracts, 66th International Exposition and annual meeting*. Denver.

Weedon, W. H. and Rappaport, C. M. (1997). A general method for FDTD modeling of wave propagation in arbitrary frequency-dispersive media. *IEEE Transactions on Antennas and Propagation*, 45(3):401–409.

Wilt, M., Lee, K., Alumbaugh, D., Morrison, H. F., Becker, A., Tseng, H.-W., and Torres-Verdin, C. (1995). Crosshole Electromagnetic Tomography: A new technology for oil field characterization. *The Leading Edge*, pages 173–177.

Wu, J.-Y., Kingsland, D. M., Lee, J.-F., and Lee, R. (1997). A comparison of anisotropic PML to Berenger's PML and its application to the Finite-Element Method for EM scattering. *IEEE Transactions on Antennas and Propagation*, 45(1):40–50.

Yee, K. S. (1966). Numerical solution of initial boundary value problems involving Maxwell's equations in isotropic media. *IEEE Transactions on Antennas and Propagation*, 14(3):302–307.

Young, J. L. (1995). Propagation in linear dispersive media: Finite–difference time–domain methodologies. *IEEE Transactions on Antennas and Propagation*, 43(4):422–426.

Yu, L., Chouteau, M., Boerner, D. E., and Wang, J. (1998). On the imaging of radio-frequency electromagnetic data for cross-borehole mineral exploration. *Geophysics Journal International*, 135(2):523–541.

Zhao, L. and Cangellaris, A. C. (1996). A general approach for the development of unsplit-field time-domain implementations of perfectly matched layers for FDTD grid truncation. *IEEE Microwave and Guided Wave Letters*, 6(5):209–211.

Zhou, B., Fullagar, P., and Fallon, G. (1998). Radio frequency tomography trial at Mt. Isa Mine. *Exploration Geophysics*, 29:675–679.

Ziolkowski, R. W. (1997a). The design of Maxwellian absorbers for numerical boundary conditions and for practical applications using engineered artificial materials. *IEEE Transactions on Antennas and Propagation*, 45(4):656–671.

Ziolkowski, R. W. (1997b). Time-derivative Lorentz material model-based absorbing boundary condition. *IEEE Transactions on Antennas and Propagation*, 45(10):1530–1535.

Index